

MICROSTRUCTURE AND WEAR OF ALUMINIUM - SILICON ALLOY - GRAPHITE COMPOSITES

by

SATYABRATA DAS

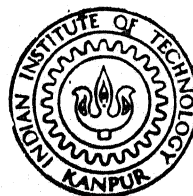
ME

1988

D

DAS

MIC



DEPARTMENT OF METALLURGICAL ENGINEERING

INDIAN INSTITUTE OF TECHNOLOGY, KANPUR

DECEMBER, 1988

MICROSTRUCTURE AND WEAR OF ALUMINIUM - SILICON ALLOY - GRAPHITE COMPOSITES

A Thesis Submitted
In Partial Fulfilment of the Requirements
for the Degree of
DOCTOR OF PHILOSOPHY

by
SATYABRATA DAS

to the
DEPARTMENT OF METALLURGICAL ENGINEERING
INDIAN INSTITUTE OF TECHNOLOGY, KANPUR
DECEMBER, 1988

12 JUL 1990
CENTRAL LIBRARY
I. I. T., KANPUR
Acc. No. A.108432

Th
669.722
D26 m

ME-1900-D-DAS-MIC

*Dedicated
To
My Parents*

CERTIFICATE

This is to certify that the thesis entitled,
'MICROSTRUCTURE AND WEAR OF ALUMINIUM-SILICON ALLOY-GRAPHITE COMPOSITES'
by Mr. Satyabrata Das has been carried out under our supervision and
that the work has not been submitted elsewhere for a degree.

S.V. Prasad

(S.V. Prasad)
Scientist,
R.R.L.(CSIR)
BHOPAL.

T.R. Ramachandran

(T.R. Ramachandran)
Professor
Dept. of Metallurgical Engineering
I.I.T., KANPUR.

ACKNOWLEDGEMENTS

I wish to record my deep sense of gratitude and appreciation to my thesis supervisors, Professor T.R. Ramachandran, Department of Metallurgical Engineering, I.I.T., Kanpur and Dr.S.V. Prasad, Scientist, R.R.L., Bhopal for suggesting the problem and valuable guidance throughout the course of this work.

Also, I take this opportunity to express my gratitude to Professor P.K. Rohatgi, Materials Department, The University of Wisconsin-Milwaukee, USA, for his encouragement and guidance at the initial stage of this thesis while he was the Director of Regional Research Laboratory (CSIR), Bhopal.

The author is grateful to Director, Regional Research Laboratory (CSIR), Bhopal for kind permission and extending facilities including those for experimental studies.

Special thanks are due to all my colleagues who have provided me with their timely assistance whenever it was sought for.

I can not express in words my feelings towards my wife, for her extraordinary patience, moral support, understanding and all kinds of help during this period of ordeal.

My word of thanks goes to Mr. M. Davood Khan, Department of Electrical Engineering, M.A. College of Technology, Bhopal for his skilful typing and patience and to Mr. B.K. Jain, I.I.T., Kanpur for neat tracing of figures.

Satyabrata Das.
(Satyabrata Das)

TABLE OF CONTENTS

	Page
LIST OF TABLES	x
LIST OF FIGURES	xii
SYNOPSIS	xx
CHAPTER 1 INTRODUCTION	1
CHAPTER 2 BACKGROUND LITERATURE	11
2.1 Microstructure of Al-Si Alloys	11
2.1.1 Solidification Behaviour and Micro-structure of Al-Si Alloys	11
2.1.2 Modification of Eutectic Silicon	12
2.1.3 Refinement of Primary Silicon	20
2.1.4 Rapid Solidification Processing	21
2.2 Aluminium Alloy Composites	26
2.2.1 Steps Involved in the Solidification Processing of Cast Metal Matrix-Particle Composites	30
2.2.2 Techniques of Introducing Particles in the Melt	32
2.2.3 Interfaces and Role of Wettability	32
2.2.4 Interaction Between Suspended Particles and Growing Solids	39
2.2.5 Microstructure of Composites	40
2.2.6 Physical and Mechanical Properties	43
2.2.7 Rapidly Solidified Metal Matrix-Particle Composites	46
2.3 Wear	48
2.3.1 Sliding Wear of Aluminium-Silicon Alloys	50

2.3.2	Study of Wear Surfaces	53
2.3.3	Subsurface Deformation	54
2.3.4	Aluminium-graphite Composites	54
2.3.4.1	Dry Sliding Wear	54
2.3.4.2	Lubricated Wear	55
2.3.4.3	Bearing Performance	58
2.3.4.4	Subsurface Deformation	58
2.3.4.5	Oil Spreadability	61
2.3.4.6	Component Testing	61
CHAPTER 3	SCOPE OF THE PRESENT WORK	62
CHAPTER 4	MATERIALS AND METHODS	64
4.1	Materials	64
4.1.1	Matrix Alloys	64
4.1.2	Graphite Particles	64
4.2	Melting Procedure	64
4.2.1	Composite Preparation	65
4.2.2	Production of Rapidly Solidified Ribbons	68
4.2.3	Heat Treatment	71
4.3	Methods	71
4.3.1	Particle Size Analysis	71
4.3.2	Optical Microscopy	71
4.3.3	Scanning Electron Microscopy	72
4.3.4	X-Ray Diffraction	72
4.3.5	Tensile Testing	72
4.3.6	Hardness	72

4.4	Sliding Wear	73
4.4.1	Dry Sliding Wear	73
4.4.2	Partially Lubricated Sliding Wear	73
4.4.3	Subsurface studies	75
4.4.4	Abrasion Test	75
4.4.5	Surface Roughness Measurement	76
CHAPTER 5	RESULTS	78
5.1	Introduction	78
5.2	Characterisation of Graphite Particles	78
5.2.1	X-Ray Diffraction	78
5.2.2	Particle Size Analysis	81
5.2.3	Scanning Electron Microscopic Studies	81
5.3	Microstructure	81
5.3.1	LM6 Alloy and Composites	81
5.3.2	LM13 Alloy and Composites	90
5.3.3	LM30 Alloy and Composites	100
5.3.4	Microdistribution of Graphite Particles in Al-Si Alloy Matrices	108
5.3.5	Microstructure of Rapidly Solidified Al-Si Alloy and Composites	116
5.4	Mechanical Properties of Al-Si Alloys and Composites	121
5.4.1	Ultimate Tensile Strength	121
5.4.2	Hardness	121
5.5	Wear	123
5.5.1	Dry Sliding Wear	123
5.5.1.1	Effect of Pressure	123
5.5.1.2	LM6 Alloy and LM6-graphite Particle Composites	129

5.5.1.3	LM13 Alloy and LM13-Graphite Particle Composites	132
5.5.1.4	LM30 Alloy and LM30-Graphite Particle Composites	135
5.5.1.5	Coefficient of Friction	138
5.5.2	Scanning Electron Microscopic Examination of Worn Surfaces	138
5.5.2.1	LM6 Alloy and LM6-Graphite Particle Composites	142
5.5.2.2	LM13 Alloy and LM13-Graphite Particle Composites	145
5.5.2.3	LM30 Alloy and LM30-Graphite Particle Composites	149
5.5.3	Scanning Electron Microscopic Examination of Wear Debris	153
5.5.4	X-Ray Diffraction Studies of Wear Debris	164
5.5.5	Scanning Electron Microscopic Examination of Subsurface	173
5.5.6	Partially Lubricated Sliding Wear	176
5.5.6.1	P-V Limits of Die Cast LM6, LM13 and LM30 Alloys	176
5.5.6.2	LM6 Alloy and LM6-Graphite Particle Composites	178
5.5.6.3	LM13 Alloy and LM13-Graphite Particle Composites	180
5.5.6.4	LM30 Alloy and LM30-Graphite Particle Composites	193
5.5.7	Abrasive Wear of Rapidly Solidified LM13 Alloy	195

CHAPTER 6	GENERAL DISCUSSION	209
6.1	Introduction	209
6.2	Microstructure of Al-Si Alloys	209

6.3	Microstructure of Al-Si Alloys in the presence of Dispersed Graphite Particles	210
6.4	Modification of Eutectic Silicon	212
6.5	Refinement of Primary Silicon	213
6.6	Heat Treatment	215
6.7	Shape and Morphology of Silicon in Al-Si Eutectic	215
6.8	Tribology of Graphite	218
6.9	Role of Interfaces	218
6.10	Role of the Matrix	220
6.11	Delamination	221
6.12	Sources of Crack Nucleation and Effect of Silicon Morphology	221
6.13	Graphite Film Formation and Wear of Composites	226
CHAPTER 7	CONCLUSIONS	229
REFERENCES		233

LIST OF TABLES

Table No.		Page
I.1	Alloy designation, compositions and mechanical properties of Al-Si alloy castings	4-5
I.2	Applications of aluminium-silicon alloys	6
I.3	Intermetallic phases in aluminium-rich aluminium alloy system	7
II.1	List of manufacturer of aluminium alloy-fibre composites	27-28
II.2	Particle dispersed aluminium alloy composites synthesised in recent years	29
IV.1	Heat number and sequence of addition of phosphorus, sodium and graphite	69
V.1	X-Ray diffraction results of graphite particle	79
V.2	Graphite particle size distribution	82
V.3	Distribution of interparticle spacing	96-97
V.4	Graphite particle size distribution	98-99
V.5	Average interparticle spacing	101
V.6	Average particle size	101
V.7	X-Ray diffraction results of rapidly solidified Al-Si(LM6) alloy and composites	120
V.8	Mechanical properties of Al-Si (LM6, LM13 and LM30) alloy and composites	122
V.9	Particle size distribution of equiaxed wear debris	128
V.10	Coefficient of friction of LM6 alloy and composites (dry sliding wear)	139
V.11	Coefficient of friction of LM13 alloy and composites (dry sliding wear)	140
V.12	Coefficient of friction of LM30 alloy and composites (dry sliding wear)	141

V.13	Particle size distribution of flaky wear debris of die cast LM13 alloy	162
V.14	Particle size distribution of flaky wear debris of LM13-graphite composite in heat treated condition	162
V.15	Particle size distribution of flaky wear debris of die cast LM30 alloy	166
V.16	Particle size distribution of sharp-edged silicon wear debris obtained from die cast LM30 alloy	166
V.17	X-Ray diffraction results of wear debris (die cast LM30 alloy)	171
V.18	X-Ray diffraction results of wear debris (Heat treated LM30-graphite and LM6-graphite)	172
V.19	Maximum temperature attained during partially lubricated sliding wear of LM6 alloy and composites	181-182
V.20	Coefficient of friction of LM6 alloy and composites (during partially lubricated sliding wear)	183-185
V.21	Maximum temperature attained during partially lubricated sliding wear of LM13 alloy and composites	188
V.22	Coefficient of friction of LM13 alloy and composites (during partially lubricated sliding wear)	189-192
V.23	Maximum temperature attained during partially lubricated sliding wear of LM30 alloy and composites	196-197
V.24	Coefficient of friction of LM30 alloy and composites (during partially lubricated sliding wear)	198-201

LIST OF FIGURES

Fig.No.		Page
2.1	Binary phase diagram of aluminium-silicon alloy	12
2.2	Enlarged diagram of the aluminium-rich solidus and solvus	13
2.3	Impact of modification by sodium addition on the location of liquidus curves and eutectic equilibrium temperature. Full lines show the equilibrium phase diagram	16
2.4	Impact of high cooling rates (1 to 2 °C/s) on location of the liquidus curves and eutectic equilibrium temperature in the Al-Si system. Full lines show the equilibrium phase diagram	17
2.5	Location of liquidus curves and eutectic lines in aluminium-silicon system under high hydrostatic pressure	19
2.6	Effect of silicon on the lattice parameter of quenched aluminium solid solution (■ and X were quenched from single phase solid region; others were liquid quenched)	22
2.7	T ₀ curves and metastable extensions of the phase boundaries	24
2.8	Steps involved in solidification processing of cast composites	31
2.9	Schematic of transfer of a particle from a gas to a liquid indicating the various surface energy contributions and contact angle	34
2.10	Strength versus volume fraction of graphite particle in aluminium-graphite system	44
2.11	Wear of Al-8% Si alloy	51
2.12.	(a) Wear rate against load of as-cast low silicon alloy pins sliding on a hard steel bush at a surface speed of 196 cm/s	52
	(b) Wear rate against load of as-cast silicon alloy pins sliding on a hard steel bush at a surface speed of 196 cm/s (high silicon alloy)	52

2.13	(a) Variation of coefficient of friction with graphite addition	56
	(b) Variation in temperature rise with graphite addition	56
2.14	Normalised wear rate	57
2.15	Typical curve of temperature change with time for alloys with continuous lubrication and lubrication discontinued after one minute	59
2.16	Galling behaviour of graphite aluminium alloys as a function of graphite content (over a size range of 20 to 400 μm)	60
4.1	(a) Stirrer assembly for preparation of composites	67
	(b) Melt spinning unit	70
4.2	(a) Pin-on-disc wear test apparatus, (b) magnified view of disc (A) and sample holder (B) and (c) shows the actual position of pin and disc during wear testing	74
4.3	Stylus apparatus (Talysurf 6)	77
5.1	Typical X-Ray diffractograms of : (a) as received particles and (b) heat treated graphite particles	80
5.2	Size distribution of graphite particles	83
5.3	(a) Scanning electron micrograph of graphite particles and (b) magnified scanning electron micrograph of graphite particles	84
5.4	Scanning electron micrographs of LM6 alloy: (a) die cast condition (b) magnified micrograph of die cast alloy showing plate-shaped eutectic silicon (c) sodium modified and (d) magnified view of the sodium modified alloy	85
5.5	(a) Scanning electron micrograph of an intermetallic phase observed in die cast LM6 alloy (b) Aluminium X-Ray mapping and (c) Iron X-Ray mapping, corresponding to (a)	87
5.6	Scanning electron micrographs of LM6 alloy in heat treated condition showing: (a) spherical silicon particles (b) coarse irregular silicon particles and intermetallic phase and (c) coarse intermetallic phase	88

5.7	Optical micrographs of LM6-graphite composite: (a) showing distribution of graphite particles (b) graphite particles in heat treated matrix and (c) nearly spherical silicon particles around the graphite particle	89
5.8	Micrographs of LM13 alloy: (a) die cast condition (b) interconnected eutectic silicon (c) heat treated condition (d) magnified view of (c) and (e) optical micrograph of heat treated sample showing inter- metallic compound with different etching behaviour	91
5.9	Optical micrograph of LM13-graphite composite showing distribution of graphite particles	92
5.10	Distribution of particles: (a) interparticle spacing and (b) particle size in die cast LM13 alloy- graphite composites across three different section along the ingot length, (i) top, (ii) middle and (iii) bottom for three successive pouring-initial, int- ermediate and final	93-94
5.11	Optical micrographs showing distribution of graphite particles in (a) top, (b) middle and (c) bottom portion of casting	95
5.12	Optical micrographs of LM30 alloy (a) die cast (b) plate-shaped eutectic silicon in the interdendritic region, (c) combination of primary silicon plates originating from a common nucleating point and primary aluminium halo formation around the primary silicon	102
5.13	Optical micrographs of LM30 alloy: (a) unrefined condition, (b) refined primary silicon with phosphorus (c) showing unmodified eutectic silicon in refined alloy and (d) refined and modified primary and eutectic silicon respectively	103
5.14	Unmodified eutectic silicon when sodium was added in LM30 alloy composites after dispersing graphite	105
5.15	Optical micrograph showing: (a) graphite particles in refined and modified LM30-graphite composite and (b) primary silicon nucleating around the graphite particle	106
5.16	Scanning electron micrographs of heat treated LM30-graphite composites: (a) showing graphite particle, primary silicon, primary aluminium and eutectic silicon (b) aluminium X-Ray mapping (c) silicon X-Ray mapping, (d) carbon X-Ray mapping and (e) near spherical eutectic silicon	107

5.17	Intermetallic phases in heat treated LM30-graphite composites: (a) showing intermetallic phases (b) aluminium X-Ray mapping (c) silicon X-Ray mapping (d) iron X-Ray mapping and (e) copper X-Ray mapping	109
5.18	intermetallic phases in heat treated LM30-graphite composites:(a)intermetallic phase (b) aluminium X-Ray mapping (c) copper X-Ray mapping (d) iron X-Ray mapping	110
5.19	Scanning electron micrographs of LM13-graphite composites: (a) showing graphite particles in the last freezing eutectic liquid and (b) magnified view showing Al-Si eutectic phase around the graphite particle	111
5.20	Schematic representation of microstructure between two graphite particles for the conditions: (a) $IPS \gg 2DAS$, (b) $IPS = 2 DAS$ and (c) $IPS < 2DAS$ IPS:Interparticle spacing, DAS:Secondary dendrite arm spacing	113
5.21	(a) Nucleation of primary aluminium between two graphite particles in LM13 alloy-graphite composite and (b) magnified picture showing layer of silicon particle between primary aluminium and graphite particle	114
5.22	Schematic representation of the microstructure of hypoeutectic Al-Si alloy in the presence of graphite particle for the conditions:(a) $D \gg X$ and (b) $D \leq X$; D = Distance between dendrite tip and particle, X = length of the eutectic silicon in conventionally die cast Al-Si alloy without graphite particle	115
5.23	(a) Scanning electron micrograph showing modified and unmodified eutectic silicon around the graphite particle and (b) micrograph showing modified eutectic silicon between two graphite particles	117
5.24	Scanning electron micrograph showing: (a) microstructure of rapidly solidified LM6 alloy, (b) rapidly solidified LM6-graphite composite (c) magnified picture showing plate-shaped eutectic silicon near the graphite particle and (d) microstructure well away from the graphite particle (e) microstructure of rapidly solidified LM13 alloy	118
5.25	Effect of pressure on the dry sliding wear rate of die cast LM6, LM13 and LM30 alloys (sliding speed:2.68 m/s	124

5.26	Micrographs of (a) worn surface of die cast LM6 alloy (pressure:1.0 MPa), (b) Wear debris collected from wear test (a), (c) worn surface of die cast alloy (pressure:1.5 MPa) and (d) wear debris corresponding to (c)	126
5.27	Particle size distribution of equiaxed wear debris corresponding to Fig.5.26 (b)	127
5.28	Effect of pressure on dry sliding wear of LM6 alloy and composite (sliding speed: 2.68 m/s, S: seizure)	130
5.29	Time-temperature relationship in LM6 alloy and composite during dry sliding wear	131
5.30	Effect of pressure on the dry sliding wear of LM13 alloy and composite	133
5.31	Time-temperature relationship of LM13 alloy and composite	134
5.32	Effect of pressure on the dry sliding wear of LM30 alloy and composite	136
5.33	Time-temperature relationship of LM30 alloy and composite	137
5.34	Micrographs of : (a) worn surface of die cast LM6 alloy showing continuous grooves and damaged regions, (b) magnified view of the region marked 'A' in (a) and (c) worn surface showing delaminated region and cracks running along the wear track and transverse direction to the wear track	143
5.35	Micrograph of (a) worn surface of die cast LM6 alloy showing grooves and damaged region and (b) iron X-Ray mapping of (a)	144
5.36	Micrographs of worn surface of LM6-graphite composite showing: (a) continuous grooves and delaminated region (b) and (c) flaky particles about to detach from the wear surface and (d) parallel lips along the wear scar	146
5.37	Micrographs of worn surface of die cast LM13 alloy showing: (a) continuous grooves and damaged region, and (b) number of cracks joining together to form wear debris	147
5.38	Micrographs of worn surface of die cast LM13-graphite composite: (a) parallel grooves and damaged region and (b) parallel lips along the wear scar	148

5.39	Micrographs of worn surface of heat treated LM13 alloy showing: (a) grooves and damaged region (b) transverse cracks and damaged region (c) magnified view of the region marked by arrow in (b) and (d) transverse cracks	150
5.40	Micrographs of worn surface of LM13-graphite composite in heat treated condition, showing: (a) graphite layer on composite surface and (b) graphite layer and surface damage where there is no graphite layer	151
5.41	Micrographs of worn surface of (a) die cast LM30 alloy showing continuous grooves and damaged regions, (b) LM30-P-Na, showing fine transverse cracks and damaged regions and (c) LM30-graphite composite showing grooves and damaged regions	152
5.42	(a) Micrograph of worn surface of heat treated LM30-graphite composite and (b) carbon X-Ray mapping corresponding to (a)	154
5.43	Scanning electron micrograph of flake-shaped debris particles: (a) from die cast LM30 alloy at a pressure of 3.0 MPa, (b) from die cast LM13 alloy at a pressure of 1.5 MPa (c) a typical debris particle and (d) aluminium X-Ray mapping	156
5.44	(a) typical debris particle collected from die cast LM13 alloy, (b) aluminium X-Ray mapping and (c) silicon X-Ray mapping	157
5.45	(a) typical flake-shaped debris particle collected from LM6 alloy (b) aluminium X-Ray mapping (c) debris particle collected from LM6 alloy; the thickness of the debris is relatively higher than those shown before	158
5.46	(a) Wear debris collected from heat treated LM13 alloy-graphite composite (b) particle size distribution of flaky wear debris obtained from LM13 alloy (die cast), (c) from heat treated LM13 alloy-graphite composite and (d) die cast LM30 alloy	159-1
5.47	Sharp-edged faceted particles obtained from (a) LM6 alloy (die cast), (b) silicon X-Ray mapping (c) and (d) are obtained from die cast LM30 alloy, and (e) from heat treated LM13-graphite composite (pressure: 3.0 MPa)	163
5.48	Particle size distribution of sharp-edged silicon particles obtained from die cast LM30 alloy (pressure: 3.0 MPa)	165

5.49	A typical debris particle characteristics of machining chips, obtained from heat treated LM13 alloy	167
5.50	X-Ray diffraction trace of debris from (a) die cast LM30 alloy, (b) heat treated LM30-graphite (c) LM6-graphite and (d) double sided adhesive tape	168- 174
5.51	Subsurface structure of LM30 alloy showing (a) deformed silicon (b) fragmentation of primary silicon, (c) LM6-graphite composite showing fragmented silicon and graphite particles (d) fragmented eutectic silicon in the subsurface region and (e) unaffected eutectic silicon away from the subsurface	175
5.52	Pressure-velocity limit for die cast LM6, LM13 and LM30 alloys	177
5.53	Pressure-velocity limits for LM6 alloy and composites	179
5.54	Pressure-velocity limits for LM13 alloy and composites	186
5.55	Pressure-velocity limits for LM30 alloy and composites	194
5.56	Effect of sliding distance on the abrasive wear of die cast and rapidly solidified LM13 alloy	202
5.57	(a) Effect of applied load on the abrasive wear of die cast and rapidly solidified LM13 alloy (b) Effect of applied load on the relative abrasion (Ra) of die cast and rapidly solidified LM13 alloy	203 205
5.58	Scanning electron micrographs of abraded samples of LM13 alloy: (a) and (b) die cast alloy; (c) and (d) rapidly solidified alloy (Load 1.4 N)	206
5.59	Scanning electron micrographs of abraded samples of LM13 alloy: (a) and (b) die cast alloy: (c) and (d) rapidly solidified alloy (Load: 7.0 N)	207
5.60	Scanning electron micrograph of the opposite side of abraded sample of rapidly solidified LM13 alloy (Load: 7.0 N)	208
6.1	(a) l/d ratio of LM6 alloy and composites (b) l/d ratio LM13 alloy and composite	216 217

6.2	Schematic drawing illustrating the importance of particle-matrix interfacial bond during sliding wear G: Graphite, M: Matrix	219
6.3	Schematic representation of the various stages involved in the formation of delamination wear sheets	222
6.4	Schematic representation of silicon morphologies in Al-Si alloy	224
6.5	Schematic illustration of the conditions: (i) graphite not offering lubrication and (ii) graphite offering lubrication	225
6.6	Coefficient of friction of Al-Si alloys and composites under dry sliding wear	227

MICROSTRUCTURE AND WEAR OF ALUMINIUM-SILICON ALLOY-GRAPHITE COMPOSITES

SYNOPSIS

The casting characteristics of aluminium can be improved to a great extent by the addition of silicon. Such an improvement is imparted by the presence of relatively large volume fraction of Al-Si eutectic in the melt. Besides this, Al-Si alloys possess a combination of desirable properties such as high strength to weight ratio, good corrosion resistance and bearing properties and low coefficient of thermal expansion, making them useful in the manufacture of automobile components such as pistons and cylinder liners in internal combustion engines. However, these alloys are prone to seizure, particularly under poor lubricating conditions, when there is insufficient oil supply between the sliding surfaces; this can also occur under fluid film lubricating conditions due to localised breakdown of the oil film, thereby causing direct metal to metal contact between the tribo-components. One way of minimizing this problem is to disperse solid lubricant particles, such as graphite, in the Al-Si alloy matrix.

Graphite has a hexagonal structure. The carbon atoms in the basal plane form strong covalent bonds while the bond between the layers is relatively weak (van der Waals) so that the basal planes are sheared easily. This contributes to smearing on the sliding surfaces thereby providing lubrication. It is clear from the material presented in the previous paragraph that the study of the wear behaviour of Al-Si alloy containing silicon with various morphologies and with graphite dispersion would be of great interest. In the recent years, several attempts have been made to synthesise aluminium alloy-graphite particle composites using solidification processing techniques. The steps involved in the synthesis are as follows: melting the alloy, creating a vortex by mechanical stirring, addition of preheated graphite particles during stirring and casting the composite melt into a metallic mold.

The three Al-Si alloys chosen for the present investigation are: LM6 (Al-10 to 13%Si-0.6%Fe-0.1%Cu-0.5%Mn*) and LM13 (Al-11 to 13%Si-1.2%Fe-1.5%Cu-0.35%Mn-1.3%Mg) of near eutectic composition and LM30 (Al-16 to 18%Si-1.3%Fe-4.5%Cu-0.1%Mn-0.45 to 0.65%Mg) of hypereutectic composition. The composites contain 3.0 wt.% graphite particles dispersed in the alloys. Both the alloy and composite melts are solidified in a cast iron mold. In view of the differences in density between Al-Si alloy (2.699 gm/cc) and graphite (2.3 gm/cc), it is expected that the latter would float and be concentrated in the upper regions of the casting, thereby leading to a heterogeneous distribution. Also during the solidification of the molten alloys, the dendrites of primary aluminium are expected to push the graphite particles into the last freezing eutectic liquid thereby giving rise to non-uniform distribution. The thermal conductivity of graphite is roughly one half of that of the matrix. As such the microstructure of the aluminium-silicon alloys near the graphite particle is expected to be different from that in a region well away from the particles. All these facts imply that a careful microstructural examination of various regions of the casting is necessary. This aspect has received considerable attention in this thesis.

The effect of die casting, modification, refinement and modification and heat treatment (essentially to spheroidise silicon) and graphite particle dispersion on dry and partially lubricated wear behaviour of the alloys is studied in detail paying particular attention to the following aspects: load dependence of wear rate, friction force, temperature of the wear sample during sliding, examination of worn surfaces, debris analysis, subsurface deformation and pressure-velocity (P-V limits) only in partially lubricated condition. The conventional way of rating the performance of a material for bearing application is in terms of its P-V limits i.e., the maximum allowable bearing pressure (P) at a particular speed (V).

Chapter 1 of this thesis deals with a brief introduction to the development of aluminium alloys, particularly the cast ones. The effect of various alloying elements e.g., copper, nickel, magnesium, manganese, zinc, iron, on the

*Compositions are given in weight% unless otherwise stated.

properties of Al-Si alloys is briefly mentioned; typical applications of these alloys are listed. A brief introduction to aluminium alloy matrix-fibre composites is given. Finally, the present status of the aluminium alloy matrix-particle composites with special reference to aluminium-graphite composite is outlined.

Chapter 2 contains the background literature based on the subject matter related to the present investigation. The binary Al-Si equilibrium diagram is discussed and the possible microstructures are described. The effect of rapid cooling, modification and high pressure application on the phase diagram are also outlined. Since the commercial alloy contains iron, copper, nickel, magnesium etc., a number of intermetallic compounds are expected to form. The details of these intermetallic compounds are included in this chapter. A detailed account of the preparation of aluminium alloy-graphite particle composites, interaction between particles and growing phases, microstructure, physical and mechanical properties of the composites is given. The wear behaviour of the Al-Si alloy and aluminium-graphite composites is discussed with particular reference to load, silicon content, sliding distance dependence of wear rate, studies of worn surfaces, examination of debris particles, heat treatment and sub-surface deformation.

Chapter 3 deals with the scope of the present work.

Chapter 4 deals with a description of the melting procedure, preparation of composites and rapidly solidified ribbons, heat treatment of the alloys and composites. The details of the techniques used in the present investigation to characterise the materials are given. The results of the microstructures of Al-Si alloys and Al-Si-graphite particle composites in various conditions e.g., die cast, modified, refined and modified, heat treated, and their effect on dry and partially lubricated sliding wear behaviour is presented in chapter 5 and discussed in chapter 6. Some of the important results are briefly summarised in the following paragraphs.

The microstructure of the die cast hypoeutectic Al-Si alloys (LM6 and LM13) consists of primary aluminium with dendritic morphology; the secondary arms of the dendrites have an average spacing (i.e., centre to centre distance

between two neighbouring dendrites) of the order of $18\text{ }\mu\text{m}$. Plate-shaped eutectic silicon appears in the interdendritic region and around the dendrites. Typical dimensions of the silicon plates are $14\text{ }\mu\text{m}$ long and $2\text{ }\mu\text{m}$ wide. Such sharp edged plate-shaped eutectic silicon particles act as stress riser and offer preferential sites for crack nucleation. To restrict the undesirable growth of eutectic silicon it is proposed to add modifier to Al-Si alloy melt just before pouring. Elemental sodium was used to modify the eutectic silicon in hypoeutectic Al-Si alloys. The average dimensions of the modified eutectic silicon in die cast LM6 alloy are $3.5\text{ }\mu\text{m}$ long and $1\text{ }\mu\text{m}$ wide. In the hyper-eutectic alloy, the microstructure consists mainly of primary silicon, primary aluminium and eutectic Al-Si phases. The large cuboids of primary silicon and plate-shaped eutectic silicon are refined and modified respectively by the simultaneous addition of phosphorus and sodium to LM30 alloy. For instance, by the addition of phosphorus in LM30 alloy, the average size of primary silicon was reduced from $100\text{ }\mu\text{m}$ in die cast (unrefined) condition to $50\text{ }\mu\text{m}$ in refined condition. Al-Si (LM6 and LM13 alloys are subjected to heat treatment following standard cycles: solution treated at 520°C for 8 hours quenched in warm water at 60°C followed by ageing at 180°C for 6 hours, whereas, LM30 alloy is solution treated at 495°C for 9 hours, quenched in warm water at 60°C and aged at 175°C for 8 hours. Solution treatment alters the silicon morphology from plate-shaped to near spherical and also increases the silicon solubility in aluminium solid solution. During ageing treatment, fine precipitates are expected to form; however, they could not be identified by scanning electron microscopy in the present investigation. An attempt has also been made to study the distribution of graphite particle in cast-composites. This is represented in terms of % frequency of inter-particle spacing and particle size.

The observed microstructure is explained with the help of a model. Model experiments show that when a hypoeutectic Al-Si alloy solidified between the two graphite particles, the primary aluminium which is the first phase to solidify, avoids graphite particle and preferentially nucleates between the particles. If the spacing between the two graphite particles is very small then the excess silicon i.e., more than the equilibrium solid solubility, will be rejected by the aluminium and is concentrated around the graphite

particles. On the other hand, if a particle is pushed into the last freezing eutectic liquid then the structure around the particle will be simple Al-Si eutectic. It is seen in some instances that graphite particles act as physical barrier to the anisotropic growth of the eutectic silicon. In the hyper-eutectic Al-Si alloy (LM30), the first phase to solidify is primary silicon; it nucleates preferentially on the surface of the dispersed graphite particles as large cuboids. It is also interesting to note that the primary aluminium halos around the primary silicon are absent in the graphite containing composites. The results also show that the microstructure of die cast Al-Si alloys is not significantly affected by the addition of graphite particles. However, a marked change in the microstructure is observed around the graphite particles in rapidly solidified Al-Si-graphite composites. It is noted that the morphology of silicon is found to change from plate like near graphite particles to nearly spherical in regions well away from the particles.

The results of dry sliding wear tests show an increase in the wear rate as the pressure is increased. Die cast LM30 alloy is found to be superior to LM6 and LM13 alloys. Two distinct regions could be observed in the wear rate versus pressure curves; the mild wear regime occurring at lower pressures and the severe wear regime at higher pressures. The onset of severe wear regime in the case of LM6 and LM13 alloys is around 1.5 MPa; however, this region is not observed in the LM30 alloy upto a pressure of 4 MPa. Wear debris collected from samples tested under low pressure (1.0 MPa) is characterised by small equiaxed particles (less than 6 μm in size) compared to the large flaky particles found at higher pressures. Wavelength dispersive X-ray analysis confirms that the small equiaxed particles are mainly of aluminium.

The wear rates of die cast LM6 and LM13 alloys are found to be higher than those of the same alloys subjected to modification, heat treatment and dispersion of graphite particles. The least amount of wear is observed in heat treated alloy-graphite composites. However, a different behaviour is observed in die cast LM30-graphite composites. It is noted that graphite particle dispersion in LM30 alloy resulted in increased wear rates at higher applied pressure both in die cast and refined and modified conditions. As with other alloys the optimum result was obtained for the composite in heat treated condition. Although the pressure at which seizure occurred is the

same for all the conditions of the LM30 alloys, the wear rate of the heat treated composite is found to be much less than that of the other samples. The temperature of the wear sample is noted during the test and the results show that there is a direct relationship between the time-temperature plots and wear rates versus applied pressure plots. For instance, at an applied pressure of 2.0 MPa the temperature of LM6 pin rose to 140°C, whereas the temperature of the heat treated composite at 2.0 MPa rose to only 70°C. Similarly, in the case of the die cast LM13 alloy the temperature of the pin rose to 140°C at an applied pressure of 2.0 MPa; in contrast the temperature of the composite specimen in heat treated condition rose to only 90°C at the same pressure. Similar trends are also observed in LM30 alloys.

The worn surfaces of Al-Si alloys and composites are examined with a view to understanding the mechanism of material removal. At low load region i.e., at mild wear the worn surface contains groove marks, and fine equiaxed particles. However, in regimes subjected to severe wear, the worn surface is characterised by long and continuous grooves running from one end of the specimen to the other. The observation of a large number of flaky debris particles under these conditions suggests that delamination is the predominant wear mechanism. However, material removal by stick-slip wear mechanism is also confirmed.

The transfer of iron from steel disc to Al-Si alloy wear pin is also found. In some cases parallel lips are seen along the wear scar in LM6 and LM13-graphite composites. The presence of a significant number of large faceted silicon wear debris particles suggests the fracture and subsequent removal of silicon from the mating surface. When delamination is the operating wear mechanism, tensile strength and ductility of the material control the crack propagation and the overall wear behaviour. The dispersion of graphite particles would reduce the tensile strength of composites. The tensile strength of the LM13 alloy in die cast condition is measured to be 200 MPa; this was reduced to 180 MPa by the addition of 3% graphite particles. The corresponding values for the LM30 alloy are 140 and 90 MPa respectively. The loss in strength will offset the positive effect of dispersed solid lubricant. The stress concentration effect associated with sharp edged silicon particles can be reduced by changing the morphology either by modification or heat treatment. X-ray diffraction and electron microprobe analysis of flake-shaped debris particles show that they consist mainly of aluminium

and silicon. Subsurface studies of the worn alloys and composites show a significant amount of fragmentation of the eutectic and primary silicon particles. The results of pressure-velocity limits show that the load bearing capacity of a particular alloy or composite is decreased as the sliding speed increased. LM30 alloy shows better load bearing capacity at low speeds; however, at higher speed its performance is inferior to that of LM13 alloy but still superior to that of LM6 alloy. The optimum wear properties are observed in the case of heat treated composites.

Results of the present study show that under both dry and partially lubricated conditions optimum wear properties were observed in the case of heat treated composites. It is interesting to note that the worn surfaces of heat treated composites showed graphite film formation on the sliding composite surfaces; whereas no such graphite film was detected on the wear surface of diecast composites. The combined effect of the increase in tensile strength and the reduction in metal to metal contact i.e., between Al-Si alloy and steel due to presence of graphite film on the mating surface might have resulted in the observed improvement in the wear properties of heat treated composites.

A limited amount of studies have been carried out on the abrasion resistance of LM13 alloy in the die cast and rapidly solidified conditions. At low load, the abrasion resistance of rapidly solidified alloy is superior to that of the die cast condition. A reversal in the wear behaviour is observed for loads exceeding 2N. This is probably related to the limited thickness of the rapidly solidified materials.

CHAPTER 1

INTRODUCTION

Aluminium has an excellent combination of properties such as low density, good thermal and electrical conductivities and good corrosion resistance. As-such it finds many industrial applications essentially in electrical transmission and distribution of power, telecommunication, transport, defence, aerospace, building and construction industries. However, the relatively poor mechanical properties of aluminium (yield strength:30 MPa, tensile strength: 70 MPa (1) of 99.6 % pure aluminium) limits its use on a wider scale. Realising the potential as well as availability of aluminium, considerable efforts are being made to explore the possibilities of improving the mechanical strength so as to meet the requirements for various applications. Introducing components made of aluminium with competitive properties in place of relatively heavier components leads to considerable savings of fuel and energy.

One such quantum jump in improving the mechanical strength of aluminium is the development of age hardenable Al-Cu alloys. The tensile strength of age hardenable Al-5.5 % Cu alloy is found ^{to be} around 390 MPa (2), which is five times more than the 99.6 % pure aluminium. Further development in improving the mechanical strength of Al-5.5 % Cu alloy is achieved by addition of 1.5% Mg. The ultimate tensile strength of Al-5.5 % Cu-1.5 % Mg alloy in heat-treated condition is found ^{to be} 490 MPa. Such a remarkable improvement in strength makes these alloys amenable to use in aircraft structure (2). A number of other alloying elements e.g., Mn, Si, Zn, Mg, Li etc., are also alloyed with aluminium to improve the mechanical properties. Amongst the various aluminium alloys, Al-Zn-Mg alloys are found to show tremendous improvement in mechanical strength. For instance, Al-6.3 to 7.3% Zn-2.4 to 3.1 % Mg-1.6 to 2.4 % Cu-0.5% Fe-0.4 % Si-0.3 % Mn alloy shows excellent mechanical strength (tensile strength:610 MPa, % elongation:10) in heat treated condition (2). Al-Mn and Al-Mn-Mg alloys are strain hardening alloys; the improvement in strength arises from cold working. These alloys are available in the form of sheet, plate, tube, wire, foil etc.

A significant amount ($\sim 20\%$) of aluminium is used for the manufacture of cast alloys which find applications in the transportation sector. A variety of aluminium castings are available these days depending upon the alloying elements; these are: Al-Cu, Al-Mg, Al-Si, Al-Zn and Al-Sn. The initial effort was made in United States to make castings out of Al-4 % Cu alloys. Al-10 %Cu alloy was tried out for the production of pistons in internal combustion engines. Cast Al-Mg alloys show excellent corrosion resistance, good machinability and attractive appearance when anodised. Addition of 0.5 % Si to Al-4 % Mg alloy, reduces the tensile strength but it improves the castability and the use of these alloys is restricted to only decorative purposes, where corrosion resistance is the major requirement.

Amongst the various cast aluminium alloys used these days, Al-Si alloys are studied in detail due to their excellent combination of properties such as fluidity, low coefficient of thermal expansion, high wear resistance, high strength to weight ratio and good corrosion resistance. Al-5 % Si alloy shows good ductility, better corrosion resistance and pressure tightness (3). Al-12 % Si alloy has also good corrosion resistance and is found to be superior to Al-5 % Si alloy in terms of castability and pressure tightness. Al-7 % Si-0.2 % Fe alloy has also good corrosion resistance and has high ductility when cast in permanent mold and in heat-treated conditions (3). This alloy is used when impact resistance is the primary consideration. In general, binary Al-Si alloy is not amenable to heat treatment but addition of various alloying elements e.g., Cu, Mg, Ni makes this alloy respond to heat treatment. Copper increases strength and improves machinability at the expense of reduced castability, ductility and corrosion resistance. Al-9 % Si - 3.5% Cu alloy is developed for permanent mold casting. Al-7% Si - 0.3 % Mg alloy shows excellent casting characteristics, weldability, pressure tightness and corrosion resistance. These alloys are amenable to heat treatment and offer various combination of tensile and physical properties that are attractive for many applications including aircraft and automotive parts. Another group of alloys in Al-Si alloy system are those that contain Mg, Cu and Ni. One example of such alloy is B.S. LM13 (Al-12% Si-1 % Cu-1 % Mg-1.5 % Ni) used for making pistons in internal combustion

engines (4). Addition of nickel to Al-Si alloys improves the elevated temperature properties by forming stable intermetallic compounds that cause dispersion hardening. Hypereutectic Al-Si alloys are currently being tried out for making pistons for heavy duty IC (internal combustion) engines (5). It is reported(6) that cylinder blocks out of hypereutectic Al-Si alloys (B.S.LM30: Al-17 % Si-4.5% Cu-0.5 % Mg) are made without iron liners or electroplating on the cylinder bores. The outstanding wear resistance, low coefficient of thermal expansion and better physical and mechanical properties of LM30 alloy are used to advantage in the production of diesel engine pistons. Table I.1 shows the chemical compositions and mechanical properties of various Al-Si alloys and their applications are shown in Table I.2 (1,5). Presence of various alloying elements e.g., Cu, Mg, Ni, Mn, Fe etc. in aluminium rich Al-Si alloys leads to the formation of intermetallic phases. Table I.3 shows some of the commonly observed intermetallic phases, their crystal structures and lattice constants (7).

In hypereutectic Al-Si alloys, the first phase to solidify is primary silicon as large cuboids and this in turn hampers the mechanical properties as well as machinability and casting characteristics. The most effective way of reducing the size of primary silicon is by the addition of phosphorus to the molten alloy. Phosphorus combines with aluminium in the melt to form insoluble aluminium phosphide (AlP) which, due to its similar crystal structure (diamond cubic) and lattice constants ($a_{Si}:0.5430$ nm, $a_{AlP}:0.5451$ nm), acts as potential nuclei for the formation of primary silicon (6,8,9). Jorsted(6) has pointed out that the degree of refinement of primary silicon is markedly affected by the solidification rate. Castings solidified at a relatively slower rate, e.g., in sand casting and heavy sections of permanent mold castings, contain primary silicon phase which are not well refined even though the optimum nucleant addition is made, unless they are heavily chilled. Silicon in eutectic Al-Si phase grows anisotropically as sharp edges (plate-shaped) observed under two-dimensional microscopy. Such anisotropic growth of silicon largely hampers the mechanical strength, ductility and controls the fracture behaviour. To impede the undesirable growth of silicon the eutectic silicon is modified by adding foreign elements e.g., Na or Sr, prior to the onset of solidification (10-14). Of the various mechanisms proposed to account

Table I.1 : Alloy Designation, Compositions and Mechanical Properties of Al-Si Alloy Castings (1,2)

Alloy and Temper Designation	Chemical composition (wt.%)						Mechanical Properties			
	Si	Fe	Cu	Mg	Ni	Zn	Tensile Strength (MPa)	Yield Strength (MPa)	% Elongation	Hardness (BHN)
359 (T62)	9.0	0.2	0.2	0.6	-	-	345	290	5.5	-
360 (F)	9.5	0.2	0.6	0.5	-	-	324	172	3.0	75
A360 (F)	9.5	1.5	0.6	0.5	-	-	317	165	5.0	75
354	9.0	0.2	1.8	0.5	-	-	-	-	-	-
333 (F)	9.0	1.0	3.5	0.3	-	1.0	234	131	2.0	90
333 T5	9.0	1.0	3.5	0.3	-	1.0	234	172	1.0	100
333 T6	9.0	1.0	3.5	0.3	-	1.0	290	207	1.5	105
333 T7	9.0	1.0	3.5	0.3	-	1.0	255	193	2.0	90
A 333	9.0	1.0	3.5	0.3	-	3.0	-	-	-	-
332 (T5)	9.5	1.2	3.0	1.0	-	1.0	248	193	1.0	105
361	10.0	1.2	0.5	0.5	-	-	-	-	-	-
384 (F)	11.3	1.3	3.75	0.1	-	3.0	324	172	1.0	-
336 T551	12.0	1.2	1.0	1.0	2.5	0.35	242	193	0.5	105
336 T65	12.0	1.2	1.0	1.0	2.5	-	324	296	0.5	125

413 (F)	12.0	2.0	1.0	0.10	-	-	296	145	2.5	80
A413 (F)	12.0	1.3	1.0	0.10	-	-	241	110	3.5	80
390 (F)	17.0	1.3	4.5	0.55	-	-	279	241	1.0	120
390 T5	17.0	1.3	4.5	0.55	-	-	296	265	1.0	-
A390(F)sand cast	17.0	0.5	4.5	0.55	-	-	179	179	1.0	100
A390 T5	17.0	0.5	4.5	0.55	-	-	179	179	1.0	100
A390 T7	17.0	0.5	4.5	0.55	-	-	250	250	1.0	115
A390 die cast(F)	17.0	0.5	4.5	0.55	-	-	250	200	1.0	110
A390 die cast T5	17.0	0.5	4.5	0.55	-	-	200	200	1.0	110
A390 die cast T6	17.0	0.5	4.5	0.55	-	-	310	310	1.0	145
A390 die cast T7	17.0	0.5	4.5	0.55	-	-	262	262	1.0	120
392 (F)	19.0	1.5	0.6	1.0	-	0.5	290	262	0.5	-

INDEX

F: As-fabricated

T5: Cooled from an elevated temperature shaping process and then artificially aged.

T6: Solution heat-treated, quenched and then artificially aged.

T7: Solution heat-treated and stabilized.

T62:Solution treated, quenched and natural ageing.

T551:Cooled from an elevated temperature following shaping process, stress relieved by controlled stretching and then artificially aged.

Table I.2 : Applications of Aluminium-Silicon Alloys (1,2)

Alloys (B.S.Standard)	Applications
LM6	Thin walled castings, domestic cook ware, pump casting, automobile castings.
LM13	Pistons
LM30	Heavy duty internal combustion engines pistons, cylinder blocks, computer disc spacers, pistons for air conditioning compressors, air compressor bodies, master brake liners.

Table I.3 : Intermetallic Phases in Aluminium-rich Aluminium Alloy System(7)

Intermetallic Phase	Structure Type	Lattice Parameter Å		
		a	b	c
CuAl_2	Body Centered Tetragonal	6.066	-	4.874
FeAl_6	Orthorhombic	6.464	7.440	7.779
$(\text{Fe,Cu})(\text{Al,Cu})_6$	Orthorhombic	7.464	6.441	8.786
MnAl_6	Orthorhombic	6.498	7.552	8.870
NiAl_3	Orthorhombic	6.611	7.366	4.812
Mg_2Si	Face Centered cubic	6.351	-	-
Cu_2FeAl_7	Tetragonal	6.336	-	14.870
CuMgAl_2	Face Centered Orthorhombic	4.01	9.25	7.15
Cu_3NiAl_6	Body Centered Cubic	14.6	-	-

for the modification of eutectic silicon, the most widely accepted mechanism is that the modifying atom (Na or Sr) gets selectively absorbed at the re-entrant twin grooves and reduces the rate of atomic attachment to the silicon growth tips (15). The tensile strength of chill cast Al-13 % Si alloy is increased from 195 MPa in normal chill cast to 220 MPa in modified conditions. The percentage elongation is also increased from 3.5 in normal cast condition to 8% in modified alloy and hardness is increased from 63 to 72 Rockwell B after modification (16). It has also been realised that refinement and modification of primary and eutectic silicon respectively could also be achieved by chill casting (13,17,18) and by rapid solidification processing (19).

In recent years there is growing interest in synthesising aluminium alloy matrix composites in order to achieve a combination of properties which are not normally attained in any of the constituent phases. These composites can be broadly classified into two categories depending upon the geometry of the second phase. In fibre and whisker reinforced composites the second phase has an aspect ratio (l/d ; l :length of the fibre, d : diameter of the fibre) ranging from 100 to 10,000; a number of these composites with reinforcement of carbon (20), boron (20), silicon carbide (20,21) and alumina (20,22) fibres are now commercially produced for structural applications requiring exceptionally high specific strength and specific modulus. In fibre reinforced composites, the matrix serves to transmit the load to the fibres, protect fibres from surface damage and also separate the individual fibres. For instance, the reinforcement of 14 vol. % alumina fibres (tensile strength: 1.4 GPa, modulus of elasticity: 380 GPa) in Al-4 %Mg alloy increases the ultimate tensile strength from 188 MPa of Al-Mg alloy to 205 MPa of composites and the modulus from 63 GPa to 87 GPa (22). Increasing the concentration of fibres further to 23 vol. % the ultimate tensile strength and modulus of elasticity of Al-4 % Mg alloy increase to 263 MPa and 105 GPa respectively (22).

The second category of composites involves the dispersion of soft solid lubricant or hard ceramic particles; these are of great interest to tribological applications. Unlike dispersion strengthening alloys in which the particle

size varies between 0.1 to 2.0 μm , interparticle distance is less than 5 μm and the volume fraction of dispersoids is generally below 0.10, in metal matrix-particle composites, the second phase particles have typical size in the range 10 μm to 200 μm and spacing of the same order of magnitude. In dispersion hardened materials the strength arises due to dislocation bowing between the particles; the same is not true for metal matrix particle composites in which the distance between the particles is too large to yield any strengthening effect. A large number of aluminium alloy particle composites containing dispersions of solid lubricant particles like graphite(23-27), mica (28,29), coconut shell char (30) and talc (31) as well as hard ceramic particles such as zircon (32), alumina (33,34), silica (35) and silicon carbide (36,37) have been synthesised and are discussed in detail in a recent review article (38). Since the central theme of the present thesis is solely based on the Al-Si alloy dispersed with solid lubricant particle graphite, the following chapters will deal only with the various aspects of Al-Si alloys and Al-Si-graphite particle composites with special reference to microstructure and wear behaviour.

It is already mentioned in the preceeding sections that Al-Si alloys are extensively used in tribological application such as pistons, cylinder blocks in internal combustion engines. Although Al-Si alloys meet many of the requirements for above applications, these alloys are prone to seizure particularly under poor lubricating conditions when there is insufficient oil supply between the sliding surfaces; this can also occur under fluid film lubrication conditions due to localised breakdown of the oil film thereby causing direct metal to metal contact between the tribocomponents. One way of minimizing this problem is to disperse solid lubricant particles, such as graphite in Al-Si alloy matrix, using solidification processing techniques.

Graphite has a hexagonal structure ($c=3.35 \text{ \AA}$, $a=1.41 \text{ \AA}$). The carbon atoms in the basal plane form strong covalent bonds while the bond between the layers are relatively weak (van der Waals) so that the basal planes are sheared easily. During sliding action graphite layers are smeared on the tribo-surfaces thereby providing lubrication.

There are some reports on the microstructure of Al-4.5 % Cu alloy reinforced with fibres; these deal specifically with the effect of fibre on the secondary dendrite arm spacing in aluminium (39,40). The presence of fibre is shown to influence the amount of microsegregation (39,40). Krishnan and Rohatgi (41) have stated that the dispersion of graphite particles in Al-Si alloys tends to modify the eutectic silicon. However, the exact mechanism for modification has not been shown and the discussion was solely based on the microstructural aspects of nucleation and growth of phases.

There is some information available in the literature describing the sliding wear behaviour of aluminium alloy-graphite particle composites under both dry (42-44) and lubricated (26,45,46) conditions. In lubricating sliding wear, aluminium-graphite system reported to improve wear behaviour; however, this behaviour is not observed during dry sliding wear. Biswas and Pramila Bai (43) have shown that during dry sliding wear of Al-Si alloy dispersion with 2.7 and 5.7 wt.% graphite composites, the wear rate is increased as compared to that of the matrix alloy. Similar findings are also reported by Gibson and coworkers (42) for aluminium alloy composites containing higher (>8 wt.%) graphite content. The loss in tensile strength and ductility due to dispersion of graphite particle was believed to be the cause for such anomalous behaviour with the wear properties.

The present study is therefore aimed at understanding the effect of dispersed graphite particles on the microstructure of cast Al-Si alloys and the possible location of dispersed graphite particles in die-cast microstructure. The effect of graphite particle on the nucleation and growth of phases during solidification of Al-Si alloys is also examined. A detailed study on the wear behaviour of Al-Si alloys (with various matrix microstructures) and Al-Si-graphite particle composites both in dry as well as partially lubricated conditions are studied under a wide range of loads and sliding speeds. The worn surfaces and debris particles generated during the sliding wear are also studied in detail. A limited amount of studies is carried out on the abrasive wear of Al-Si (LM13) alloy both in die-cast and rapidly solidified conditions.

CHAPTER 2

BACKGROUND LITERATURE

2.1 Microstructure of Al-Si Alloys

Aluminium-silicon is an abnormal eutectic system, unlike Al-Cu (normal eutectic system), in which one phase (silicon) solidifies in a faceted manner and the other (aluminium) non-faceted. During solidification one of the solid phases of the eutectic projects into the liquid far in advance of the other solid phase. The solidification of faceted-non-faceted system leads to irregular freezing faces and no crystallographic orientation relationship exists between the phases and no marked metallographic periodicity is observed. Such a system is very sensitive to solidification conditions and the morphology of faceted phase could be altered to a great extent by changing the solidification conditions (cooling/growth rates) and addition of foreign elements.

In the following sections a description of Al-Si phase diagram and the effect of cooling rate, addition of modifiers, effect of pressure on the phase diagram is given. The refinement and modification of primary and eutectic silicon will be described in greater detail. Finally, the microstructure of rapidly solidified Al-Si alloys is reviewed.

2.1.1 Solidification Behaviour and Microstructure of Al-Si Alloys

The Al-Si alloy phase diagram is shown in Fig.2.1. In this system an eutectic is formed at 11.8 at.% Si at 577°C. The maximum solid solubility of silicon in aluminium is 1.59 at.% at the eutectic temperature and less than 0.05 at.% at room temperature. The enlarged portion of aluminium-rich solidus and solvus curves of Al-Si phase diagram is shown in Fig.2.2. The solid solubility of aluminium in silicon is 0.0001 at.% at the eutectic temperature.

At slow rate of solidification, a hypoeutectic Al-Si alloy produces primary aluminium with a dendritic morphology and eutectic silicon in the interdendri-

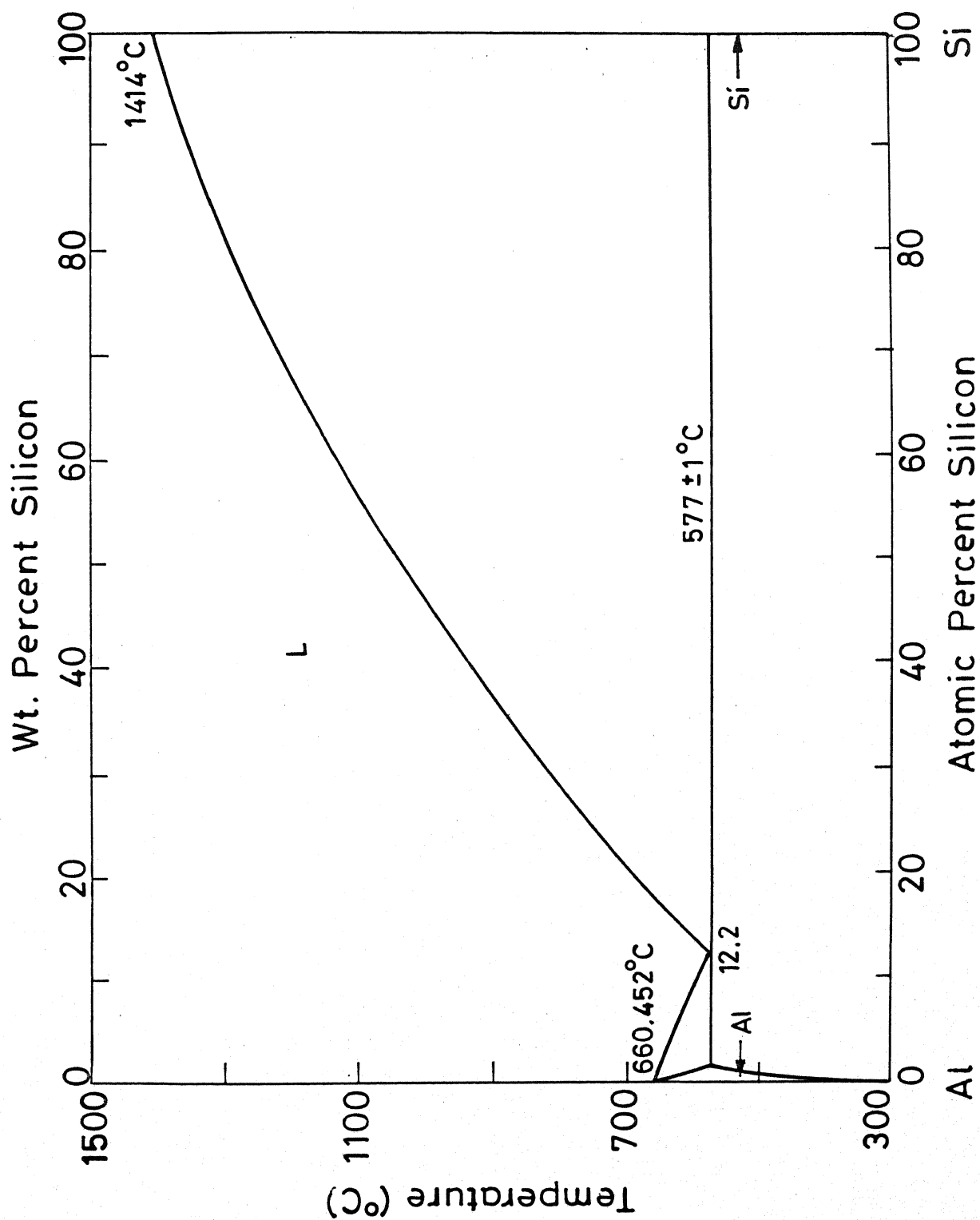


Fig. 2.1 Binary Equilibrium Phase Diagram of Aluminium - Silicon Alloy.

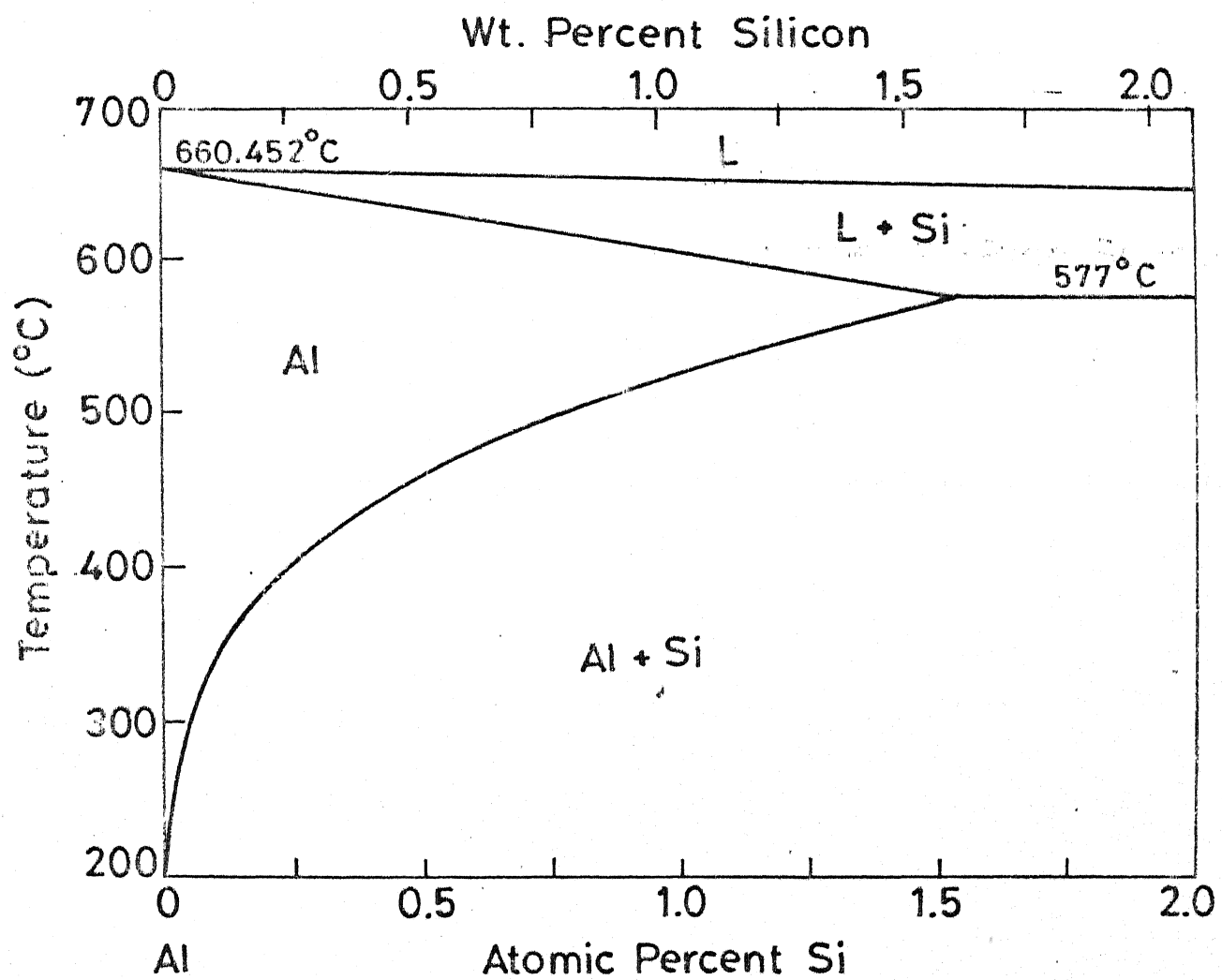


Fig.2.2 Enlarged Diagram of the Al-Rich Solidus and Solvus.

tic region and around the dendrites. Silicon, in Al-Si eutectic phase, grows anisotropically as large plates; it grows straight for some distance and then branches off or changes its direction through large angle (47), in response to local conditions at the growth interface. The growth of eutectic silicon takes place by twin plane reentrant edge mechanism in which branching and direction changes of the silicon plates or flakes occur by multiple twinning (47). However, it has been indicated that some of the silicon plates are interconnected (48) but in general most of them are completely separated from the rest.

In hypereutectic Al-Si alloys, the first phase to solidify is primary silicon and the remaining liquid solidifies as primary aluminium and Al-Si eutectic. After the nucleation of primary silicon, the liquid composition around the primary silicon is enriched with aluminium and the liquid composition moves down the liquidus along the metastable extension until aluminium is formed. With the nucleation of primary aluminium the liquid composition shifts back towards the coupled growth region on the phase diagram, causing solidification of the Al-Si eutectic.

2.1.2 Modification of Eutectic Silicon

It has been mentioned in the preceeding section that eutectic silicon grows with large plate-shaped morphology. Such morphology of silicon is highly undesirable as it acts as a stress riser and brittle nature of silicon hampers mechanical strength as well as ductility of the cast alloy. With a view to restricting the undesirable anisotropic growth of silicon, a number of investigators (10-18,47) have studied the shape modification of eutectic silicon by adding minute quantities of alloying elements such as Na or Sr to the melt just prior to solidification. The modification of eutectic silicon in Al-Si alloy was discovered quite accidentally some 68 years ago, when sodium fluoride (NaF) was added as a flux (10). Since then considerable research has been conducted on the modification of eutectic silicon. Various mechanisms have been proposed to explain the modification of silicon phase based on changes in phase equilibrium or differing nucleation and growth kinetics. However, modification mechanism is primarily concerned with the growth of the silicon. The thermal analysis data show that (15,49) there are

depressions of the eutectic and primary silicon arrest on cooling by 5 to 10 °C but no such depression was observed on heating. This suggests that there is no recalescence to raise the growth temperature towards that of the eutectic isotherm. There is no effect upon the freezing point of aluminium phase. Fig.2.3 shows the effect of sodium on the phase diagram of Al-Si alloy system. The liquidus curves are depressed and the eutectic temperature is lowered (13). The equilibrium eutectic temperature is suppressed by 10-15°C and the eutectic composition moves right to 13.5 at.%Si. Of the various mechanisms proposed to account for the modification of eutectic silicon by alloying elements, such as Na or Sr the most widely accepted mechanism is that the impurity atoms get selectively absorbed at the reentrant twin grooves and reduce the rate of atomic attachment to the silicon growth tips (18,47,50). Recently Lu and Hellawell (51) have made a careful investigation of the mechanism of modification of silicon by sodium in Al-Si eutectic alloy. Their studies show that modifiers are preferably absorbed on the (111) plane, change the stacking sequence and lead to impurity induced twinning. The sodium modified silicon fibres are reported to be rough or micro-faceted and they contain a very high twin density on the four {111} planes; the preferred growth axis is a $\langle 100 \rangle$ direction, with symmetrical branching in $\langle 211 \rangle$ direction.

It is also realised that the anisotropic growth of eutectic silicon could be altered by increasing the solidification rate, since the faceting phase is sensitive to solidification condition notably quenching rate. It has also been shown that the liquidus lines are depressed by 10-20°C and the equilibrium eutectic composition shifts towards higher silicon contents (~ 13.5 at.%Si) by chill casting (cooling rate 1-2°C/s) of Al-Si alloy (13), Fig.2.4. This indicates that rapid cooling of the Al-Si alloy produced a similar effect on the equilibrium phase diagram to that obtained by sodium modification. Plumb and Lewis (11) have examined chill modified structure with the help of electron microscope and concluded that the structure produced by rapid cooling and that by sodium modification are alike. Dey and Hellawell (52) have also studied the microstructure of Al-Si alloys and their study concluded that there is no difference between the quenched and sodium modified structure. Kobayashi and Hogan (47) have proposed that the reduction in lead

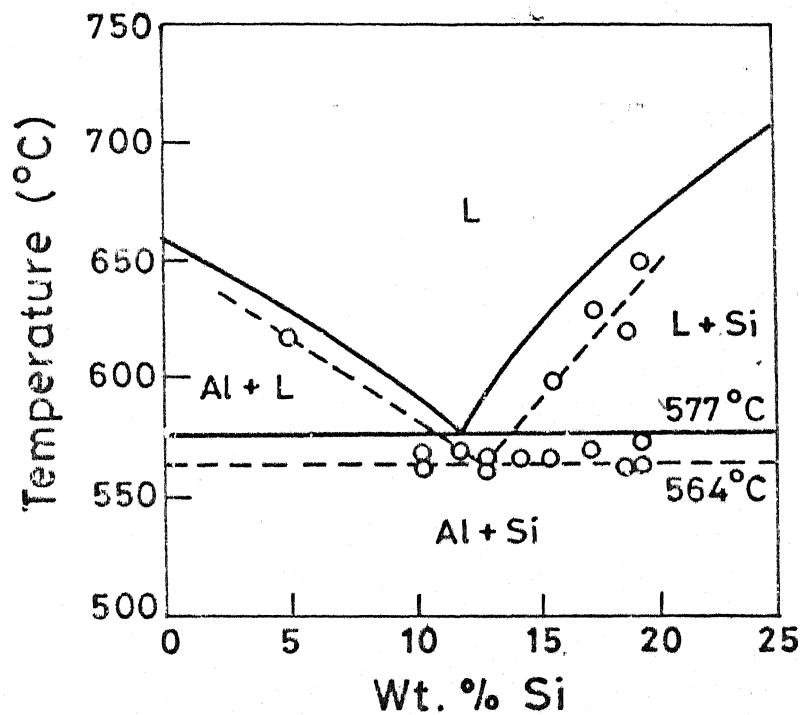


Fig. 2.3 Impact of Modification by Sodium Addition on the Location of Liquidus Curves and Eutectic Equilibrium Temperature. Full Lines Show the Equilibrium Phase Diagram.

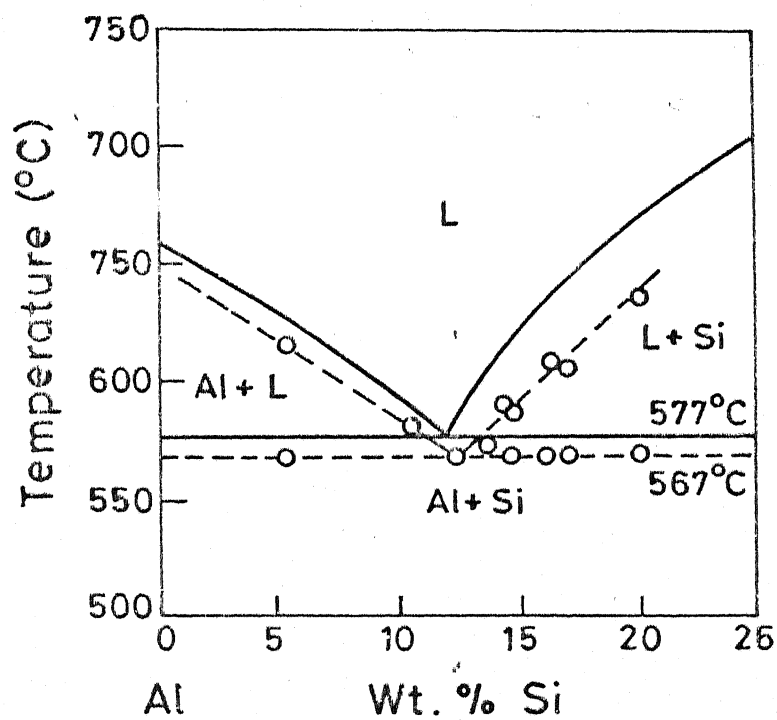


Fig. 2.4 Impact of High Cooling Rates (1 to 2°C/s) on Location of the Liquidus Curves and Eutectic Equilibrium Temperature in the Al-Si System. Full Lines show the Equilibrium Phase Diagram.

distance between aluminium and silicon during chill modification is mainly due to the differential reduction in diffusion rate of the two species in the eutectic melt, so that the growth rate of aluminium phase decreases less rapidly with falling temperature than that of the silicon phase. However, a recent study by Lu and Hellawell (51) have indicated that quench modified silicon fibres are quite smooth on external surfaces and are more often twin-free. They have also added that quenching leads to a transition from anisotropic to more or less isotropic growth and the molecular attachment kinetics are insensitive to internal twins.

The application of hydrostatic pressure during solidification, as is obtained in the squeeze casting technique, also leads to modification of eutectic silicon. A significant improvement in the mechanical strength of Al-Si alloys is achieved by this technique (53,54). It can be seen from thermodynamic considerations that the melting point of a metal, which shrinks during solidification (aluminium shrinks about 6%), increases if sufficiently high hydrostatic pressure is applied. The increase in the freezing temperature can be calculated from Clausius-Clapeyron equation:

$$\frac{\Delta T}{\Delta P} = \frac{T_m (v_2 - v_1)}{Q} \quad \text{.....2.1}$$

where Q is the latent heat of fusion

v_2 is the specific volume of liquid phase

v_1 is the specific volume of solid phase

and T_m is the melting temperature at atmospheric pressure

Fig.2.5 shows the location of liquidus lines and eutectic lines in Al-Si system under high hydrostatic pressure (13). It can be seen that the eutectic temperature rises from 577°C at atmospheric pressure to 660°C at 28 k bar. It is also interesting to note that the maximum solid solubility of silicon in aluminium can be raised to 3.37 at.%Si under a pressure of 25 k bar. or 6.77 at.%Si at 50 k bar. The reason behind the modification of eutectic silicon lies in the fact that due to applied pressure the actual melting temperature is raised, but the temperature of the liquid would remain at a lower value than that it would have at high pressure. This gives rise to undercooling of Al-Si alloy melt, and subsequent solidification alters the growth morphology

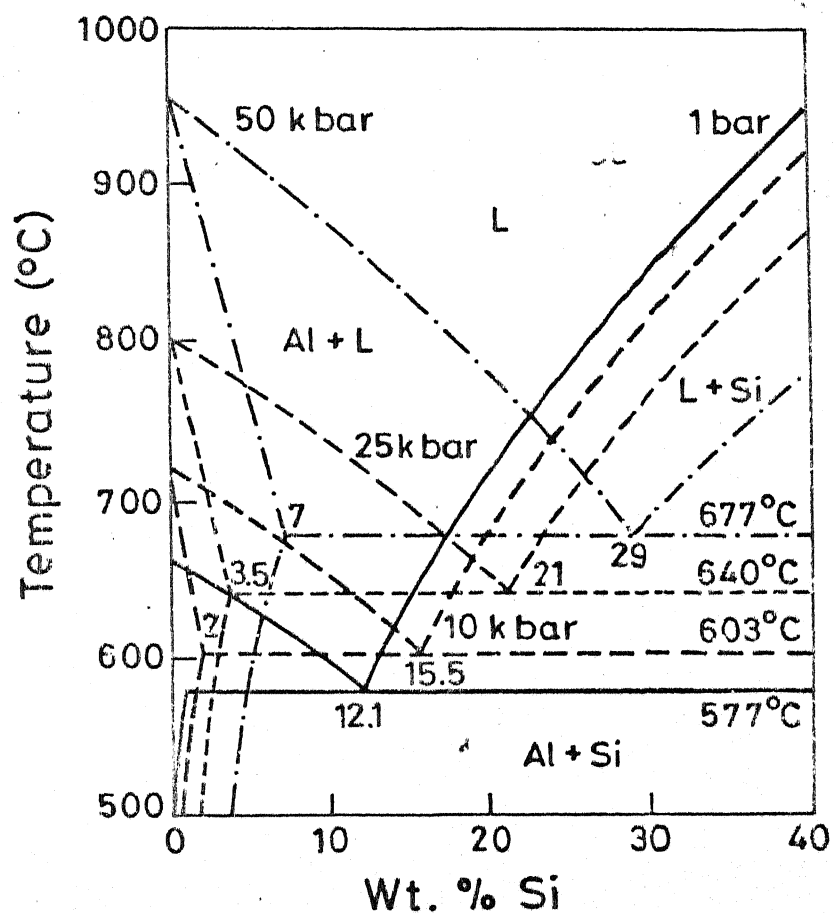


Fig. 2.5 Location of Liquidus Curves and Eutectic Lines in Aluminium Silicon System under High Hydrostatic Pressure.

of eutectic silicon as observed with sodium modification as well as in chill castings.

2.1.3 Refinement of Primary Silicon

During liquid to solid transformation of hypereutectic Al-Si alloy, the first phase to crystallise is primary silicon as large cuboids. Such coarse primary silicon particles greatly hamper tensile properties and also increase difficulties in machining. With a view to achieving optimum properties and better machining characteristics, it is essential that the primary silicon should be refined. In Al-Si foundry practice, refinement of primary silicon is accomplished by addition of phosphorus to the molten alloy (6,7,9,55). Phosphorus reacts with aluminium to form small insoluble particles of aluminium phosphide (AlP) which, due to its similar crystal habit and lattice constants acts as potential sites for heterogeneous nucleation of primary crystals. The amount of phosphorus in the range of 0.01 to 0.5% is enough to refine the primary silicon.

It is logical to add both phosphorus and sodium in hypereutectic alloys to refine as well as modify the primary and eutectic silicon respectively. Some studies are carried out in this direction to achieve both the refinement and modification of primary and eutectic silicon respectively (56-58). Clegg and Das (56) have reported that addition of sulphur followed by sodium in LM30 alloy refined and modified both the primary and eutectic silicon respectively. Cisse et al. (55) added a master alloy of sintered aluminium powder rods (SAP) with alumina in Al-Si alloy and found that direct additions of finely dispersed alumina nucleated silicon but not aluminium. Quaternary alloys containing both alumina (added as SAP) and sodium showed primary silicon refinement and eutectic modification. Freshly made alumina (i.e. not added externally but formed in the melt by chemical reaction) is generally an effective nucleant for aluminium (55).

Mascre (57) has stated that sodium has a tendency to decrease the effectiveness of phosphorus, when both are added in the melt at the same time. This may be due to the fact that sodium and phosphorus react together and form Na_3P (59). In contrast Sugiyama et al. (58) have indicated that the

simultaneous introduction of phosphorus and sodium promotes both refinement and modification of primary and eutectic silicon respectively. There are some reports (47,49,60) describing the change in the growth mode of primary silicon, due to overmodification by sodium, to roughly spheroidal form.

2.1.4 Rapid Solidification Processing

Rapid solidification processing is being recognised as having high technological potential; it is capable of producing a unique class of material directly from the melt. In this process, liquid metals or alloys are solidified at a rate (10^7 - 10^9 °C/s) fast enough to achieve phase or phase mixtures which are generally not obtainable in conventional processing techniques. There are numerous effects of rapid solidification on the as-quenched structure; some of these are:

- i. refinement of microstructure,
- ii. extension of terminal solid solubility of solute atoms in primary phase and change in segregation patterns eventually leading to the reduction or elimination of the second phase,
- iii. modification of segregation pattern,
- iv. formation of metastable phases, and
- v. refinement of insoluble particles such as Al-Fe-Si bearing compounds

The equilibrium phase diagram of Al-Si alloy system shows that the maximum solid solubility of silicon in aluminium solid solution is 1.59 at.% at eutectic temperature (577°C). Such equilibrium solid solubility limit can be enhanced upto eutectic composition (11.8 at.%Si) by rapid quenching, as reported by many authors (61-63). The lattice parameters of aluminium rich solid solution as a function of silicon concentration as reported by various authors, are shown in Fig.2.6. The metastable extension of lattice parameter of aluminium solid solution upto 11 at.%Si is made by extrapolation of lattice parameter data obtained by solid quenched Al-0.93 at.%Si (64) and Al-2 at.%Si (65) alloys. Shingu et al. (63) have measured the lattice parameter of aluminium solid solution in splat quenched Al-Si alloys (silicon content upto 11 at.%) and their results are found to agree well with the metastable extension,

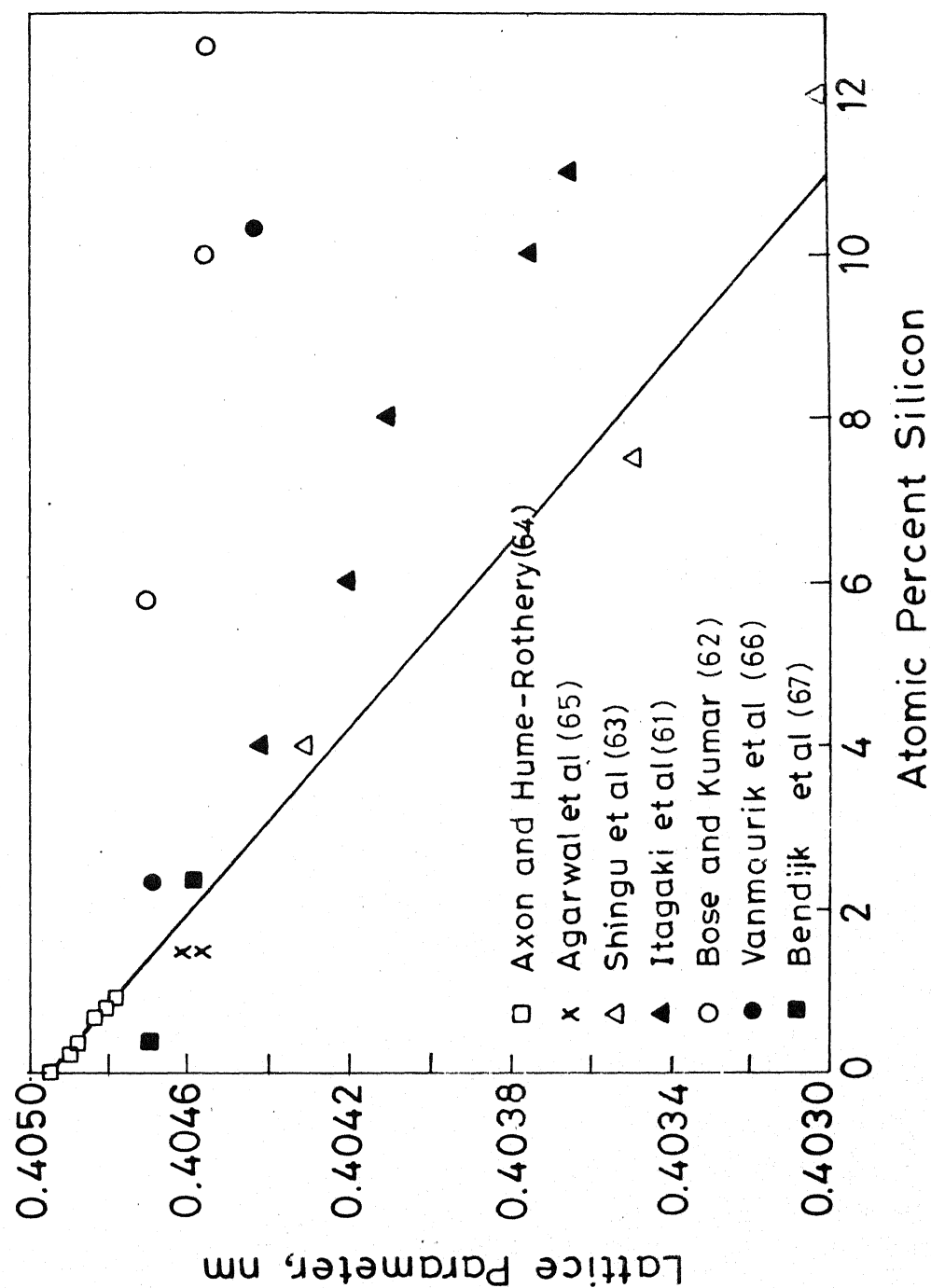


Fig.2.6 Effect of Silicon on the Lattice Parameter of Quenched Aluminium Solid Solution. (□ and x were Quenched from Single Phase Solid Region; others were Liquid Quenched)

Fig.2.6. However, large deviation in the lattice parameters of aluminium solid solution, in rapidly solidified Al-Si alloys, from the metastable extension are reported by various investigators (61,62,66,67), Fig.2.6. Ishihara and Shingu (68) have shown, based on thermodynamic calculation⁵, that the increase in solid solubility of silicon in aluminium is a function of the degree of supercooling during solidification.

Baker and Cahn (69) have discussed the thermodynamics of nonequilibrium solidification and have indicated that the solid with maximum composition can be formed from a liquid when the solidification is completed below a temperature T_0 where both the solid and liquid phases have the same free energies. Additionally, Lavi and Mehrabian (70) have also shown based on the microstructure of Al-Si submicron droplets that the segregation free solidification requires sufficiently large undercooling of the melt associated with the rapid rate of extraction of latent heat of solidification during recalescence, so that no part of the alloy should reach above the T_0 temperature line as discussed by Baker and Cahn (69). The T_0 curves and metastable extension in Al-Si phase diagram are shown in Fig.2.7.

The microstructure of Al-Si alloys is altered markedly by rapid solidification processing. Mueller et al. (71) have studied the microstructure of Al-Si alloys produced by droplet emulsion technique in conjunction with differential thermal analysis, to monitor melting and solidification at controlled heating and cooling rates. Their results stress upon the fact that the degree of supercooling during solidification modify the structure greatly. For instance, Al-7%Si alloy undercooled to 160°C resulted in a structure consisting of aluminium cells and silicon particles segregated in the intercellular regions. Their results also indicate that the reduction in the degree of undercooling, to a value of 57°C, due to nucleation of primary aluminium, yielded a structure consisting of significant amount of primary aluminium solid solution and the remaining liquid solidified in an irregular eutectic morphology. Levi and Mehrabian (70) have also studied the microstructure of Al-Si alloy powders produced by electrohydrodynamic (EHD) process. They have reported that decreasing the particle size, increased the achievable undercooling and solid-liquid interface velocity during growth. This reduces the extent of micro segregation during solidification. A plane front solidification was also reported due to substantial undercooling prior to nucleation and high interface velocity

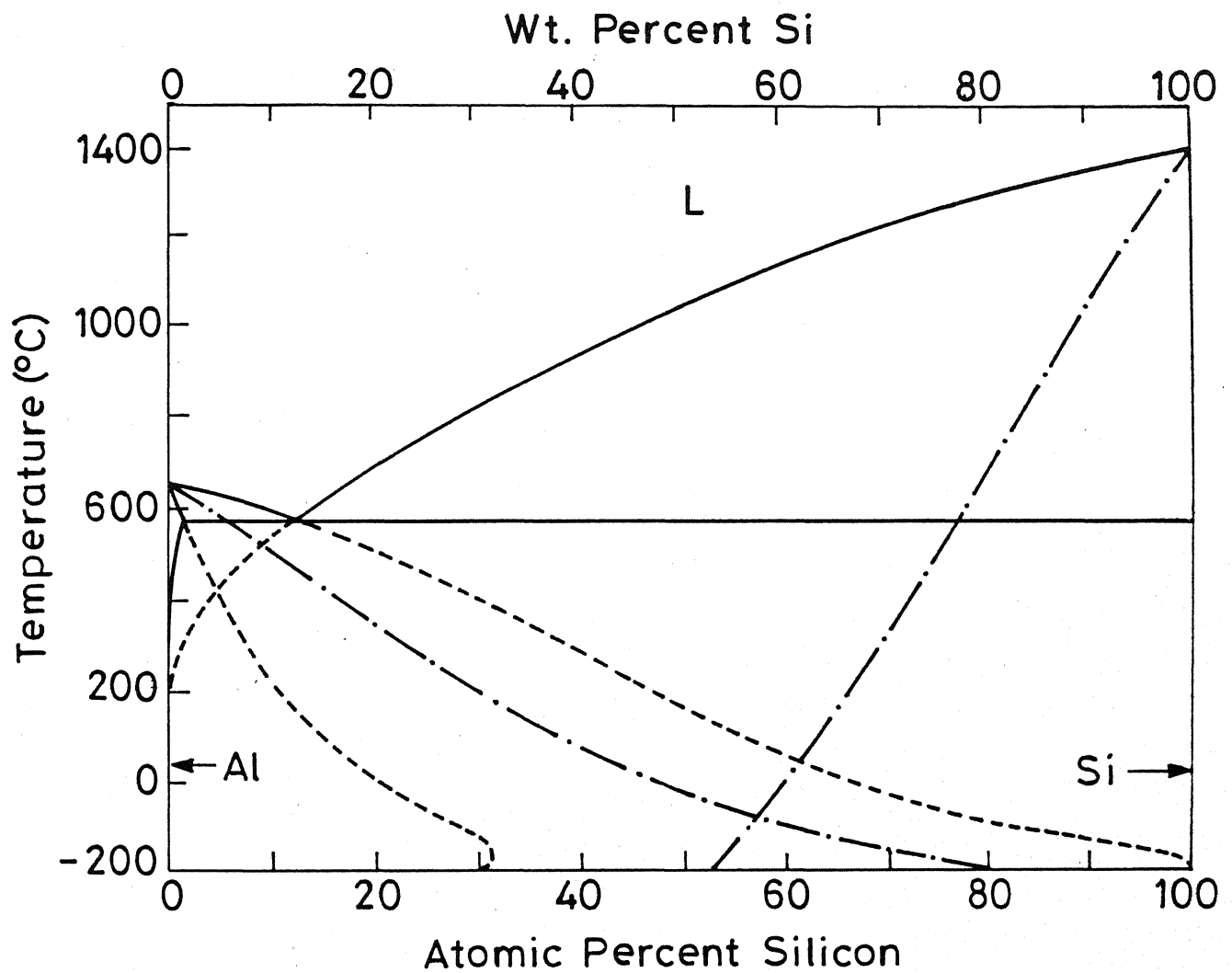


Fig. 2.7 T_0 Curves and Metastable Extensions of the Phase Boundaries.

during recalescence. Vander Hoven et al. (72) have reported that rapidly solidified Al-Si alloy forms three distinct regions; these are: (i) very fine grains (near the wheel side) (ii) columnar zone and (iii) equiaxed grains at the upper side. They have also reported (72) that the solidification of the alloy has not only proceeded from the wheel side but also from the upper side too. The X-ray microanalysis studies of these ribbons across the thickness have indicated that the concentration of silicon is higher at the centre, lowest at the upper side and an intermediate value near the wheel side. Near the wheel side, highest cooling rate is expected which leads to very fine grains, which is reported to be solidified without diffusion. Delhez et al. (73) have studied the microstructure of melt spun ribbon of Al-2.5 at.% Si and Al-33.9 at.% Si alloys using optical and scanning electron microscopy. In both hypo and hyper eutectic alloys a thin featureless zone at the wheel side is observed. In hypo-eutectic alloy the aluminium rich phase at the wheel side shows a preferred orientation different from the one at the upper side whereas, silicon rich phase is randomly oriented. In hyper-eutectic alloy no significant texture is reported.

Paidassi and Chevrier (74) have also made a careful study on the silicon concentration across the cross section by electron microprobe of melt spun Al-12% Si alloy. Their results indicated that no solute rejection could be detected on the wheel side; silicon distribution was only found at the upper side of the ribbon. Papon and Paidassi (75) have studied the rapidly solidified Al-Si alloy produced by planar flow casting in vacuum. The rapidly solidified materials were characterised using transmission electron microscopy corresponding to different depths in the as-quenched and in annealed ribbons. Their results indicate that planar front solidification occurred for the first solidified layers and a transition to cellular solidification occurred later along the solidification path. They have also reported that in Al-12% Si alloy, silicon rich amorphous phase is formed and is thermally stable upto a temperature of 400°C.

2.2 Aluminium Alloy-Composites

Composites are becoming important as high performance materials combining properties generally not obtainable in individual materials. A composite material can be synthesised by the assembly of two or more components—a filler or reinforcing agent and a compatible matrix in order to obtain specific characteristics and properties. Composites can be broadly classified into two categories depending upon the geometry of the reinforcing phase. In fibre and whisker reinforced composites the second phase has an aspect ratio (l/d ; l :length of fibre and d :diameter of the fibre) ranging from 100 to 10,000; a number of such composites with reinforcement of carbon (20), boron (20), silicon carbide (20,21) and alumina (20,22) fibres are now commercially produced for structural applications requiring exceptionally high specific strength and specific modulus. A list of such commercial composites, their manufacturers and applications are shown in Table II.1 (76-79).

The second category of composites involves the dispersion of soft solid lubricant (24,27,80-83) and hard ceramic particles (32-37), as shown in Table II.2. These composites are of great interest in tribological applications. In the case of particle dispersed composites, of the type shown in Table II.2, there can be some reduction in tensile strength, ductility and fracture toughness (84), and these composite materials are primarily developed for tribocomponents where strength is not the main criterion.

Aluminium alloys containing dispersions of (discontinuous) fibres and particles can be commercially produced by conventional powder metallurgy route involving blending, compacting and sintering (76,78). Casting or ingot metallurgy route can also be used to produce aluminium alloy-composites with short discontinuous fibres and particles. Essentially the process involves melting the aluminium alloy, dispersing the short fibres/particles and casting the composite aluminium alloy melt in a suitable mold. On the commercial scale, Science Applications International Corporation (SAIC), USA, has developed this casting route to synthesise aluminium alloys reinforced with silicon carbide whiskers (76). The processes described above are suitable for producing composites containing particle and short (discontinuous) fibre disper-

Table II.1 : List of Manufacturer of Aluminium Alloy-Fibre Composites

Manufacturers	Materials	Fabrication Techniques	Use/Product	References
1. Imperial Chemical Industries (ICI), UK	Aluminium alloy-alumina	i. Squeeze casting ii. Powder Technology iii. Pressure Infiltration Technique	Materials for high temperature applications	76
2. Science Application International Corporation, USA	Aluminium Alloy-SiC	Casting Technology Steel, Sand, Investment casting approach	Thin Walled Tubing	76
3. Material concepts Inc. (MCI) USA	Aluminium-graphite fibre	Liquid metal infiltration technique	For high performance air craft and combustion engine	76
4. Pechiney Centre de Recherches et Development	Al-12Si-Cu-Ni-Al ₂ O ₃ (SAFFIL) or SiC (TOKAMAX)	Squeeze casting	For elevated temperature application in the automotive industries	79
5. ARCO Chemical Company, USA	Aluminium alloy-SiC	Powder Technology	Parts for ring laser gyroscopes, mirrors for infrared sighting assemblies, tactical missile fins, automobile racing pistons, gas turbine wheel, Aircraft hinge mounts with complex webs, horse shoe etc.	76

- | | | | | | |
|-----|-------------------------------------|---|---|---|----|
| 6. | Honda Giken Kogyo Co. Ltd., Japan | Aluminium alloy-stainless Steel fibres | Squeeze casting | Connecting rods | 78 |
| 7. | DWA Composite Specialities Inc. USA | Aluminium alloy-SiC or graphite or B ₄ C composites | | Aluminium-composites material development for defence applications. | 76 |
| 8. | Alcoa's Technical Centre | 7XXX, and 2XXX series aluminium alloy-SiC particle composites | i. Powder Technology
ii. Liquid metal infiltration technique | Composite materials development | 78 |
| 9. | Toyota Motor Corporation | SAE 321 aluminium alloy-Al ₂ O ₃ or Al ₂ O ₃ +SiO ₂ fibres | Squeeze casting | Pistons | 78 |
| 10. | NASA Lewis Research Centre | Aluminium alloy-SiC or B or carbon fibres. | | Application in advanced gas turbine engines. | 77 |

**Table II.2 : Particle Dispersed Aluminium Alloy Composites Synthesised
in Recent Years (38,190)**

Dispersoids	Size	Amount	Matrix alloy
Graphite flake	20-60 μm	0.90-0.815%	Al-(2-25)%Si
Graphite granular	15-500 μm	1-8%	Al-5.7 Cu(2011)
Carbon microballoons	40 μm , thickness:1-2 μm		Al-9.3%Si-2.9%Cu Sn-babbit metal
Shell char	Porous irregular avg. size:125 μm	15%	Al-11.8%Si-(3-6)Mg
Mica	Flake (l/d 20) l=40-180 μm	3-10%	Al-4.5%Cu-1.5%Mg
Talc	Flake, 45-150 μm	3%	Al-11%Si
Zircon	Nodular 40-200 μm	60%	Aluminium, Al-11.5%Si
Titanium carbide	46 μm	15%	Al-4%Cu
Silicon nitride	40 μm	10%	6061 aluminium alloy
Boron nitride	46 μm	8%	6061 aluminium alloy
Alumina	Irregular particle:3-200 μm	3-30%	Al-(5-16)%Si alloy
Silicon carbide	Irregular particle:16-120 μm		Al-(5-16)%Si
Silica	Nodular:5-53 μm		Al-(0.4-12)%Si

in mechanical strength of continuous fibre reinforced composites can be advantageously used in designing components where strength requirements in a particular direction are much higher than those in the other two directions. Diffusion bonding (85) and pressure infiltration (85) techniques are most commonly used to fabricate continuous fibres reinforced aluminium alloys. Pultrusion process (86) in which bundles of fibres are pulled through a molten aluminium alloys bath has also been developed for fabricating various aluminium alloy-composites. Chou et al. (85) have reviewed the various fabrication techniques available for producing fibre reinforced metal matrix composites.

The present study is concerned with the investigation of the microstructure and wear of Al-Si alloys and composites. Since the composites of the present study are produced by solidification processing techniques, various steps involved in the process are briefly reviewed in the following sections.

2.2.1 Steps Involved in the Solidification Processing of Cast Metal Matrix-Particle Composites

The fundamental requirement for transferring graphite particles into the molten aluminium alloy is the good wettability between graphite particles and molten aluminium. Graphite particles are poorly wetted by molten aluminium; hence for successful introduction of the particles, the wettability should be improved and sufficient energy must be supplied to the particles to overcome the gas-liquid energy barrier across the interface. The solidification synthesis of cast aluminium alloy-graphite particle composites essentially consists of the following steps (38), Fig.2.8,

- i. melting of the aluminium alloy,
- ii. introduction of graphite particle in the melt,
- iii. creation of a homogeneous dispersion of particle in the melt and
- iv. solidification of the aluminium alloy-graphite particle suspension under selected conditions to achieve the desired particle distribution in the cast matrix.

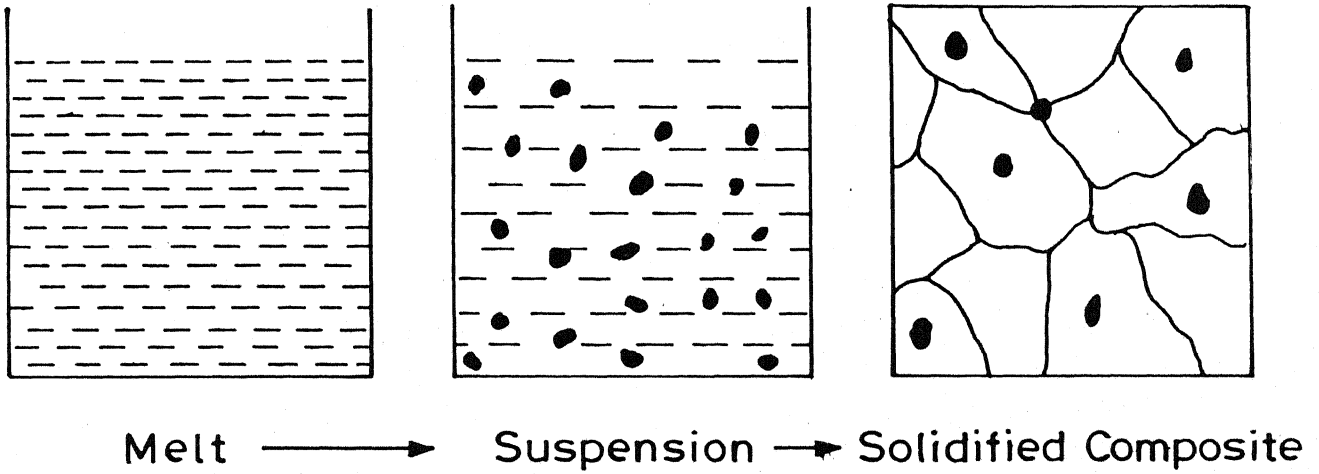


Fig. 2.8 Steps Involved in Solidification processing of Cast Composite.

2.2.2 Techniques of Introducing Particles in the Melt

The techniques developed for introducing solid particles into a molten alloy have recently been reviewed by Rohatgi, Asthana and Das (38). These include the following:

- i. injection of particles entrained in an inert carrier gas into the melt with the help of an injection gun (87-89),
- ii. addition of particles to molten alloys after mechanically stirring the melt with an impeller to create a vortex (22,35,90-93),
- iii. using centrifugal acceleration to preferentially segregate particles or microballoons at specific regions in the solidifying melt (94),
- iv. injection of solid particles into the melt subjected to ultrasonic vibrations (95),
- v. introducing particles into vigorously agitated partially solid slurries of alloy held between its liquidus and solidus temperatures (compo-casting) (29,33),
- vi. producing a dispersion within the melt by means of a chemical reaction (96,97) and
- vii. pressure infiltration of particles prepacked in the mold (98).

2.2.3 Interfaces and Role of Wettability

The fundamental consideration in the transfer of particles from a gas phase to a molten alloy is the wetting between the particles and the melt. Generally the ceramic particles are not wetted by molten metal and alloys, the basic reason being that the particles, particularly oxides, are ionic or covalent in nature and are not compatible with metallic melts. Hence for their successful entry into the melt, wettability should be induced and also sufficient energy must be supplied to allow these particles to overcome the energy barrier at the gas-liquid interface. The wettability between the dispersed particles and liquid metal is important since it affects the ease of dispersing particles, interface bond formation between the solid particle and liquid metal matrix and the defects in the resulting castings. A measure of quantifying the wetting characteristics is the contact angle ' θ '.

Fig.2.9 shows a schematic of the equilibrium configuration of a solid particle entering in a liquid surrounded by vapour phase. At equilibrium, the contact angle is determined by the surface energy of the solid (γ_{gP}), surface energy of the liquid (γ_{Lg}) and the particle-liquid interfacial energy (γ_{PL}). The relationship between the surface energies and contact angle is given by the young's equation (99)

$$\gamma_{gP} = \gamma_{PL} + \gamma_{Lg} \cos\theta \quad \text{.....} \quad (2.2)$$

$$\text{or, } \cos\theta = \frac{\gamma_{gP} - \gamma_{PL}}{\gamma_{Lg}} \quad .$$

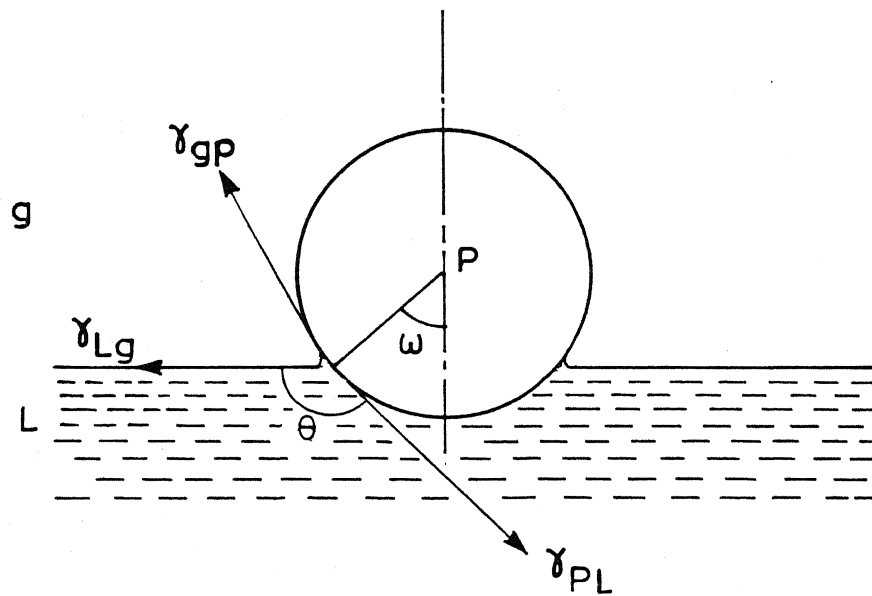
According to equation (2.2) wettability can be improved (i.e., contact angle reduced) by (i) increasing the surface energy of the solid (γ_{gP}) (ii) decreasing the particle liquid interfacial energy (γ_{PL}) or (iii) decreasing the surface energy of the liquid (γ_{Lg}). Besides satisfying the condition for wetting of a liquid to spread on a solid (i.e., $\gamma_{gP} > \gamma_{PL} + \gamma_{Lg} \cos\theta$), the particle liquid interface should also be stable; that means, the work of adhesion (W_a), defined as the bonding force between the liquid and solid phase represented by the relationship,

$$W_a = \gamma_{Lg} + \gamma_{gP} - \gamma_{PL} \quad \text{.....} \quad (2.3)$$

should be high. Combining equations (2.2) and (2.3) gives,

$$W_a = \gamma_{Lg} (1 + \cos\theta) \quad \text{.....} \quad (2.4)$$

The above relation suggests that the bonding force between the solid and the liquid phase may be expressed in terms of the surface energy of the liquid (γ_{Lg}) and the contact angle θ . Since large values of γ_{gP} and γ_{Lg} should increase W_a as dictated by equation (2.2) and since surface energies γ_{gP} for particles are small compared to γ_{PL} for pure liquid metals, the wetting condition $\gamma_{gP} > \gamma_{Lg} \cos\theta + \gamma_{PL}$ can be satisfied by minimizing the liquid surface energy γ_{Lg} which tends to minimize the bonding force between the solid and the liquid phases. Various techniques have been evolved to induce wettability between the dispersed particles and liquid metals and alloy based



- g : Gas
- L : Liquid
- P : Particle
- γ_{gp} : Surface Energy of the Solid
- γ_{Lg} : Surface Energy of the Liquid
- γ_{PL} : Particle-Liquid Interfacial Energy
- ω : Semi Apex Angle
- θ : Contact Angle

Fig.2.9 Schematic of Transfer of a Particle from a Gas to a Liquid Indicating the Various Surface Energy Contributions and Contact Angle.

on the principle that the contact angle ' θ ' can be decreased by increasing the surface energy of the solid γ_{gp} , decreasing the particle-liquid interfacial energy γ_{PL} or by decreasing the surface energy of the liquid γ_{Lg} . A variety of techniques used to induce wettability are explained below:

- i. **Use of Metal Coating:** Coatings like nickel or copper on particles can induce wettability by raising γ_{gp} . Nickel and copper coated graphite (87, 100, 101) and shell char (102) particles have been successfully dispersed in molten aluminium alloys. Electroless nickel or copper coatings on alumina (103) particles were used to prepare nickel or copper based cermets, containing alumina. Recently considerable attempts are being made to prepare metal matrix composite using pressure infiltration technique (39,40). In this technique a preform fibre or uniformly packed powder specimen, is placed in a mold and liquid metal is caused to flow within the interstices. The amount of pressure required to flow the liquid metal depends on the wetting characteristics between the prepacked solid and liquid metal. A recent study (104) shows that electroless nickel plated pitch 55 graphite fibres dispersed uniformly in a 2024 aluminium alloy whereas, uncoated fibres were pushed together and exhibited no infiltration.
- ii. **Addition of Reactive Elements:** Additions of reactive elements to metallic melts promotes wettability by (a) reducing the surface energy (γ_{Lg}) of the liquid, (b) decreasing the solid-liquid interfacial energy (γ_{PL}) or (c) formation of stable chemical compounds by reaction at the interface causing reduction in γ_{PL} . In general elements that have a higher affinity for oxygen tend to decrease the interface tension of liquid metals with oxide. An alkali or alkaline earth metal present in molten metal can chemically reduce the surface energy of several ceramic oxides and glass forming oxides, since the free energy of formation of these reactive metal oxides is lower than that of other metal oxides. A number of investigators have used reactive elements in order to improve melt-particle wettability. Lithium has been found to be a very attractive alloying element to improve wettability for reinforcement of alumina, silicon carbide and carbon fibres (105-107). Magnesium addition to aluminium, Al-Si

and Al-Cu alloys have been reported to facilitate dispersion of graphite (108), alumina (92), silica (109), mica (110), glass (111), shell char (30) and rice husk ash (112) particles in these alloys. Magnesium wets the above particles because of its much lower surface energy (0.559 N/m as compared to ^{that of} pure aluminium 0.760 N/m and Al-11.8%Si alloy, 0.817 N/m) at molten aluminium temperature (113). Addition of magnesium to Al-Si alloys containing zircon particles improved wetting and dispersability of zircon in the melt (91). Both magnesium and silicon were reported to be accumulated at the particle-matrix interface, suggesting chemical reaction at the interface. Similarly, in ZrO_2 and TiO_2 dispersed aluminium alloys containing magnesium as an additive, magnesium enrichments at the particle-matrix interface were reported (114). A recent patent describes (115) a process of dispersing upto 30 wt.% graphite particles in aluminium alloys by addition of vanadium, chromium, zirconium, titanium and niobium to the melt. Chou et al. (115) have critically studied the effect of alloying elements on the wettability between graphite and liquid aluminium. The wetting behaviour has been explained with the help of a term called wetting nucleus creation rate. It has been reported that the rate constant for wetting increased by alloying with (a) and (b) group elements. Oh et al. (116) have studied the effect of alloying elements on the wetting angle of SiC/Al-alloy at 800°C. The observation depicted that magnesium addition is found to induce wettability while that of copper increases the wetting angle. Levi et al. (117) have studied interface reactions in short alumina fibre reinforced aluminium alloys. Cast Al-Mg-alumina fibre composites showed magnesium enriched regions around the fibres which persisted even after heat treatment, indicating the presence of a stable chemical reaction product at the interface. Auger spectroscopy and electron diffraction studies on these composites showed the presence of ^{the} mineral spinel $MgAl_2O_4$ at the fibre/matrix interface, apparently formed either by reaction of Al_2O_3 and MgO produced from direct oxidation of magnesium in the melt, or by reduction of alumina in the fibre by magnesium, or by preferential formation of fine alumina from oxidation of the melt. The spinel phase promoted

fibre matrix interfacial bonding since it forms strong bonds with both metals and ceramics. Small quantities of CuAl_2 and an iron rich phase CuFeAl_7 were detected at the alumina fibre interface in Al-4.5%Cu alloy (117). In as-cast condition copper accumulated at fibre edges, although largest copper concentrations did not necessarily occur in the fibre matrix interaction zone. After heat treatment, only residual copper content was observed in the zone that was almost equal to the matrix level. Finally, in Al-4.5%Cu-2%, Mg alloys, effect of magnesium was to significantly reduce the extent of interaction zone observed in Al-Cu- Al_2O_3 composites, although magnesium and copper enrichments were again detected at the fibre boundary. After heat treatment while most of the non-equilibrium second phase CuAl_2 and CuMgAl_2 of the matrix dissolved, a thin copper rich ring was left around the alumina fibre (117). The more stable MgAl_2O_4 was reported to have enveloped copper spinel preventing outward diffusion of copper during heat treatment. A composite reinforced with polycrystalline alumina fibres (10 vol.%) in the matrix of an aluminium alloy containing 0.5-5.5 wt.% lithium has been prepared by pressure infiltration of fibre preforms. Lithium was found to react with alumina fibres forming LiAlO_2 at the interface and improving melt-fibre wettability (118).

- iii. Heat Treatment: Contact angle in metallic melt-ceramic particle system e.g., Al/Sapphire, Ag/graphite and Cu/graphite decreases with increasing temperatures, thereby promoting wettability (119). Contact angles of aluminium with alumina and graphite measured by sessile drop method were found to decrease with increasing temperatures (120, 121). Heat treatment of silica particles prior to their dispersion in aluminium and Al-Mg alloys resulted in uniform dispersion in the melt (35). Uncoated refractory particles, suitably heat treated, are easily transferred to molten aluminium alloys (90). Agarawala and Dixit (122) have reported that there was no retention of graphite particles when the graphite particles were not preheated, whereas the particles were retained when preheated.

- iv. **Ultrasonic Treatment of Particles:** A clean surface provides better opportunity for melt particle interaction and hence wetting. Ultrasonic technique can be used to break up surface layers. Banerjee and Rohatgi (114) have successfully dispersed ultrasonically pre-treated zirconia and titania particles in Al-11.8%Si-1%Mg alloy. It was suggested by these authors that the absorbed gases on the surface of these particles decrease their surface energy according to the relation $\gamma_{Pg} = \gamma_{Po} - p$ where γ_{Pg} and γ_{Po} are the surface energies of the solid particles in vapour phase and vacuum respectively, and p is the surface pressure of the absorbed gas on the solid. Infrared (IR) spectral analysis of as-received oxide particles showed the presence of hydroxyl ions and molecular water at the surface of the particles. These were absent in the IR spectra of ultrasonically treated powders, indicating desorption of absorbed gases.
- v. **Compocasting:** In compocasting the non metals are dispersed in a vigorously agitated partially solid slurries of alloys held between their liquidus and solidus temperatures. The particles are mechanically entrapped between the primary solid phase in the slurry and prevented from settling, floating or agglomeration, due to increased effective viscosity. With increasing mixing times after addition of particles, interactions between particles and the matrix promote wetting and bond formation. Gibson et al. (25,123) have squeeze cast Al-(4-16%)Si alloys containing 2-8% graphite particles which were introduced in the alloy by compocasting technique. A special rotor design was used (25) to prevent surface agitation of the melt and consequent air entrapment. The optimum combination of shear rate, graphite content and initial volume percent solid in slurry were determined to give a viscosity suitable for casting. Better particle distribution was obtained in squeeze cast hypoeutectic alloys compared to near eutectic and hypereutectic alloys which showed some evidence of graphite clustering. It was suggested (123) that the significantly higher proportion of solid present in hypoeutectic alloy slurries aids the separation and distribution of particles. The process parameters for incorporation of the maximum level of alumina particles in compocast slurries of Al-Mg alloys have been optimised by Ghosh et al. (124). These authors noted a linear increase in the porosity level of the composite casting with increasing additions of alumina.

2.2.4 Interaction Between Suspended Particles and Growing Solids

The suspended particles in matrix melt are generally present in the last freezing liquid presumably pushed by the advancing solidification front. While the entrapment of the particles within the cells and dendrites would have resulted in a more uniform distribution, their segregation in the last freezing liquid leads to inhomogeneity in the spatial microdistribution of the particles in the metallic matrix. Model experiments using transparent organic materials containing a variety of solid particles have been conducted to study particle engulfment as well as capture by growing crystals (125-128). For each particle-liquid combination, a critical solidification front velocity (V_c) representing transition from rejection to engulfment configuration was found to exist. When the growth velocity is smaller than V_c , the particle is found to be pushed whereas particle engulfment is observed for values of velocities exceeding V_c .

Uhlman et al. (125) have suggested that the increase in specific surface energy of particle with decreasing separation between the particle and the advancing solid-liquid front provides the driving force for diffusional transport of fluid in the region between the particle and the crystallisation front. The particle is captured when the liquid can not diffuse sufficiently under the suspended particle and unable to ensure growth of the crystals. The theoretical critical velocity (V_c) above which the particles are captured by the solidification front is given by the expression (125),

$$V_c = \frac{n+1}{2} \left[\Delta H \rho_L \Omega_0 a_0 \frac{D}{KT R^2} \right] \dots 2.5$$

where, n is a constant

ΔH is the enthalpy of fusion

ρ_L is the density of liquid,

Ω_0 is the atomic volume,

a_0 is the atomic spacing,

D is the diffusivity of liquid,

KT is the Boltzmann factor and

R is the particle radius.

For aluminium-graphite system (129) the estimated V_c lies in the range of 0.0022 $\mu\text{m}/\text{sec}$ to 0.0001985 $\mu\text{m}/\text{sec}$ for graphite particle sizes from 30 μm to 100 μm respectively; the local solidification velocity is of the order of 0.5 $\mu\text{m}/\text{sec}$ in permanent molds. Contrary to the predictions of Uhlman

et al. (125), experiments on aluminium-graphite system (129) show that all the graphite particles are pushed by primary aluminium dendrites into the last freezing liquid, even though the actual solidification velocity is much higher than the theoretical critical velocity for capture. This discrepancy persists even after a modified value V_c is obtained taking into account the existence of grain boundary grooves and grain boundary triple points (126). This suggests the need to evolve different criterion for particle pushing in metal-particle systems where the thermal properties of phases are very different. The theoretical predictions of Zubkov et al. (131) and experimental observation of Omenyi and Newmann (128) and particle capture or rejection by growing crystals, have shown that thermal conductivity criterion *has* failed in some cases e.g., polystyrene particles in diphenyl and naphthalene solvents. Surappa and Rohatgi (130) have tried to obtain an empirical relationship for predicting the rejection or entrapment of particles by growing crystals, called heat diffusivity criterion according to which the ratio of the heat diffusivity of the particle to that of the liquid should be greater than unity for capture of particles, i.e.,

$$\left(\frac{\lambda_p C_p \rho_p}{\lambda_L C_L \rho_L} \right)^{1/2} > 1 \quad \dots 2.6$$

where, λ_p is the thermal conductivity of particle,

λ_L is the thermal conductivity of liquid,

C_p is the heat capacity of particle,

C_L is the heat capacity of liquid,

ρ_p is the density of particle and

ρ_L is the density of liquid.

This criterion has been successfully tested in both metallic and nonmetallic systems at slow growth rates. This criterion has a different physical basis than that of Omenyi and Newman (128) and thermal conductivity criterion proposed by Chernov and Melnikova (127).

2.2.5 Microstructure of Composites

The microstructure of cast metal matrix composites is controlled largely by the interaction between the dispersoids and the solidification kinetics of cast metal matrix. A thorough understanding of the solidification mechanism of metal matrix in presence of dispersoids offers opportunity to suitably design a microstructure required for a particular application. A wide range of

microstructure of the cast composites may be synthesised by controlling the size, shape and volume fraction of the dispersoids.

Several attempts have been made to study the microstructure of aluminium alloys in the presence of graphite particles. It is conceivable that the dispersed graphite particles in molten aluminium alloys tend to float because of lower density than that of the molten aluminium alloys and segregate at the top portion of the castings. Badia and Rohatgi (87) have studied the microstructural distribution of nickel-coated graphite particles in various Al-Si-Ni alloys. Their observations depicted that graphite particles are pushed into the interdendritic regions associated with the ternary Al-Si-NiAl₃ eutectic, instead of being entrapped by the growing α -aluminium dendrites. In an another (87) experiment graphite particles are distributed among the plate shaped dendrites of NiAl₃ and the interdendritic ternary Al-Si-NiAl₃ eutectic in Al-9.2 Si-6.3 Ni base alloy. In Al-16 Si-2 Ni base alloy, graphite particle is associated with the primary silicon particles (87). The microstructure of LM13 alloy in presence of dispersed graphite particles is studied by Asthana et al. (132). Their results show that dispersion of 3 and 5 wt.% graphite particles in LM13 alloy resulted in an average dendrite arm spacing around 15 and 16 μm respectively, which indicated insignificant change in the microstructure (132). However, the graphite particles are reported to be pushed into the last freezing eutectic liquid, presumably due to the rejection by the solidifying liquid (132). There are some results available in the literature on the solidification microstructure of aluminium alloys in presence of fibres. In hypoeutectic Al-Si alloys, the large eutectic region is surrounded by the fibres (133-136). In hypereutectic Al-Si alloys, the primary silicon grew from the fibres into the interfibre spaces (133). In Al-Mg-alumina fibre composites, the second phase was observed on the fibres (134-137). In Al-Li-alumina fibre composites, small amount of LiAl intermetallic phase is present in the matrix presumably due to interfacial reaction (138). Al-Cu alloys were also solidified in the same fashion with the primary phase avoiding the fibres. The eutectic is precipitated into the fibres or between individual dendrite arms (134,135,138-142). However, Fukunage et al.(140) have reported that the alpha phase nucleates and grows on the cold fibres. The Cu-rich liquid is rejected to the centre of the interfibre regions. In Al-9%Si-4%Cu alloy (39) infiltrated with carbon fibre bundles, the CuAl₂ phase surrounded the fibres as observed in Al-Cu alloys (133).

Gungor et al. (143) have made a model experiment with Al-4.5% Cu-55 vol.%Al₂O₃ and showed that when the matrix alloy is solidified at a relatively faster rate, when the average dendrite arm spacing is less than the average interfibre spacing, the effect of fibre on microsegregation is negligible. However, when the solidification rate is low, so that the average dendrite arm spacing is more than the average interfibre spacing, microsegregation is reduced significantly as compared to the unreinforced matrix material (143).

The dispersed particles in metallic melt are expected to have a rather low probability of being suitably oriented with respect to the advancing solidification front to form specific low energy interface (132,144). However, the presence of a variety of particles like graphite, shell char, zircon, illite clay and massive alumina in solidifying Al-Si alloys has been reported (30,41,145) to lead to preferential nucleation of primary silicon on the surfaces of these particles. Cisse et al. (55) added a master alloy of SAP rods containing 10% of Al₂O₃ in hypereutectic Al-Si alloy and found that direct additions of finely dispersed alumina nucleated silicon but not aluminium. Quaternary alloys containing both alumina (added as SAP) and sodium showed primary silicon refinement and eutectic modification. Freshly made alumina (i.e., not added externally but formed in the melt by some chemical reaction) is generally an effective nucleant for aluminium. Krishnan and Rohatgi (41) have reported that dispersion of 3 wt.% graphite particles in LM13 alloy melt leads to partial modification of the eutectic silicon. The modification is complete when sodium in elemental form or as a salt (Coveral 29A) is added to LM13-3wt.% graphite particle composites, prior to graphite particle dispersion in the melt (41). This indicates that mechanical stirring of the melt during dispersion of graphite particles does not hamper the modification of eutectic silicon. In experiments in which the modification treatment was carried out after the dispersion of graphite particles only elemental sodium could lead to successful modification; total rejection of graphite particles was noted when halogen based coveral 29A was used after the dispersion of graphite particles. This could be due to the adverse effect of chlorine or chlorine bearing gases on the wetting of graphite particles with molten aluminium. The modification of eutectic silicon in the presence of suspended particles appears to be atleast partially promoted by the preferential concentration of silicon on the surfaces of these particles. However,

the exact mechanism for modification of eutectic silicon in presence of dispersed particles has not been discussed and the discussion is solely confined to the microstructural features of growth of the phases.

2.2.6 Physical and Mechanical Properties

The density of aluminium alloys is found to decrease with the addition of graphite particles (38). The thermal conductivity and expansion coefficient of aluminium alloys decrease with graphite addition (146). The damping capacity of aluminium base alloys is improved by incorporation of graphite particles in the matrix (147). It is reported (148) that the damping capacity of aluminium alloy spherical graphite particle composites (size: 350-550 μm) is superior to that of aluminium alloy-flake-shaped mica particle (size: 40 μm) with the same volume percentage of particle. It has been suggested that graphite particles may be more effective than mica in increasing the damping capacity since the lower shear strength of graphite compared to mica can dissipate a considerable fraction of the energy of the propagating elastic wave by microplastic deformation of the particle itself (147).

Hardness and tensile strength of aluminium alloy decrease with progressive addition of graphite particles. Based on micromechanical modelling, Majumdar et al. (84) have shown that for homogeneous distribution of graphite particles in aluminium alloys, the values of strength obey a two third ($2/3$) power law of the form,

$$\frac{\sigma_c}{\sigma_m} = 1 - 1.5 F_p^{2/3} \quad \dots\dots 2.7$$

where, σ_c and σ_m are the ultimate tensile strength (UTS) of composites and pure matrix respectively and F_p is the volume fraction of particles. Fig.2.10 shows the normalised ultimate tensile strength of aluminium-graphite composites (84). Porosity in the castings of metal matrix particle composites can considerably reduce the ultimate tensile strength (149). A linear decrease of UTS of cast particulate composites with increases of porosity level in castings has been reported in (149) in the low porosity regime. Considerable improvement in strength, ductility and hardness of aluminium-alloys particle composites have been reported (150-158) as a result of thermomechanical processing e.g., hot extrusion, rolling and forging. Hot extrusion of squeeze cast Al-Si alloys containing graphite particles in different sizes and amounts

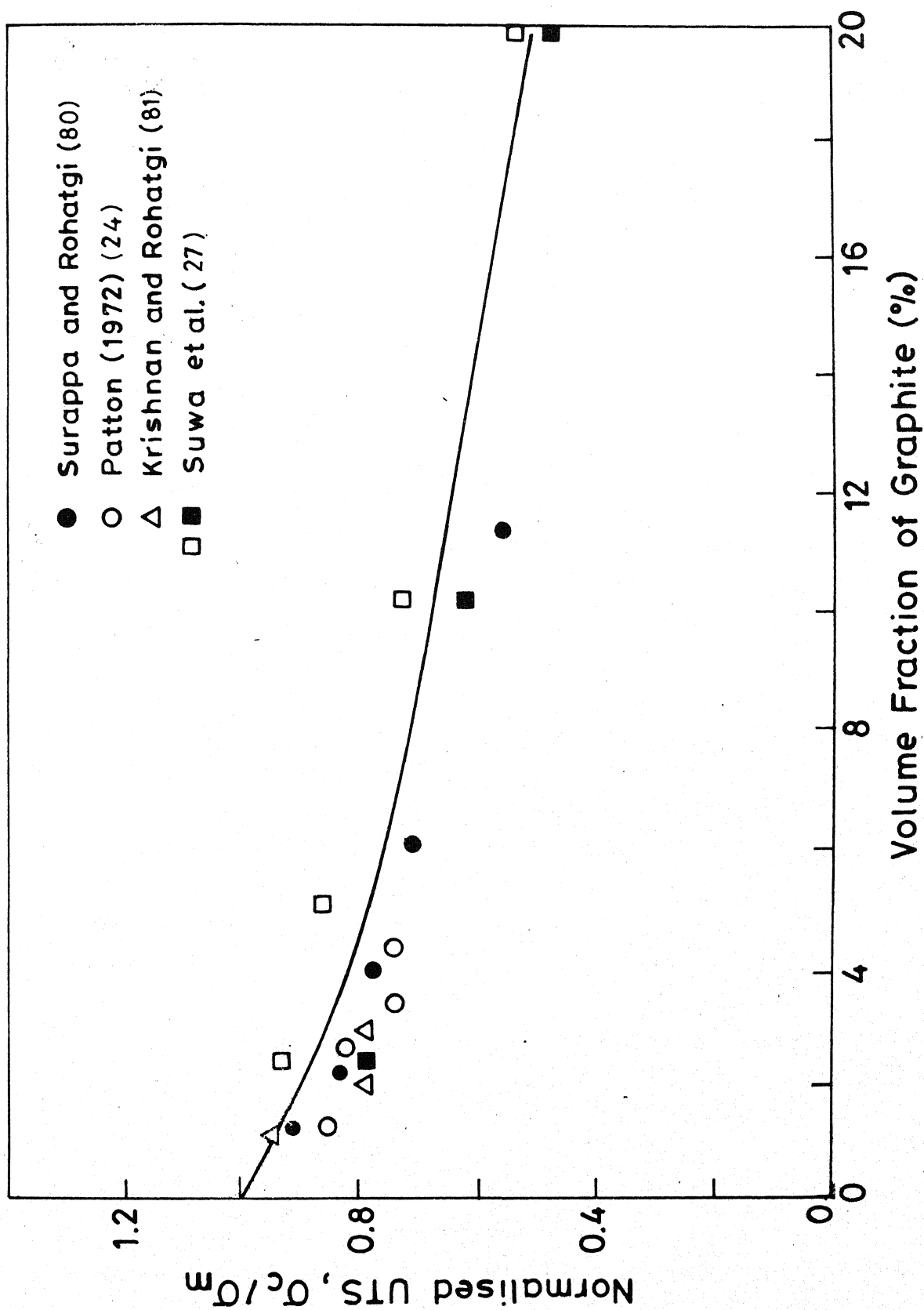


Fig.2.10 Strength vs Volume Fraction of Graphite Particles in Al-Graphite Composites.

showed that UTS and ductility of extruded rods increased with increase of extending ratio (aspect ratio) of graphite particles (154). Hot extruded samples showed cleavage fracture of graphite along tension direction (154,155). Extending ratio of graphite stringers decreased almost linearly with increase of extrusion temperature. The UTS of graphite dispersed hot extruded alloys decreases with decrease of graphite content and increase in graphite size. With increasing degree of deformation, the aspect ratio of graphite particles increases possibly due to the fact that the ratio of the hardness of particles to that of matrix becomes less than a critical value (158). This ratio goes up with rise in temperature. Polycrystalline graphite has a low shear modulus along the basal plane and hence it is easier to deform it under the combined effect of shear and compressive stresses which exist during the thermomechanical processing operations. The improvement in mechanical properties, resulting from hot working, has been attributed (151) to a number of factors like refinement of structure, work hardening of the matrix, decrease in the size and number of pores, and deformation of particles into stringers. Fracture toughness of cast and forged aluminium-graphite particle composites has been determined, as a function of dispersoid size and amount by Pillai et al. (156) and a thermodynamic model has been proposed for the fracture of cast particulate composite by Ray (157).

During the solidification processing of cast aluminium-graphite fibre composites residual stresses could develop owing to mismatch of thermal expansion of matrix and fibres (158). Mismatch of expansion coefficient and consequently residual stresses have been found to be low along transverse direction owing to the anisotropy of graphite fibres (158). Studies on cyclic deformation of composites show that fatigue life of cast Al-Si-Graphite particle composites is impaired by both increase in silicon and graphite contents (129).

The length of the chip produced during machining of aluminium alloys is considerably reduced by progressive addition of graphite particles (147), finer particle dispersions leading to shorter chip length at a given machining speed. The decrease in chip size will be of advantage in automated, fast machining operations where long chips have a tendency to get wrapped round the tool. Microscopic examination of machining chips showed that graphite particles on the chip surface are frequently smeared in a plane parallel to the chip surface (147). This could account for reduced power consumption

and less wear of tool during machining of the composites. Recently, Brown and Surappa (159) have reported that forces required for machining is less in Al-Si-graphite composites than those for Al-Si alloys, because of lower tool-chip friction. The machined surfaces of Al-graphite composites is reported to be rougher than similar surface without graphite.

2.2.7 Rapidly Solidified Metal Matrix-Particle Composite

In recent years considerable attempts are made to produce rapidly solidified aluminium alloy matrix-particle composites in order to combine the advantage of dispersed particle and rapidly solidified structures of the matrix. Various techniques are evolved to synthesise rapidly solidified metal-matrix particle composites, some of these are described below:

- i. **Spray Codeposition:** Spray codeposition technique has been developed by Singer and coworkers (160,161) at the University College of Swansea, U.K. In this process, the second phase particles are injected into the atomised stream of molten matrix material in such a way that a homogeneous matrix is formed in flight which is then deposited onto a suitable substrate. The above operation is followed by the consolidation of as-deposited strip to finished composite strip. This technique overcomes the difficulties of gravity separation of the particles and interaction with the matrix. Singer and coworkers (161) have successfully incorporated particles including SiC, Al_2O_3 , chilled iron, graphite, sand particles and mixtures of these upto 36 vol.% in a matrix of aluminium and aluminium-silicon alloys. The microstructural examination of as-codeposited and consolidated composite showed that a homogeneous distribution of particles was obtained and no significant interfacial compound was formed. This^{is} possibly because of very short time of solidification of the matrix. The tensile strengths of the composite materials were found to be slightly higher than those of the matrix material itself for aluminium matrix composites. The coefficient of friction of these composites were found to be higher compared with that of the conventional friction material.
- ii. **Laser Melt Particle Injection:** The recent availability of high power directed energy sources such as the electron beam and the different

types of lasers, has led to the development of rapid melting and solidification techniques in which a bulk substrate which is in intimate contact with a molten layer, acts as the quenching medium. Since the melt and the substrate are in intimate contact, the heat transfer coefficient between the two tends to infinity. Ayers et al. (162-164) at the Naval Research Laboratories (NRL), Washington, USA, have developed laser melt-particle injection process in which surface of a wide variety of metals and alloys are impregnated with hard wear resisting particles. Attempts have been made to disperse WC and TiC particles in various matrix materials e.g., Ti-6Al-4V, commercial purity Ti, 304 stainless steel, 4340 tool steel, 1018 steel, Inconel X-750, 5052, 2024, 6061 aluminium, aluminium bronze etc. The carbide powders are blown into the melt pool by a stream of helium gas and is directed towards the melt by a fine copper nozzle.

- iii. Melt Spinning: In this technique, the second phase particles are injected by a sand blasting gun, operated by pressurised helium gas, after the liquid metal or alloy is blown through the nozzle but before it freezes into a ribbon. This method minimizes the contact time between the second phase particle and the liquid alloy and offers a potential route for adding wide variety of particles since it restricts the opportunity for reaction at the particle matrix interface. Zielinski and Ast (165) have dispersed TiC and WC in rapidly solidified amorphous $\text{Ni}_{75}\text{Si}_8\text{B}_7$ ribbon. Their result showed that the WC particles could enhance the yield strength of the amorphous ribbon and are capable of altering the slip distribution of the specimen. Kumura et al. (166) have dispersed Cr_2O_3 , ZrO_2 particles in amorphous $\text{Co}_{70.5}\text{Fe}_{4.5}\text{Si}_{10}\text{B}_{15}$ alloy with an intention to develop magnetic composite.

2.3

Wear

Wear is defined as the gradual removal of material from the rubbing surfaces. Wear of a material is controlled by the material characteristics as well as test parameters such as applied pressure, sliding speed, environment and the type of sliding interaction. Burwell (167) classified wear into the following major groups: adhesive, abrasive, corrosive, surface fatigue and erosive.

(i) Adhesive or sliding wear: Adhesive or sliding wear occurs as a result of relative sliding between two surfaces under the influence of an applied load (168). In general, on a microscopic level, the machined surface of a material is not exactly flat but consists of sharp asperities. When two solid surfaces are brought in close proximity, the surface would be touching only at a few points, and they adhere strongly to each other and form asperity junctions. As the contact area is very small, the pressure exerted on each asperity is extremely high. This results in elastic and plastic deformation of the softer of the two materials in contact, until the areas of the contact junctions are large enough to support the load. If the strength of the junction is more than the shear strength of the softer material then during sliding action the tangential force will shear the softer junctions and leave clean surface at the softer asperity.

A critical evaluation of the assumptions of the adhesion theory of wear leads to the following points (169):

- a. The adhesion theory of wear assumes that the material removal due to shearing of junctions is only possible when the strength of the junction is more than the shear strength of the softer material. This proposition is questionable because the interface can not be stronger than the contacting materials since it is likely to contain vacancies, impurities or oxides. Therefore, complete adhesion and material removal may not be possible.
- b. Adhesion theory does not make any concrete predictions on how the fracture occurs in one of the surfaces.
- c. The theory also ignores the controlling effect of friction force on the wear rate.

- d. Adhesion theory does not consider the structure and the mechanical properties of the materials.

Suh et al.(169) have proposed the delamination theory in order to explain the sliding wear of material and the generation of flake-type wear debris. This theory describes the following sequential events which lead to loose wear particles: during sliding wear, the normal and tangential loads are transmitted through the contact points by adhesive and plowing action. The asperities of the softer material may either be deformed or fractured. This makes the surface of the soft material smooth and the contact is not just an asperity to asperity, but rather asperity to plane. The surface traction exerted by the hard asperities on the softer surface induces plastic deformation. The continuous deformation results in void formation below the sliding surfaces. Void nucleation on the surface is ruled out as the compressive state of stress is maximum at the surface. Once, the cracks are nucleated further loading and deformation cause cracks to propagate. When these sub-surface cracks reach a critical length they become unstable and shear to the surface at some weak positions.

(ii) Abrasive Wear: Abrasive wear is accomplished by plowing or cutting action of hard particles on a relatively softer surface of the material. The hard particles may be either loosely held between two sliding surfaces as in three body abrasive wear or part of the second surface as in two body abrasive wear using abrasive papers. A semi-quantitative expression to predict abrasive wear was derived by Rabinowicz and coworkers(170,171) assuming that the asperities on the hard surface are conical in nature.

(iii) Corrosive Wear: Corrosive wear occurs whenever sliding takes place in corrosive environments. Corrosion products are formed and their removal from the surface is accomplished by sliding action.

(iv) Surface Fatigue Wear: Surface fatigue wear is caused by the removal of particle from the surface due to cyclic loading. This is generally associated with the surfaces in a rolling contact, where the friction coefficient is negligible. The wear mechanism is mainly governed by the formation of surface or sub-surface cracks and fatigue crack propagation.

(v) **Other Types:** Among the other types of wear, erosion is the most important one. Erosive wear by solid particle impingement arises from the impact of hard abrasive particles on a target surface. Erosive wear is caused mainly by cutting and deformation processes. In metals, the cutting action is dominated at a low angle of particle impact and deformation at high angle of particle impact.

Since the present study involves the wear behaviour of aluminium-silicon alloy-graphite particle composites, it would be worthwhile to first review the literature on the sliding wear behaviour of Al-Si alloys.

2.3.1 Sliding Wear of Aluminium-Silicon Alloy

There have been several reports describing the wear of Al-Si alloys against steel disc (172-188). Effect of factors like applied load, silicon content, silicon morphology on dry sliding wear of Al-Si alloys have been established and described below.

(i) **Effect of Load:** In general, laws of adhesive wear predict a linear relationship between the wear rate and applied load (168). However, such a relationship is not found to be valid for Al-Si alloys. These alloys show a non-linear wear behaviour and the wear rate increases as the pressure is increased. Shivanath et al.(174) have reported a transition from mild wear to severe wear as the load is increased (See Fig.2.11). This transition load has been reported to depend upon the silicon content, as is clearly shown in Fig.2.12. Clarke and Sarkar (175) have also shown that the variation in wear rate with applied load depends upon the silicon content. The wear rates of Al-Si alloys with silicon content 1.8 and 6.3% increased with load at an accelerating rate (Fig.2.12a) and for alloys containing 11,13,15,16 and 21% silicon, the wear rate increased with load at diminishing rate (Fig.2.12b).

(ii) **Effect of Silicon Content:** There is a controversy over the optimum silicon content in aluminium as far as wear resistance is concerned. It has been reported (173,175,180) that near eutectic Al-Si alloys offer better wear resistance than the hypereutectic alloys. Some investigators (184,185) have, however, shown that hypereutectic Al-Si alloys offer better wear resistance. Okabayashi and Kawamoto (183) have reported that it is the amount of primary silicon present in hypereutectic alloy rather than the degree of

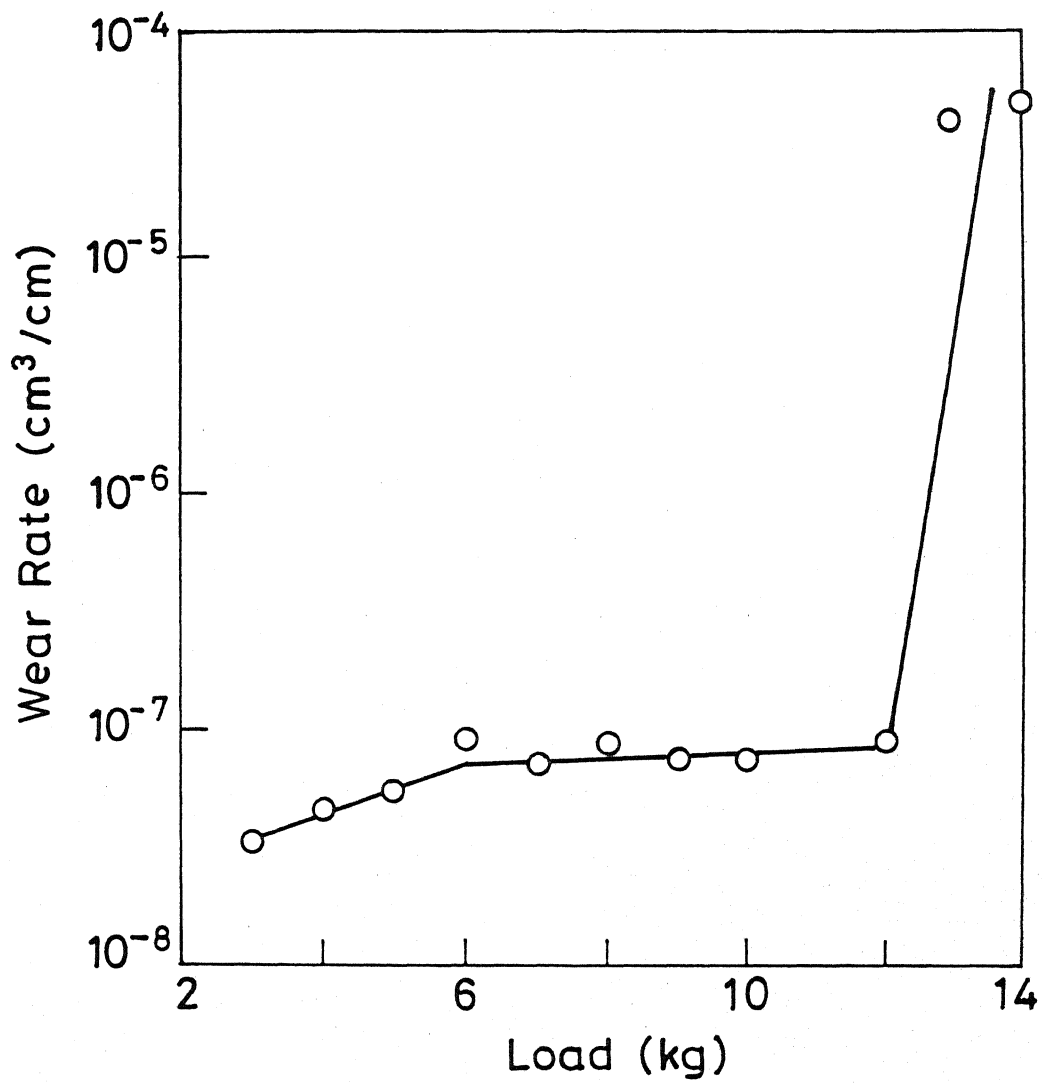


Fig.2.11 Wear of Al-8%Si Alloy.

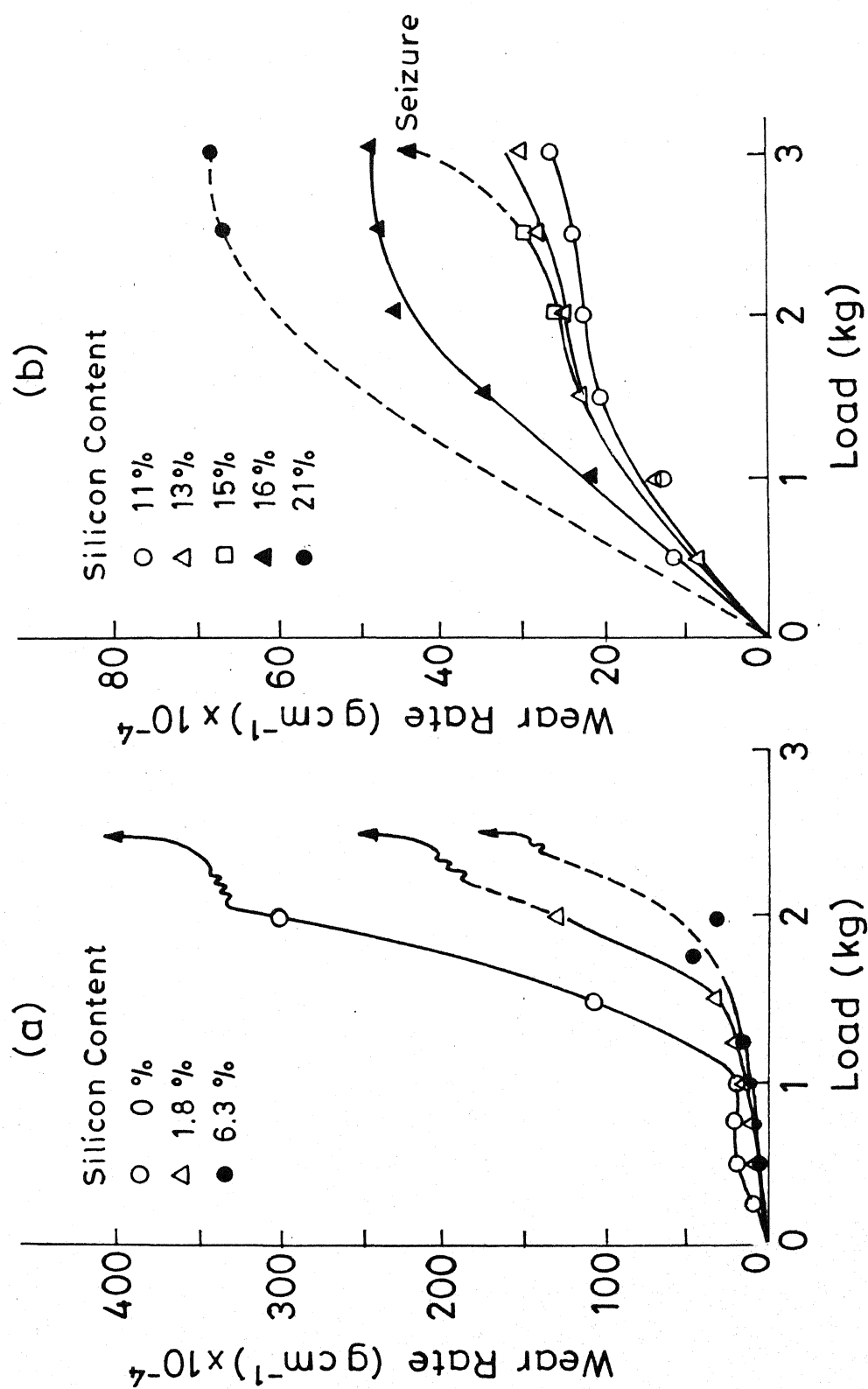


Fig. 2.12 (a) Wear Rate Against Load of as-cast Low Silicon Alloy Pins Sliding on a Hard Steel Bush at a Surface Speed of 196 cm s^{-1}
 (b) Wear Rate Against Load of as-cast Al-Si Alloy Pins Sliding on a Hard Steel Bush at a Surface Speed of 196 cm s^{-1} .

silicon refinement obtained which improved the wear resistance. Shivanath et al. (174) have also shown that increasing the silicon content is beneficial as far as the wear resistance of the alloys is concerned. Wear behaviour of aluminium containing 14.5, 17 and 25% silicon showed that intermediate amount of silicon has the maximum wear resistance (184).

(iii) Effect of Silicon Morphology: The effect of silicon morphology on the wear behaviour of Al-Si alloys has been studied by several investigators (56,183,186-188). Okabayashi and Kawamoto (183) varied the silicon size by modification with phosphor-copper and found that decrease in silicon size improved the tensile strength but had no effect on the wear rate. Similar observations were made by Colligan (186). Based on the observation of clutches, cylinder liners and pistons in service, Stonebrook (187) has reported that the quantity rather than the size of the silicon is an important parameter controlling the wear rate and a higher silicon content would be desirable. Clegg and Das (56) have reported that structural modification of hyper-eutectic Al-Si alloy did not produce any significant difference in the wear resistance of the alloy. However, Subramanian and Kishore (44) have shown that the initial size of silicon controls the wear rate of near eutectic Al-Si alloys. Their results indicate that modification of eutectic silicon with coverall 36A as well as hot working improves the wear resistance.

2.3.2 Study of Wear Surfaces

Studies of the wear surface of Al-Si alloys have been carried out by a number of investigators (172-182,188) and the mechanisms of wear discussed extensively. Clarke and Sarkar (178) proposed that transfer and back transfer of low yield stress material results in formation of loose wear particles. As the sliding action begins, the low yield stress material is transferred and deposited on hard counterfaces. Once it exceeded a critical number of layers, wear particles were produced. It has also been reported that the wear debris are generated by the mechanism of nucleation and propagation of cracks in the surface as well as in the subsurface region (176) by continuous plastic deformation. The subsurface studies confirmed that the cracks are propagated along the wear track and terminated at the surface forming the wear particles. Clarke and Sarkar (177) have studied the surface topography of Al-Si alloys in dry sliding condition and shown various topographical features such as adhesive delamination, granular delamination, plow cracking, shear dimpling, roof tile lamination and inclined shear plates.

2.3.3 Subsurface Deformation

Subsurface deformation studies on Al-Si alloys were reported by several investigators (172,176,179). The depth of the subsurface deformation was found to increase with bearing pressure and sliding speed (179). Rohatgi and Pai have reported (172) that deformed subsurface of Al-11%Si alloy consists of fragmentated silicon needles uniformly distributed in primary aluminium matrix. The average size of fragmentated silicon was not a function of the bearing pressure and sliding speed (179). A recent study by Antoniou and Borland (182) has shown a correlation between the wear particles and wear surfaces. They have reported that deformation, compaction and fracture mechanisms governed the formation of debris at low load region and at high loads debris are formed by a ductile shear mechanism. However, both the mechanisms were reported to be operative at intermediate loads.

2.3.4 Aluminium-graphite Composites

Although Al-Si alloys possess many of the essential properties for tribological applications, their use as an efficient antifriction material has been limited because of the poor resistance to seizure when run under boundary lubrication condition. To minimize the seizure, several authors have dispersed graphite, a well known solid lubricant, in Al-Si alloys.

There have been several studies to evaluate both the dry (42-44) and lubricated (23,26,45,46,189) sliding wear of aluminium alloy-graphite particle composites, measured against rotating steel disc using a pin-on-disc apparatus. Since there is no universally accepted procedure for evaluating the sliding wear, different investigators have used different experimental procedures and conditions, including hardness and roughness of sliding surfaces, sliding distance, sliding speed and load. To avoid the effect of some of these test variables Prasad and Rohatgi (190) have used normalised wear rates, defined as the ratio of the wear rate of the composites to that of the matrix alloy.

2.3.4.1 Dry Sliding Wear

Gibson et al. (42) have studied the effect of graphite dispersion in Al-Si alloys on the dry sliding wear behaviour. The composites were produced

by compocasting followed by squeeze-casting. The coefficient of friction and temperature rise of the composite pin in pin-on-disc wear test are shown in Fig.2.13. It can be seen that both coefficient of friction and temperature rise of the wear pin decrease with increase in graphite content. They have also reported that dispersion of 2 wt.% graphite particles in Al-Si alloys improves the wear resistance of the base alloy and the alloy is found to maintain mild wear. However, at higher (>8 wt.%) graphite contents, the alloy is so weakened that yielding occurs and a severe rate of wear is maintained. Biswas and Pramila Bai (43) have also evaluated the dry sliding wear of cast LM13 alloy containing 2.7 and 5.7 wt.% graphite particles (size: 50-200 μm). Their results showed that dispersing graphite particle in Al-Si alloy deteriorated the wear resistance. This contradicts the results of Gibson et al.(42) for low graphite composites; however for high graphite composites the results are in agreement. Such disagreement in the results of wear behaviour of low graphite content composites is expected because of higher ductility achieved in composites produced by compocasting followed by squeeze-casting as compared to that in cast composites. For example, the percentage elongation of compocast followed by squeeze-cast Al-12%Si-4% graphite composites is reported to be 5% whereas, the elongation is below 1% for cast Al-12%Si (LM13) alloy-3% graphite particle composites. Subramanian and Kishor(44) have evaluated the effects of graphite type, modification of eutectic silicon and hot working on the wear behaviour of Al-Si alloy-graphite particle composites. Their results show that the modification of eutectic silicon in Al-Si-graphite composites structure and hot working of composites improved the wear behaviour as compared to the as-cast composites.

2.3.4.2 Lubricated Wear

Under lubricated conditions aluminium-graphite composites showed improved seizure resistance (45,46) and better bearing performance (189). Prasad and Rohatgi (190) have compiled the normalised wear rates of a variety of aluminium alloy-graphite composites (Fig.2.14). It can be seen that the normalised wear rates of aluminium alloy containing different weight percentages of graphite particles is less than unity. Pai et al.(46) have shown considerable reduction in friction coefficient at the mating interface and reduction in temperature rise in wear pins made from aluminium alloy-graphite particle composites. The temperature of some Al-Si-Ni alloy-graphite composites as a func-

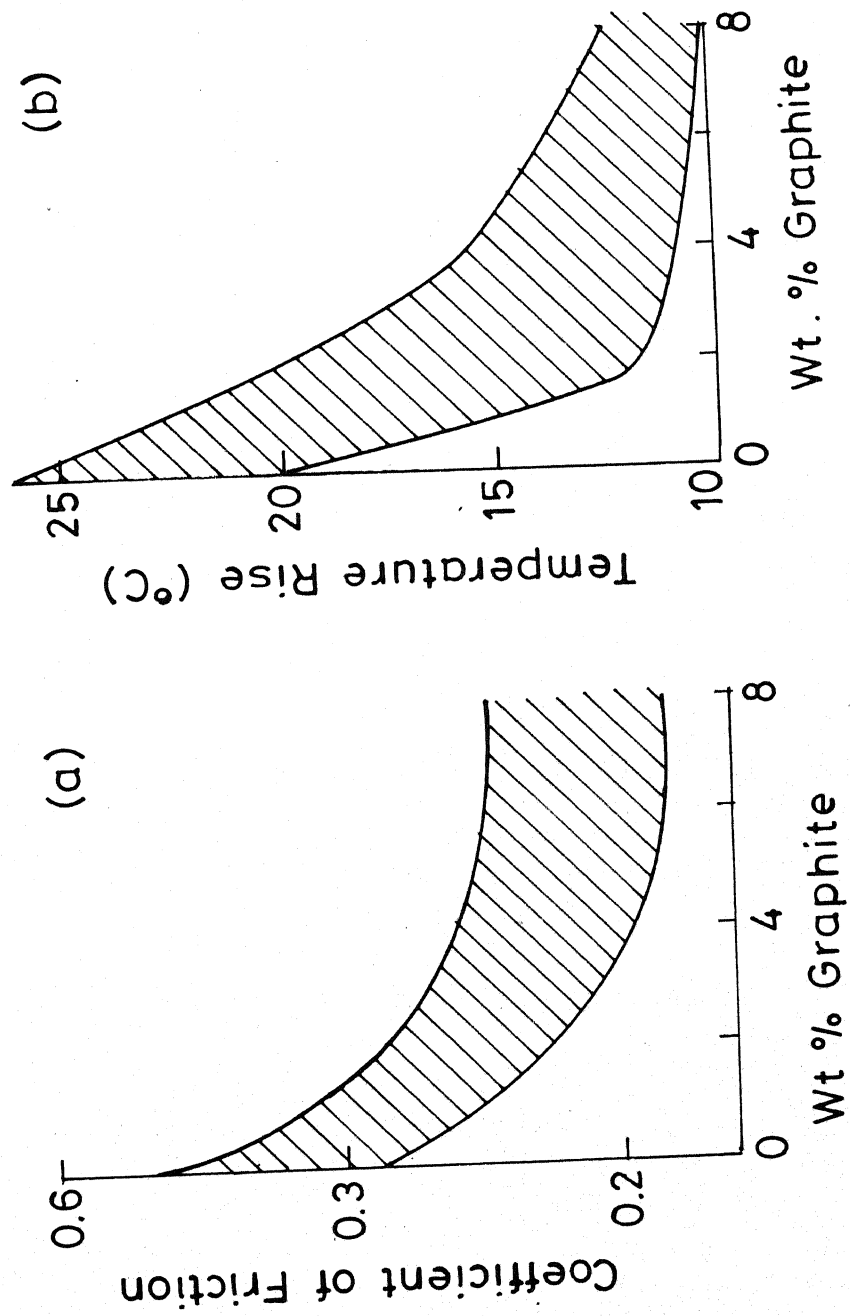


Fig. 2.13 (a) Variation in Coefficient of Friction with Graphite Addition
(b) Variation in Temperature Rise with Graphite Addition.

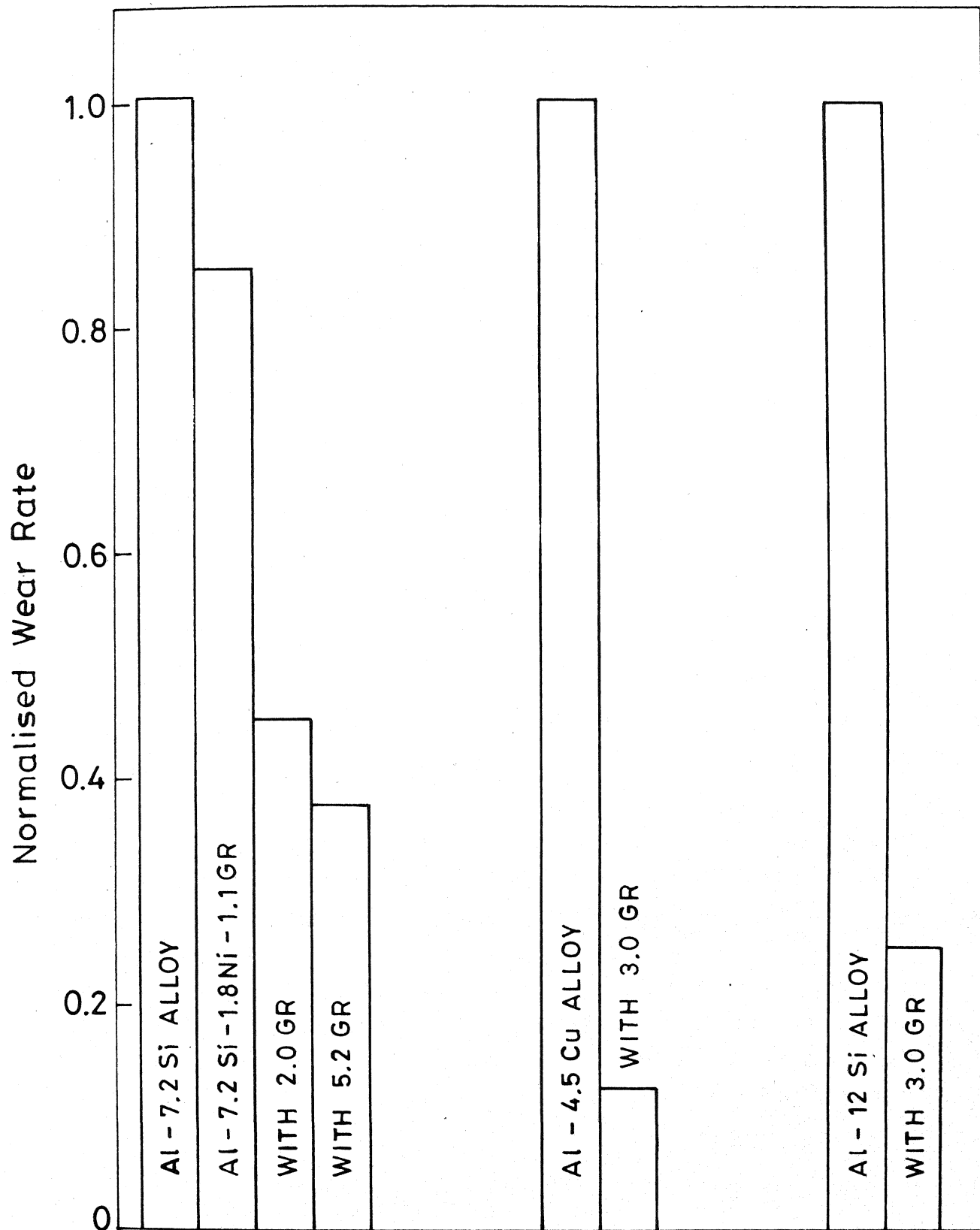


Fig. 2.14 Normalised Wear Rate

tion of time was monitored at a pressure of 0.0372 kg/mm^2 with continuous lubrication and when the supply of lubrication was discontinued after one minute of running (Fig.2.15). For alloys with 2.0 and 6.2% graphite the temperature reached a constant value after about 5 minutes. For other alloys with 0 and 1% graphite, the temperature rise was steep when lubrication was cut off. Bruni and Iguera (26) have also studied the sliding wear of hypereutectic Al-Si alloy dispersed with nickel coated graphite particles. An improvement in wear resistance of composites as compared to that of base alloy was reported.

2.3.4.3 Bearing Performance

Rohatgi and Pai (45) have used the concept of minimum bearing parameter defined as ZN/P (where, Z is the coefficient of viscosity, N is the speed and P is the bearing pressure) as a measure of the seizure resistance (i.e., resistance of a material to welding under pressure during sliding contact) of aluminium-graphite composites. During wear tests the composite specimens were subjected to progressively deteriorating lubricating conditions (i.e., lower ZN/P). Lower the value of bearing parameter before seizure, higher is seizure resistance of the material. Pai and Rohatgi (45) have reported that for Al-12 Si-5.3 Ni alloy containing various percentages of graphite particles, the minimum bearing parameter decreases with increasing graphite content upto 2.0wt.% graphite (Fig.2.16) and thereafter remains constant. In other words, 2.0wt.% graphite addition to the above alloy increases its seizure resistance enabling it to run under boundary lubrication conditions. The lowest ZN/P parameter reached by Al-12%Si based composite containing graphite of various sizes fell within a narrow band when plotted against graphite content. This relative independence of shape and size of graphite particles was attributed to the extensive deformation of graphite on the mating surfaces during wear cycle.

2.3.4.4 Subsurface Deformation

The excellent bearing properties of aluminium-graphite composites have been attributed to yielding of aluminium alloy matrix at relatively low stresses which enhances the tribo-induced deformation and fragmentation of surface and subsurface graphite particles even after a short running in period (23,189).

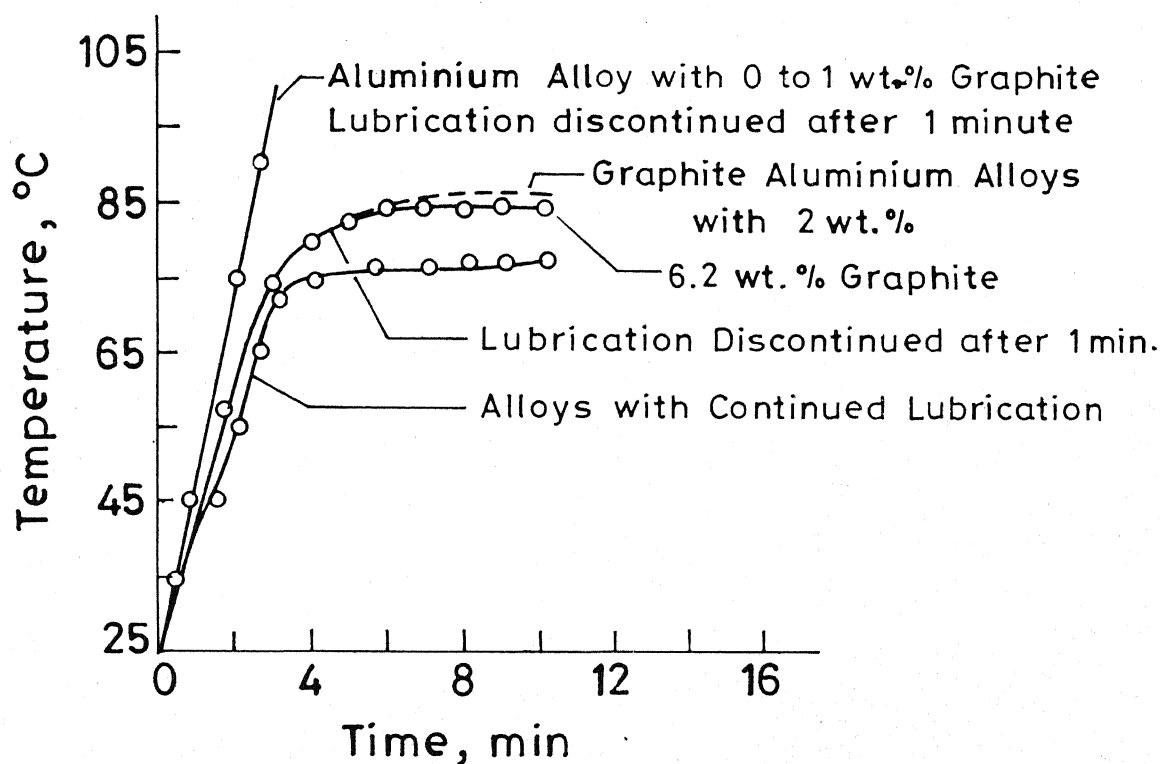


Fig. 2.15 Typical Curve of Temperature Change with Time for Alloys with Continuous Lubrication and Lubrication Discontinued After 1 min.

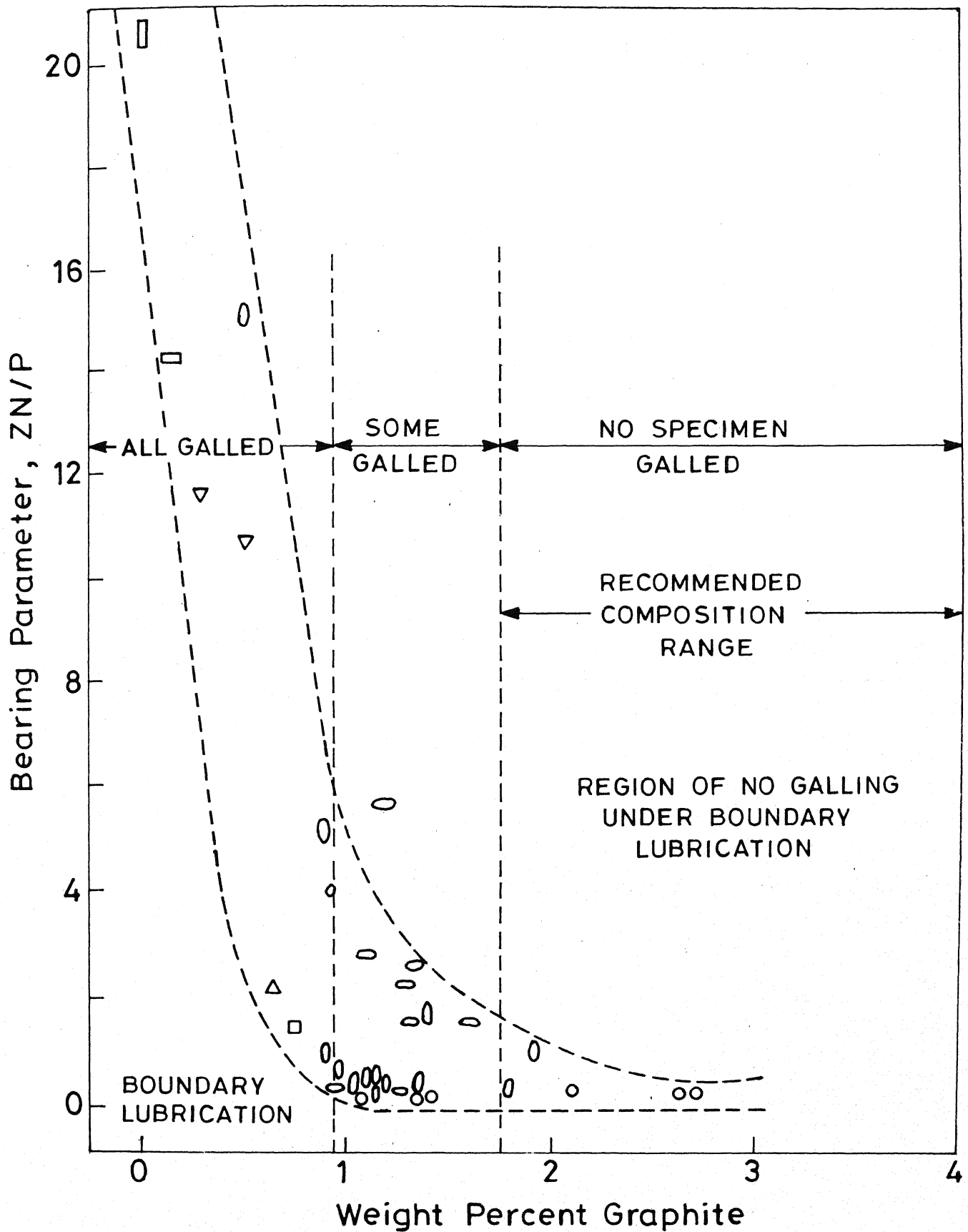


Fig. 2.16 Gallium Behaviour of Graphite Aluminium Alloys as a Function of Graphite Content (Over a Size Range 20 to 400 Microns)

This provides a continuous layer of graphite at the mating interface which prevents metal to metal contact and thereby prevents seizure.

2.3.4.5 Oil Spreadability

Krishnan et al.(191) have studied the spreadability of SAE 30 oil on the surface of LM13 alloy and LM13 alloy-graphite composites. The area of spread of liquid film on the solid surface is taken as a measure of spreadability. Their results show that the spreadability of oil on Al-12%Si (LM13) alloy increased with increasing percentages of graphite dispersion. They have also reported that the oil spreadability of composites is higher than the matrix alloy.

2.3.4.6 Component Testing

Bruni and Iguera (26) have evaluated the performance of Al-Si-graphite particle composite (SILGRAF) cylinder liners in a 125 cc two stroke engine , a 1300 cc four stroke engine and a Ferrari Formula I 3000 cc four stroke engine. Their results showed that the use of composite cylinder liners could lead to higher power out-put compared to the conventional cast iron liners. Wear rates proved to be negligible in all the cases examined and sliding surfaces showed a thin film of graphite on liners after the tests. Use of an Al-Si alloy-3% graphite piston in a diesel engine has been reported (192) to result in reduction in the specific fuel consumption, at full load compared to graphite free standard piston. Journal bearing made out of aluminium-graphite composites have been evaluated under mixed and boundary lubrication conditions and are found to be superior to leaded phosphor bronze bearing (193).

CHAPTER 3

SCOPE OF THE PRESENT WORK

It can be seen from the material presented in chapter 2 that a number of attempts have been made to synthesise aluminium alloys dispersed with soft and hard particles. The object of dispersing particles in aluminium matrices is either to make the alloy harder (hard particle composites) so as to improve resistance to abrasion or to minimize friction between the sliding surfaces (solid lubricant particle composites) by interposing layer of solid lubricant between the sliding surfaces, so that direct metal to metal contact is avoided. The present investigation is centered on the latter type of particle composites.

In the present studies, commercial LM6, LM13 and LM30 (Al-Si) alloys are used as the matrix and graphite particles are dispersed in these alloys by solidification processing techniques, which essentially consists of (i) melting of the aluminium alloy, (ii) introduction of graphite particles, (iii) creation of homogeneous dispersion and (iv) solidification of the aluminium alloy particle composite melt.

Graphite is a well known solid lubricant and during sliding action, layers of graphite are formed on the composite surfaces; these minimize friction and consequently wear of material. The solidification behaviour of aluminium alloy melt dispersed with graphite particles is very important as far as the final distribution of the particles is concerned. Graphite particles, generally, tend to float due to density differences to the top of the casting. It is therefore desirable to solidify the composite melt with a high cooling rate so that less time is available for the graphite particles to float. The compatibility between the primary crystallizing phase e.g., aluminium in hypoeutectic Al-Si alloys and graphite particle is essential for better distribution of particle. However, such compatibility does not exist between the liquid aluminium and graphite particle and it is likely that the graphite particles are pushed by the primary aluminium dendrites into the eutectic liquid which is ^{the} last phase to solidify. Therefore, it is an interesting subject to be studied the exact location of graphite particles in the composite matrix.

It is clearly established in the last chapter that subsurface deformation, crack nucleation and propagation at subsurface region are the basic mechanisms involved in the wear of material. This suggests that matrix microstructure plays an important role in controlling the wear behaviour. To make the alloy stronger and more ductile, it is proposed to alter the silicon morphology from faceted plates to more or less spheroidal. This mitigates the stress concentration effect in the matrix and minimizes the propensity for crack nucleation. To confirm the above proposition a set of experiments are formulated, where the silicon morphology is changed right from coarse plate-shaped (in die cast condition) to an intermediate state of fine microfaceted (in Na-modified) to finally fine spheroidal (in heat treated condition) and the effect of variation in silicon morphology on the wear behaviour of Al-Si alloy and composites is studied. It has also been realised that the morphology of silicon can be altered by rapid quenching from the molten state wherein the growth of silicon is nearly isotropic, primary aluminium dendrites are refined and the solid solubility limit is increased. Rapid cooling techniques normally lead to the formation of ribbons, this imposes limitations on carrying out dry sliding wear experiments with the available facilities. However, the abrasion resistance of rapidly quenched Al-Si alloys has been studied in the present investigation. The results obtained are compared with that of die cast alloy.

The literature presented in the preceding chapter indicates that aluminium alloy-graphite composite offers excellent wear resistant material in lubricated sliding wear. It has been reported that the excellent bearing properties of aluminium alloy-graphite composites are due to yielding of the aluminium alloy matrix at relatively low stresses which enhances the triboinduced deformation and fragmentation of surface and subsurface graphite particles even after a short running-in period. Oil spreadability is increased due to presence of graphite dispersion. However, results on dry sliding wear behaviour of aluminium alloy-graphite composites are conflicting; indicate improved wear resistance by the dispersed graphite particles but no indication for the formation of graphite film on the composite surface is given. Therefore, the main objective of the present work is to show the conditions for graphite film formation on the composite surface during dry sliding wear and ranking the material (the various aluminium-silicon alloys) both in dry as well as partially lubricated conditions.

CHAPTER 4

MATERIALS AND METHODS

4.1 Materials

4.1.1 Matrix Alloys

Aluminium-silicon alloys are used extensively for the production of various types of castings due to their excellent fluidity and casting characteristics. In the present studies aluminium-silicon alloys (LM6, LM13 of near eutectic and LM30, hypereutectic) are used as matrix materials. The compositions of the alloys used are shown in Table.I.1

In the molten state, the LM6 alloy has a high degree of fluidity and its low shrinkage on solidification enables castings of intricate sections. LM13 alloy responds to heat treatment and possesses low coefficient of thermal expansion and good bearing properties. It is used for elevated temperature applications e.g., piston in internal combustion engines. Hypereutectic Al-Si alloys, such as LM30, have outstanding wear resistance and low value of thermal expansion. LM30 alloys are used to produce heavy duty internal combustion engine pistons. All the above mentioned Al-Si alloys are procured from Hindustan Aluminium Company, Renukoot, U.P., India.

4.1.2 Graphite Particles

Graphite Particles are obtained from Hindustan Electro Graphites (HEG), Mandideep, Bhopal, India. The particles are sieved using standard sieving practice with an intention to get particles within the size range of 63 to 120 μm .

4.2 Melting Procedure

The aluminium-silicon alloys are melted in a A-100 graphite crucible. In each experiment the quantity of aluminium alloy taken is fixed at 10 KG. A coke fired pit furnace is used for melting the alloys; when the alloy reaches a semi-pasty stage the surface is covered with a fluxing agent, Coveral-11, marketed by M/s. Fosco Greaves, Pune. About 70 grams of

the flux are added to 10 kg. of the molten alloy. The dross is removed from the surface of the melt using a refractory coated skimmer. The dissolved gases are removed by passing dry nitrogen gas into the melt for 3 minutes. Dross is also removed by nitrogen gas bubbling, most probably by mechanical action i.e., inert gas carrying the oxides to the surfaces of the melt. After degassing, the surface is again cleaned and the temperature of the melt increased to 740°C. It is worth mentioning that during degassing, the temperature of the melt is brought down to 680°C. This takes care of minimum gas absorption during bubbling. This melting procedure is followed for all the three Al-Si(LM6, LM13 and LM30) alloys.

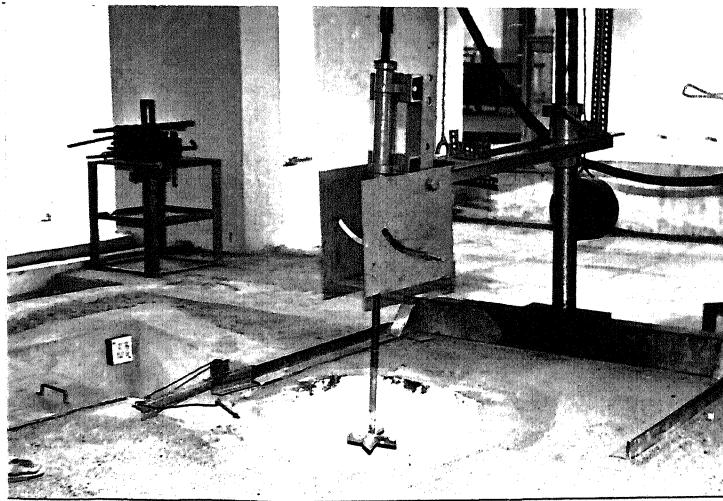
Eutectic silicon in LM6 alloy is modified by the addition of elemental sodium. About 0.02 wt.% sodium is pushed into the LM6 alloy melt with the help of a plunger to the bottom of the crucible, before pouring. It is a well known fact that sodium has a tendency to fume off at the melting temperature, so care has been taken not to hold the melt for a long time after sodium addition. In LM30 alloy, the silicon appears as large cuboids of primary silicon and plate shaped eutectic silicon. The refinement of primary silicon and modification of eutectic silicon are done by adding phosphorus and sodium respectively into the melt. Phosphorus refines the primary silicon and sodium modifies the eutectic silicon. Optimum properties are obtained by the addition of phosphorus followed by sodium addition (e.g., ^{with} in 3 minutes of the addition of the former). Before pouring, the melt temperature is again raised to 720°C and then poured in a 22mm diameter preheated (200°C) cast iron mold.

4.2.1 Composite Preparation

Al-Si-graphite particle composites are also prepared in the coke fired pit furnace. A-100 graphite crucible is used for melting 10 kg. of the Al-Si alloy, and A-6 graphite crucible is used for preheating the graphite particles. The main crucible, i.e., melting crucible is placed at the centre of the furnace and the small crucibles (A-6), used for preheating graphite particles, are placed around the main crucible. Weighted amount of graphite particles are placed in the small crucibles and covered with steel lid. The melting practice i.e., fluxing and degassing is the same as discussed

above for base alloys. It is worth mentioning that during degassing the temperature of the melt was brought down to 680°C and before addition of graphite particles the melt temperature was again increased to 700°C . It is necessary that during the melting of aluminium alloys, the graphite particles should reach a temperature of around 900°C . It is noted that this temperature was attained just after half an hour. To ensure this, A-6 crucible containing graphite particles are placed just below the top level of the melting crucible and covered with coke. The graphite powder is now and then agitated with the help of a small spoon to achieve uniform heating and to remove the volatile matter. A steel stirrer, coated with ceramic, is used to produce vortex in the aluminium melt. The stirrer is fixed with a flexible pipe and rotated with the help of a 3-phase motor. The stirrer is placed into the crucible, containing the melt, to a distance equal to the radius of the stirrer from the bottom of the crucible. The stirrer is located centrally and kept vertical. The speed of the stirrer is maintained around 550 rpm. Fig.4.1a shows the stirrer assembly used in the present investigation to prepare the composite material. When the vortex is being formed, the graphite particles is added on the periphery of the vortex, with the help of a spoon. The graphite particles are drawn into the melt by the churning action of the stirrer. The uniform pattern of churning is disturbed by the use of a baffle lowered into the melt along the side of the crucible. The baffle produces great amount of turbulence in the flow pattern of the melt and induces better mixing of graphite particles in the aluminium alloy melt. After complete addition of graphite particle, the speed of the stirrer is brought down to 400 rpm and the stirring continued for 3 minutes. The stirrer is then withdrawn from the melt; the bath is again degassed for 4 minutes with dry nitrogen gas. Then the composite melt is ready for casting. A graphite coated spoon is used to take out the composite melt for pouring into the cast iron mold. Care is taken to mix the melt with the help of spoon before pouring to ensure uniform dispersion of graphite particles in the Al-Si alloy melt.

Modification of eutectic silicon in LM6 alloy containingⁿ graphite particles and refinement and modification of primary and eutectic silicon respectively in LM30-graphite particle composites are done. The initial experiments to modify the eutectic silicon, in LM6 alloy-graphite particle composites failed, as the graphite particles are dispersed first and sodium is added after that, with a view to minimize the fuming of sodium. However, when sodium



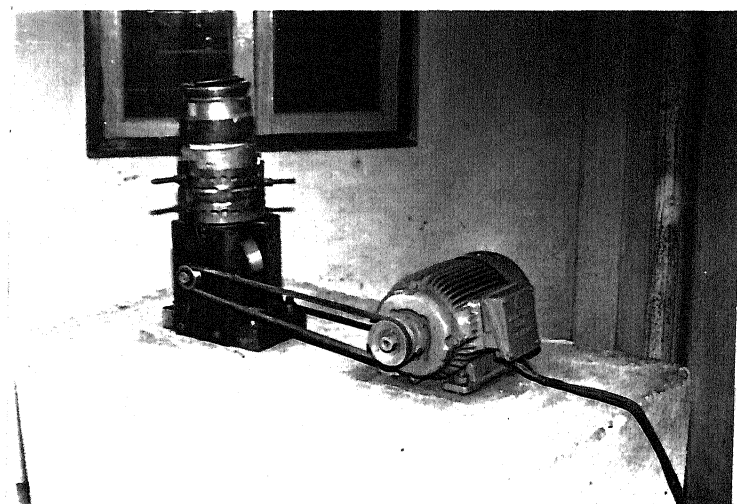
is added before dispersing graphite particles, the sequence is found to be effective. To optimize the effective refinement and modification of primary and eutectic silicon respectively in LM30 alloy-graphite composites, five sets of experiments are conducted with various combinations of sodium, phosphorus and graphite additions. In the first heat about 10 Kg. of LM30 alloy is melted in a graphite crucible using a coke-fired pit furnace. After degassing with dry nitrogen, the melt is cast in a 22 mm diameter molds. The second heat involved addition of 0.028 wt.% phosphorus to the Al-Si (LM30) alloy melt, after it is degassed with dry nitrogen gas. In the third heat, the melt is degassed and 0.028 wt.% phosphorus and after a lapse of 5 minutes 0.288 wt.% sodium are added. In the fourth set of heat, phosphorus and sodium are added in the same sequence as described in the third set and after this, melt is stirred to create a vortex and 3 wt.% graphite particles are dispersed in the melt. In the final set of experiment, 0.028 wt.% phosphorus is added after the melt is degassed. The melt is then stirred to create vortex and 3 wt.% graphite particles are dispersed in the melt. Just prior to the casting, 0.028 wt.% sodium is added. In all cases the melt is cast in 22 mm cast iron finger molds. Table IV.1 shows the heat numbers and the sequence of adding phosphorus, sodium and graphite particle in Al-Si (LM30) alloy melt.

4.2.2 Production of Rapidly Solidified Ribbons

Al-Si alloys and Al-Si-graphite particle composites are rapidly solidified using single roll melt spinning unit, Fig.4.1b. The unit consists of a copper wheel, 150 mm diameter and 38 mm wide, mounted on a shaft. The shaft is attached to a 3-phase motor and the wheel is rotated at a speed of 3000 rpm. The whole assembly is mounted on a rigid base. A graphite crucible (size: A-5) with a hole of 1.5 mm diameter is placed at a height of 6 mm above the wheel surface. The aluminium alloy as well as aluminium alloy-graphite composites are melted in coke fired pit furnace, as described in the preceeding sections, and poured in a A-5 crucible followed by pressurising the melt with argon gas in order to effect smooth flow of the melt through the hole. As the molten metal falls on the rotating substrate a solid boundary layer forms adjacent to the chill substrate; this propagates into the melt puddle to form the ribbon. The momentum transport helps to drag out the melt puddle resulting in the formation of ribbons. The ribbon is collected in a ribbon collection chute.

Table IV.1 : Heat Number and Sequence of addition of
Phosphorus, Sodium and Graphite

Heat No.	Alloy/Composites
1	LM30
2	LM30-Phosphorus
3	LM30-Phosphorus-Sodium
4	LM30-Phosphorus-Sodium-Graphite
5	LM30-Phosphorus-Graphite-Sodium



It is worth mentioning at this point that in the case of aluminium-silicon-graphite particle composites, the temperature of the melt before pouring into the A-5 graphite crucible is 760°C and the hole at the bottom is 2 mm. These changes are made to take care of the increase in viscosity of Al-Si alloy due to dispersion of graphite particles. Initial efforts showed that the composite melt choked the passage in the A-5 graphite crucible when a hole of 1.5 mm diameter is used. The increase in pouring temperature (760°C) and diameter of the hole (2mm) in the A-5 graphite crucible, takes care of the increase in viscosity of the Al-Si melt due to the presence of graphite particles.

4.2.3 Heat Treatment

Aluminium-silicon LM6 and LM13 alloys and composites are heat treated in a tube furnace. Samples are solution treated at 520°C for 8 hours, quenched in warm water at 60°C , and aged at 180°C for 6 hours. The LM30 alloy and composites are solution treated at 495°C for 9 hours, quenched in warm water at 60°C and aged at 175°C for 8 hours.

4.3 Methods

4.3.1 Particle Size Analysis

Particle size distribution of graphite is determined using MICRON PHOTOSIZER model SKO 2000, Japan. The graphite powder is dispersed in ethylene glycol using ultrasonic disperser. The instrument works on the principle of stoke's law of sedimentation and photo extinction. The results are expressed in terms of accumulated wt.% distribution curve and % frequency of particle size histogram.

4.3.2 Optical Microscopy

For optical microscopic observation the samples are polished mechanically using standard metallographic procedure, etched with Keller's reagent and observed in a Leitz optical microscope. Rapidly solidified ribbons are cold mounted and then prepared for microscopic examination.

4.3.3 Scanning Electron Microscopy

Samples are prepared, as described above for optical microscopy, and observed in a JEOL 35 CF scanning electron microscope, interfaced with wavelength dispersive X-ray spectrometer (WDXS). In order to observe the silicon morphology, the samples are etched deeply and coated with a thin layer of gold using a sputtered unit (model: JEOL JFC-1100). Worn out surfaces of wear samples are also observed in SEM. The debris particles are spread on a double sided adhesive tape and coated with gold and studied in the scanning electron microscope. Graphite particles in Al-Si matrix and in the worn surfaces are studied with the WDXS using STE as the analysing crystal.

4.3.4 X-ray Diffraction

X-ray diffraction studies of the samples are carried out using philips automated powder diffractometer employing Cu-K α radiation at 20°C. The debris particles are spread on a double sided adhesive tape and x-ray diffractogram obtained; from the 2θ values of the peaks, the interplanar spacings are calculated. The values of the latter are used for identifying the phases.

4.3.5 Tensile Testing

The tensile strength of aluminium-silicon (LM6, LM13 and LM30) alloys and aluminium-silicon-graphite particle composites in as-cast, refined and modified and heat treated conditions is measured using Instron machine (model: 1185). For tensile testing 50 mm gauge length and 10 mm diameter specimens are used, and the test are carried out at a cross head speed of 2 mm/min.

4.3.6 Hardness

The hardness of aluminium-silicon alloys and aluminium-silicon-graphite particle composites is measured using hardness testing machine (model: HMO 2450). Brinell hardness number (BHN) of the specimens is obtained using a 2.5 mm diameter hardened steel ball indenter. A load of 31.25 Kg is applied for 10 seconds.

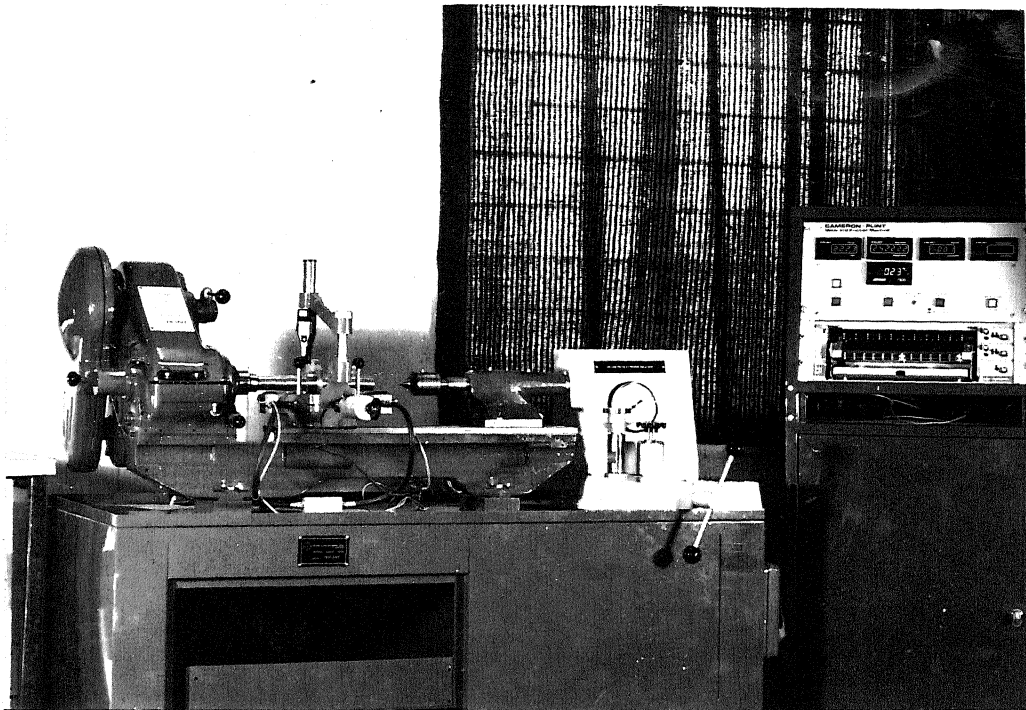
4.4 Sliding Wear

4.4.1 Dry Sliding Wear

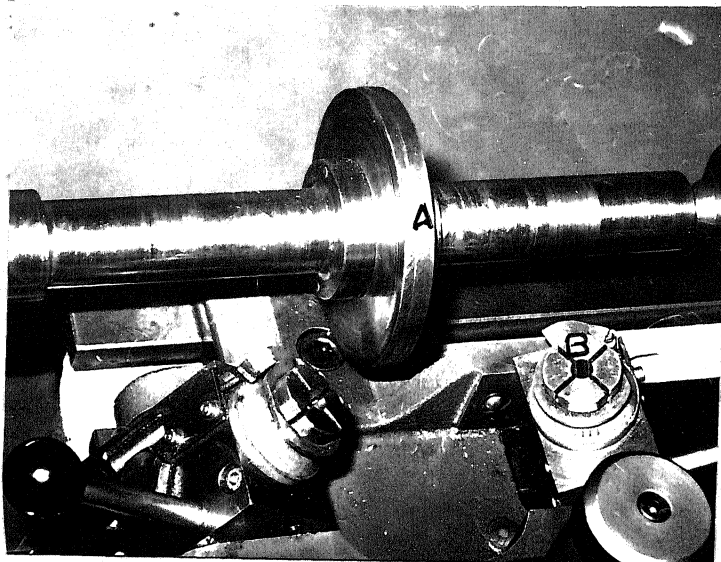
Sliding wear tests are carried out using a Cameron-Plint pin-on-disc machine (model: TE 0.97). Fig.4.2 shows a photograph of pin-on-disc machine. The machine essentially consists of a disc mounted on a mandrel with two pins pressed into contact with the opposite surfaces of the disc by means of hydraulic cylinders. However, in the present investigation only one pin is used. Fig.4.2a shows the pin-on-disc apparatus and a magnified view of the disc (A) and sample holder (B) is seen in Fig.4.2b and the actual position of the pin and disc during testing is shown schematically in Fig.4.2c. The disc is allowed to rotate with the help of a 750 watt 3 phase motor, having 14 speeds ranging from 25 to 2150 rpm. The pins which are held against the rotating disc are of 8 mm diameter and 53 mm long, are located vertically below the axis of the disc at a distance of 40 mm. The pressure on the samples is applied by means of a precision dead weight pressure tester, operated manually by hydraulic system with a plunger loaded with dead weight. Pressures upto (15 MPa) can be applied on the sample. The machine is attached with a control cabinet, indicating rpm, cumulative number of revolutions, temperature of the pin and friction force. In the present experiments, the samples to be tested are taken in the form of a pin and are allowed to slide against a heat treated steel (EN25) disc. For dry sliding wear test the disc is rotated at a constant speed of 640 rpm. Wear track diameter of 80 mm is employed. This corresponds to a sliding speed of 2.68 m/sec. The rise in temperature during the test is monitored with the help of a chromel-alumel thermocouple, which is inserted into the hole in the sample made at a distance of 1.5 mm away from the sliding surface. The wear rate is computed from weight loss measurements taken in intervals of 500 m of sliding distance. Before and after each test, samples were cleaned in methanol using an ultrasonic bath and weight is taken using a Metler H 51 AR balance, with an accuracy of 0.01 mg.

4.4.2 Partially Lubricated Sliding Wear

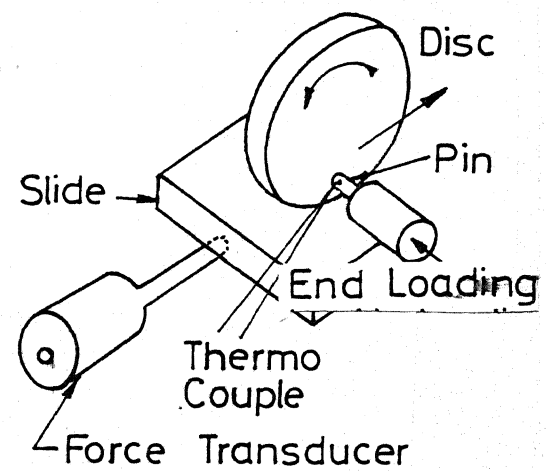
Partially lubricated wear tests are performed using a modified test procedure. In this series of experiment the heat treated, EN25 steel disc is



(a)



(b)



(c)

Fig. 4.2 (a) Pin-on-Disc Wear Test Apparatus,
 (b) Magnified view of the Disc (A) and Sample Holder (B)
 (c) Actual Position of Pin and Disc Assembly During Wear Testing.

dipped in SAE30 lubricating oil. The excess oil is flushed off from the disc by rotating it for 5 sec. before the test. The procedure adopted for evaluating the pressure (P) velocity (V) limits is given below.

All the partially lubricated sliding wear tests are carried out upto a sliding distance of 2500 m. Speed of disc rotation is fixed at 330 rpm (corresponding to a sliding velocity of 1.38 m/sec. A load of 1.0 MPa is applied on the specimen. The test is run for 2500 m. If the sample did not seize at this load, the disc is removed, cleaned, reimmersed in SAE 30 oil, excess oil flushed off as described above and the applied pressure is increased in steps of 0.5 MPa. When the applied load exceeds a certain critical value, specimen is found to seize before it could reach a distance of 2500 m. The load at which it seized is taken as the limit of the pressure at this speed. The procedure is repeated at three other speeds viz. 640 rpm (2.68 m/sec.), 800 rpm (3.35 m/sec.) and 1100 rpm (4.61 m/sec.). The temperature of the test pieces is also monitored using chromel-alumel thermocouple.

4.4.3 Subsurface Studies

The sample from which subsurface study is to be made, is placed in a mold. The cold mounting material is filled upto a certain height so that the sliding surface remained well below the top surface of the cold mount. After proper setting of the cold mount material, the wear pin is sectioned centrally in the longitudinal direction along the length of the wear pin. The sectioned surface is polished mechanically using standard metallographic procedure, etched with Keller's reagent and observed in the scanning electron microscope.

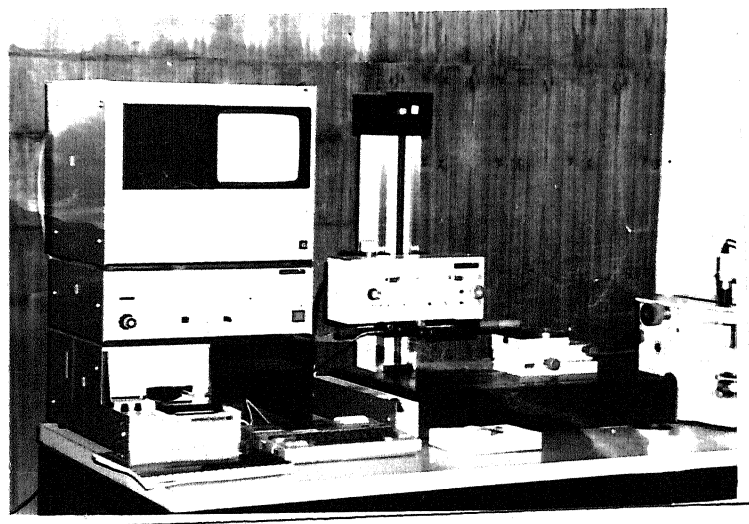
4.4.4 Abrasion Test

Abrasive wear test is performed using a Suga abrasion tester, model NUS-I, in this apparatus strips of $\text{SiC}(\beta)$ abrasive paper are fixed to the circumference of a 50 mm diameter wheel using double sided adhesive tape. The sample is held against the rotating abrasive wheel and the load is applied by a cantilever mechanism. During the test, the samples are moved horizontally back and forth and the motion of the wheel and specimen

is synchronised such that only fresh areas of the abrasive paper came into contact with the specimen. The distance covered in one full reciprocating cycle, i.e., twice the distance between two extreme positions of the specimen is 66 mm. Specimens of rapidly solidified aluminium-silicon (LM13) alloy are prepared, for the abrasion test, by glueing the strips (dimension: 40 mm long and 12 mm wide) to 4 mm thickness rectangular plate substrate. Specimens of the die cast alloy of dimensions $40 \times 60 \times 4 \text{ mm}^3$ are also subjected to the abrasion test. After a desired number of cycles (400), the samples are removed, the surfaces cleaned in methanol using an ultrasonic bath and the wear rates are computed from weight loss measurements.

4.4.5 Surface Roughness Measurement

The roughness value of the steel disc is measured using a stylus instrument model 'Talysurf 6' of Taylor-Hobson (Fig.4.3). The instrument essentially consists of a sharp pointed stylus which rests lightly on the surface and traverses slowly across it. The up and down movement of the stylus along a suitable datum can be magnified. Rotary attachment of the unit in R/ISO mode with 0.08 mm cut off length is used for roughness measurement. The roughness parameter is designated as R_a , which is a arithmetic mean of the departure of the roughness profile from the mean line. The roughness parameter of the disc is measured before commencement of each test and it is fixed at 0.03 μm .



CHAPTER 5

RESULTS

5.1 Introduction

Results on the characterisation of graphite particles as well as LM6, LM13 and LM30 (Al-Si) alloys and composites in die cast and rapidly solidified conditions are presented in the first few sections of this chapter. Graphite particles are characterised using X-ray diffraction, scanning electron microscopy and particle size analysis. The size range of the graphite particles, which are dispersed in aluminium alloys for the preparation of composites, are evaluated using, micron photosizer, particle size analyzer. Morphological studies on graphite particles are carried out by scanning electron microscopy. Wavelength dispersive X-ray microanalysis is used for elemental analysis. The results of the microstructural observations of Al-Si alloys and composites are shown in section 5.3.1, 5.3.2 and 5.3.3. Remaining sections of this chapter deal with the results of friction and wear behaviour of Al-Si alloys and composites.

5.2 Characterisation of Graphite Particles

5.2.1 X-ray Diffraction

The as-received and heat treated graphite particles are studied using a Philips 1710 automated X-ray diffractometer. Table V.1 shows the experimental parameters used in these studies. Typical X-ray diffractograms of graphite particles in as-received and heat treated conditions are shown in Fig.5.1. Peaks corresponding to (0002), $(10\bar{1}0)$, $10\bar{1}1$, (0004) and $(10\bar{1}3)$ planes of graphite are clearly seen in both the as-received and heat treated conditions. The diffraction angle (2θ), interplanar spacing (d) and relative intensities are also shown in Table V.1 alongwith the standard interplanar spacing obtained from JCPDS (Joint Committee of Powder Diffraction Standard) files.

Table V.1 : X-Ray Diffraction Results of Graphite Particle

PARAMETERS									
Voltage 40 KV Current 20 mA Scanning speed 0.02 °2θ/Sec Target Material Copper Wavelength of 1.5418 (Å) X-radiation(Cu-Kα) Recorder Full Scale 50,000 Recorder speed 1 cm/°2θ									
As-received Graphite					Heat treated Graphite				
From Standard data card (JCPDS file)									
Diffraction Angle(2θ) (degree)	Interplanar Spacing(d) (Å)	Intensity	Diffraction Angle(2θ) (degree)	Interplanar spacing(d) (Å)	Intensity	Interplanar spacing(d) (Å)	Planes (hkl)	Interplanar spacing(d) (Å)	Planes (hkl)
26.46	3.368	Very strong	26.45	3.369	Very strong	3.36	(0002)	3.36	(0002)
42.44	2.129	Very Weak	42.45	2.129	Very Weak	2.13	(1010)	2.13	(1010)
44.40	2.040	Very Weak	44.33	2.043	Very Weak	2.03	(1011)	2.03	(1011)
54.51	1.683	Weak	54.51	1.683	Weak	1.67	(0004)	1.67	(0004)
59.78	1.540	Very Weak	59.72	1.548	Very weak	1.54	(1013)	1.54	(1013)

From Standard data card (JCPDS file)

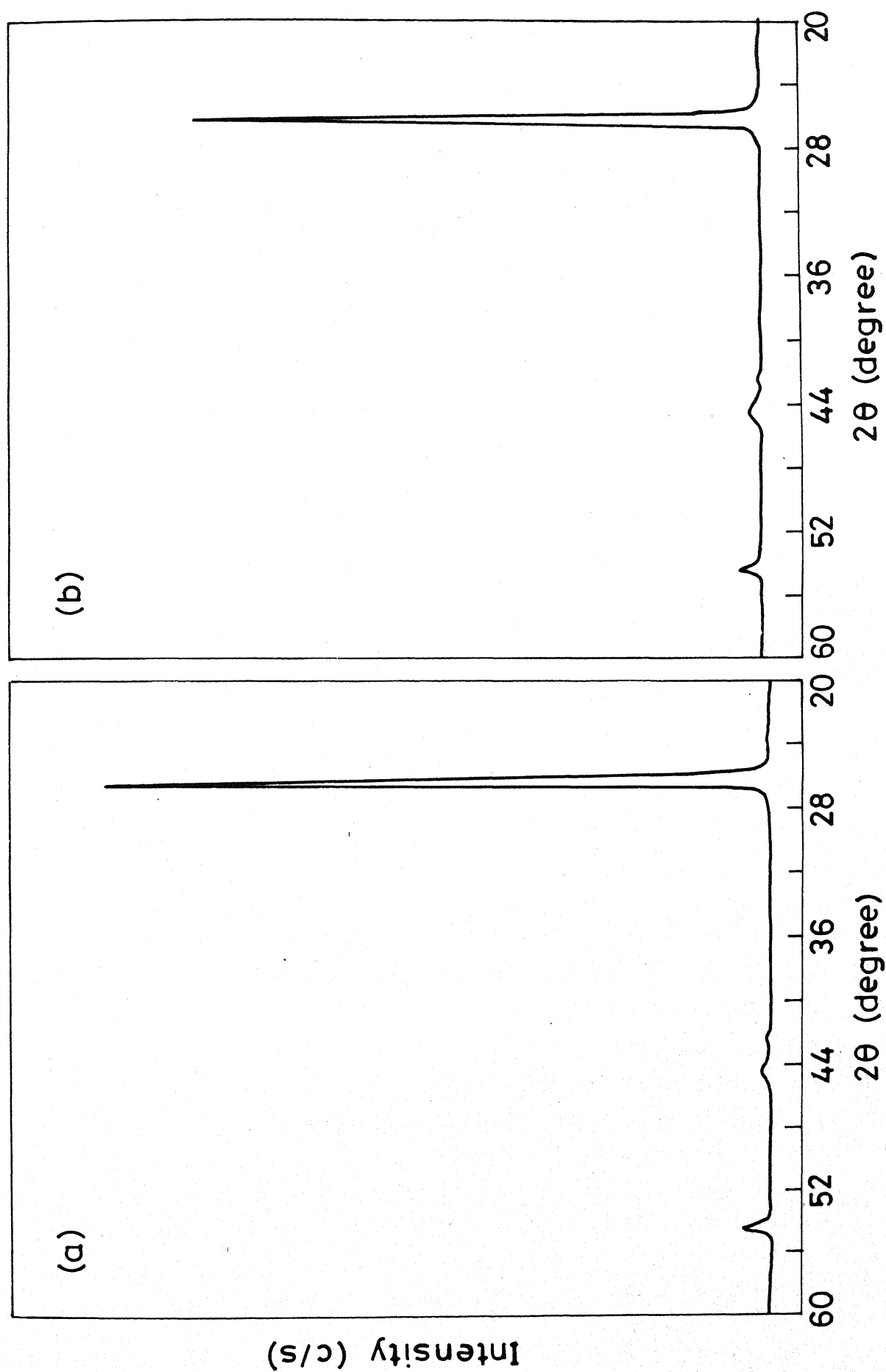


Fig. 5.1 X-Ray Diffraction Trace of Graphite Particles (a) As-received and (b) Heat Treated.

5.2.2 Particle Size Analysis

The size distribution of graphite particles is analysed using particle size analyser. Particle size distribution is expressed in terms of accumulated wt.% distribution and percentage frequency of particle size. The parameters used to ascertain the particle size distribution are shown in Table V.2. Size ranges corresponding to percentage of the total number of particles are also brought out in Table V.2. The percentage frequency of particle size distribution is shown in Fig.5.2. The results depict that 13% of particles are found to have size below 10 μm , around 8% of particles are in the size range of 10-50 μm ; 50% of the particles lie in the size range of 50-100 μm . Another 13% of particles lie in the size range of 100-130 μm and 16% of particle between 130-150 μm .

5.2.3 Scanning Electron Microscopic Studies

The morphology of graphite particles is studied by scanning electron microscopy. Typical micrographs of the graphite particles, used in the present investigation, are seen in Fig.5.3.a. It can be seen clearly in the magnified scanning electron micrograph, Fig.5.3.b, that the graphite particles are flaky in nature.

5.3 Microstructure

5.3.1 LM6 Alloy and Composites

The microstructures of Al-Si (LM6) alloy and composites are studied by optical and scanning electron microscopy. Fig.5.4 shows typical scanning electron micrographs of die cast LM6 alloy in unmodified (Figs.5.4 a & b) and sodium modified (Figs.5.4 c & d) conditions respectively. The microstructure of unmodified LM6 alloy (Fig.5.4.a) consists of primary aluminium with an average dendrite arm spacing (i.e., centre to centre distance between two neighbouring dendrites) of 22 μm . The eutectic silicon is observed in the interdendritic region and around the dendrites. The plate-shaped eutectic silicon can be seen clearly in Fig.5.4.b, which is a magnified micrograph of the portion marked 'A' in Fig.5.4.a. Plate-shaped eutectic silicon with sharp edges acts as stress riser in aluminium matrix and largely hampers the mechanical strength and fracture behaviour of the alloy. The undesirable

Table V.2 : Graphite Particle Size Distribution

<u>PARAMETERS</u>	
Sample	Graphite Particle
Sample Density	2.25 gm/cc
Dispersion Medium	Ethylene glycol
Medium Density	1.1132
Medium Viscosity	18.50
Room Temperature	23°C
Medium Temperature	23°C

Size Range	% of the total number of particles	Average Particle Size (μm)
up to 10 μm	13	
10-50 μm	8	
50-60 μm	12	
60-80 μm	25	
80-100 μm	13	76.40
100-130 μm	13	
130-140 μm	6	
140-150 μm	10	

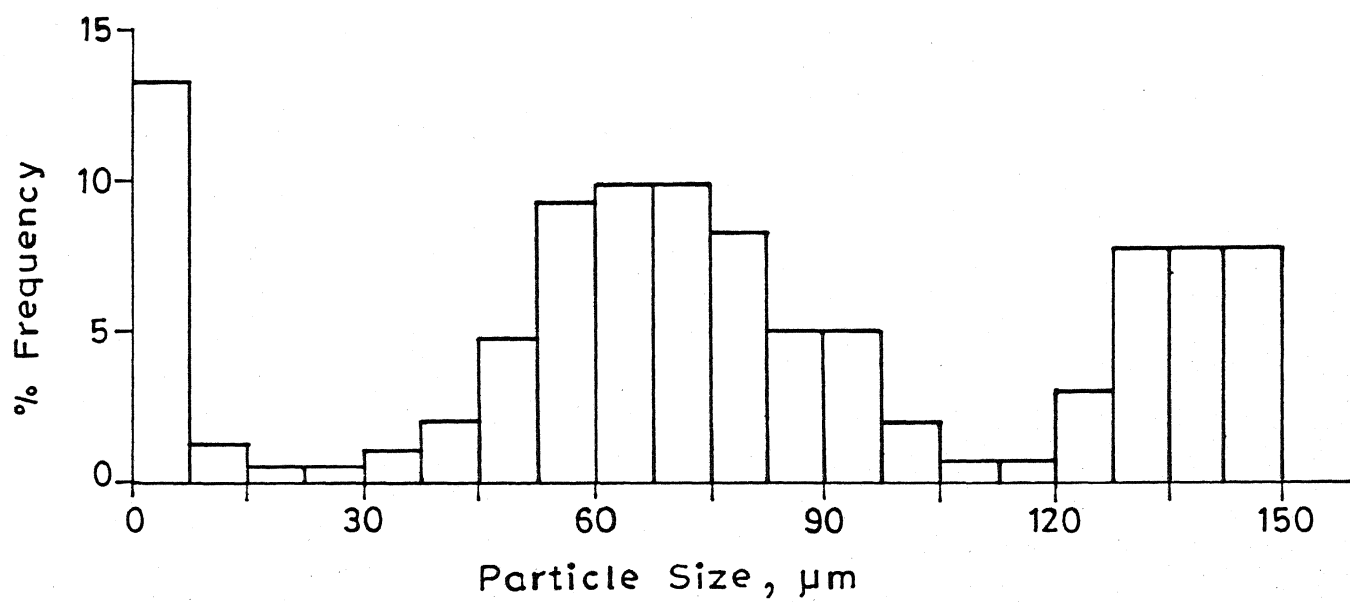
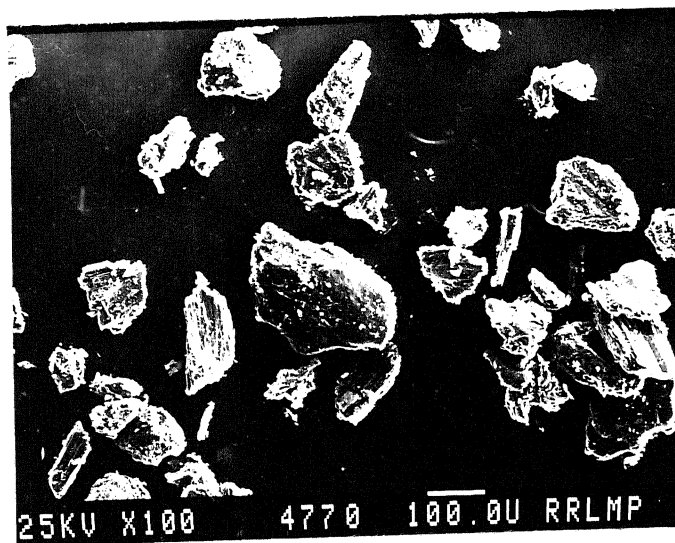
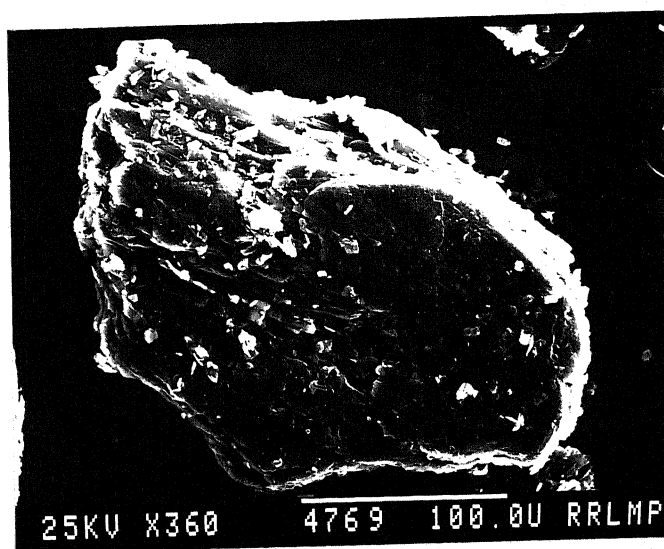


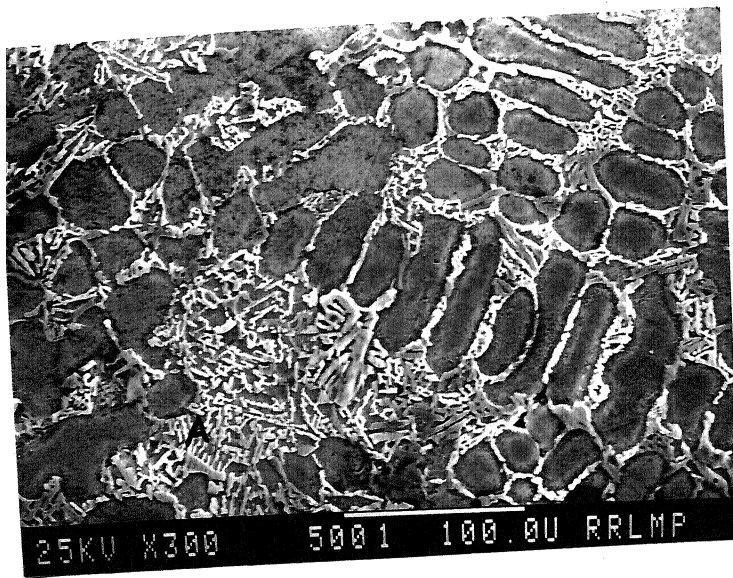
Fig. 5.2 Size Distribution of Graphite Particles.



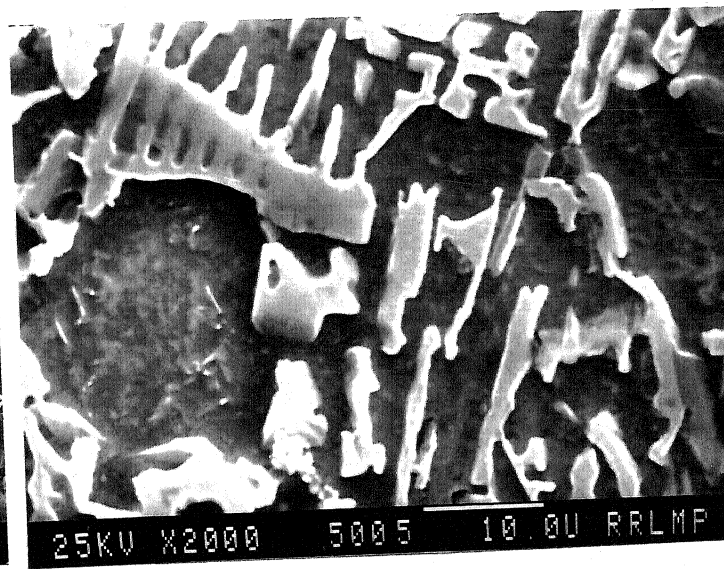
(a)



(b)



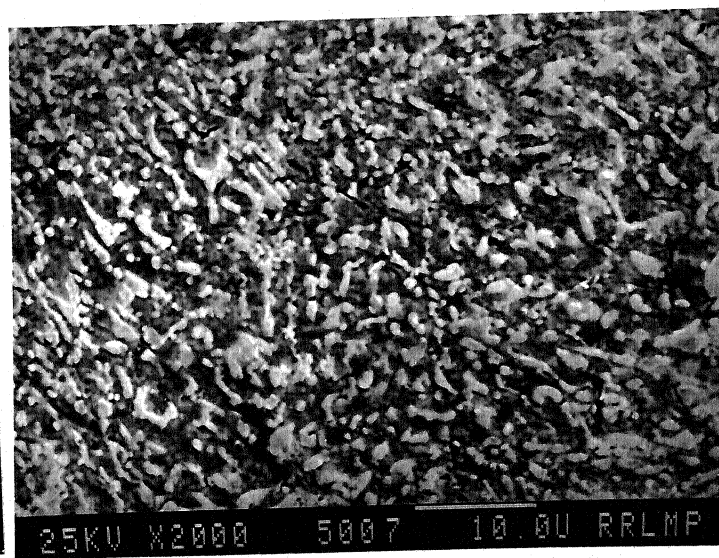
(a)



(b)



(c)

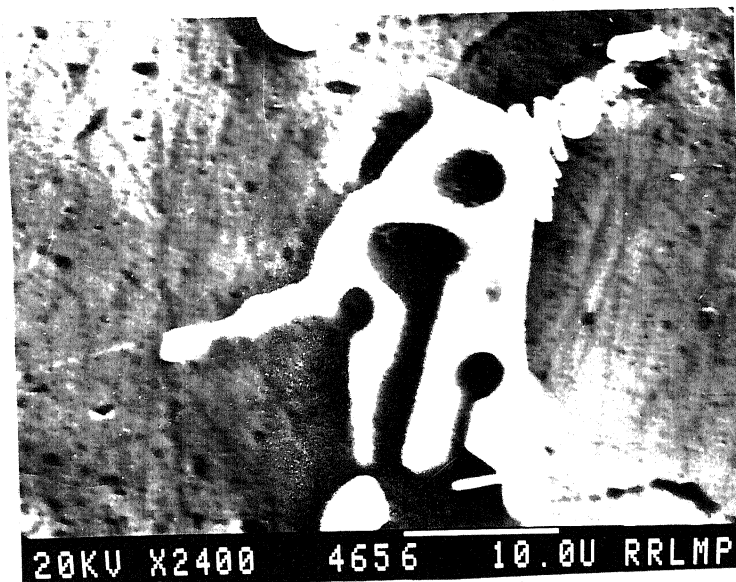


(d)

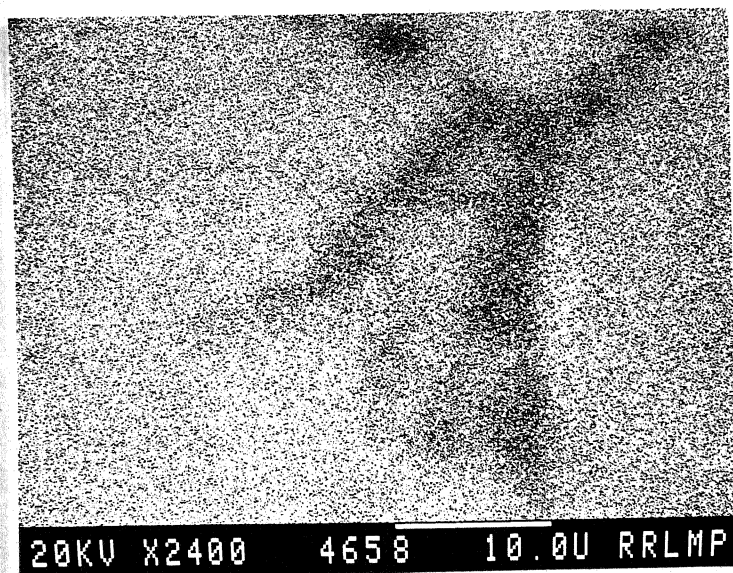
growth of eutectic silicon can be restricted to a large extent by adding minute quantities of elemental sodium. Fig.5.4.c shows a representative microstructure of sodium modified LM6 alloy. It consists of primary aluminium and modified eutectic silicon. The modified eutectic silicon is clearly seen in a magnified micrograph (Fig.5.4.d). Although the anisotropic growth of eutectic silicon is largely restricted in the modified alloy, the faceted nature of eutectic silicon is still preserved. Intermetallic phases with different etching behaviour (black needles) are clearly seen in Fig.5.4.c. Fig.5.5.a shows an intermetallic phase in the LM6 alloy. X-ray mapping of aluminium and iron corresponding to intermetallic phase (seen in Fig.5.5.a) are shown in Fig.5.4.b and c respectively. It is clear that this particle contains a significant amount of iron.

A remarkable change in the morphology of eutectic silicon is observed after heat treatment (Fig.5.6.a); the coarse plate-shaped eutectic silicon is fragmented into smaller nearly spherical particles of average size of $\sim 6 \mu\text{m}$. The faceted nature of eutectic silicon characteristic of the die cast alloy is not seen in the heat treated alloy. However, in some places coarse irregular particles with smooth surfaces (marked S) are observed (Fig.5.6.b). Coarse intermetallic phases are also observed in heat treated Al-Si, LM6 alloy (marked A) Fig.5.6.b and c), X-ray mapping shows the presence of aluminium and iron in these particles.

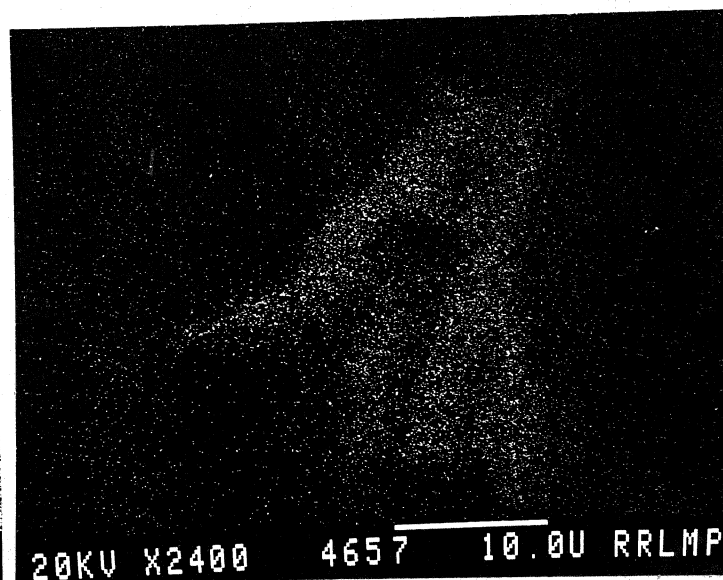
A typical optical micrograph of LM6-3% graphite particle composite is shown in Fig.5.7.a. The distribution of graphite particles is clearly seen in Fig.5.7.a. The solidification behaviour of Al-Si alloy melt in the presence of graphite particles will be discussed in the sections to follow. Fig.5.7.b shows graphite particles in heat treated LM6 alloy matrix. It clearly delineates α -aluminium dendrites and nearly spherical eutectic silicon. The graphite particles are seen to be located in the last freezing eutectic liquid. A magnified micrograph, Fig.5.7.c, reveals a graphite particle and spherical eutectic silicon around it. A number of silicon plates with smoothened edges are also seen.



(a)



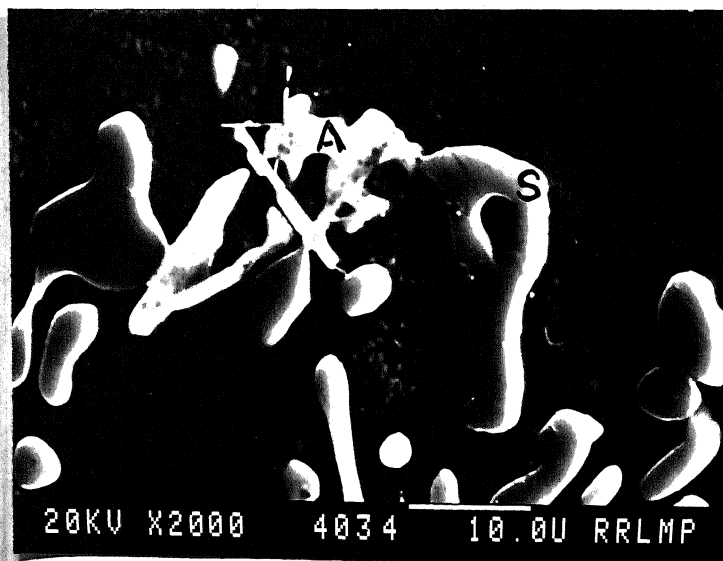
(b)



(c)



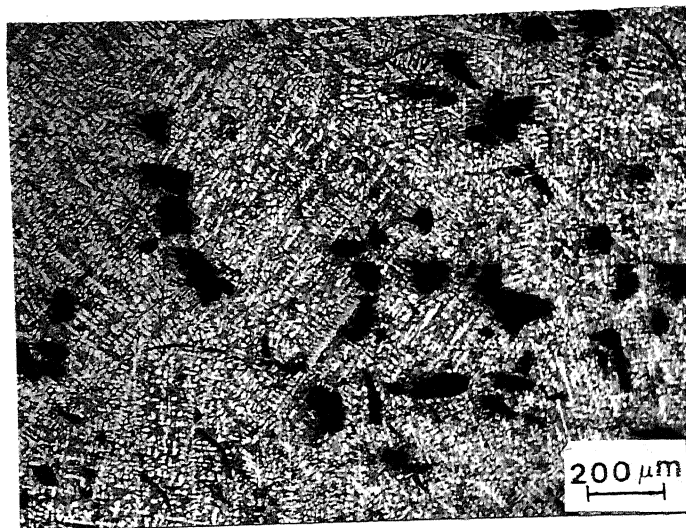
(a)



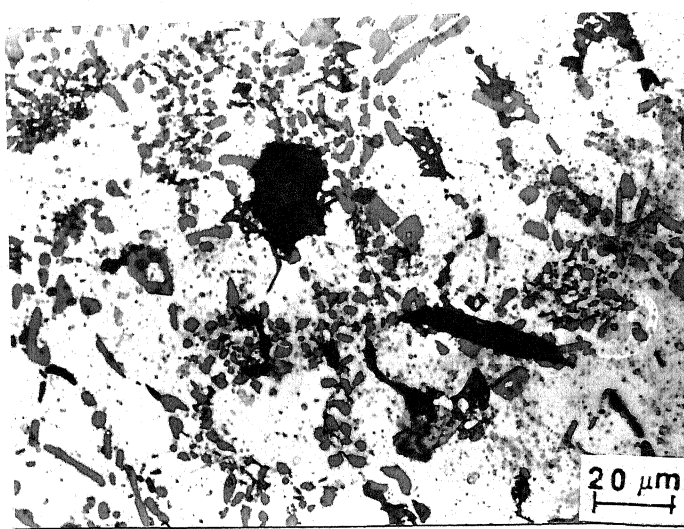
(b)



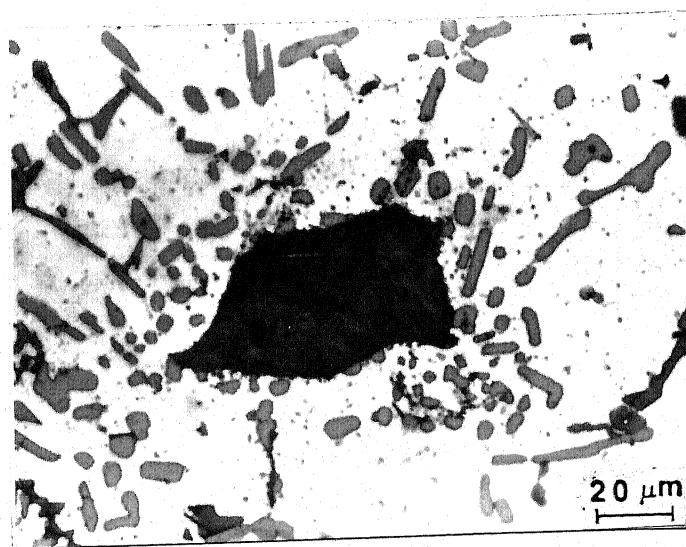
(c)



(a)



(b)



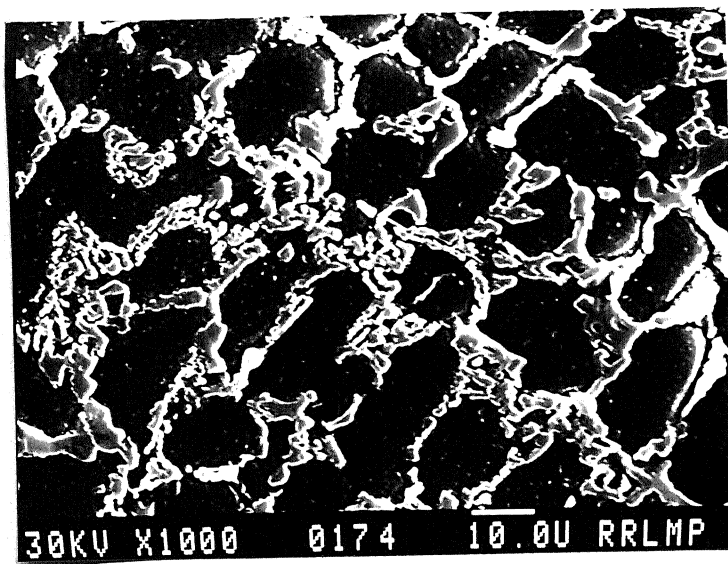
(c)

5.3.2 LM13 Alloy and Composites

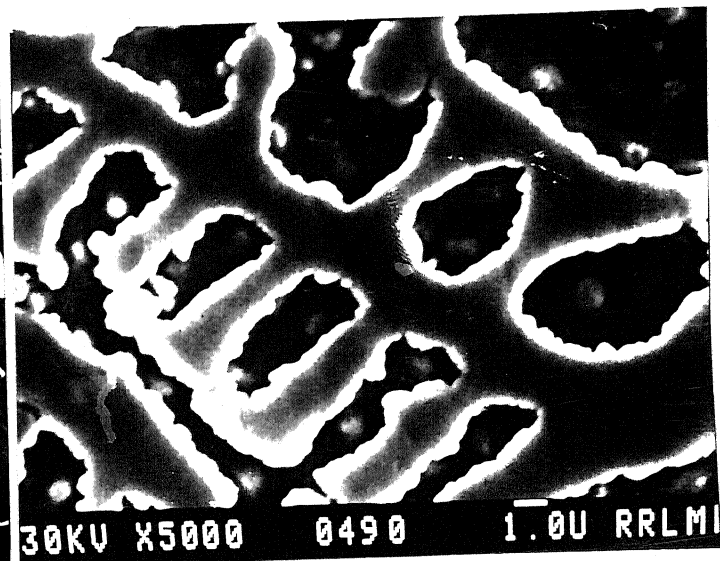
The microstructure of Al-Si, LM13 alloy is found to be very similar to that of LM6 alloy. In LM13 alloy, 1% Cu, 1% Mg and 1.5% Ni are added intentionally to make the alloy amenable to heat treatment. Fig.5.8.a shows a scanning electron micrograph of die cast LM13 alloy. It clearly shows primary aluminium dendrites; the average secondary dendrite arm spacing is of the order of 20 μm and eutectic silicon is seen in the interdendritic region and around the dendrites. Eutectic silicon has sharp edged plate-shaped morphology, similar to the microstructure observed in LM6 alloy. A typical scanning electron micrograph representing branching of eutectic silicon is shown in Fig.5.8.b. Heat treatment of LM13 alloy is also found to alter the morphology of eutectic silicon from plate-shaped to nearly spherical, Fig.5.8.c. A magnified micrograph, Fig.5.8.d, clearly reveals the morphology of eutectic silicon after heat treatment. The intermetallic phases observed in the heat treated LM13 alloy are clearly seen in Fig.5.8.e with a different etching behaviour (dark black particles, arrow marked).

A typical optical micrograph of the LM13-3% graphite particle composite is shown in Fig.5.9. The distribution of graphite particles is clearly seen in Fig.5.9. The distribution of interparticle spacing and particle size of graphite particles in a die cast LM13-3% graphite composites is characterised by using quantitative metallography. The distribution of graphite particles, across three different sections along the ingot length-top, middle and bottom is studied. Further, the measurements are made for three successive pouring-initial, intermediate and final. Both interparticle spacings, and particle size data are collected and plotted as frequency histograms in Figs.5.10 (a) and (b) respectively. The distribution of graphite particles in LM13-3% graphite composites along the casting length (a) top, (b) middle and (c) bottom portion of a casting chosen from the intermediate pouring is shown in Figs.5.11.a,b and c respectively. The percentage of the total number of particles in a specified interparticle spacing and particle size range of the composite castings are shown in Tables V.3 and V.4 respectively for initial, intermediate and last pouring of a processing schedule. The results indicated that around 56,58 and 62% of the total number of particles are

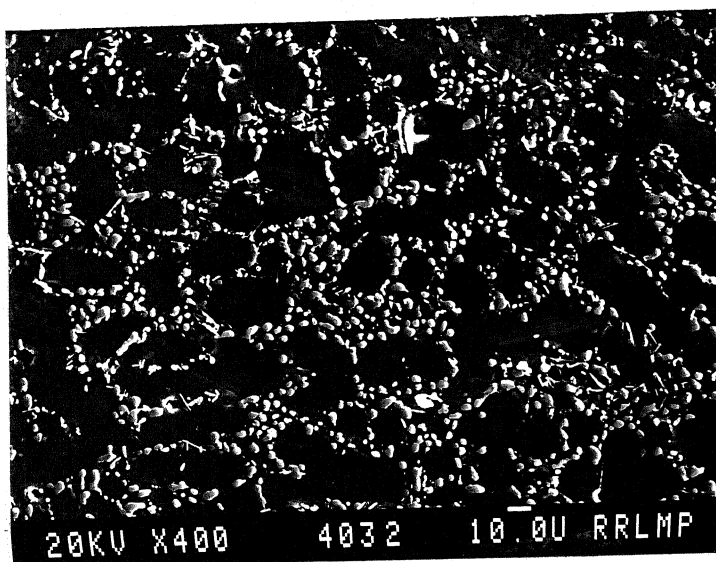
Fig.5.8 Micrographs of LM13 alloy: (a) die cast condition (b) interconnected eutectic silicon (c) heat treated condition (d) magnified view of (c) and (e) optical micrograph of heat treated sample showing inter-metallic compound with different etching behaviour



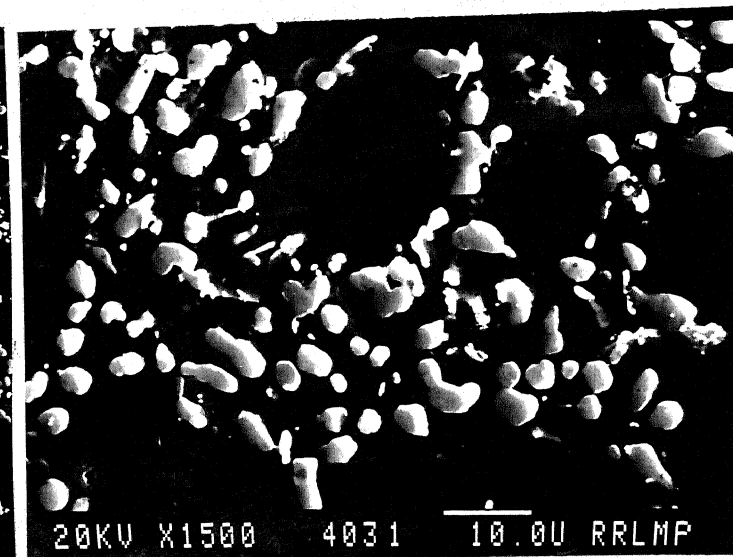
(a)



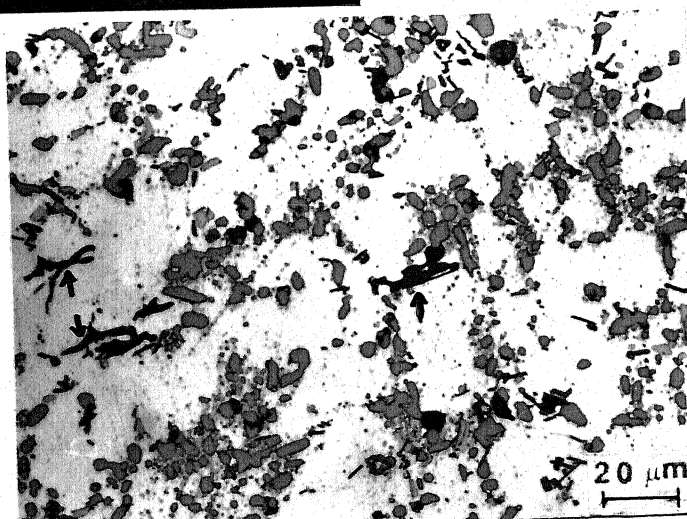
(b)

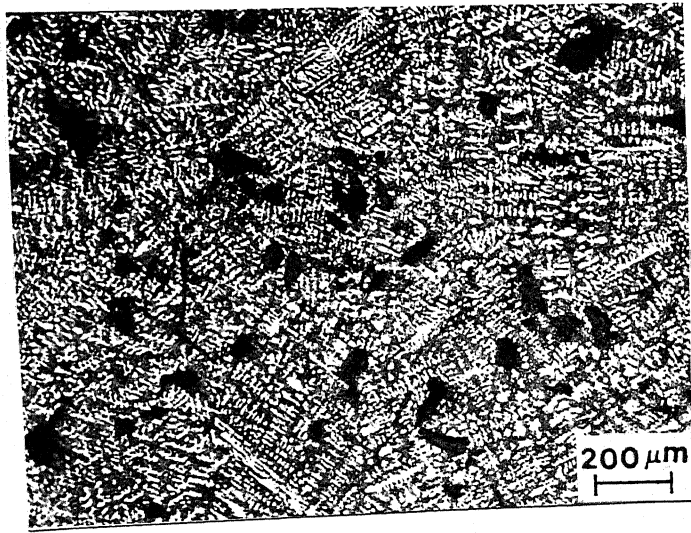


(c)



(d)





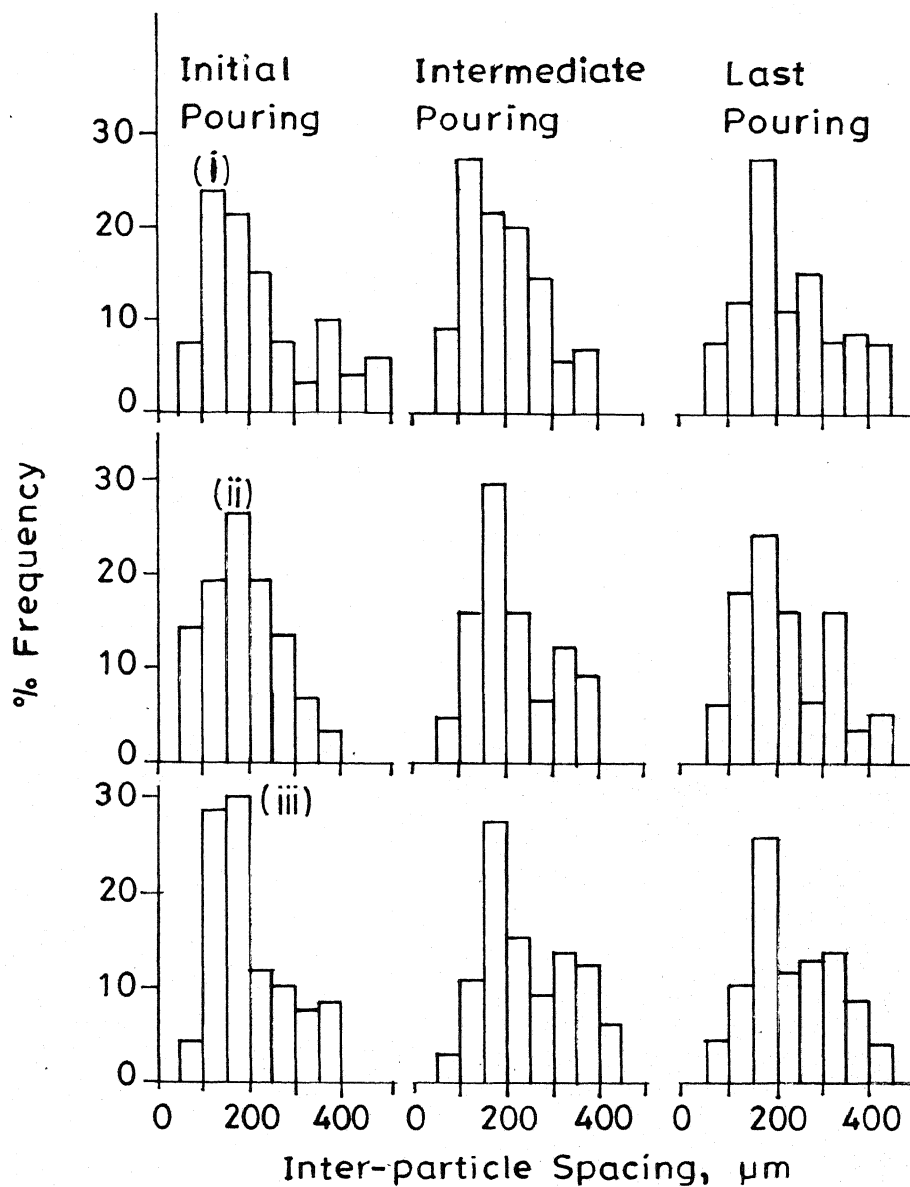


Fig. 5.10 (a) Distribution of Interparticle Spacing in Die Cast LM13 - 3 wt. % Graphite Composites Across Three Different Sections Along the Ingot Length (i) Top (ii) Middle (iii) Bottom for Three Successive Pouring - Initial, Intermediate and Final.

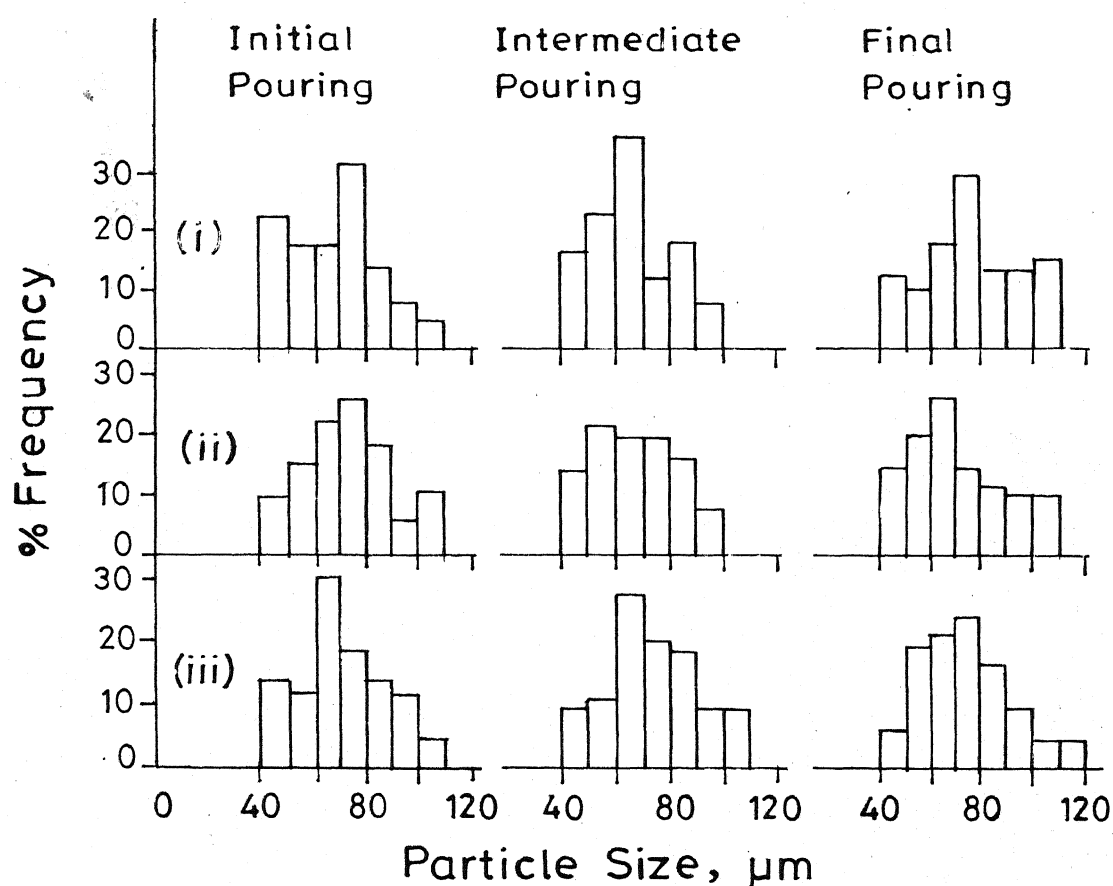
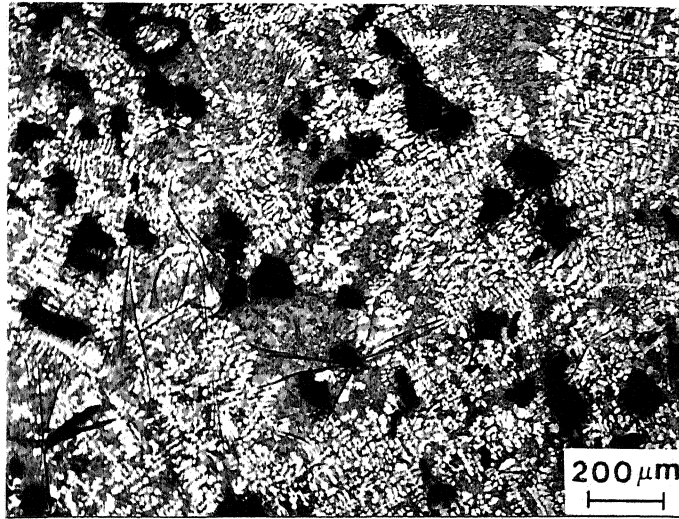
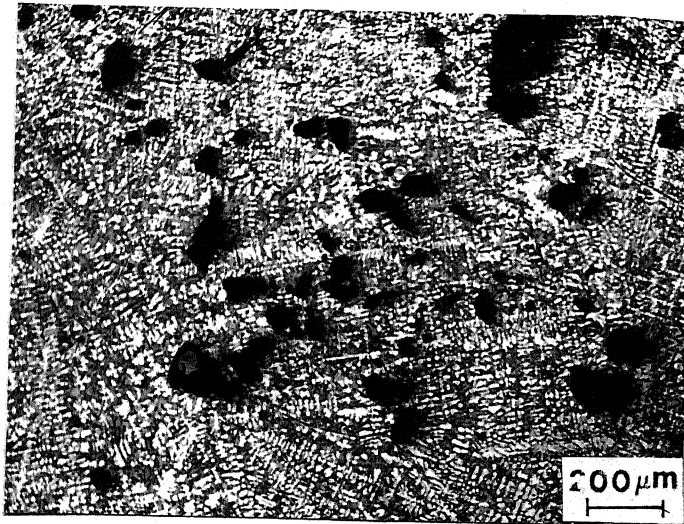


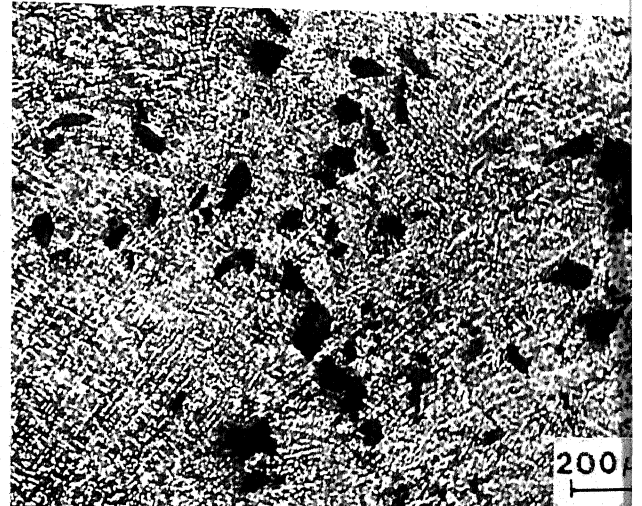
Fig.5.10 (b) Distribution of Particle Size in Die Cast LM13 - 3 wt.% Graphite Composite Across Three Different Sections Along the Ingot Length (i) Top (ii) Middle (iii) Bottom for Three Successive Pouring - Initial, Intermediate and Final.



(a)



(b)



(c)

Table V.3 : Distribution of Interparticle Spacing

(a) Initial Pouring

Top			Middle			Bottom		
Spacing range (μm)	% of the total no.of particles	Spacing Range (μm)	% of the total no.of particles	Spacing range (μm)	% of the total no.of particles	Spacing range (μm)	% of the total no.of particles	
50-100	7	50-100	14	50-100	5			
100-150	25	100-150	18	100-150	27			
150-200	24	150-200	26	150-200	30			
200-250	15	200-250	18	200-250	12			
250-300	7	250-300	13	250-300	10			
300-350	3	300-350	7	300-35	8			
350-400	10	350-400	4	350-400	8			
400-450	3							
450-500	6							

(b) Intermediate Pouring

Top Middle Bottom

50-100	8	50-100	2	50-100	5
100-150	26	100-150	12	100-150	17
150-200	22	150-200	26	150-200	30
200-250	20	200-250	15	200-250	16
250-300	14	250-300	10	250-300	8
300-350	4	300-350	15	300-350	14
350-400	6	350-400	14	350-400	10
		400-450	6		

(c) Last Pouring

50-100	6	50-100	6	50-100	4
100-150	12	100-150	20	100-150	10
150-200	23	150-200	24	150-200	27
200-250	12	200-250	16	200-250	14
250-300	16	250-300	6	250-300	15
300-350	10	300-350	16	300-350	15
350-400	11	350-400	5	350-400	10
400-450	10	400-450	7	400-450	5

Table V.4 : Graphite Particle Size Distribution

(a) Initial Pouring

Top		Middle		Bottom	
Size range (μm)	% of the total no. of particles	Size range (μm)	% of the total no. of particles	Size range (μm)	% of the total no. of particles
40-50	20	40-50	5	40-50	12
50-60	15	50-60	15	50-60	10
60-70	15	60-70	20	60-70	30
70-80	30	70-80	25	70-80	20
80-90	10	80-90	20	80-90	12
90-100	5	90-100	5	90-100	10
100-110	5	100-110	10	100-110	6

(b) Intermediate Pouring

Top	Middle	Bottom
40-50	15 40-50	8 40-50
50-60	20 50-60	12 50-60
60-70	30 60-70	26 60-70
70-80	10 70-80	20 70-80
80-90	15 80-90	14 80-90
90-100	10 90-100	10 90-100
		10 100-110

(c) Last Pouring

Top	Middle	Bottom
40-50	12 40-50	4 40-50
50-60	10 50-60	16 50-60
60-70	14 60-70	20 60-70
70-80	26 70-80	22 70-80
80-90	12 80-90	18 80-90
90-100	12 90-100	10 90-100
100-110	14 100-110	5 100-110
		5 110-120

found to be in the spacing range of 50-200 μm corresponding to the top, middle and bottom of the initial poured casting along the length, respectively. Similarly in the intermediate pouring around 56,40 and 52% of the particles are found to have spacing in the range from 50-200 μm . In last pouring around 41,50 and 41% of the particles are found to be in the spacing range from 50-200 μm . The mean interparticle spacing and size, \bar{x} , and the standard mean deviation σ were calculated and are shown in Tables V.5 and V.6 respectively. The results indicate that the mean particle size is found to be very close to the size for maximum frequency, indicating absence of particle clustering. The interparticle spacing increases from the initial to last pouring, possibly due to the flotation of particles during the intervals between pourings. In general, the graphite particles tend to float to the top of the casting due to density differences (density of graphite = 2.3 gm/cc and density of LM13 alloy = 2.7 gm/cc); however, in the present investigation it is inferred from microstructural investigations that the solidification of composite melt in 22 mm diameter cast iron mold ended up with reasonably uniform distribution of graphite particles in Al-Si alloy matrices.

5.3.3 LM30 Alloy and Composites

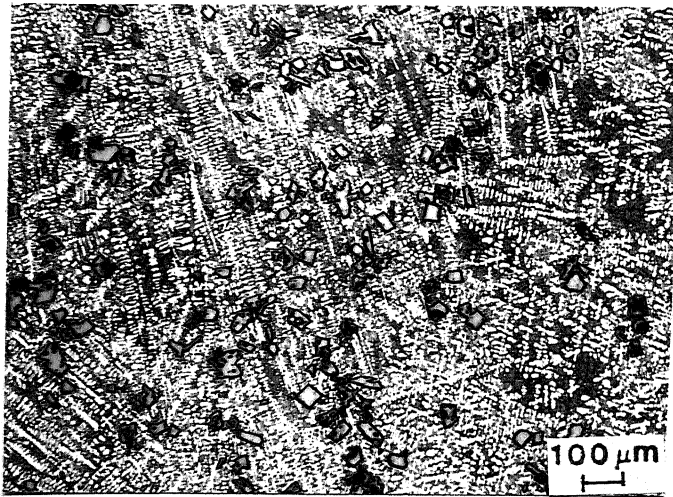
The microstructure of Al-Si, LM30, alloy from heat no.1 is shown in Fig.5.12.a. The microstructure clearly delineates cuboids of primary silicon (average size around 100 μm), dendrites of aluminium (the secondary arm spacing is measured to be 20 μm) and plate-shaped eutectic silicon. The plate-shaped eutectic silicon can be seen in the interdendritic region, Fig.5.12.b. It is noted that primary silicon crystal grows in different shapes e.g., plate-like as seen in Fig.5.12.a or combination of plates originating from a central nucleation sites as shown in Fig.5.12.c. Aluminium halo is also observed around the primary (marked A) and eutectic silicon (marked B), Fig.5.12.c. Phosphorus in elemental form was added to the hypereutectic Al-Si alloy in order to refine the primary silicon crystals. Typical microstructures of unrefined (heat no.1) and refined (heat no.2) silicon are shown in Fig.5.13 (a) and (b) respectively. It is noted from the figures that the average size of the primary silicon is reduced from 100 μm to about 50 μm due to phosphorus addition. However, the eutectic silicon appears to be

Table V.5 : Interparticle Spacing

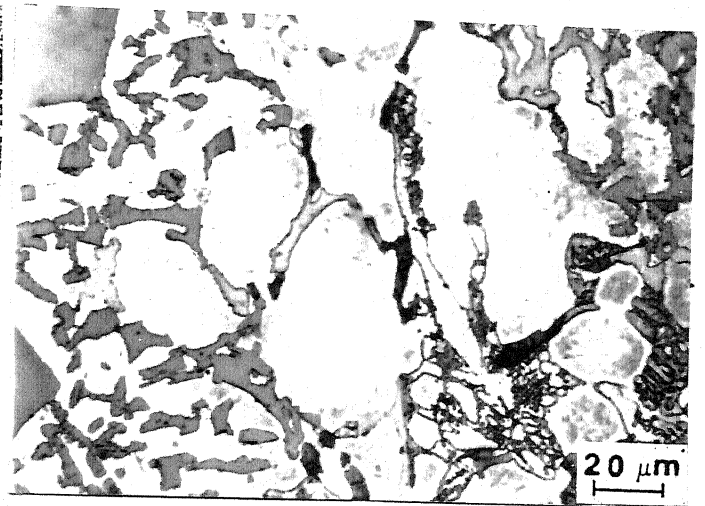
	Initial pouring		Intermediate pouring		Last pouring	
	\bar{x} (μm)	σ (μm)	\bar{x} (μm)	σ (μm)	\bar{x} (μm)	σ (μm)
Top	220.0	111.0	196.0	78.7	245.7	102.2
Middle	192.5	80.0	250.0	94.7	224.5	98.1
Bottom	200.5	82.6	218.5	85.9	243.0	91.5

Table V.6 : Particle Size

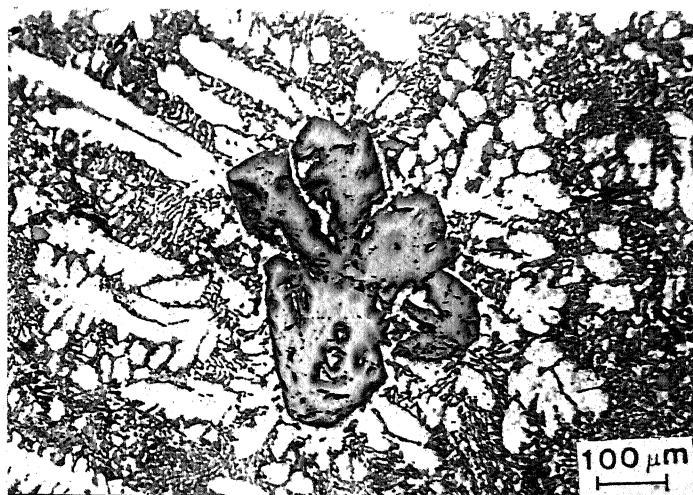
	Initial pouring		Intermediate pouring		Last pouring	
	\bar{x} (μm)	σ (μm)	\bar{x} (μm)	σ (μm)	\bar{x} (μm)	σ (μm)
Top	65.0	16.1	67.0	15.3	75.8	18.6
Middle	74.5	15.9	67.2	15.1	71.4	18.4
Bottom	70.5	16.1	74.0	17.0	75.9	17.3



(a)

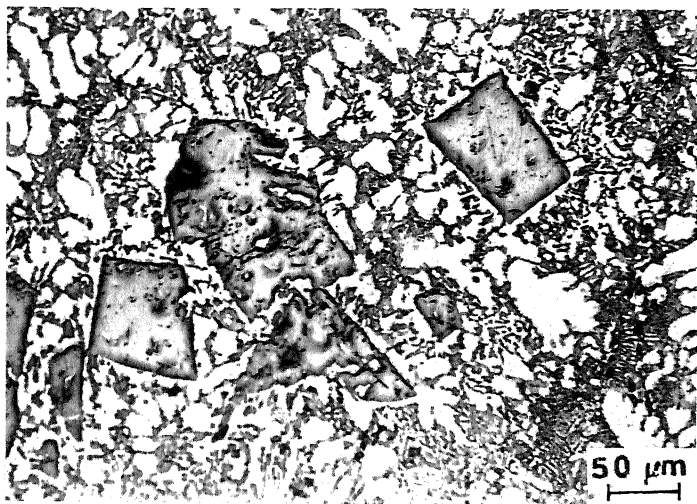


(b)

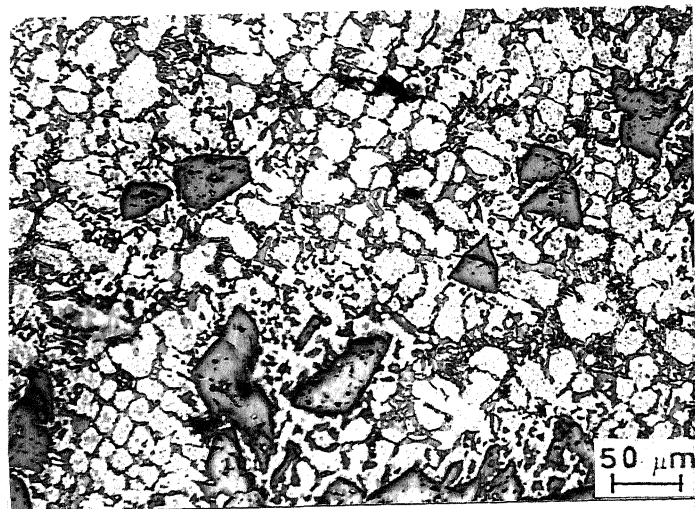


(c)

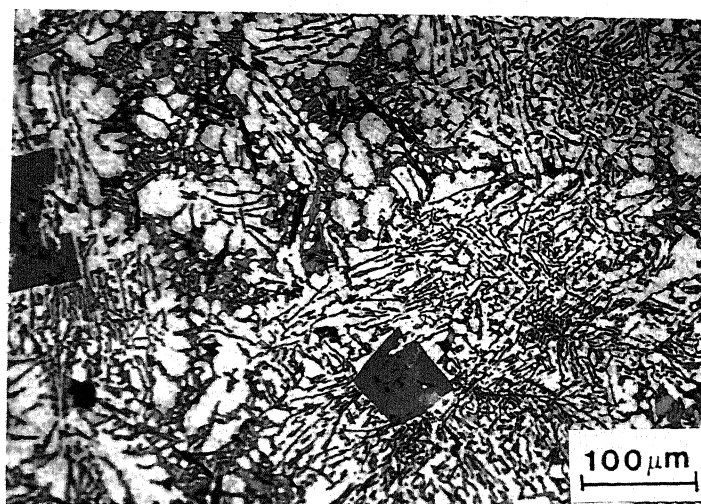
Fig.5.13 Optical micrographs of LM30 alloy: (a) unrefined condition, (b) refined primary silicon with phosphorus (c) showing unmodified eutectic silicon in refined alloy and (d) refined and modified primary and eutectic silicon respectively



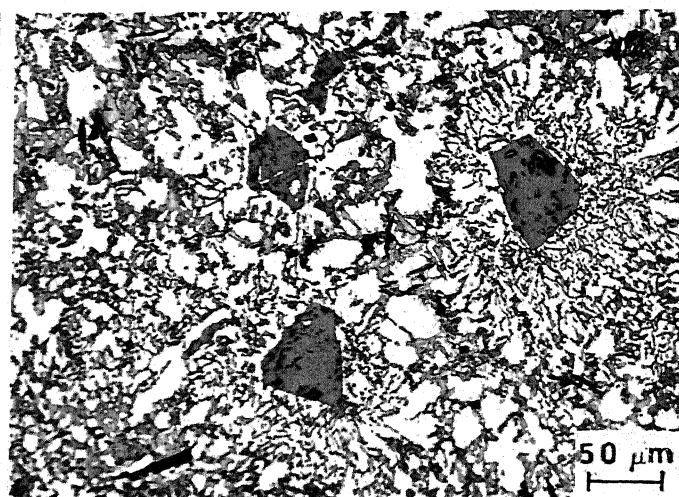
(a)



(b)



(c)



(d)

unaffected by phosphorus addition Fig.5.13.c. The microstructure produced (in heat no.3) when phosphorus and sodium were added is shown in Fig.5.13.d. It can be clearly seen that the primary silicon is refined and the eutectic silicon modified.

The refinement of primary silicon and modification of eutectic silicon are also carried out in the LM30-graphite composites. The microstructural studies confirm that the eutectic silicon remained unmodified when sodium was added after dispersing graphite particles (heat no.5) Fig.5.14, to avoid sodium fuming. In order to get the optimum properties, the sequence of addition of sodium and graphite was changed. In heat no.4 sodium was added prior to dispersion of graphite particles so as to modify effectively the shape of eutectic silicon. To take care^{of} the sodium fuming while stirring the melt during dispersing graphite particles, excess sodium is added (0.288 wt.%) in the melt which is more than the optimum quantity (0.028 wt.%) required for modification. A typical micrograph of LM30-graphite composite (heat no.4) clearly shows graphite particles (marked A) and modified eutectic silicon, (Fig.5.15.a). It is also interesting to note that in LM30-graphite composite, the primary silicon is found to nucleate on the surfaces of graphite particle (marked A), Fig.5.15.b, while the exact nucleation mechanism for selective affinities between the primary silicon and dispersed graphite particles are not clear at present. However, possible occurrence of a heterogeneous nucleation event which promotes preferential nucleation of primary silicon on the graphite particle surface can not be ruled out. Another interesting feature observed is the absence of halo formation around the primary silicon, as seen in the Fig.5.15.a.

The effect of heat treatment (details have already been provided in section 4.2.3) on the microstructure of LM30-graphite composites is illustrated in Fig.5.16. It clearly depicts graphite particles (marked A), coarse primary silicon (marked B), primary aluminium (marked C), and eutectic silicon. Wavelength dispersive X-ray mapping of aluminium, silicon and carbon are shown in Figs.5.16.b,c and d respectively. The fragmentation of eutectic silicon into nearly spherical particles of size around 5 μm is clearly seen in Fig.5.16.e. A similar behaviour has been observed in heat treated LM6 and LM13 alloys, as shown in Figs.5.6.a and 5.8.d respectively. The large

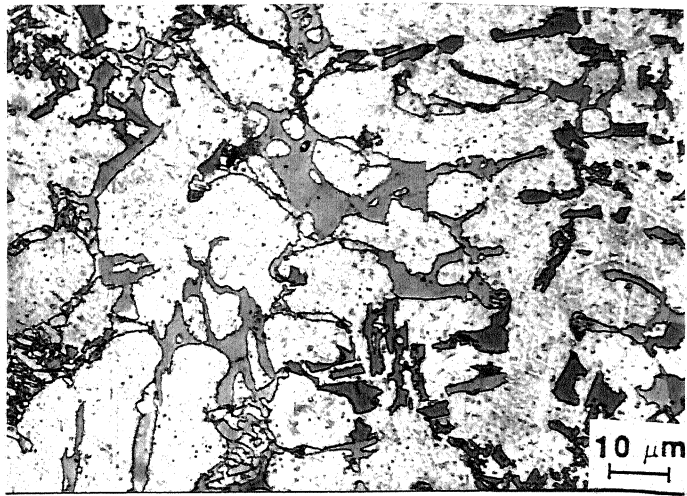
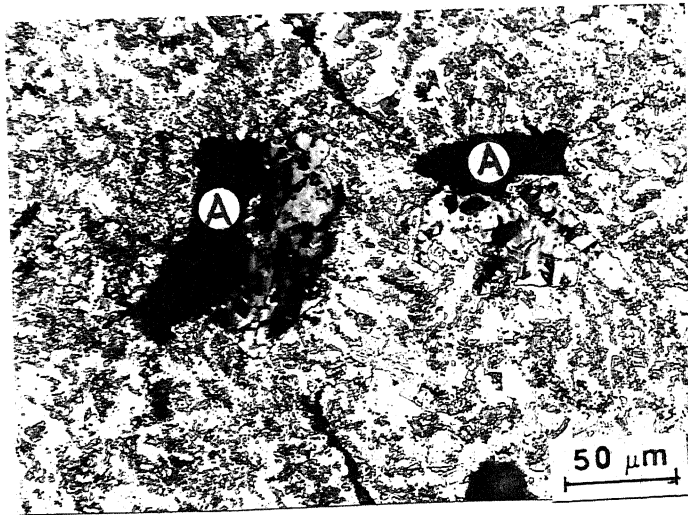
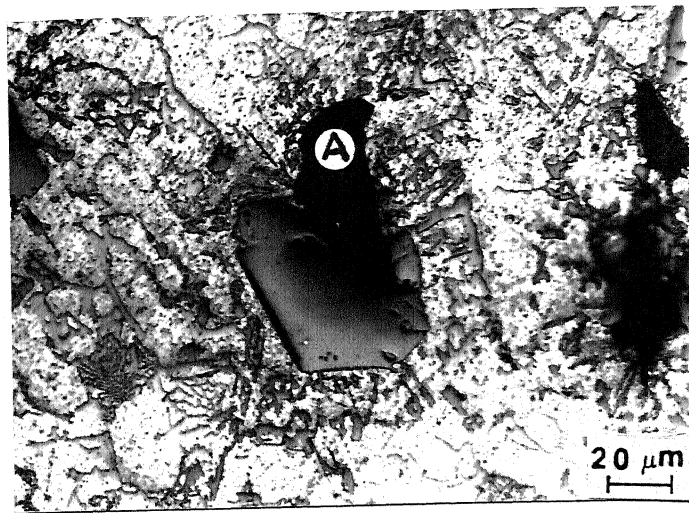


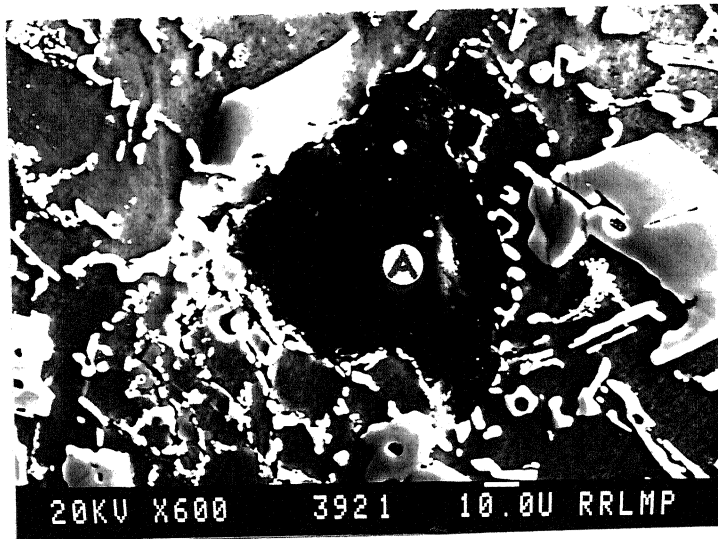
Fig.5.15 Optical micrograph showing: (a) graphite particles in refined and modified LM30-graphite composite and (b) primary silicon nucleating around the graphite particle



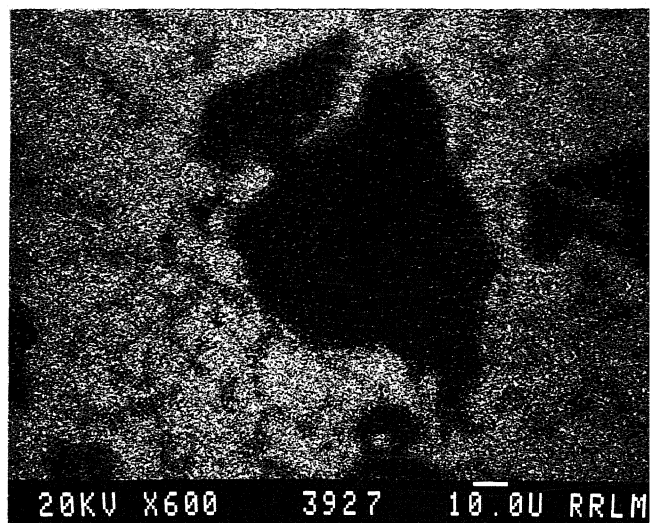
(a)



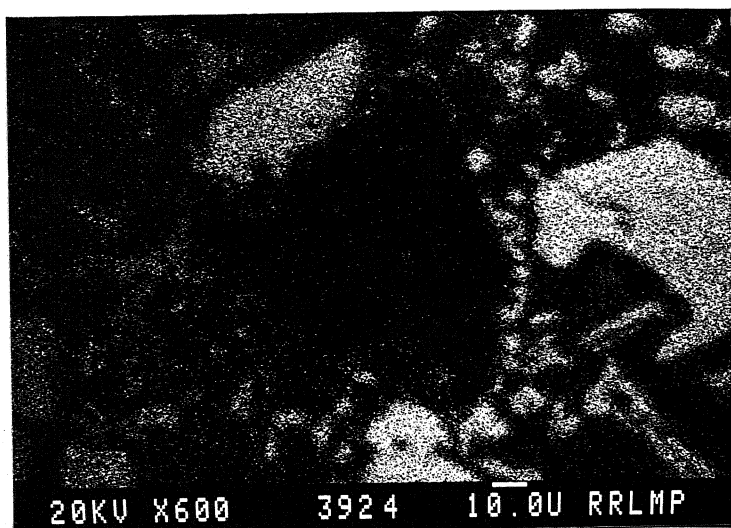
(b)



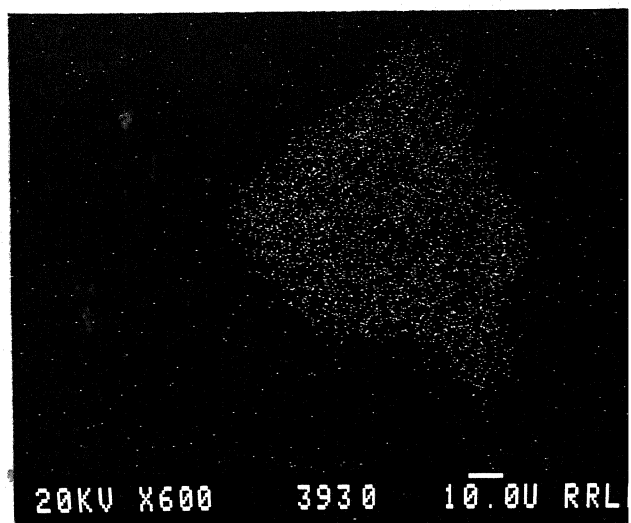
(a)



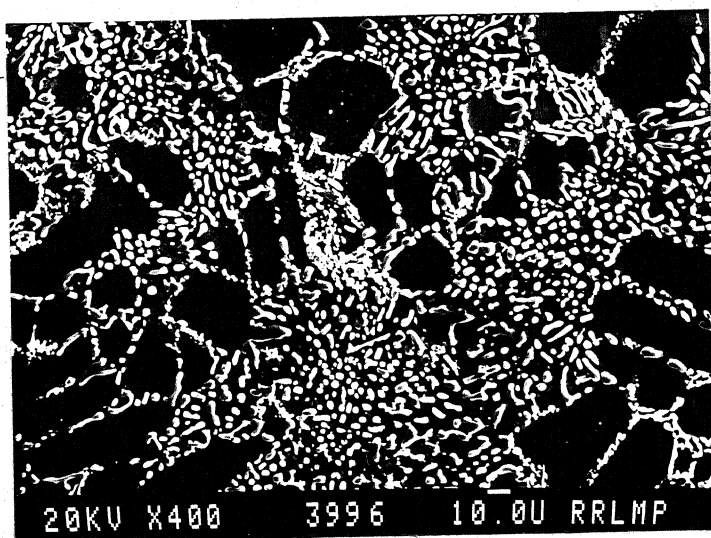
(b)



(c)



(d)

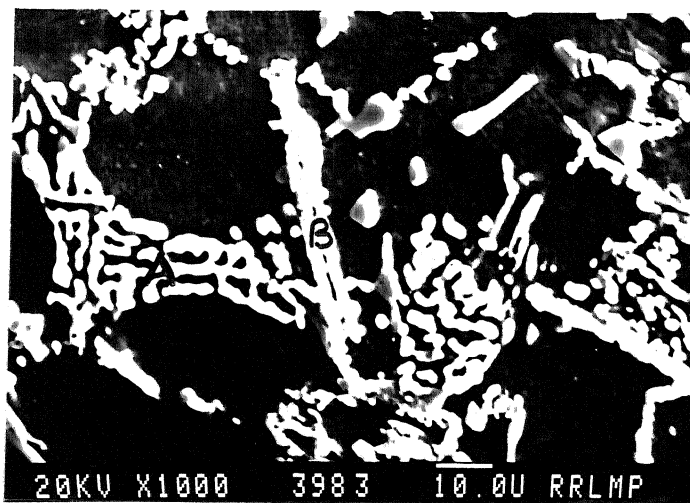


(e)

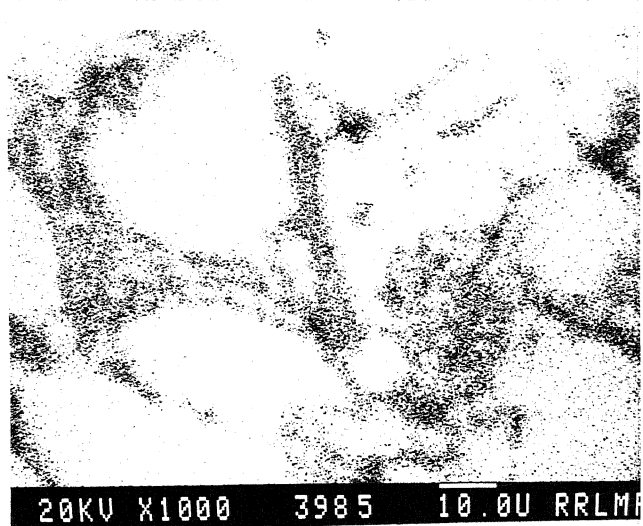
primary silicon cuboids are found to be unaltered due to heat treatment. In some instances intermetallic phases are also seen in LM30 alloy. Typical intermetallic phases are shown in Fig.5.17.a and the corresponding X-ray mapping of aluminium, silicon, iron and copper are seen in Figs.5.17.b,c, d and e respectively. It is inferred from the wavelength dispersive X-ray analysis that apart from aluminium and silicon two more phases are identified, as marked A and B in Fig.5.17.a. Phase 'A' constitute mainly of aluminium and copper and phase 'B' contains aluminium, iron and copper. Fig.5.18.a shows a scanning electron micrograph of intermetallic phases having rod like appearance and the corresponding X-ray mappings of aluminium, copper and iron are seen in Figs.5.18.b,c and d respectively. The wavelength dispersive X-ray analysis confirms that the rod shaped phase marked B in Fig.5.18.a mainly consists of aluminium, copper and iron.

5.3.4 Microdistribution of Graphite Particles in Al-Si Alloy Matrices

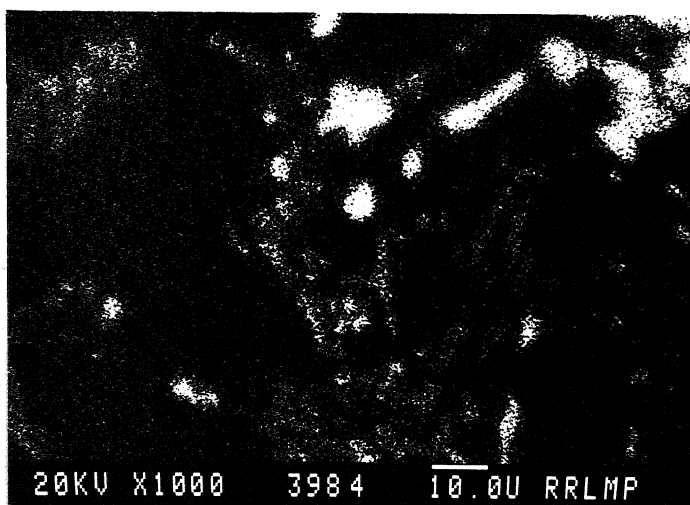
In die cast hypoeutectic Al-Si alloys the first phase to solidify is primary aluminium in dendritic manner and eutectic silicon appears in the interdendritic region and around the dendrites. In Al-Si-graphite composites, the graphite particles are simply pushed by the advancing primary aluminium dendrites to the last freezing eutectic liquid due to poor compatibility between liquid aluminium and graphite particle. Possible entrapment of graphite particles in the interdendritic region i.e., spacing between two consecutive dendrite arms is ruled out as the size of majority of particles (63-120 μm) is more than the average secondary dendrite arm spacing. However, the results of particle size analysis (Fig.5.2) depicts that some particles are in the size range below that of the secondary dendrite arm spacing. But detailed microstructural observations could not confirm the entrapment of particles in the spacings between secondary arms. A typical scanning electron micrograph of LM13-graphite composite shown in Fig.5.19.a depicts two particles (marked A) in the last freezing eutectic liquid. A magnified scanning electron micrograph (Fig.5.19.b) clearly reveals the interface between graphite particle and Al-Si eutectic (arrow marked). Plate-shaped silicon randomly oriented in Al-Si eutectic, is clearly seen in the micrograph, Fig.5.19.b. In some instances, Al-Si alloy is found to ^{be} solidified between the two graphite particles (marked A) and the resulting microstructure is dependent on the



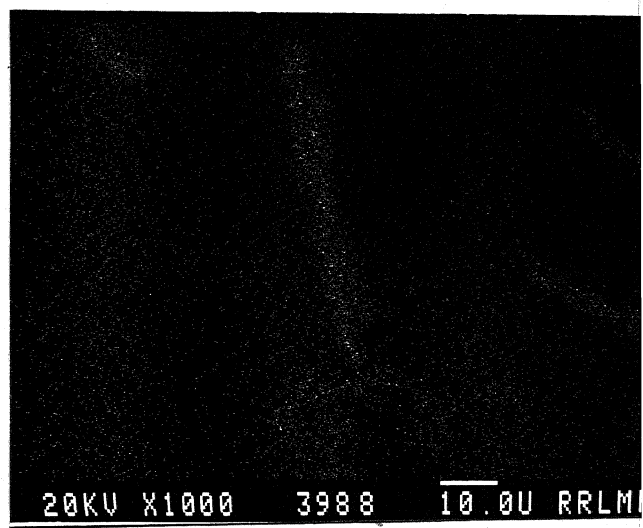
(a)



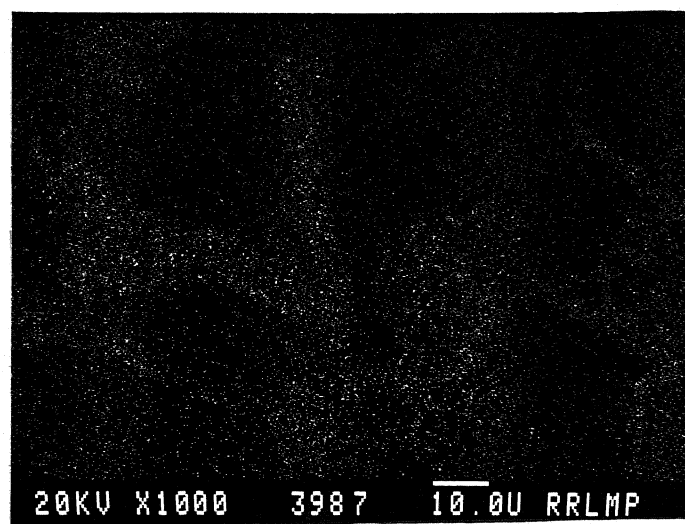
(b)



(c)

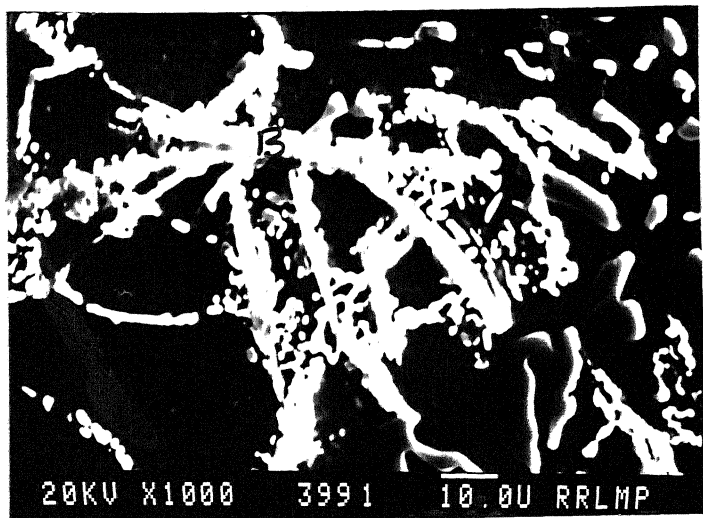


(d)

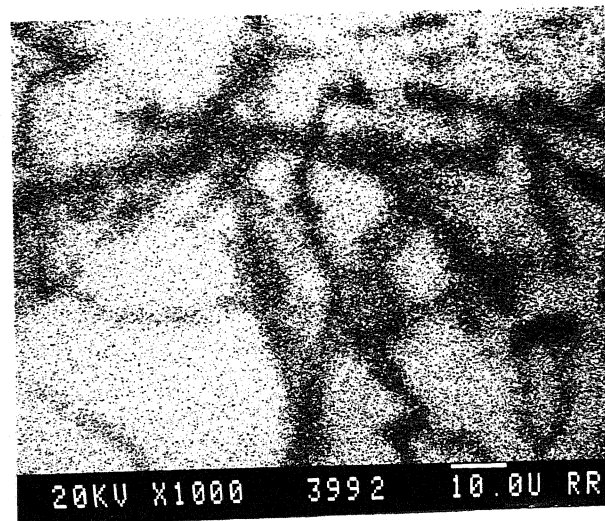


(e)

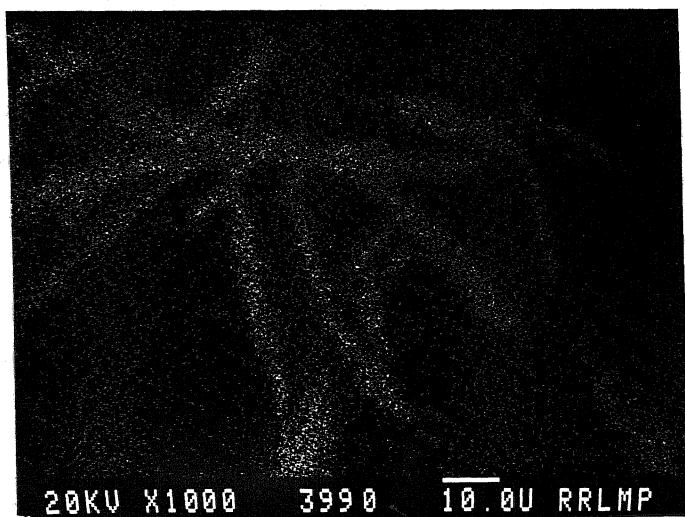
Fig.5.18 Intermetallic phases in heat treated LM30-graphite composite: (a) intermetallic phase (b) aluminium X-Ray mapping (c) copper X-Ray mapping (d) iron X-Ray mapping



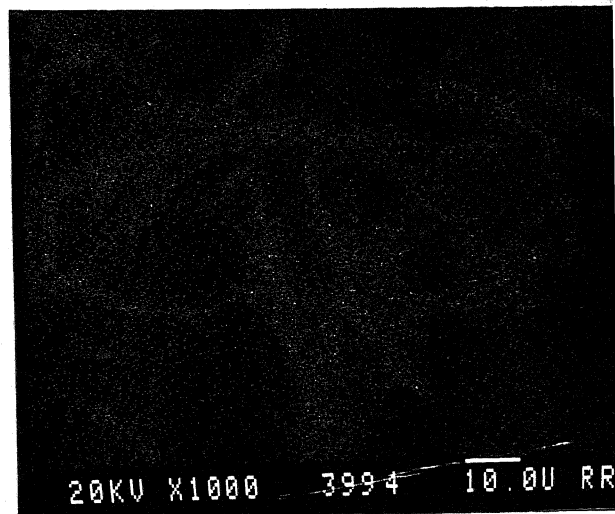
(a)



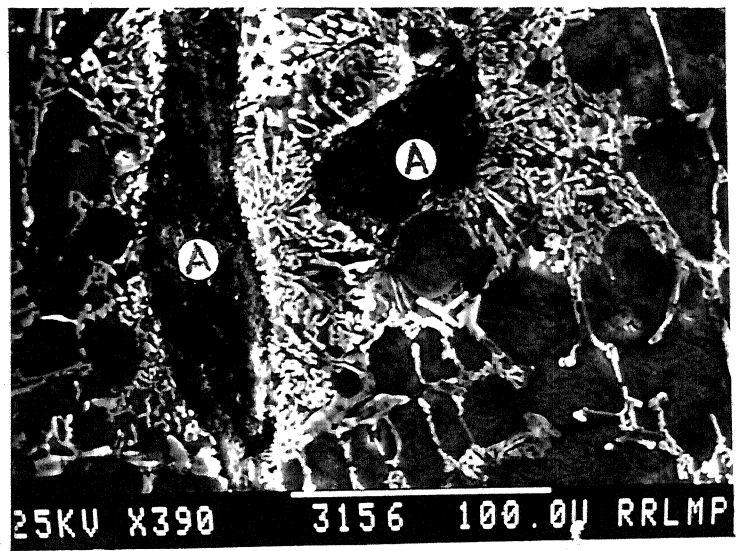
(b)



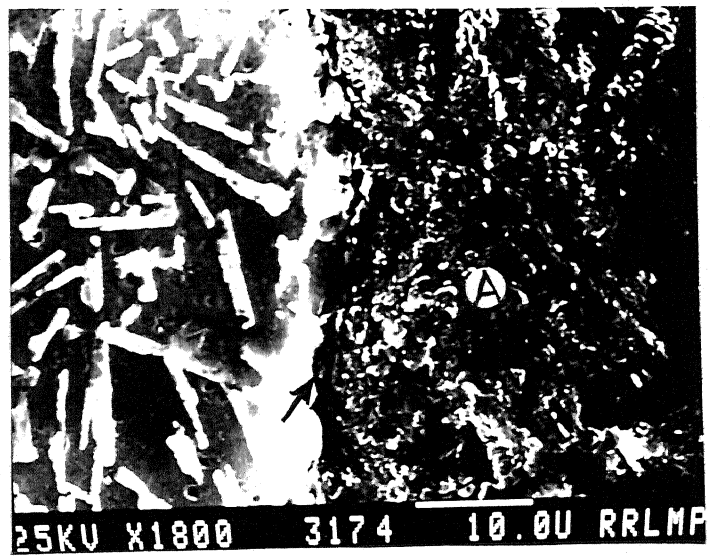
(c)



(d)



(a)

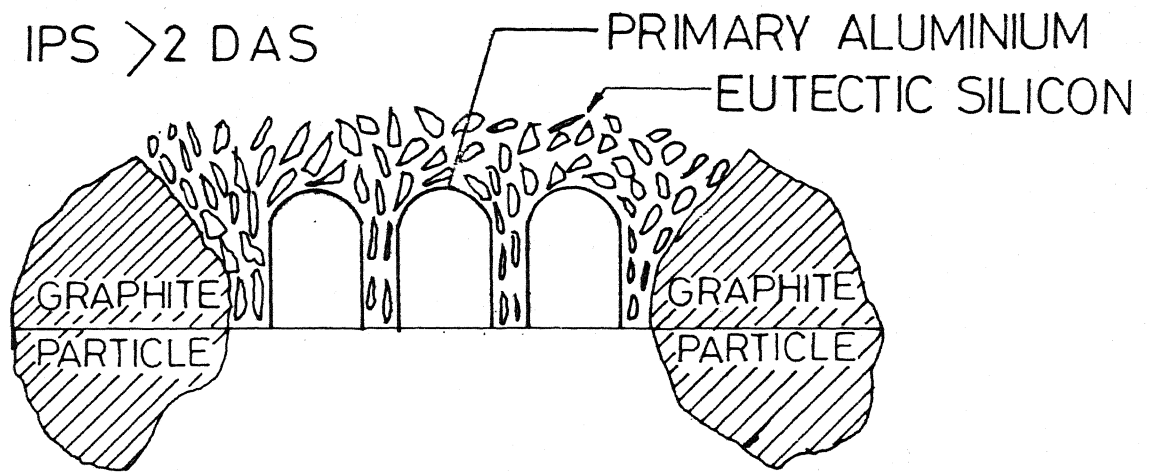


(b)

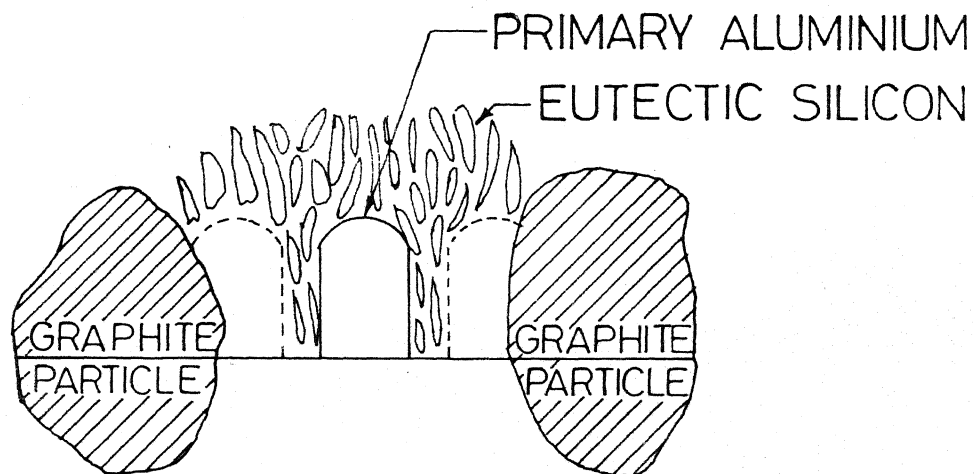
available spacing between the particles. We can now consider the evolution of the microstructure of the hypoeutectic Al-Si alloy in the presence of graphite particles; this is schematically represented in Fig.5.20. Case I deals with a situation when the interparticle spacing is greater than twice the dendrite arm spacing i.e., $IPS > 2DAS$. In this situation the first phase to solidify is primary aluminium between the two graphite particles and ^{it} rejects excess silicon beyond the equilibrium solubility limit, as it grows. In this case the microstructure between the particle will be similar to a typical representation of Al-Si alloy. In the second case the interparticle spacing is assumed to be equal to twice the dendrite arm spacing. In this situation, the primary aluminium will nucleate in between the graphite particles and reject excess silicon as it grows. As the interparticle spacing is just equal to twice the dendrite arm spacing, the probability of nucleating the next dendrite arm is negligible and this can be seen clearly in the microstructure. However, it is mentioned in the preceding sections that graphite particle is pushed by the growing solid phase due to its freedom to move but this concept may not exist in real sense because multidirectional solidification may restrict the movement of particles. In case III, the interparticle spacing is less than ^{the} twice _A dendrite arm spacing i.e., $IPS < 2DAS$. In this situation primary aluminium will nucleate between the two graphite particles (marked A) and as it grows it rejects excess silicon, ^{i.e.,} _A more than the equilibrium solubility limit. As the particles are situated closely, so the possibility of nucleation of neighbouring aluminium dendrite is _A less. In this case a layer of eutectic silicon, which is rejected from primary aluminium during its growth, should appear at the interface between graphite particle and aluminium. Fig.5.21 depicts a representative microstructure of case III. It clearly reveals primary aluminium between the graphite particles (marked A) and rejected eutectic silicon is shown at the interface between graphite particle and primary aluminium. A magnified scanning electron micrograph, Fig.5.21.b, clearly shows graphite particle (marked A), primary aluminium (marked B) and layer of silicon (marked C).

Another interesting feature observed in the microstructure of Al-Si (LM13) alloy-graphite composite is the restriction of anisotropic growth of eutectic silicon as shown schematically in Fig.5.22. In case I (Fig.5.22.a) the closest

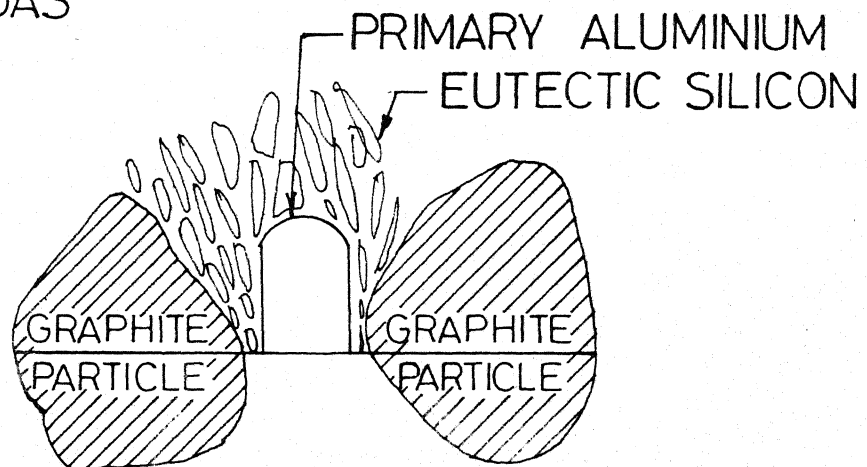
CASE I $IPS > 2 DAS$



CASE II $IPS = 2 DAS$



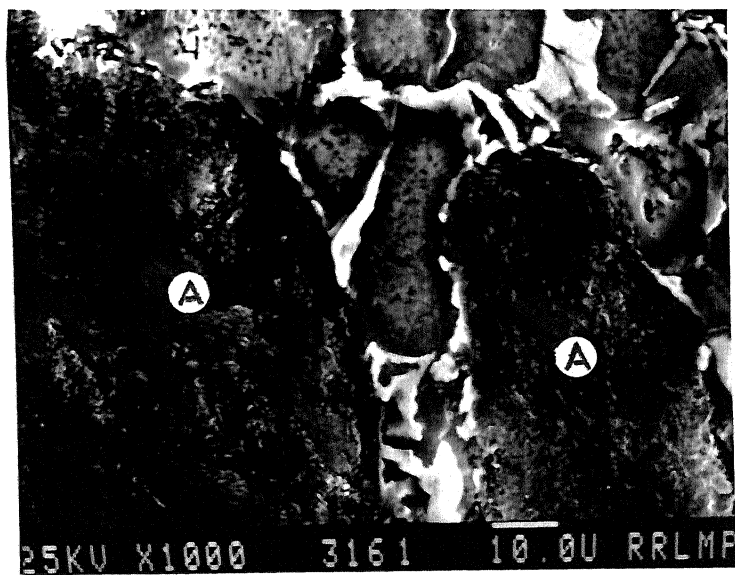
CASE III $IPS < 2 DAS$



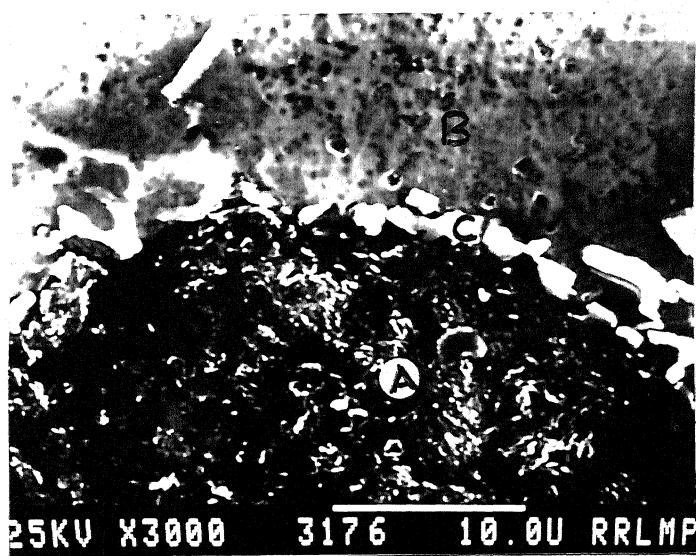
IPS - Inter-particle
Spacing

DAS - Secondary
Dendrite
Arm Spacing

Fig. 5.20 Schematic Representation of Microstructure between Two Graphite Particles for the Conditions : (a) $IPS \gg 2 DAS$, (b) $IPS = 2 DAS$ and (c) $IPS < 2 DAS$.



(a)



(b)

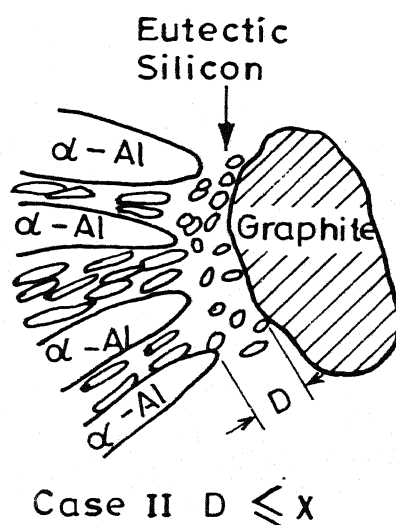
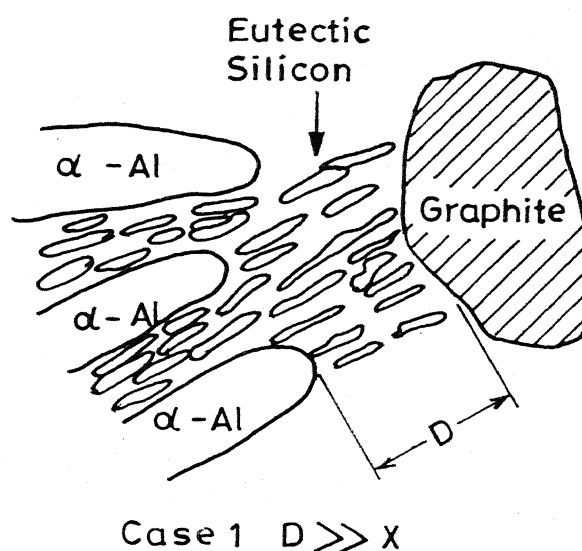


Fig.5.22 Schematic Representation of the Microstructure of Hypoeutectic Al-Si Alloy in the Presence of Graphite Particles.

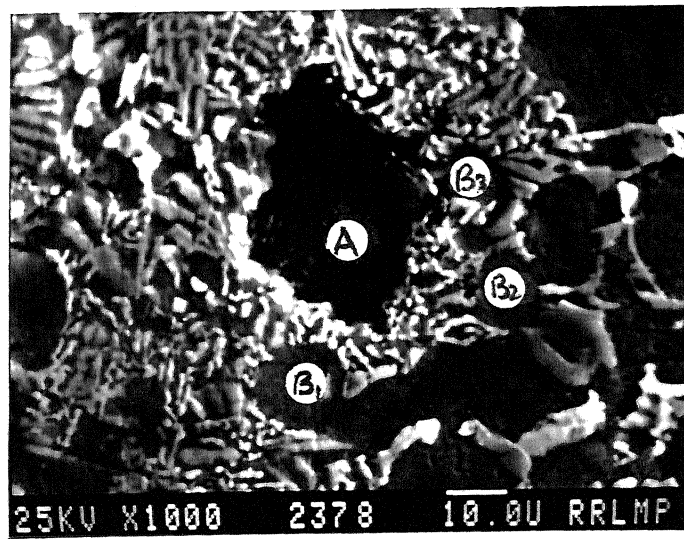
(D - Distance between Dendrite tip and Particle
 X - Length of the Eutectic Silicon in Conventional
 Die Cast Aluminium - Silicon Alloys Without
 Graphite Particle)

distance between the tip of the dendrite arm and graphite particle is higher than the average length of the eutectic silicon normally present in die cast alloy without any graphite particle dispersions i.e., $D \gg X$. In case II, this distance is of the order of or less than the length of the eutectic silicon. In the latter case the anisotropic growth of the silicon phase is physically constrained by the presence of graphite particles giving rise to near spherical shape, as depicted in Fig.5.22.b i.e., $D \ll X$. It can be seen from Fig.5.23 that the closest distance between the primary aluminium marked B_1 and B_2 and the graphite particle (marked A) are 4 and 12 μm respectively whereas one of the dendrites (marked B_3) is almost touching the graphite particle. Therefore, the silicon particles present between these primary aluminium and graphite particles are finer in size and almost spherical in shape, compared to the rest of the area in Fig.5.23.a, where the distance between the graphite particle and primary aluminium is much higher. In the latter case the silicon has the freedom to grow in an anisotropic manner as depicted in Fig.5.22.b. Figure 5.23.b shows a scanning electron micrograph of the matrix solidified between two graphite particles (marked A) separated by a distance of about 10 μm . It can be clearly seen that the morphology of the silicon between these two graphite particles is significantly modified (marked C). This study indicates that the presence of graphite particles can also lead to modification of silicon provided these particles are situated very close to each other or to the primary aluminium dendrite boundaries. The mechanism appears to be physical constraint minimising the anisotropic growth of silicon. By increasing the graphite volume fraction or reducing the graphite particle size one could arrive at a situation whereby most of the silicon needles in the microstructure of the matrix alloy could be refined.

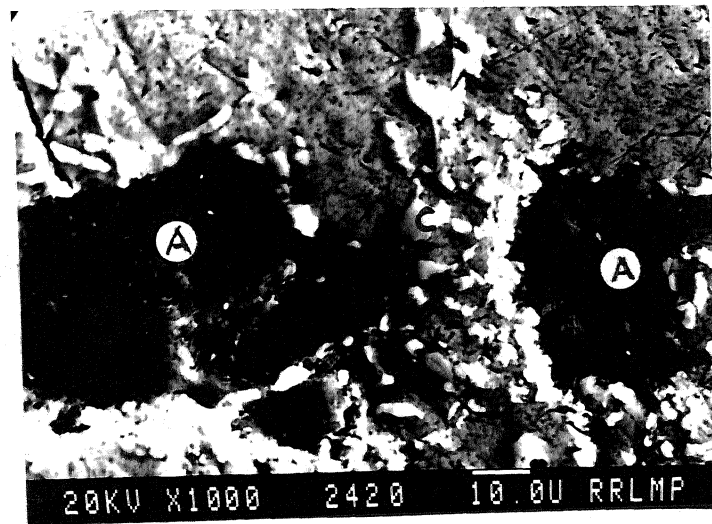
5.3.5 Microstructure of Rapidly Solidified Al-Si Alloy and Composites

A typical micrograph of rapidly solidified aluminium-silicon (LM6) alloy is shown in Fig.5.24.a. It delineates very fine cells of primary aluminium of average cell size 2 μm and near spherical eutectic silicon (size: less than 1 μm) around the cells. The maximum solid solubility of silicon in aluminium is 1.64% at the eutectic temperature of 577°C and less than 0.01% at room temperature. In the present investigation, the lattice parameter of primary aluminium solid solution of rapidly solidified LM6 alloy was determined by X-ray diffraction studies and found to be 4.0467 (\AA) as against 4.0496 (\AA)

Fig.5.23 (a) Scanning electron micrograph showing modified and unmodified eutectic silicon around the graphite particle and (b) micrograph showing modified eutectic silicon between two graphite particles

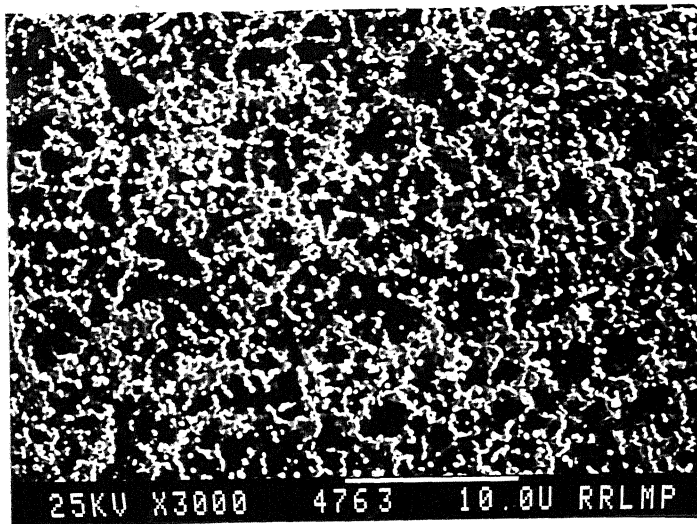


(a)

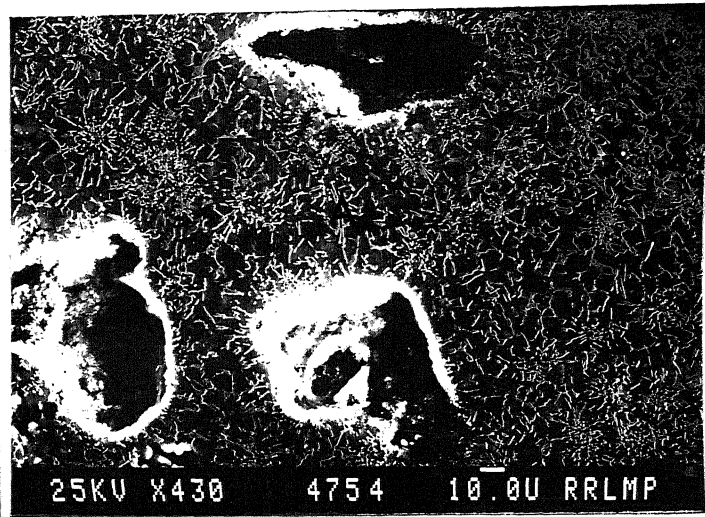


(b)

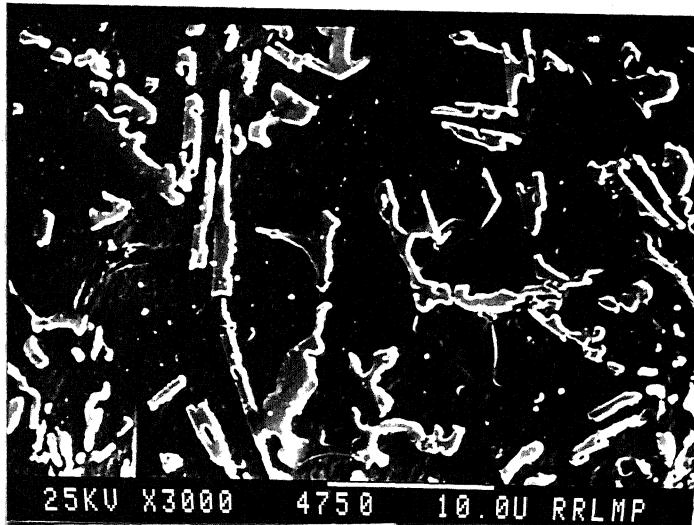
Fig.5.24 Scanning electron micrographs showing: (a) microstructure of rapidly solidified LM6 alloy, (b) rapidly solidified LM6-graphite composite (c) magnified micrograph showing plate-shaped eutectic silicon near the graphite particle (d) microstructure well away from the graphite particle and (e) microstructure of rapidly solidified LM13 alloy



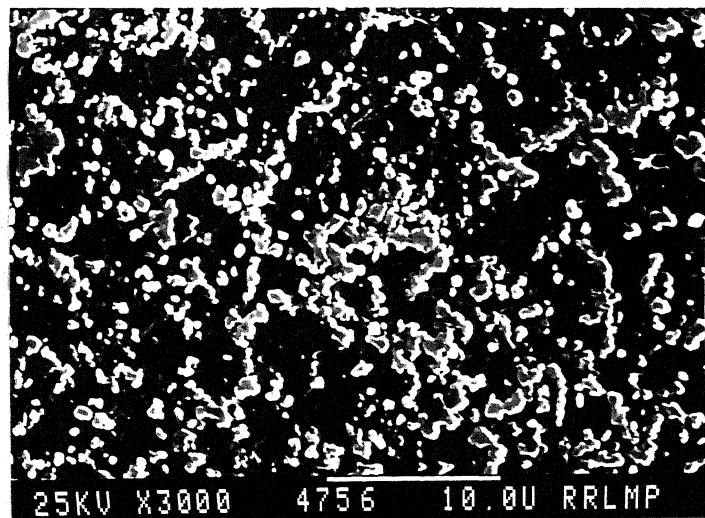
(a)



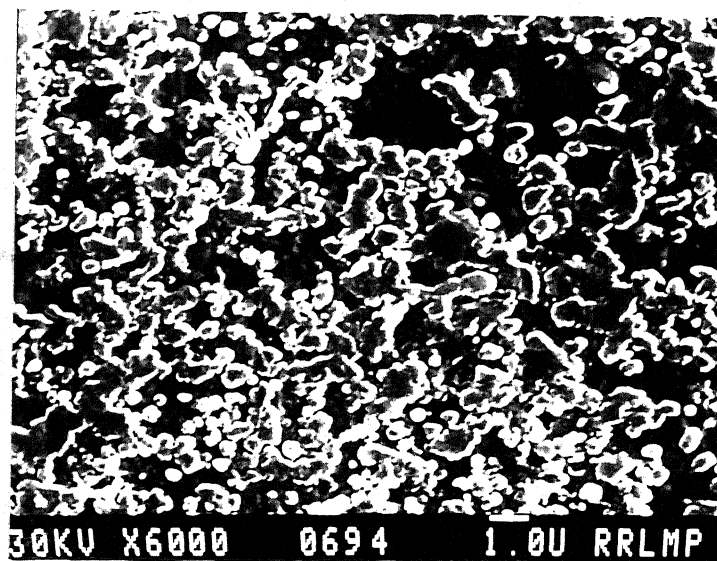
(b)



(c)



(d)



(e)

for pure aluminium. X-ray diffraction results of rapidly solidified LM6 alloy and LM6-10% graphite particle composite are shown in Table V.7. The observed lattice parameter of 4.0467 (\AA) corresponds to about 1.6% Si, a value quite close to the maximum solid solubility of silicon in aluminium under equilibrium conditions. It is to be noted that the solubility of silicon in aluminium may be affected by the presence of iron, copper and manganese in the commercial alloy. Although no quantitative data are available in the literature, the general trend is suggestive of reduction in the solubility of silicon in aluminium. The estimated solubility of 1.6% may be in error if some amount of copper is also in the dissolved state. However, in the presence of iron and manganese, copper is expected to form intermetallic phases such as $\text{Al}_6(\text{Fe,Cu})$ and $\text{Al}_7\text{Cu}_2\text{Fe}$ which would not affect the lattice parameter of the aluminium solid solution significantly. Fig.5.24.b shows a scanning electron micrograph of rapidly solidified melt spun ribbon of LM6-graphite particle composites. It clearly reveals graphite particles in the ribbon; the particles are confirmed to be graphite by wavelength dispersive X-ray microanalysis. A magnified view of the microstructure near the dispersed graphite particle (region marked 'A' in Fig.5.24.b) is shown in Fig.5.24.c. The microstructure of matrix near the dispersed graphite particles (Fig.5.24.c) appears to be significantly different from that shown in Fig.5.24.d (away from the graphite particles). It can be noted that eutectic silicon grows anisotropically as plate-shaped near the graphite particles (Fig.5.24.c) whereas it grows more or less isotropically as near spherical away from the graphite particles (Fig.5.24.d). The plate-shaped eutectic silicon is in the size range of $5\text{--}12 \text{ }\mu\text{m}$ long and $1\text{--}2 \text{ }\mu\text{m}$ wide whereas the average size of near spherical silicon away from dispersed graphite particle is around $1 \text{ }\mu\text{m}$. The lattice parameter of aluminium solid solution in Al-Si-graphite composite, estimated from X-ray diffraction data, was found to be 4.0481 (\AA) . This value is nearly equal to the equilibrium value of the lattice parameter of aluminium, i.e., 4.0496 (\AA) . It can be inferred from the above result that dispersion of graphite particles in LM6 alloy melt restricts the decrease in lattice parameter of aluminium solid solution. The meagre amount of silicon in aluminium solid solution as observed in the present investigation may be due to low degree of supercooling encountered during solidification as well as the presence of other alloying elements e.g., Cu, Fe and Mn. Furthermore, dispersing graphite particles (graphite has lower thermal

Table V.7 X-Ray Diffraction Results of Rapidly Solidified Al-Si(LM6) Alloy and Composites

LM6		LM6-10%graphite		From Standard data card (JCPDS file)		
Diffraction angle, 2 θ (degree)	Interplanar spacing, d (\AA)	Diffraction angle, 2 θ (degree)	Interplanar spacing, d (\AA)	Interplanar spacing, d (\AA)	Diffraction plane	Phase
		26.72	3.335	3.36	(0002)	Graphite
28.60	3.12	28.49	3.132	3.135	(111)	Silicon
38.68	2.327	38.48	2.339	2.338	(111)	Aluminium
44.94	2.016	44.72	2.026	2.024	(200)	Aluminium
47.52	1.913	47.37	1.918	1.92	(220)	Silicon
		56.15	1.638	1.637	(311)	Silicon
65.27	1.429	65.07	1.433	1.431	(220)	Aluminium
78.40	1.219	78.193	1.222	1.222	(311)	Aluminium
82.57	1.168	82.39	1.170	1.169	(222)	Aluminium

conductivity than Al-Si alloy) in LM6 alloy melt delays the dissipation of heat and this in turn results in a microstructure similar to die cast alloy except scale down the dimensions of phases due to higher solidification rate. It appears that coarse microstructure near the graphite particles is mainly attributed to barrier to thermal transport offered by the dispersed graphite particles.

The microstructure of rapidly solidified LM13 alloy(Fig.5.24.e) shows very similar morphology as that of LM6 alloy (Fig.5.24.a). The microstructure of rapidly solidified LM13 alloy consists of near spherical eutectic silicon uniformly distributed in aluminium matrix. The average size of the spherical silicon is found to be of the order of 1 μm .

5.4 Mechanical Properties of Al-Si Alloys and Composites

5.4.1 Ultimate Tensile Strength

The ultimate tensile strength (UTS), % elongation and hardness of Al-Si (LM6, LM13 and LM30) alloys and composites are evaluated and shown in Table V.8. It can be noted from Table V.8 that the UTS of Al-Si (LM6,LM13,LM30) alloys is decreased by $\sim 30\%$ due to the dispersion of 3 wt.% graphite particles. It is noted that the heat treatment of Al-Si alloys enhanced the UTS. For instance, the UTS, of LM6 alloy is increased from 180 MPa in die cast alloy to 260 MPa in heat treated alloy. In the case of LM13 alloy, the UTS is increased from 180 MPa in die cast alloy to 280 MPa in heat treated alloy and for LM30 alloy, the UTS is increased from 140 MPa in die cast alloy to 220 MPa in heat treated alloy. Heat treatment did not affect the percentage elongation of LM13 and LM30 alloys; while for LM6 alloy, the % elongation is enhanced from 2% in die cast alloy to 5% in heat treated alloy.

5.4.2 Hardness

The hardness of die cast Al-Si (LM6,LM13,LM30) alloys is also found to increase due to heat treatment. For example, the hardness of LM6 alloy is increased from 95 BHN to 135 BHN and for LM13 and LM30 alloys, the increase in the value is from 135 BHN to 140 BHN in both the cases. Dispersion of 3 wt.% graphite in LM6,LM13, and LM30 alloy decreases the hardness by 37%, 11% and 14% respectively.

Table V.8 : Mechanical Properties of Al-Si (LM6,LM13 and LM30)

Alloy and Composites

Alloy/Composites	Tensile Strength (MPa)	% Elongation	Hardness (BHN)
LM6 (die cast)	180	2	95
LM6 (Modified)	195	3	95
LM6 (Heat-treated)	260	5	135
LM6-Graphite	125	1	60
LM6-graphite (Modified)	130	1	65
LM6-graphite (Heat treated)	150	1	120
LM13 (Die cast)	180	1	135
LM13 (Heat treated)	280	1	140
LM13-graphite	130	1	120
LM13-graphite (Heat treated)	190	1	130
LM30 (Die cast)	140	1	135
LM30-P-Na	161	1	140
LM30 (Heat treated)	220	1	145
LM30-graphite	98	1	116
LM30-P-Na-graphite	106	1	120
LM30-graphite (Heat treated)	160	1	140

5.5 Wear

5.5.1 Dry Sliding Wear

Dry sliding wear behaviour of Al-Si alloys (LM6, LM13 and LM30) is evaluated using a Cameron-Plint pin-on-disc wear testing machine (Fig.4.2) according to the procedure described in the previous chapter. The sample in the form of a pin is held against a rotating hardened steel disc. The speed of the disc is fixed in all the experiments at 640 RPM. The radius of the wear track is 40 mm; this corresponds to a sliding speed of 2.68 m/s. At a given applied pressure, the sample is allowed to slide for a distance of 500m and wear rate is computed from weight loss measurements. The rise in sample temperature during the test is recorded using a chromel-alumel thermocouple as described in the previous chapter. After each test the disc is repolished to its original roughness value and the experiment continued by increasing the applied pressure in increments of 0.5 MPa. When the applied pressure reaches a certain critical value the sample is found to seize before reaching a sliding distance of 500 m. The onset of seizure is monitored by ^asudden increase of temperature followed by vibration and noise from the disc-pin assembly.

5.5.1.1 Effect of pressure

Effect of pressure on dry sliding wear behaviour of Al-Si alloys (LM6, LM13 and LM30) is evaluated. The wear rates of die cast LM6, LM13 and LM30 alloys at various applied pressures are shown in Fig.5.25. It can be clearly seen that the wear behaviour of all the three alloys is non-linear, and the wear rate increases as the pressure is increased. For instance, the wear rate of LM6 alloy is increased from 1.4×10^{-12} to 2.0×10^{-12} m³/m, when the applied pressure is increased from 1.0 to 1.5 MPa. Beyond 1.5 MPa i.e., when the applied pressure is increased to 2.0 MPa a drastic increase in wear rate of die cast LM6 alloy is noticed. The test is discontinued after sliding a distance of 400 m, since the temperature of the test piece rose to 140°C, and there is abnormal vibration and noise from pin-disc assembly. Similar wear behaviour is observed for die cast LM13 alloy also. The wear rate of LM30 alloy is found to be different from that of LM6 and LM13. It increased from 0.9×10^{-12} m³/m to 4.1×10^{-12} m³/m when the applied pre-

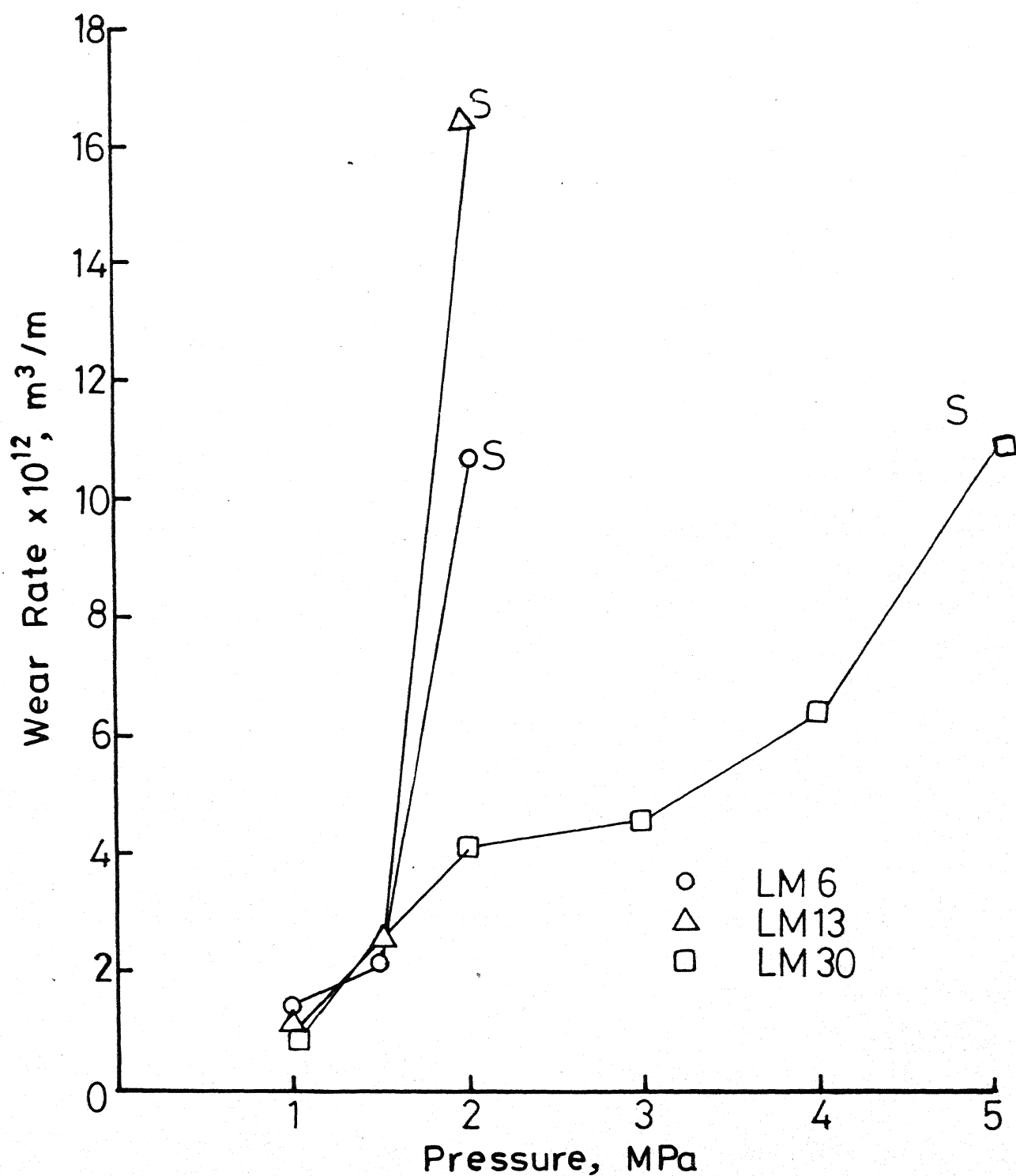
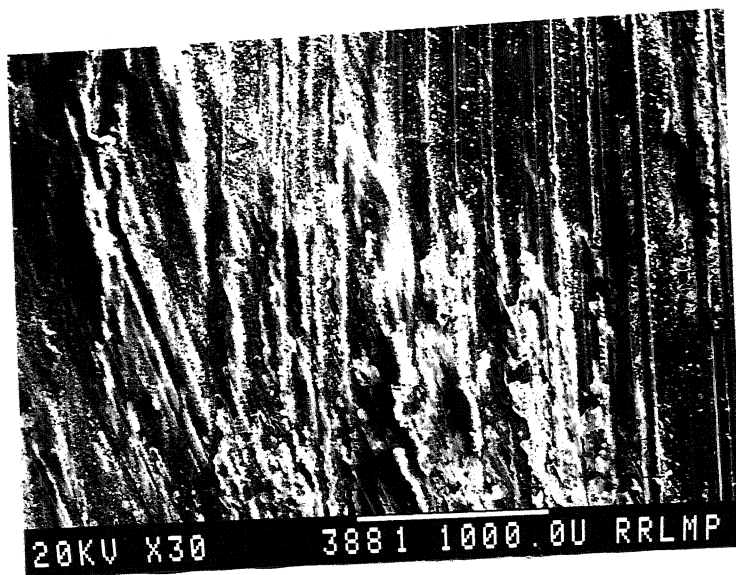


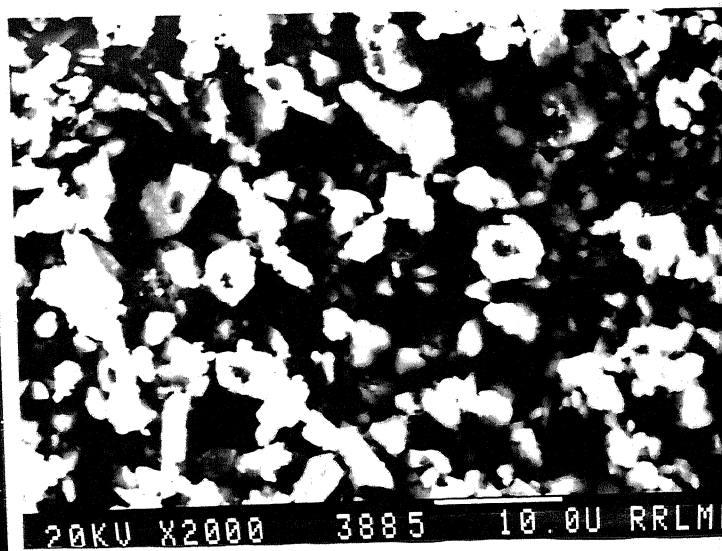
Fig.5.25 Effect of Pressure on the Dry Sliding Wear Rate of Die Cast LM6, LM 13 and LM 30 Alloys (Sliding Speed: 2.68 m s^{-1} , S : Seizure)

ssure is increased from 1.0 to 2.0 MPa. The temperature of the test piece during the experiment rose to 35°C at 1.0 MPa pressure and 80°C at 2.0 MPa pressure. Above 2.0 and upto 4.0 MPa pressure a progressive increase in wear rate of LM30 alloy is observed; this behaviour is unlike that found in LM6 and LM13 alloys. The sample temperatures during the test increased to 108 and 136°C at applied pressures of 3.0 and 4.0 MPa respectively. Further increase in the pressure to 5.0 MPa resulted in the seizure of the die cast LM30 alloy after a sliding distance of 320 m. The temperature of LM30 alloy rose to 200°C just before the seizure. It can be inferred from the above results that LM30 alloy is superior to LM6 and LM13 alloys, as far as their resistance to wear is concerned. The maximum load which can be sustained without seizure is higher for the LM30 alloy. The worn surface and wear debris of LM6, LM13 and LM30 alloys are studied by scanning electron microscopy with a view to understanding the mechanisms of wear. Fig.5.26.a shows a typical scanning electron micrograph of the worn surface of LM6 alloy. The test is carried out at an applied pressure of 1.0 MPa and is allowed to slide for a distance of 500 m, at a sliding speed of 2.68 m/s. The micrograph clearly reveals wear grooves and layers of fine particles covering the surface. A magnified micrograph of the wear debris is shown in Fig.5.26.b. The morphology of the debris particles is almost equiaxed. Fig.5.26.c shows a typical scanning electron micrograph of worn surface of LM6 alloy, tested with a higher applied pressure i.e., 2.0 MPa. The worn surface shows continuous grooves and patches of damaged areas. A typical debris particle, collected during the test, is shown in Fig.5.26.d. Debris collected at 2.0 MPa pressure are found to be much bigger in size (100 μm) and appear to be flaky in nature in contrast to the equiaxed particles found at the lower pressure. The particle size distribution of equiaxed wear debris is shown in Fig.5.27. It can be seen in the histogram that 18% of the particles are less than 0.6 μm in size and 75% particles lie in the size range of 1-6 μm . The mean interparticle spacing, \bar{x} is 3 μm and standard mean deviation is 1.7 μm (in Table V.9).

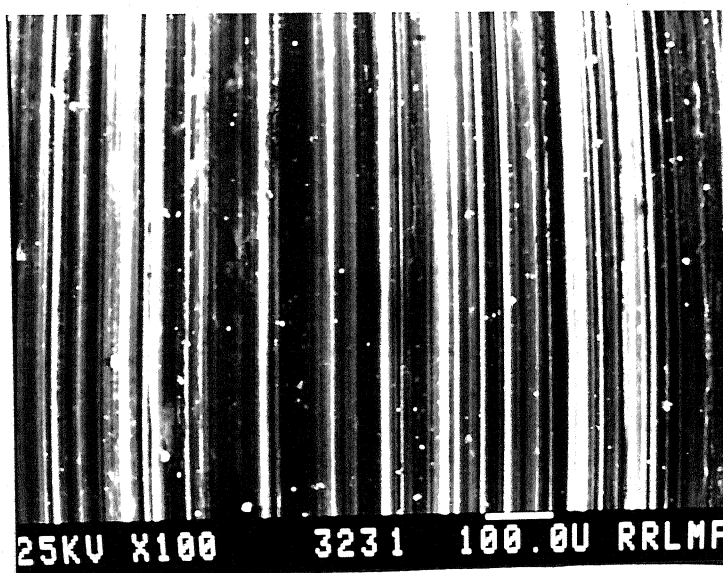
The above results suggest that die cast Al-Si alloys show two different wear regimes depending upon the magnitude of applied pressures, one is mild wear and the other one is severe wear. Mild wear occurs generally, at low



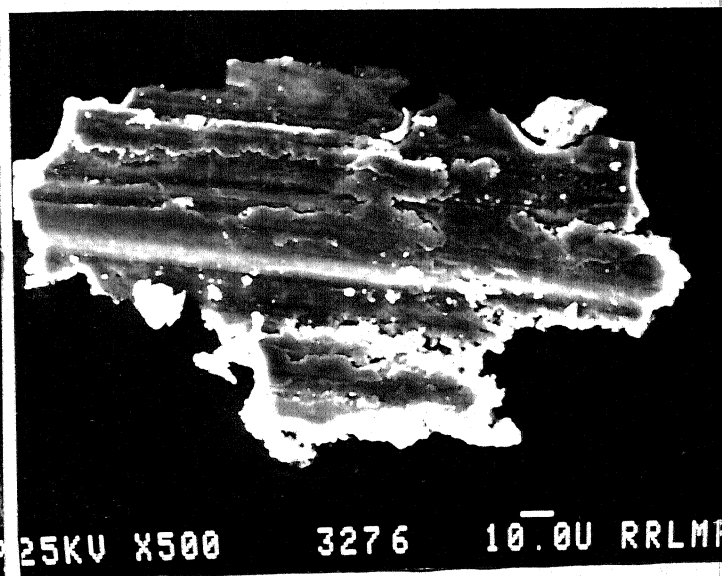
(a)



(b)



(c)



(d)

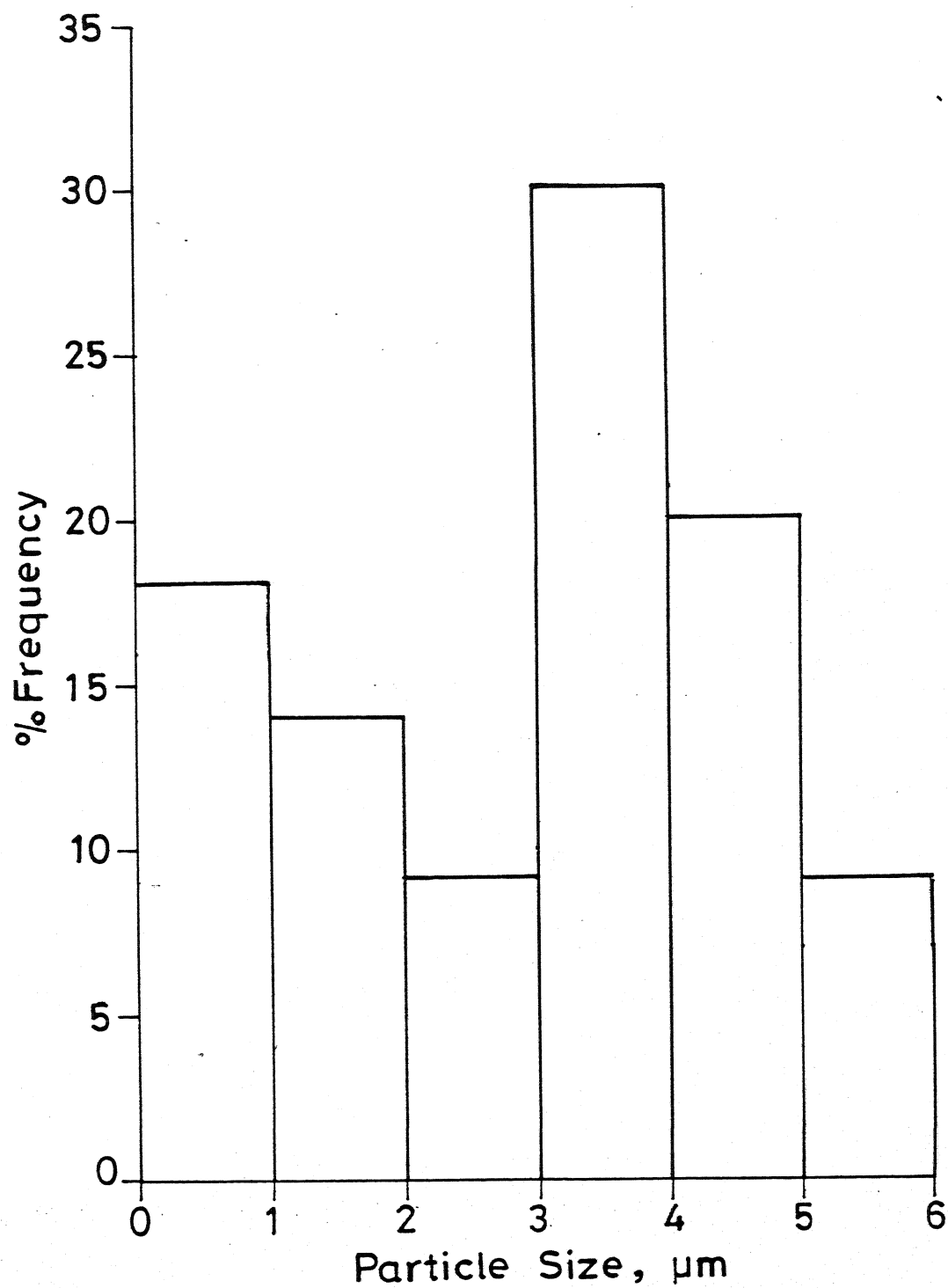


Fig.5.27 Particle Size Distribution of Equiaxed Wear Debris.
(Pressure : 1.0 MPa, Sliding Velocity: 2.68 ms^{-1})

Table V.9: Particle Size Distribution of Equiaxed Wear Debris

Particle size (μm)	% of the total no. of particles	Mean particle size (\bar{X}), μm	Standard mean deviation (σ) μm
Upto 1	18		
1 - 2	14		
2 - 3	9		
3 - 4	30	3.0	1.7
4 - 5	20		
5 - 6	9		

loads. The onset of severe wear regime in the cases of LM6 and LM13 alloys is 1.5 MPa. The LM30 alloy did not show such drastic increase in wear rate rather it increased progressively upto 4 MPa pressure. It is also interesting to note that the size and shape of debris particles in the two regimes are markedly different. In the mild wear regime, very fine ($\sim 6 \mu\text{m}$) equiaxed debris are generated whereas big flake type debris are generated in severe wear regime.

5.5.1.2 LM6 Alloy and LM6-Graphite Particle Composites

The dry sliding wear of LM6 alloy and LM6-3% graphite particle composites with three different matrix microstructures (die cast, sodium modified and heat treated) is evaluated as a function of applied pressure. The results are shown in Fig.5.28. It can be seen from Fig.5.28 that the wear rates of both matrix alloys and composites increase with load in a nonlinear manner.

As pointed out in the previous section the onset of severe wear regime for the die cast LM6 alloy begins at stress value between 1.5-2.0 MPa. Both graphite particle dispersions and microstructural changes of the matrix alloy are found to influence the onset of severe wear regime. LM6 alloy in modified and heat treated conditions and composites in die cast and modified conditions exhibited similar wear behaviour. In all these cases the samples seized between 2 and 3 MPa and the onset of severe wear regime is at 2 MPa. Heat treated composites gave by far the best wear results. The seizure of heat treated composites occurred at 3.5 MPa. It can be concluded that optimum dry sliding wear resistance of LM6 alloy can be achieved by a combination of graphite particle dispersion and the heat treatment of the matrix alloy as described in the previous section.

The temperature rise during sliding is plotted as a function of time in Fig.5.29, for the die cast LM6 alloy, modified and heat treated LM6 alloys, LM6-graphite composites and LM6-graphite composites with modified and heat treated microstructures. There is a direct comparison of Fig.5.28 with 5.29; similarities between time-temperature plots and the wear rates vs applied pressure plot can be found. In both cases there is a marked difference

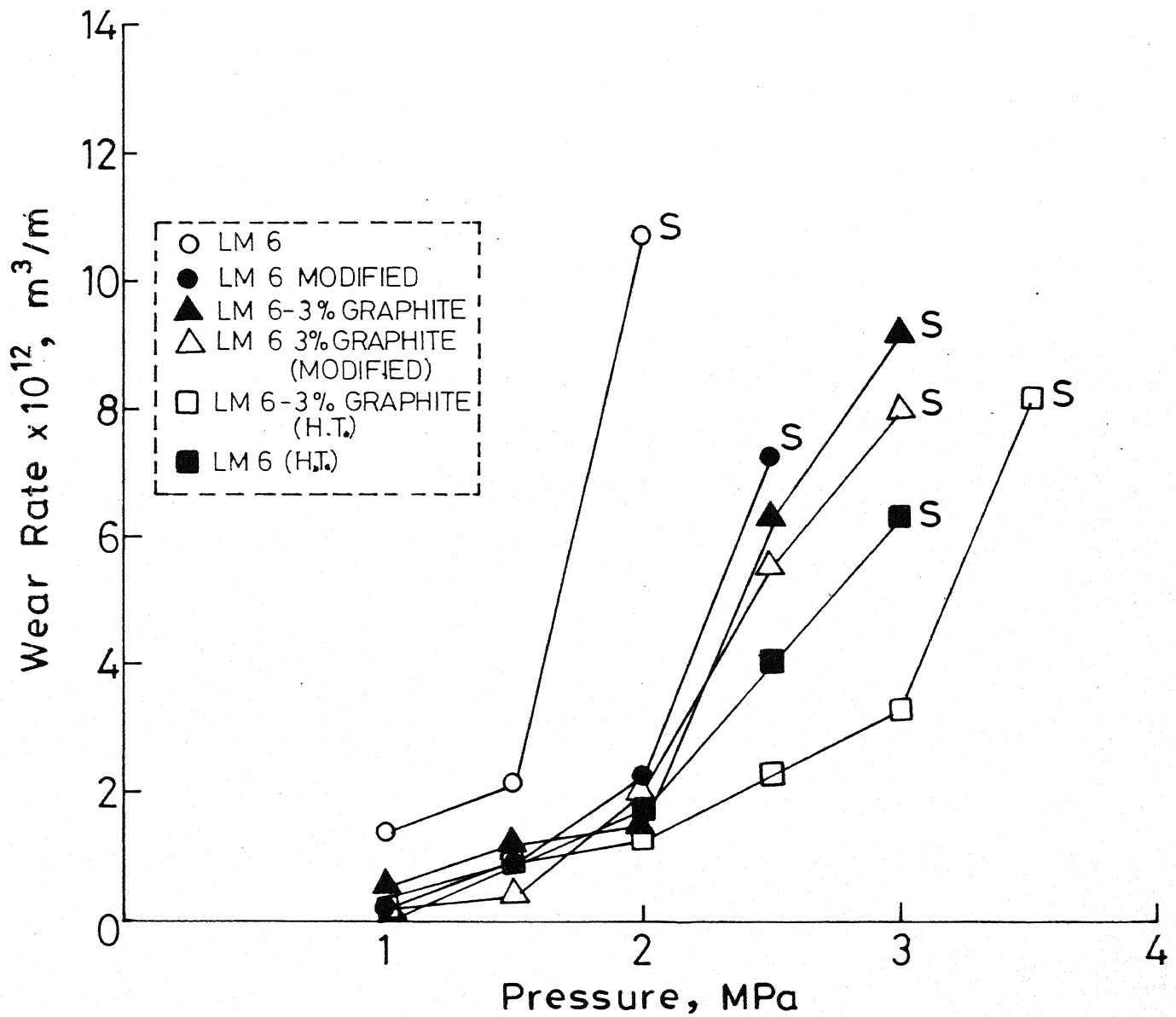


Fig. 5.28 Effect of Pressure on Dry Sliding Wear of LM6 Alloy and LM6-3 wt.% Graphite Particle Composites (Sliding Speed : 2.68 ms^{-1} S : Seizure)

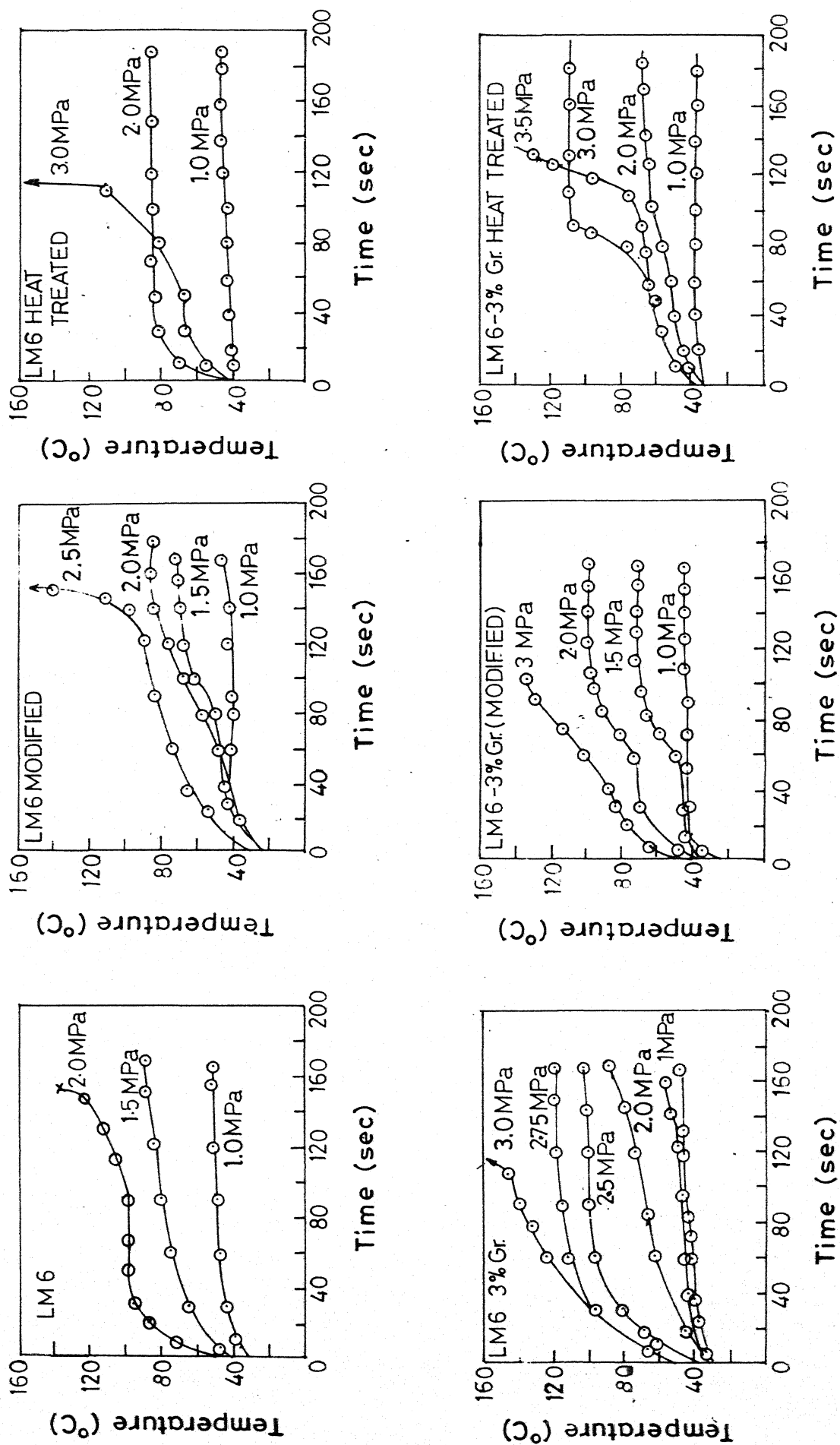


Fig. 5.29 Time - Temperature Relationship in LM6 Alloy and LM6 - 3 wt % Graphite Particle Composites During Dry Sliding Wear.

in the trend when the sample is about to seize. The temperature rose gradually in the mild wear regime and after some interval of time it began to stabilise. However, during the severe wear regime the sample temperature exhibited a very sharp rise before the onset of seizure. Comparing the temperature-time relationship of die cast and heat treated composites one can find that the temperature rise in case of heat treated composites is much lower than that of the base alloy. For example, at an applied pressure of 1 MPa, the temperature of LM6 pin rose to 50°C whereas the temperature rise in case of graphite composites stabilised at 40°C. In an applied pressure of 2.0 MPa the temperature of LM6 pin rose to 140°C after 150 seconds corresponding to a sliding distance of 402 m, whereas the temperature of the heat treated composites, rose to only 70°C for the same pressure. Even at the pressure of 3.0 MPa, temperature of the heat treated composites stabilised around 110°C. The results of these studies show that optimum results can be achieved by a combination of graphite dispersion and proper heat treatment.

5.5.1.3 LM13 Alloy and LM13-Graphite Particle Composites

The effect of heat treatment and graphite particle dispersion on the dry sliding wear behaviour of LM13 alloy is shown in Fig.5.30. As mentioned earlier the die cast LM13 alloy seized at an applied pressure of 2 MPa and there is a sharp increase in wear rate when the applied pressure is increased from 1.0 to 2.0 MPa. Heat treated alloy showed better performance as compared to die cast alloy; it seized at an applied pressure of 2.5 MPa. Graphite particle dispersed composites showed a far better performance as compared to matrix alloy in die cast and heat treated conditions. Composites specimen seized at 3.5 MPa as in the case of the LM6 alloy. Optimum wear performance are obtained for the composites in the heat treated condition. The seizure load in this case is maximum (4.0 MPa).

Time-temperature plots for LM13 and LM13-3% graphite particle composites in die cast and heat treated condition are shown in Fig.5.31. Once again there is a direct relation between time-temperature and applied pressure-wear rate plots. Comparing the time-temperature relationship of die cast and heat treated composites it can be noted that in the case of LM13 die cast alloy the temperature of the pin rose to 140°C at an applied pressure of 2.0 MPa

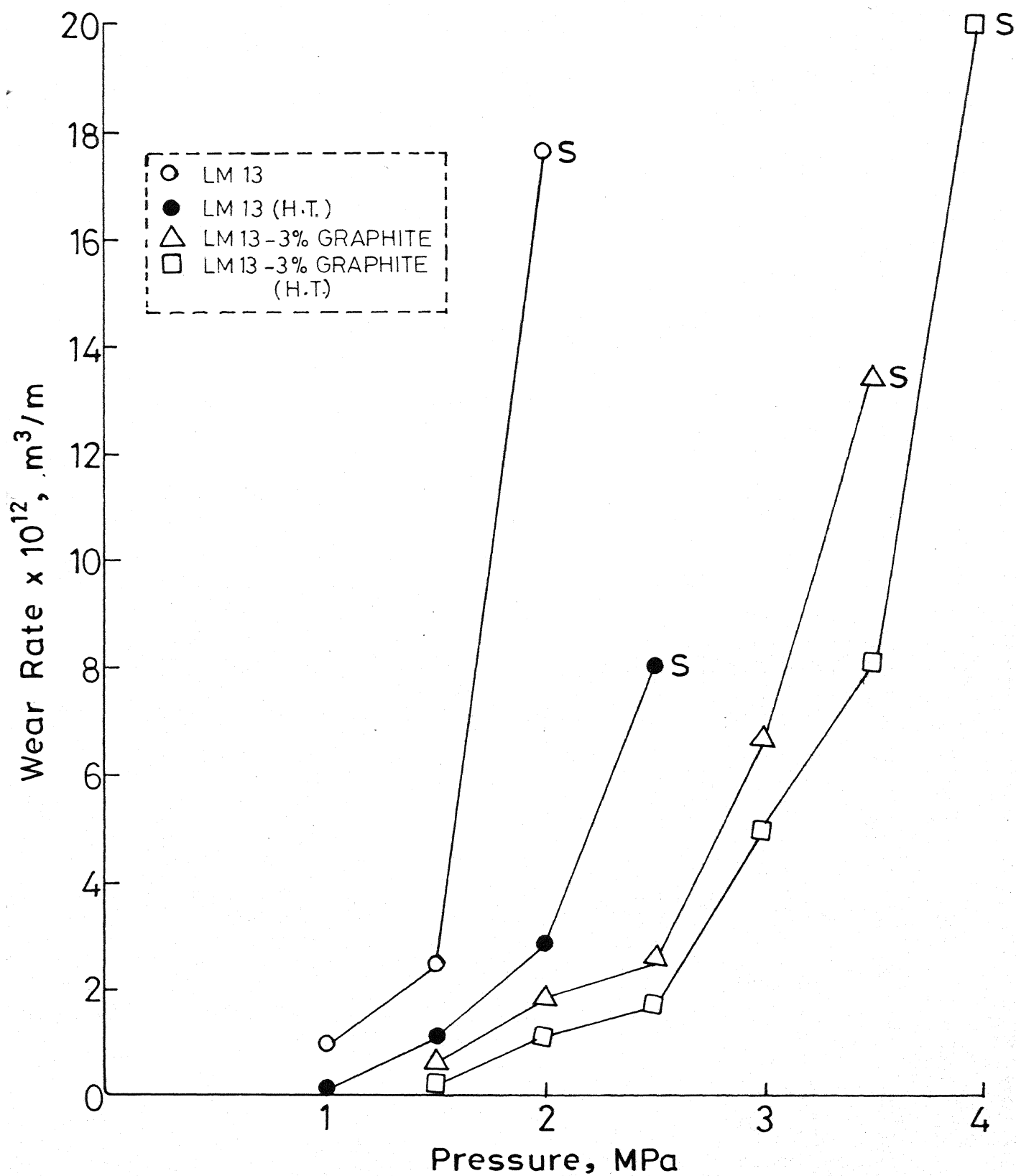


Fig.5.30 Effect of Pressure on the Dry Sliding Wear of LM13 Alloy and LM13-3 wt.% Graphite Particle Composites (Sliding Speed- 2.68 ms^{-1} , S - Seizure)

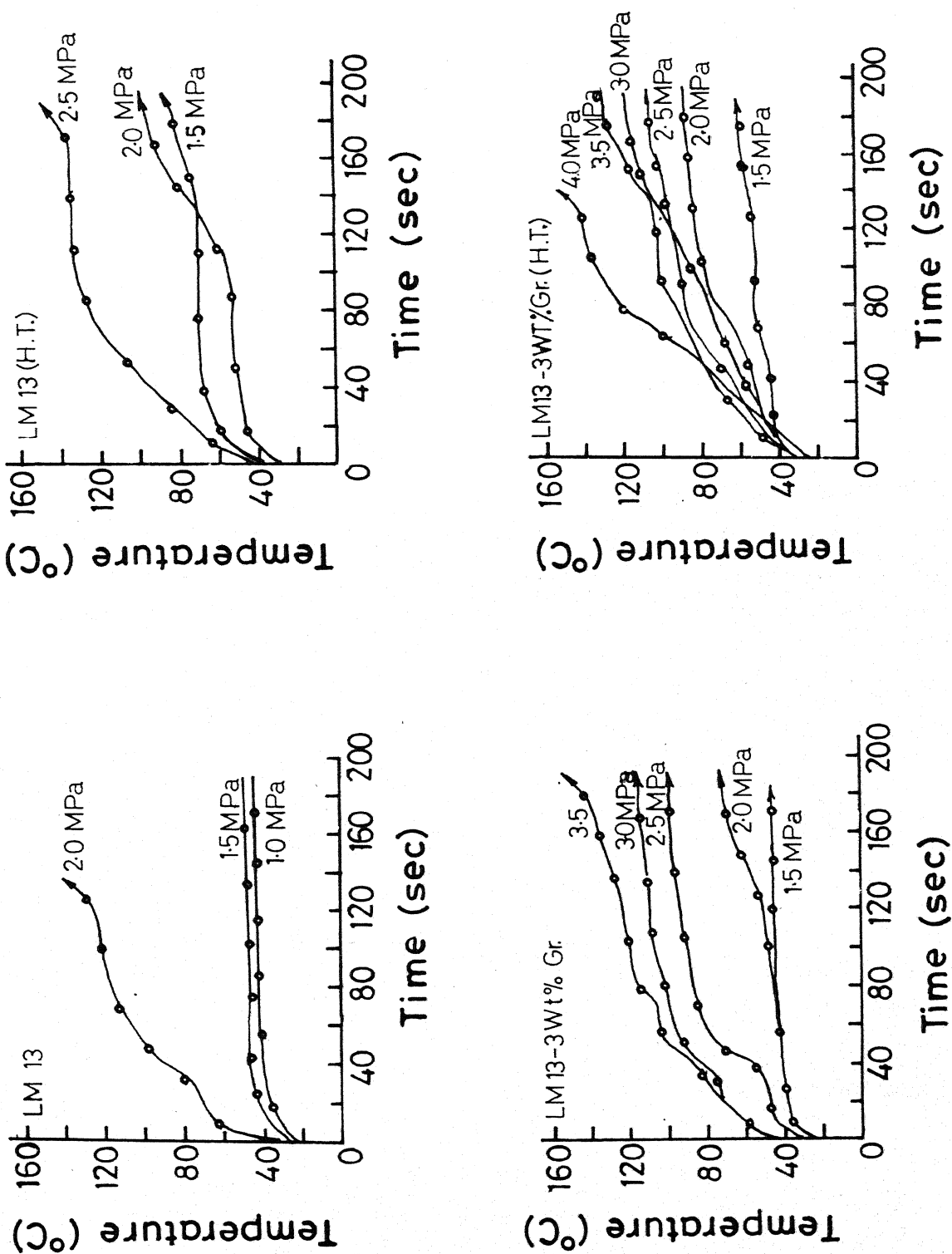


Fig. 5.31 Time-Temperature Relationship of LM 13 Alloy and LM 13-3 wt % Graphite Particle Composites During Dry Sliding Wear.

well before the specified sliding distance. By contrast temperature of the composites specimen in heat treated condition rose to only 90°C at an applied pressure of 2.0 MPa.

5.5.1.4 LM30 and LM30-Graphite Particle Composites

Unlike LM6 and LM13, LM30 is a hypereutectic Al-Si alloy. Silicon in LM30 alloy is present in the form of large cuboids of primary silicon and needle shaped eutectic silicon (Fig.5.12.a). Primary silicon is refined and eutectic silicon is modified by adding phosphorus and sodium in elemental form. In addition, LM30 alloy is also subjected to heat treatment as described in chapter 4.2.3. Matrix alloy as well as composites with different matrix microstructures are subjected to dry sliding wear test as in the previous two cases. The results are shown in Fig.5.32. Comparing the data in Fig.5.25, it can be noted that the performance of die cast LM30 alloy is superior to that of LM6 alloy and LM13 alloy in die cast condition. It is also interesting to note that dispersion of graphite particles resulted in increased wear rates at higher applied pressures. At an applied pressure of 4 MPa, wear rate of die cast composites was found to be $14 \times 10^{-12} \text{ m}^3/\text{m}$ in contrast to that of $6.5 \times 10^{-12} \text{ m}^3/\text{m}$ for the matrix alloy in die cast condition. At this applied pressure the LM30 composite is found to chip near the edges of the sample resulting in enhanced wear. This may be due to low strength of LM30 composite (see Table V.8). Refinement of primary silicon and modification of eutectic silicon resulted in a marginal decrease in wear of the LM30 alloy and graphite containing composites as compared to the die cast structure. It can be seen from Fig.5.32 that optimum wear result is obtained for the composites in heat treated condition. Although the heat treated composites seized at 5 MPa pressure like the other samples, its wear rate is much less than the other samples. For instance, at an applied pressure of 3.5 MPa, the wear rate of die cast LM30 alloy is found $4.8 \times 10^{-12} \text{ m}^3/\text{m}$ whereas, the wear rate is decreased to a value of $3 \times 10^{-12} \text{ m}^3/\text{m}$ in heat treated composites.

Time-temperature plots of LM30 alloy and composites with different microstructure are shown in Fig.5.33. The trend is similar to that observed in

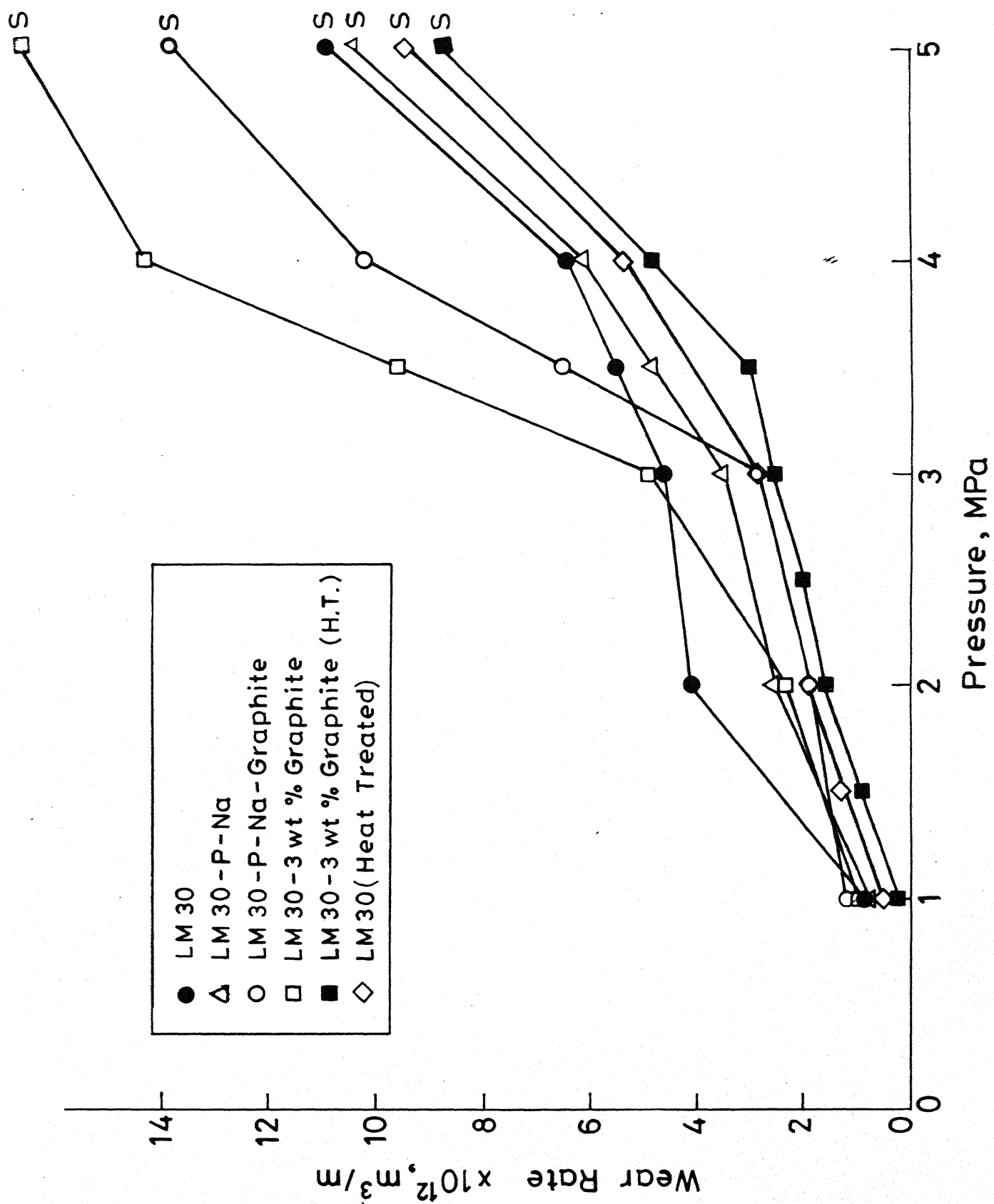


Fig. 5.32 Effect of Pressure on the Dry Sliding Wear of LM 30 Alloy and LM 30 Graphite Particle Composites. Sliding Speed:

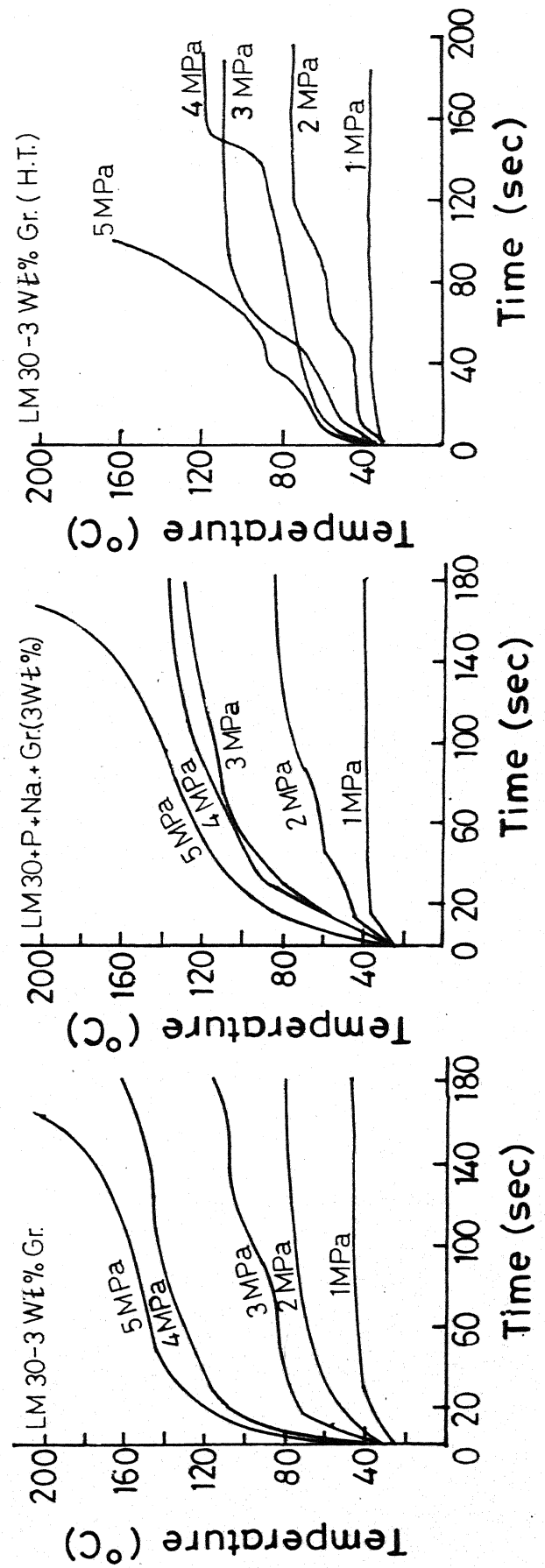
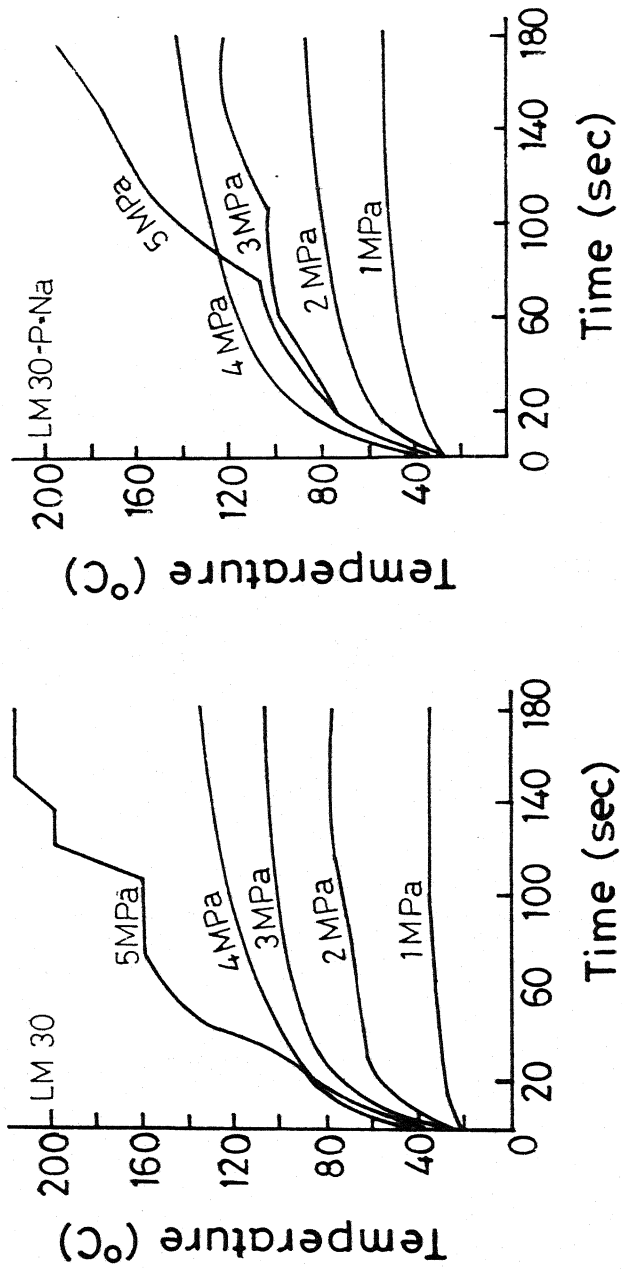


Fig.5.33 Time-Temperature Relationship of LM30 Alloy and LM30-3 wt % Graphite Particle Composites During Dry Sliding Wear

the other two alloys. It can be noted from Fig.5.33 that the maximum temperature rise at 4 MPa is 118°C for the heat treated composites whereas temperature rise in all other samples at 4 MPa ranged from 136 to 162°C.

5.5.1.5 Coefficient of Friction

Frictional force measurements at various applied pressures till seizure are made with the help of a force transducer (schematically shown in Fig.4.2.c); the latter is calibrated using dead weights. The apparatus provides the values of frictional force directly in Newtons. The coefficient of friction is calculated by dividing the frictional force with normal force. Values for the coefficient of friction for the three matrix alloys and their composites in die cast, modified and refined and heat treated conditions are shown in Tables V.10, V.11 and V.12. It can be seen from Tables V.10 and V.11 that the coefficients of friction for two near eutectic alloys namely LM6 and LM13 are very nearly same in die cast condition. However, the coefficient of friction for die cast hypereutectic alloy (LM30) is 28% higher than that of the die cast LM6 alloy. Presence of large primary silicon in hypereutectic (LM30) alloy may be responsible for the increase in the coefficient of friction. There is only marginal decrease of coefficient of friction of matrix alloy due to heat treatment. Similarly, dispersion of graphite had no significant effect on the coefficient of friction while measurement is made on composite surface of die cast condition. By contrast, the coefficient of friction of all the three composites in heat treated condition is reduced by 50%. It is also interesting to note that the coefficient of friction for the graphite dispersed hypereutectic Al-Si alloy is nearly the same as that of neareutectic Al-Si-graphite composites in heat treated condition.

5.5.2 Scanning Electron Microscopic Examination of Worn Surfaces

The worn surfaces of Al-Si alloys and Al-Si-graphite particle composites are studied using scanning electron microscopy with a view to understanding the mechanisms of material removal. The results are presented in the following sections.

**Table V.10 : Coefficient of Friction of LM6 Alloy and Composites
(dry sliding wear)**

Alloy	Normal force (N)	Friction force (N) Range*	Coefficient of friction	Average coefficient of friction
LM6 die cast	50.24	5.5-7.0	0.11-0.14	0.13
	56.52	6.5-8.0	0.12-0.14	0.13
	62.80	7.0-9.0	0.11-0.15	0.13
LM6 (modified)	50.24	4-6	0.08-0.12	0.11
	62.80	6.0-8.0	0.09-0.13	0.12
	75.36	9.0-12.0	0.12-0.16	0.14
LM6 (H.T)	50.24	6.5-8.0	0.13-0.16	0.14
	100.48	8-10.0	0.08-0.10	0.09
LM6-Gra- phite(die cast)	50.24	6.0-8.0	0.12-0.16	0.14
	62.80	6.5-10.0	0.10-0.16	0.14
	75.36	9.0-11.0	0.12-0.15	0.14
LM6-Gra- phite (modified)	50.24	3-5	0.06-0.10	0.09
	75.36	3.5-6.0	0.04-0.08	0.06
	100.48	8-10	0.08-0.10	0.09
	125.60	10-12	0.08-0.09	0.08
LM6-Gra- phite (H.T)	50.24	3-5.5	0.06-0.11	0.09
	100.48	6.0-9.0	0.06-0.09	0.07
	150.72	6.0-8.0	0.04-0.05	0.04

* Three measurements were made at each load.

Table V.11 : Coefficient of friction of LM13 alloy and composites
(dry sliding wear)

Alloy	Normal force(N)	Friction force(N) Range*	Coefficient of friction	Average coefficient of friction
LM13 (die cast)	50	5.0 - 7.0	0.10 - 0.14	0.12
	75	9.0 - 11.0	0.12 - 0.15	0.13
LM13 (Heat Treated)	50	3.0 - 5.0	0.06 - 0.10	0.08
	75	8.0 - 10.0	0.11 - 0.13	0.12
	110	10.0 - 14.0	0.10 - 0.13	0.11
LM13-Graphite	75	8.0 - 10.0	0.11 - 0.13	0.12
	100	9.0 - 12.0	0.09 - 0.12	0.10
	125	9.0 - 11.0	0.07 - 0.09	0.08
	150	13.0 - 16.0	0.09 - 0.11	0.10
LM13-Graphite (Heat Treated)	75	6.0 - 8.0	0.08 - 0.11	0.09
	125	4.0 - 6.0	0.03 - 0.05	0.04
	150	6.0 - 8.0	0.04 - 0.05	0.04

* Three measurements were made at each load.

**Table V.12 : Coefficient of friction of LM30 alloy and composites
(dry sliding wear)**

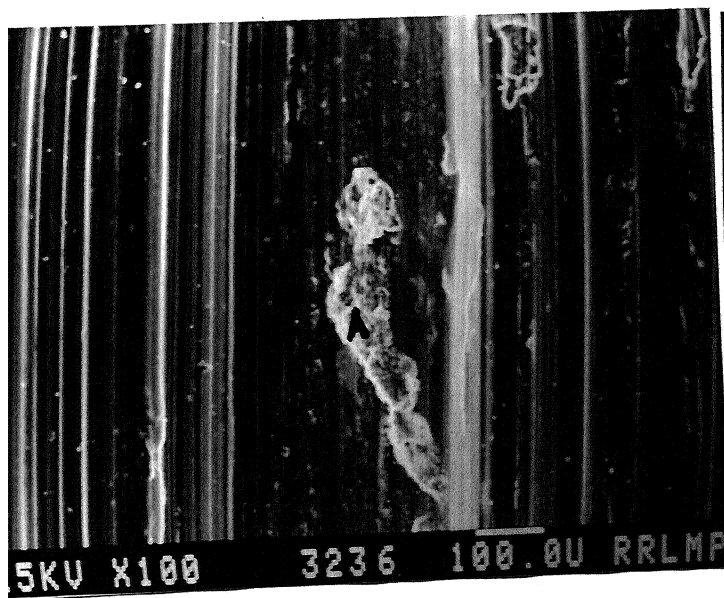
Alloy	Normal force(N)	Friction force(N) Range*	Coefficient of friction	Average coefficient of friction
LM30 (die cast)	50.24	8-10	0.16-0.20	0.18
	100.48	17-19	0.17-0.19	0.18
	150.72	22-25	0.15-0.17	0.16
LM30-P-Na	50.24	8-10	0.16-0.20	0.18
	100.48	14-16	0.14-0.16	0.15
	150.72	19-21	0.13-0.14	0.13
LM30 (Heat Treated)	50.24	7-9	0.14-0.18	0.16
	100.48	13-15	0.13-0.15	0.14
	150.72	19-22	0.13-0.15	0.14
LM30-Graphite	50.24	5-9	0.10-0.18	0.14
	100.48	14-16	0.14-0.16	0.15
	150.72	19-21	0.13-0.14	0.13
LM30-P-Na- Graphite	50.24	8-11	0.16-0.22	0.19
	100.48	11-13	0.11-0.13	0.11
	150.72	21-23	0.14-0.15	0.14
LM30-Graphite (Heat Treated)	50.24	2-5	0.04-0.10	0.07
	100.48	7-9	0.07-0.09	0.08
	150.72	9-11	0.06-0.07	0.06

* Three measurements were made at each load.

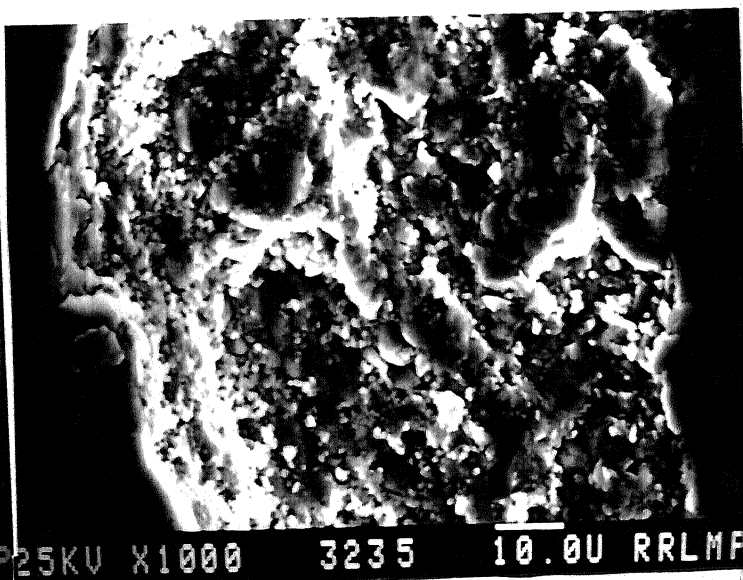
5.5.2.1 LM6 Alloy and LM6-Graphite Particle Composites

Typical scanning electron micrographs of worn surfaces of die cast LM6 alloy are shown in Fig.5.34(a,c). The microstructure is characterised by long and continuous grooves running from one end of the specimen to the other and patches of severely damaged region (position A marked in Fig.5.34.a). A higher magnification micrograph of a typically damaged region (Fig.5.34.b) shows that the damaged portion consists of fine spherical particles of size 2 to 4 μm . Scanning electron micrograph in Fig.5.34.c shows a large number of cracks running longitudinal to the sliding direction as well as in transverse direction. According to Suh (194) subsurface crack nucleation and propagation occurs during sliding contact ultimately resulting in delamination of a portion of the wear surface as per the following description. During sliding wear the normal and tangential loads are transmitted through the contact points by adhesive and plowing action. Plastic deformation induced by constant cyclic loading results in nucleation of cracks below the surface layers. Further loading and deformation cause the propagation of cracks along the sliding direction. The joining of cracks to the wear surface at weak positions will lead to the formation of loose wear particles. The formation of such wear particles by delamination mechanism can be clearly seen in Fig.5.34.c.

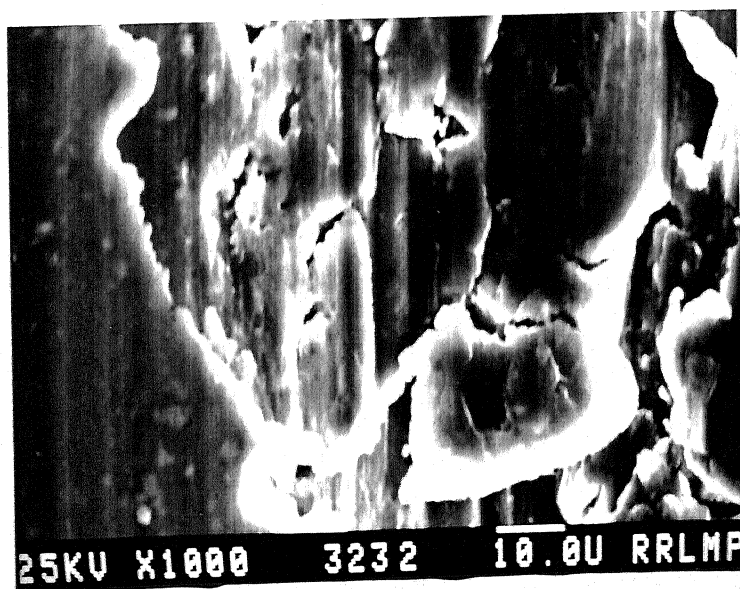
Another interesting feature observed is the transfer of iron from the steel disc to the wear surface of LM6 alloy. Fig.5.35.a shows a wear surface of LM6 alloy. The corresponding X-ray dot mapping of iron is shown in Fig.5.35.b. It is well known that when two dissimilar materials, e.g., Al-Si (LM6) alloy and steel as in the present investigation, slide over each other, the transfer of low yield stress material i.e., LM6 alloy to harder surface takes place, and builds up a layer by adhesion mechanism. However, in the present investigation it appears that iron pick up by aluminium-silicon alloy pin also takes place simultaneously. Sasada et al.(195), based on their observations on copper sliding over ferrous materials, reported that the direction of transfer changed with time. At short sliding distances, copper was transferred to the iron and at longer sliding distances a reversal in behaviour (i.e., transfer of iron to copper) was reported. Shivnath et al. (174) have also reported the transfer of iron from steel disc to the Al-Si wear pin.



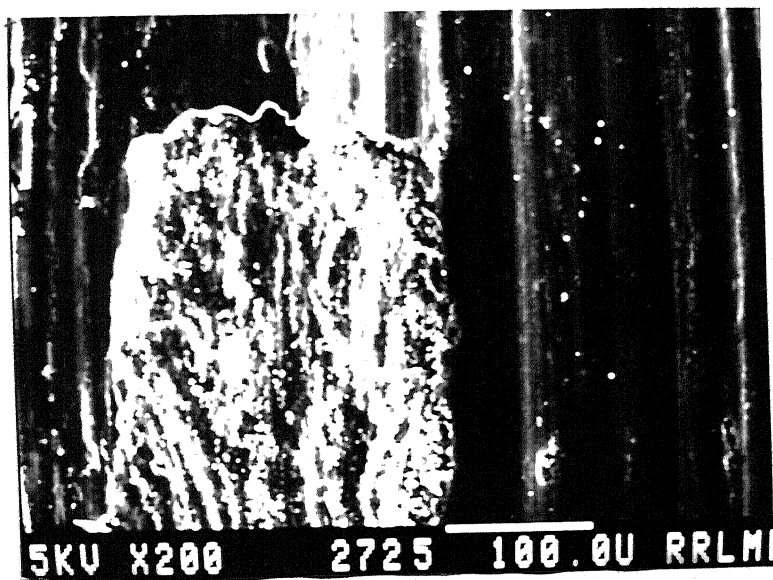
(a)



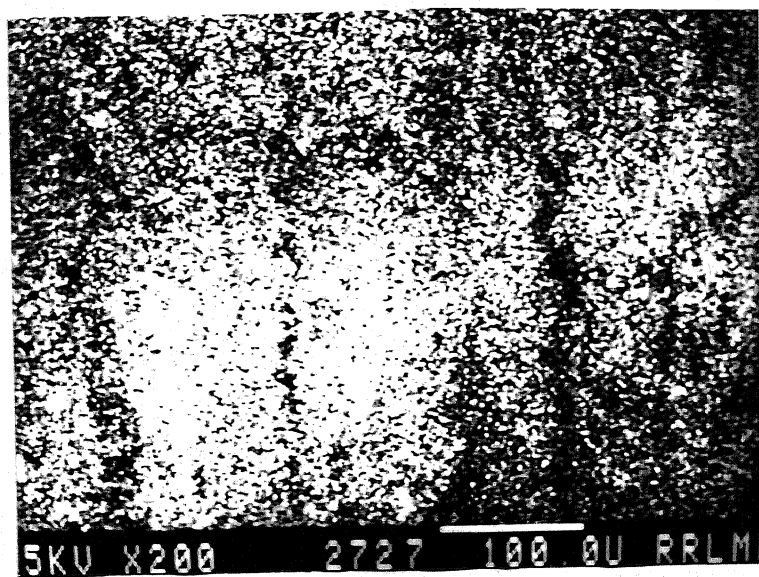
(b)



(c)



(a)



(b)

Wear surfaces of LM6-3% graphite particle composites also show similar pattern as those of LM6 alloy surfaces. As in the previous case, wear surfaces (Fig.5.36.a) show continuous grooves, regions of damaged areas and delamination sheets of material about to delaminate are clearly seen in Figs.5.36.b&c. In some instances, parallel lips are generated along the wear scar as seen in Fig.5.36.d. Modified LM6 alloy and LM6-3% graphite particle composites also exhibited similar wear behaviour as that of the die cast LM6 alloy and composites. However, wear surfaces of heat treated LM6 alloy and LM6-3% graphite particle composites differed significantly as can be seen in the following section.

5.5.2.2 LM13 Alloy and LM13-Graphite Particle Composites

The microstructure of a typical worn surface of diecast LM13 alloy is shown in Fig.5.37.a. This structure consists of continuous grooves and cracked areas. Transverse as well as longitudinal cracks can be clearly seen in the higher magnification micrograph of the worn surface shown in Fig.5.37.b (arrow-marked). Several cracks can be seen joining together at the surface. A wear particle about to be delaminated from the surface due to the joining of such cracks can be seen in Fig.5.37.b (region marked A). Similar observations have been reported for the LM6 alloy (Section 5.5.2.1 and Fig.5.36.b&c).

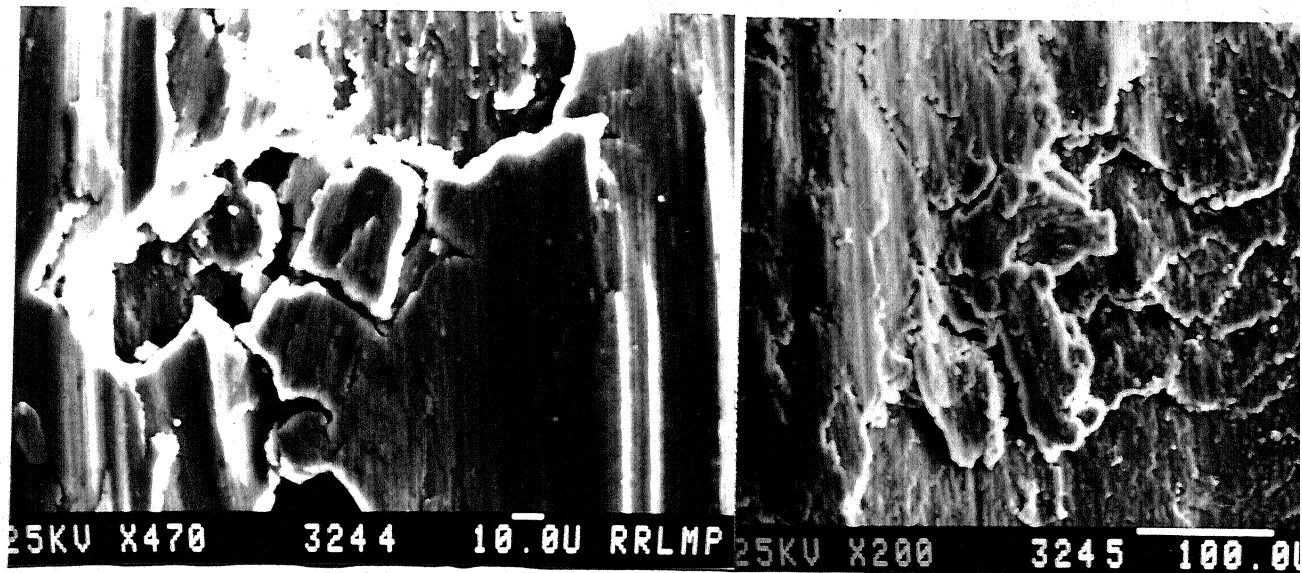
The worn surfaces of LM13-3% graphite particle composites show continuous grooves, damaged regions and presence of surface cracks, Fig.5.38.a. Damaged regions show granular appearance similar to those found on the worn surfaces of LM6 alloy (Fig.5.34.b). Wavelength dispersive X-ray analysis of the worn surface confirms iron pick up by Al-Si alloy pin from steel disc. Parallel lips are seen along the wear scar in some places of the wear surface (Fig.5.38.b). These lips are similar to those found on the worn surface of LM6-3% graphite particle composites. One of the main intentions of dispersing graphite particles in Al-Si alloy matrices is to minimize direct metal to metal contact brought about by the formation of graphite film on the worn surface. But in the present investigation no such graphite film formation on the die cast LM13-graphite and LM6-graphite composite surfaces is found. The absence of graphite film on the wear surfaces is confirmed by wavelength dispersive

Fig.5.36 Micrographs of worn surface of LM6-graphite composites showing: (a) continuous grooves and delaminated region (b) and (c) flaky particles about to detach from the wear surface and (d) parallel lips along the wear scar



(a)

(b)



(c)

(d)

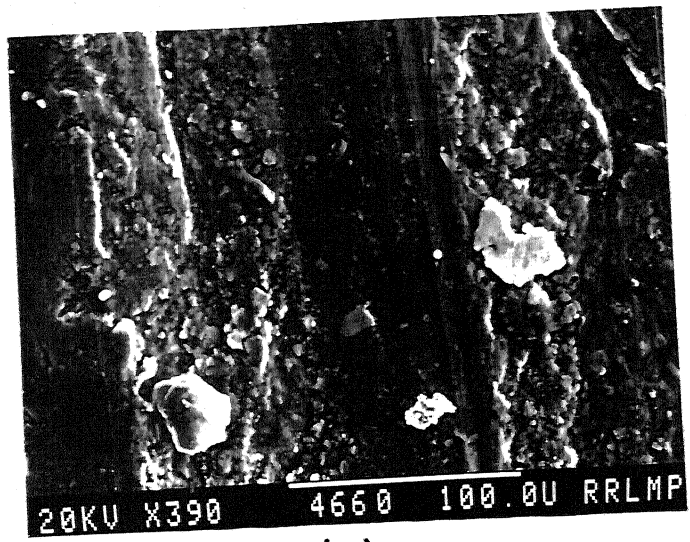
Fig.5.37 Micrographs of worn surface of die cast LM13 alloy showing: (a) continuous grooves and damaged region, and (b) number of cracks joining together to form wear debris



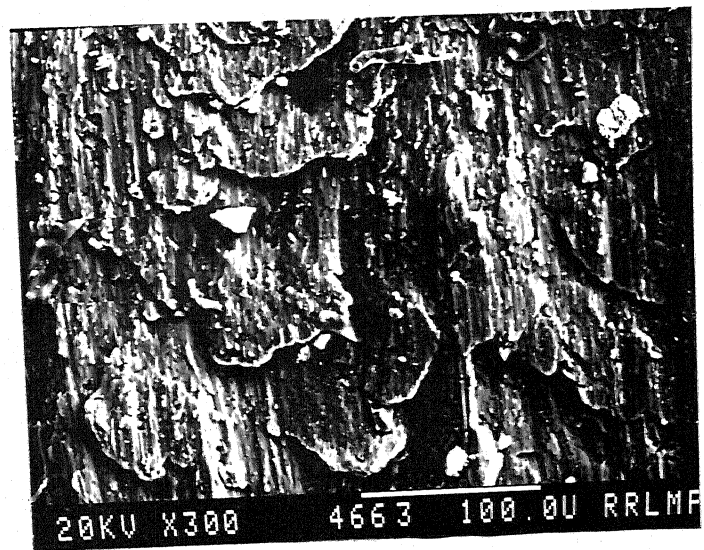
(a)



(b)

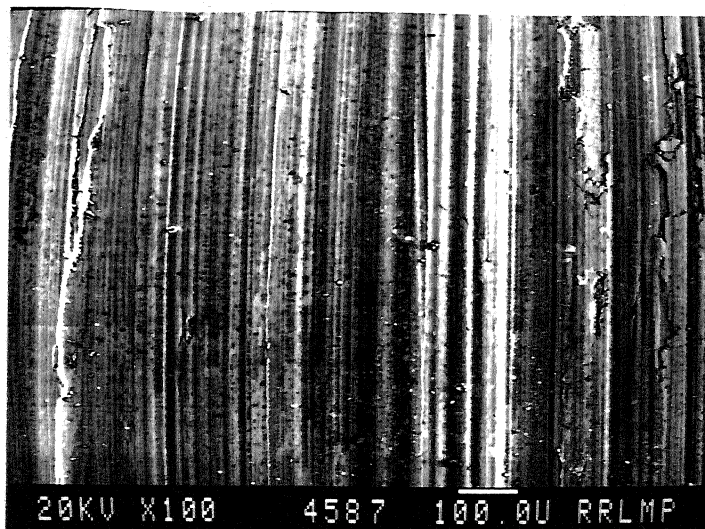


(a)

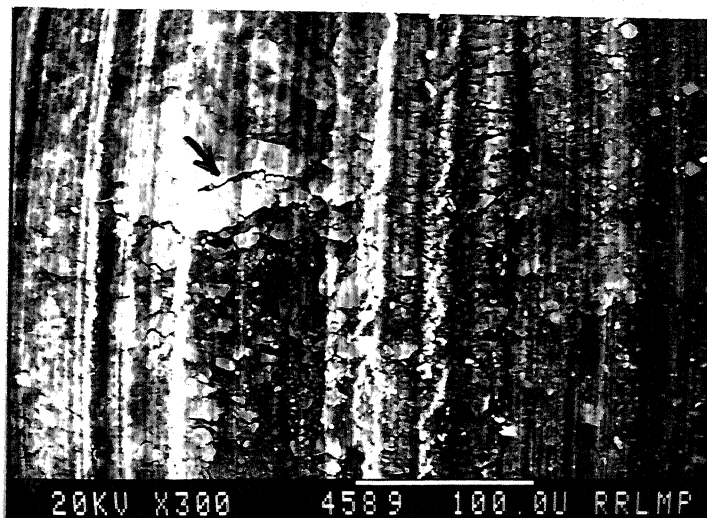


(b)

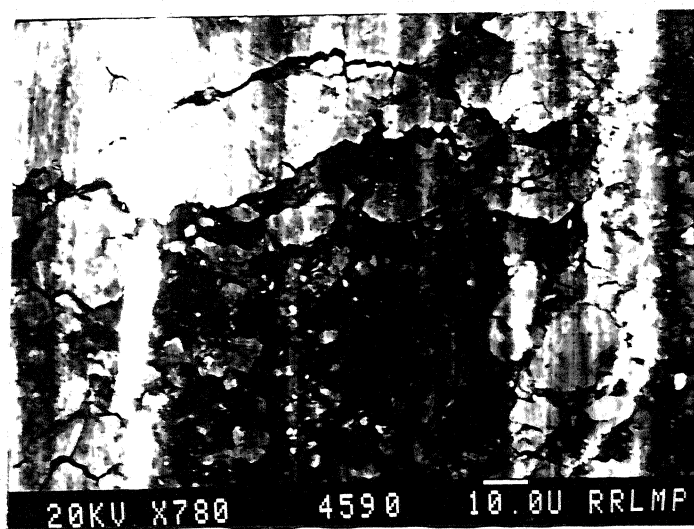
Fig.5.39 Micrographs of worn surface of heat treated LM13 alloy showing: (a) grooves and damaged region (b) transverse cracks and damaged region (c) magnified view of the region marked by arrow in (b) and (d) transverse cracks



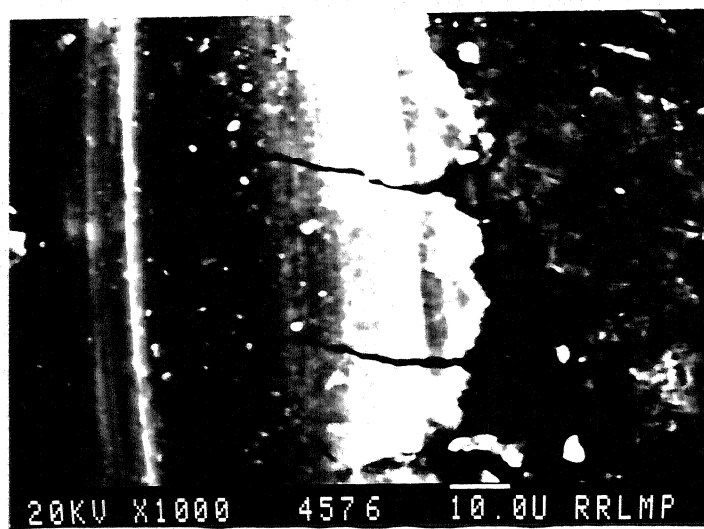
(a)



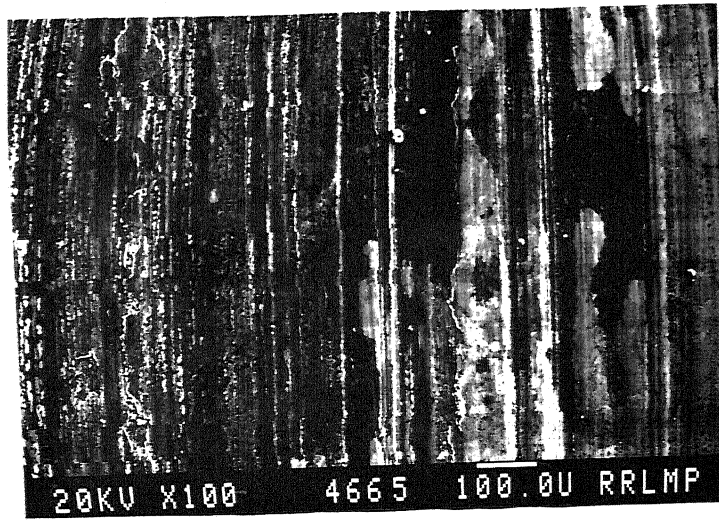
(b)



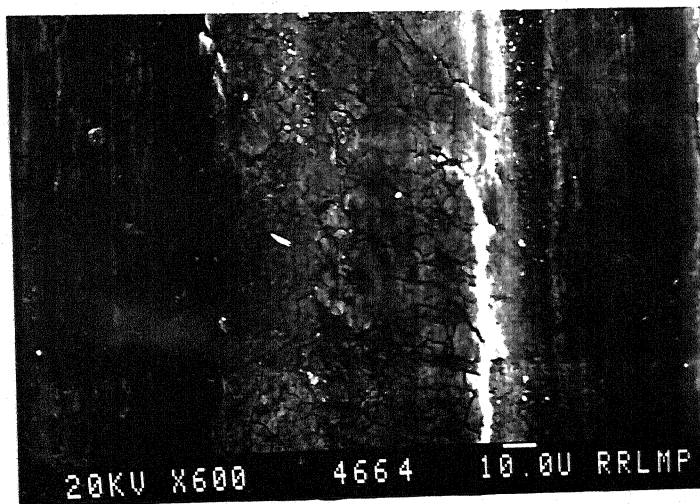
(c)



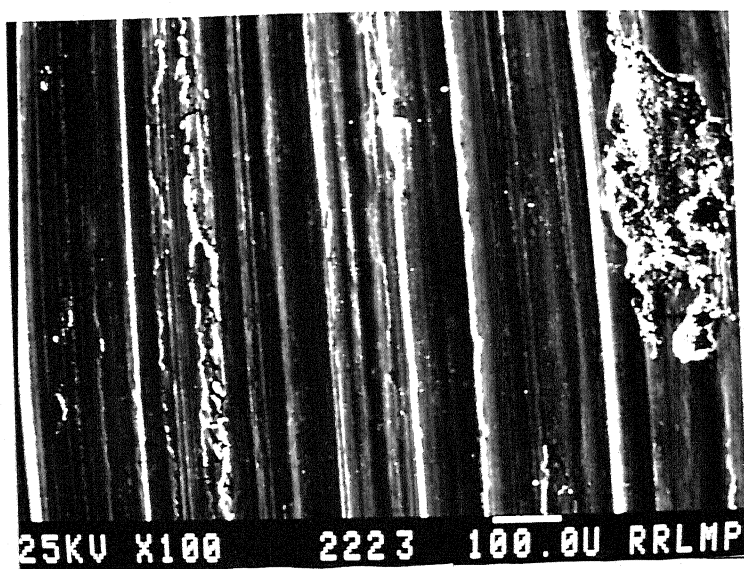
(d)



(a)



(b)



(a)



(b)

(c)

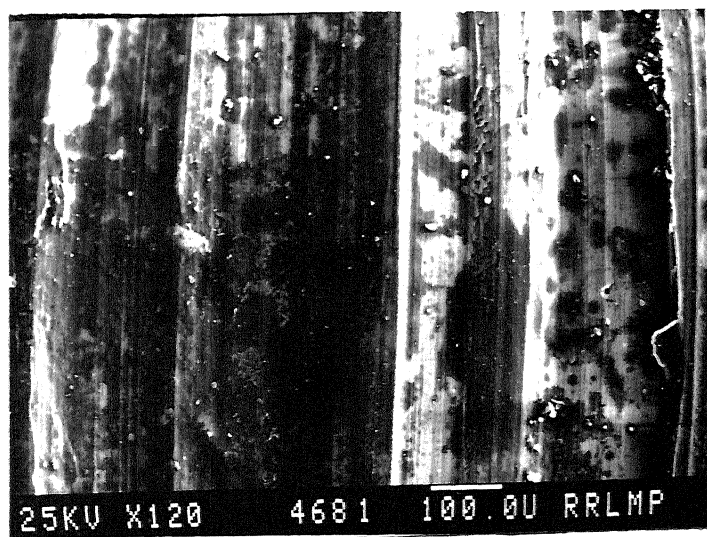
It is worth noting that no evidence for the formation of graphite layer on the die cast composite surfaces is found from wavelength dispersive X-ray analysis. It is reasonable to conclude from the above observations that the material removal mechanisms for die cast LM30, LM30-P-Na and LM30-P-Na-graphite composites are similar. However, heat treated LM30-graphite composite behaves differently from that of die cast LM30 alloy-graphite composites. A representative scanning electron micrograph of worn surfaces of heat treated LM30-graphite composites is shown in Fig.5.42.a and a corresponding wavelength dispersive X-ray dot mapping of carbon in Fig.5.42.b. The micrograph in Fig.5.42.a clearly reveals the presence of graphite layers on the wear surfaces of composite pin, in contrast to die cast composites. It can be noted from Fig. 5.42.a that the entire worn surface was not covered by the graphite layer. Comparing the micrographs in Figs.5.41.a and 5.42.a it can also be noted that the wear surface of heat treated composite is much smoother than that of the unheat-treated composite surface. In the former case there are practically no damaged regions and the grooves are much shallow in nature.

5.5.3 Scanning Electron Microscopic Examination of Wear Debris

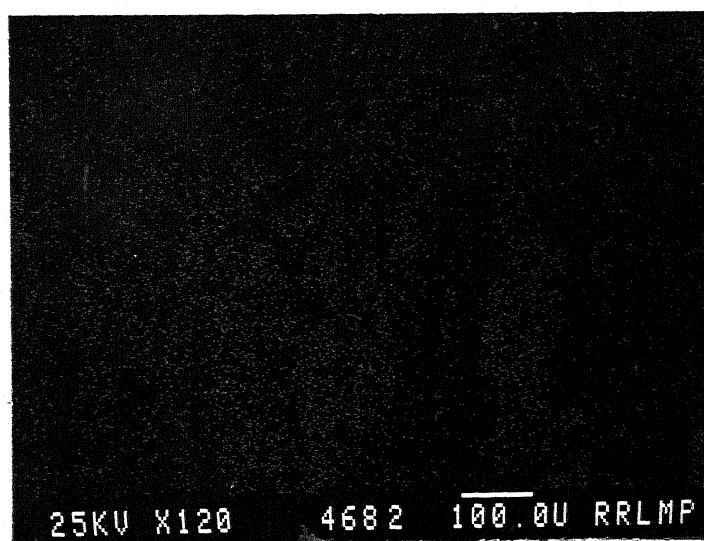
Wear debris particles are mounted on brass studs using a double sided adhesive tape, sputtered with a thin layer of gold and examined in the scanning electron microscope. A range of shape and size of wear debris is found:

(i) small equiaxed particles, (ii) flakes, (iii) sharp-edged faceted particles of silicon and (iv) in some instances machining chips. Detailed description of these various types are given below:

(i) Small equiaxed particles: The first type of debris particle is small and equiaxed. Such particles are found during mild wear regime which occurs at low applied pressure (< 1.5 MPa). Scanning electron micrograph in Fig.5.26.b shows typical small, equiaxed particles collected during the sliding wear of die cast LM6 alloy against a rotating steel disc at an applied pressure of 1.0 MPa and sliding speed of 2.68 m/s. The particle size distribution of equiaxed particle is also shown in Fig.5.27. These debris particles are analysed using wavelength dispersive X-ray analyser and confirmed as aluminium.



(a)

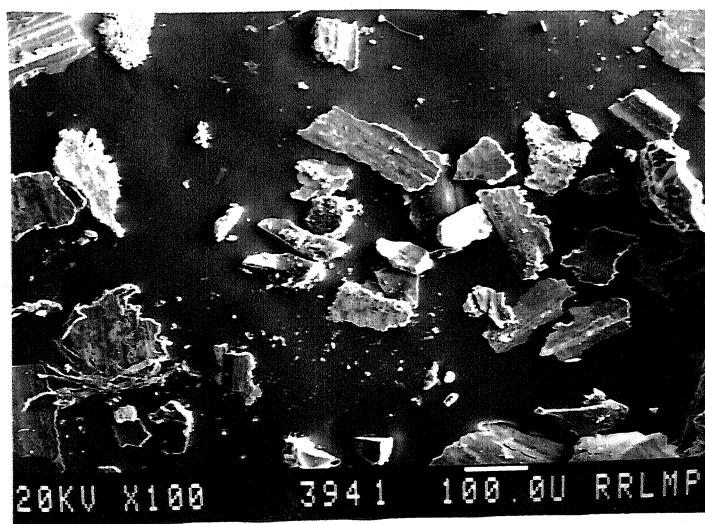


(b)

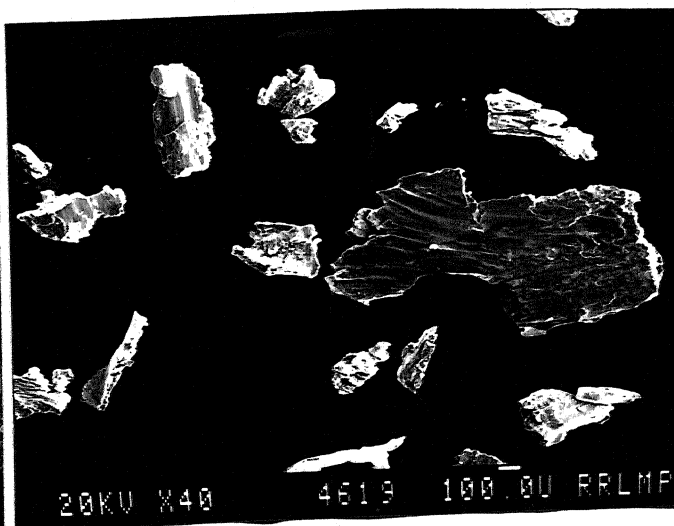
(ii) Flake shaped debris: The second type of debris particles is flake shaped. These particles are commonly found in the severe wear regime at relatively higher pressure. The basic mechanisms involved in the generation of such flake shaped particles are proposed by Suh and coworkers (169) in the form of well known delamination theory of wear, as mentioned in section 5.5.2.1. Fig.5.43.a shows typical flake-shaped particles collected during sliding wear of LM30 alloy at a pressure of 3.0 MPa. In some instances, very big flaky particles are generated (dimensions: 1500 μm long and 650 μm wide) as seen in Fig.5.43.b. The length is defined as that dimension parallel to the sliding direction and is measured parallel to the fine scoring marks on the surface of the debris. These debris are collected during the sliding wear of die cast LM13 alloy. A typical flaky particle generated during the sliding wear of die cast LM13 alloy is shown in Fig.5.43.c; cracks can be clearly seen on this debris particle. The wavelength dispersive X-ray dot mapping corresponding to aluminium is shown in Fig.5.43.d. Presence of silicon in this debris could not ^{be} confirmed by WDXS. Another type of debris particle which is not quite flaky and found in die cast LM13 alloy (Fig.5.44.a is seen to consist of both aluminium and silicon as evidenced by the corresponding X-ray dot maps of aluminium and silicon shown in Figs.5.44.b and 5.44.c respectively.

Fig.5.45.a shows another typical die cast LM6 alloy debris particle. Continuous grooves are seen on the particle surface. The cracks, on the particle surface, are shown by the arrow marks. X-ray dot mapping of Fig.5.45.a corresponding to aluminium is shown in Fig.5.45.b. Another type of LM6 debris particle which is not as thin as those shown ^{is illustrated in} earlier Fig.5.26.d. can be seen in Fig.5.45.c. This debris particle is generated at an applied pressure of 1.5 MPa. Debris particles collected during the sliding wear of heat treated LM13 alloy are shown in Fig.5.46.a. It is worth noting that although the majority of debris are flaky in nature their sizes are relatively small as compared to those found in the case of unheat-treated alloys.

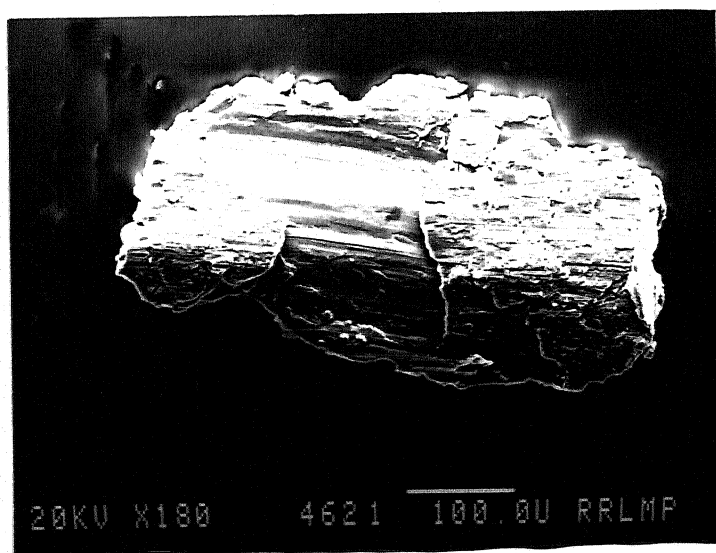
The particle size distribution of flake-shaped wear debris is shown in Fig.5.46 b,c and d. The distribution is represented in the form of histogram. The size distribution of flaky wear debris of die cast LM13 alloy is shown in



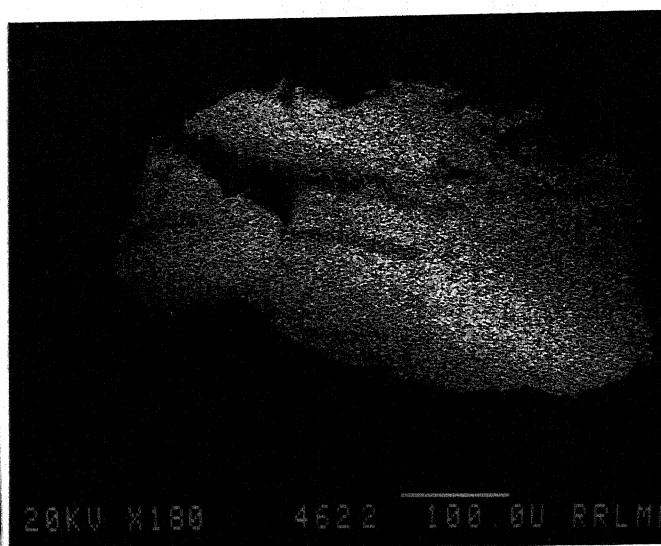
(a)



(b)

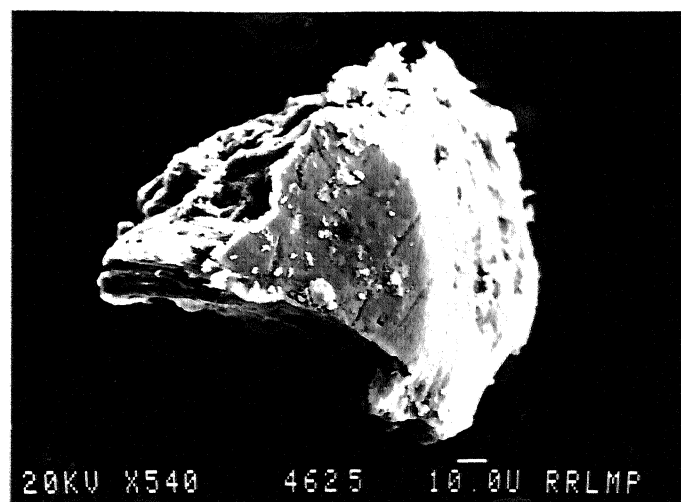


(c)

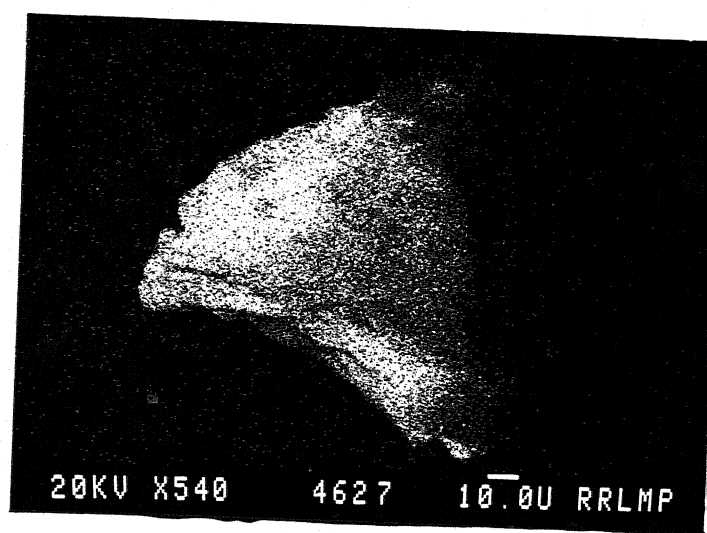


(d)

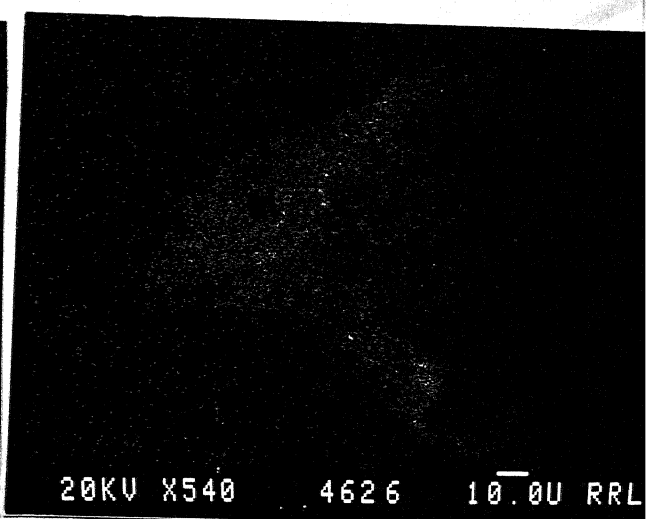
Fig.5.44 (a) Typical debris particle collected from die cast LM13 alloy, (b) aluminium X-Ray mapping and (c) silicon X-Ray mapping



(a)

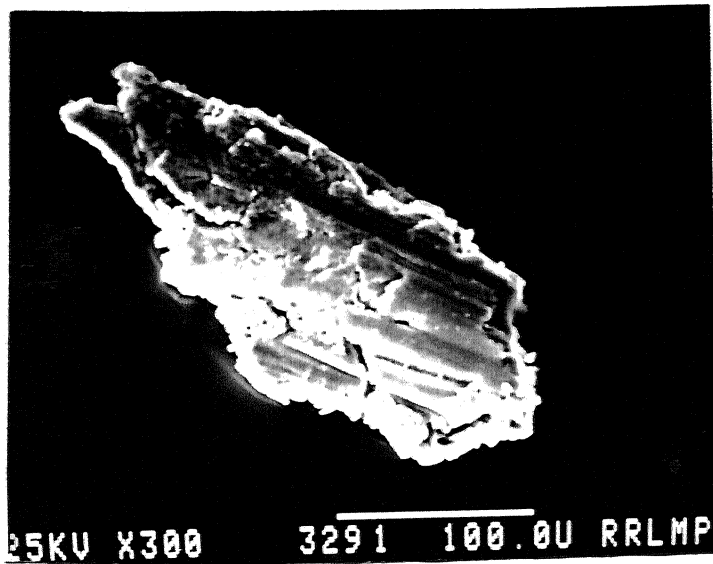


(b)

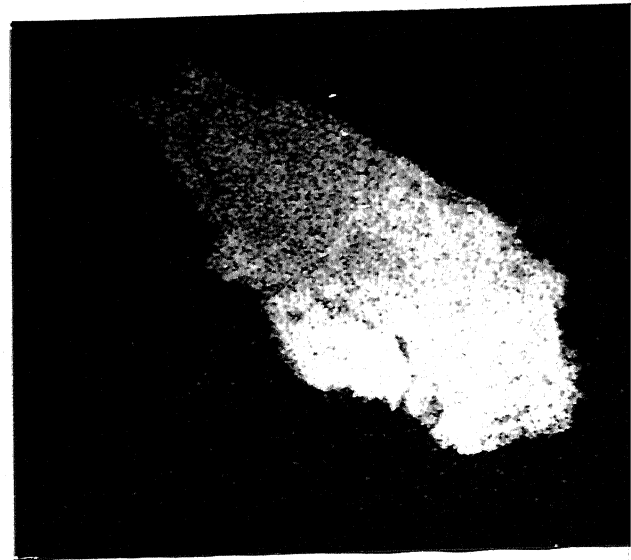


(c)

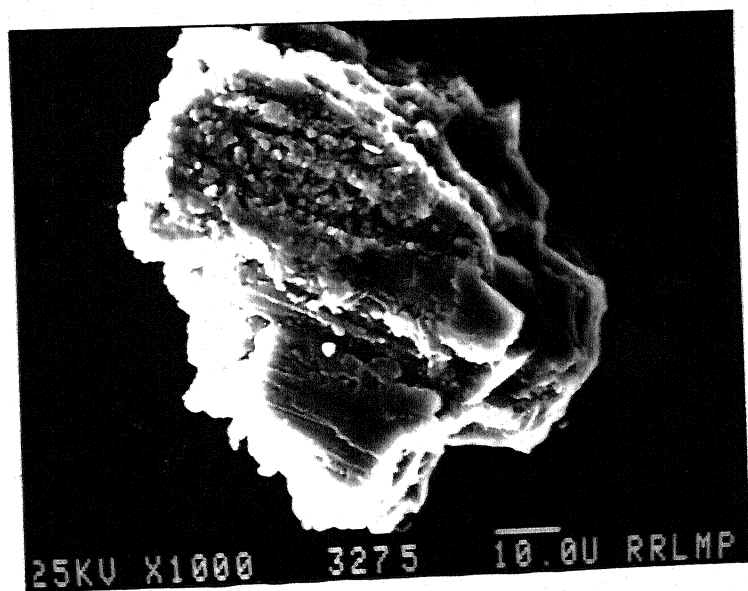
Fig.5.45 (a) Typical flake-shaped debris particle collected from LM6 alloy (b) aluminium X-Ray mapping (c) debris particle collected from LM6 alloy; the thickness of the debris is relatively higher than those shown before



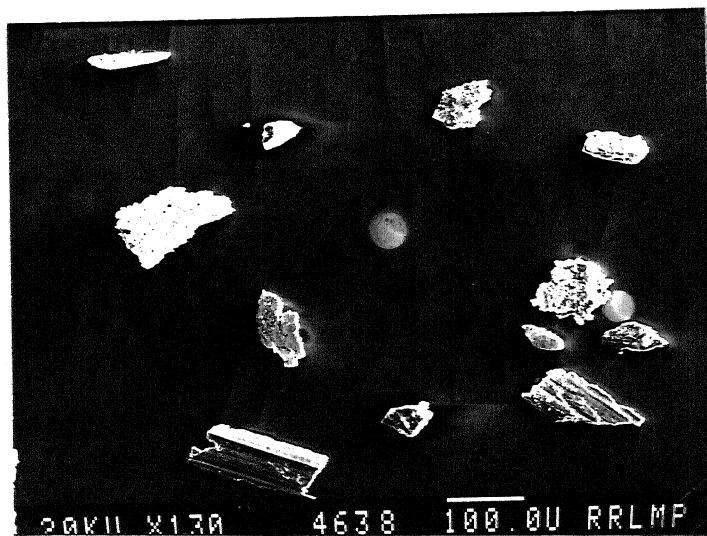
(a)



(b)



(c)



20KV X130

4638

100.0U RRLMP

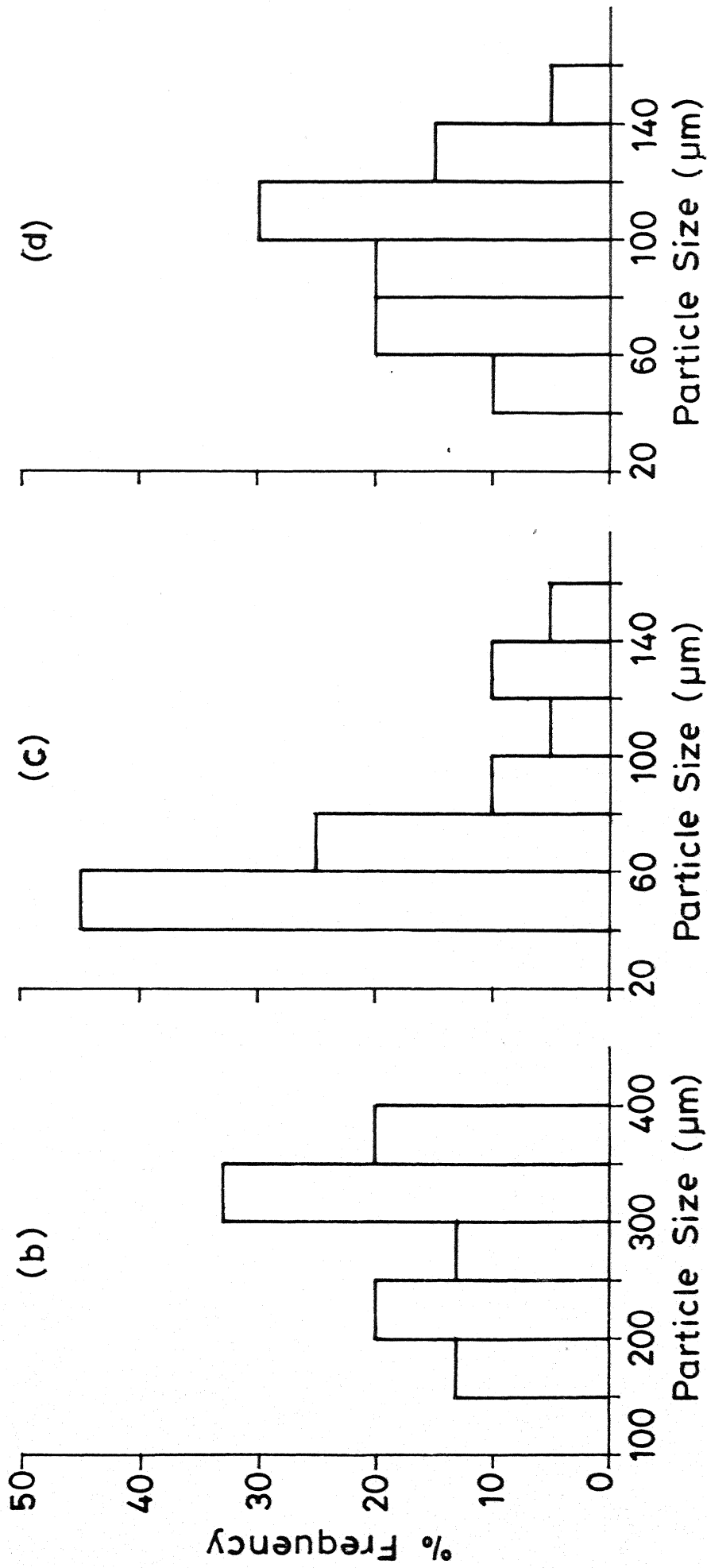


Fig. 5.46 Particle Size Distribution of Flaky Wear Debris obtained from
 (b) Die Cast LM13 Alloy (c) Heat Treated LM13 - Graphite Composite and
 (d) Die Cast LM30 Alloy.

Fig.5.46.b. The histogram (Fig.5.46.b) depicts that the wear debris contains a wide size range from 150 to 400 μm . Around 15% of the particles lie in the size range of 150-200 μm and 35% lie in the range of 200-300 μm and remaining 50% of the particles lie in the size range of 300-400 μm i.e., the major portion of the particles are found in the size range of 300-400 μm . The mean particle size (\bar{x}) and the corresponding standard mean deviation (σ) are calculated and are shown in Table V.13. The average particle size is $289 \pm 66.7 \mu\text{m}$. The size distribution of flaky wear debris of LM13-3% graphite composite in heat treated condition is shown in Fig.5.46.c. It can be seen in the histogram that 45% of the particle lie in the size range of 40-60 μm ; 25% lies in the size range of 60-80 μm and remaining 30% of the particles ^{are} found in the size range of 80-160 μm . This suggests that heat treatment tends to decrease the size of the flaky particles generated during wear test. The mean particle size (\bar{x}) and the corresponding standard mean deviation (σ) are calculated and shown in Table V.14. The mean particle size is $75.5 \pm 31.1 \mu\text{m}$. This indicates that dispersing graphite particle and heat treatment reduced drastically the crack nucleation and propagation and consequently wear sheet formation by delamination mechanism. The particles size distribution of flaky wear debris of die cast LM30 alloy is also shown in Fig.5.46.d. The histogram shows that only 10% of the particle lie in the size range of 40-60 μm and 40% in the size range of 60-100 μm , 30% of the particle lie in the size range of 100-120 μm and 20% in the size range of 120-160 μm . It can be seen that near about 50% of the particles lie in the size range of 100-160 μm . The mean particle size (\bar{x}) and the corresponding standard mean deviation (σ) are calculated and shown in Table V.15. The mean particle size is $97.25 \pm 27.5 \mu\text{m}$.

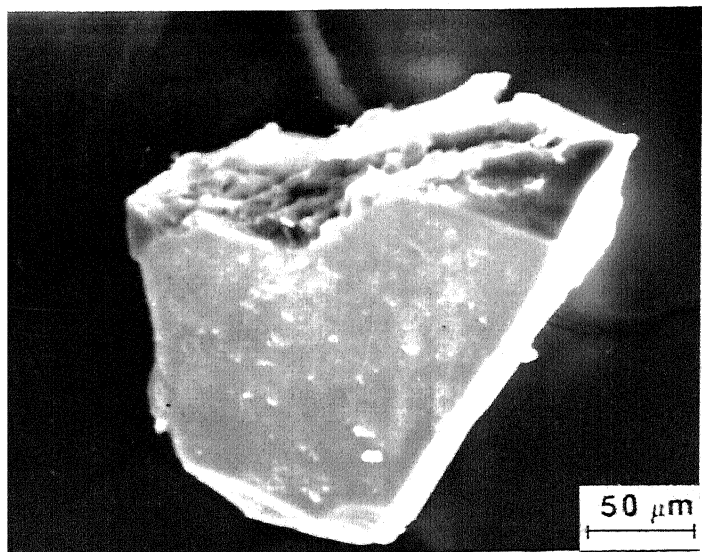
(iii) Sharp-edged faceted particles: The third type of wear debris particle is of the sharp edged faceted morphology. A typical sharp edged faceted particle collected from die cast LM6 alloy at a pressure of 1.5 MPa, is shown in Fig.5.47.a; X-ray dot mapping of this particle corresponding to silicon is shown in Fig.5.47.b. This indicated that during sliding wear, the hard faceted silicon phase is fragmented due to normal and tangential components of the applied pressure. Some more fractured silicon particles can be seen in Figs. 5.47.c and d. These debris are generated during the sliding wear

Table V.13 : Particle size distribution of Flaky Wear Debris of Die Cast LM13 Alloy

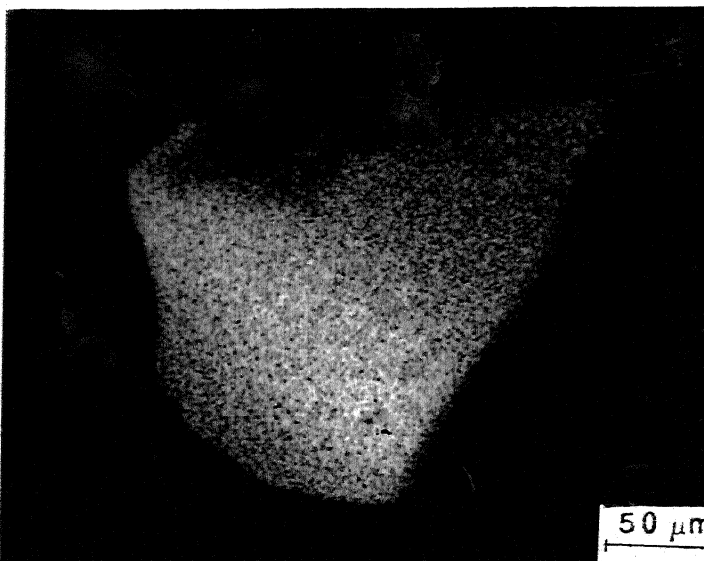
Size range (μm)	% of the total no. of particles	Mean particle size (μm)	Standard Mean deviation (μm)
150-200	13		
200-250	20		
250-300	13	289.0	66.7
300-350	34		
350-400	20		

Table V.14 : Particle size distribution(Flaky Wear Debris)of LM13 Graphite Composite in Heat Treated Condition

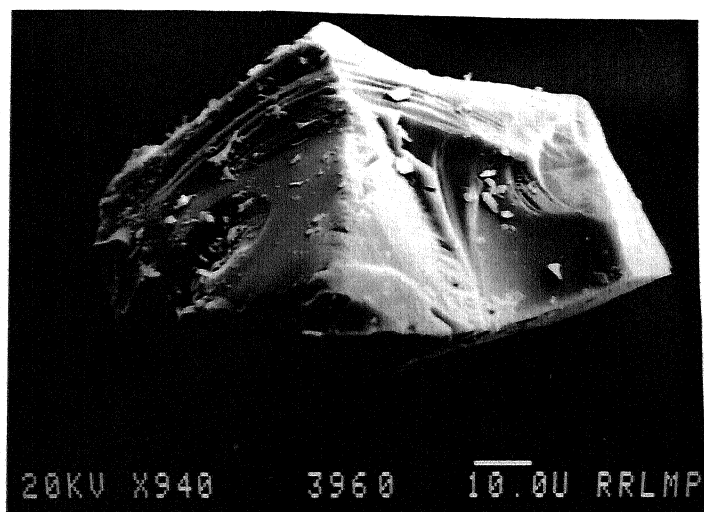
Size range (μm)	% of the total no.of particles	Mean particle size (μm)	Standard Mean deviation (μm)
40-60	45		
60-80	25		
80-100	10	75.5	31.1
100-120	5		
120-140	10		
140-160	5		



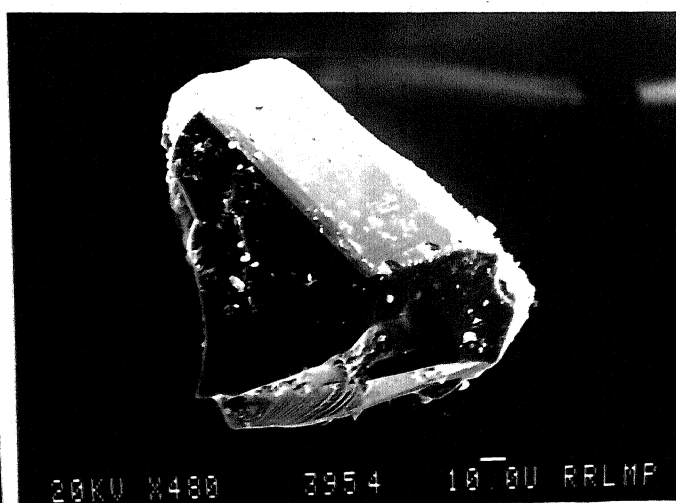
(a)



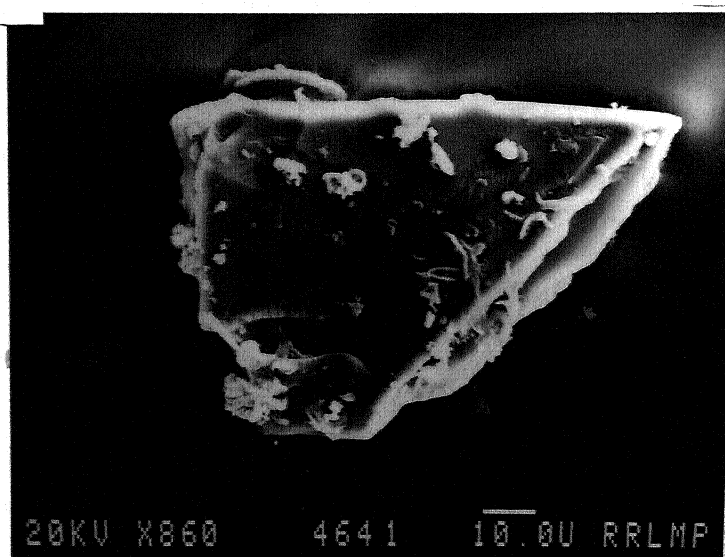
(b)



(c)



(d)



(e)

of die cast LM30 alloy. It has been mentioned in the preceding section that heat treatment of Al-Si alloy markedly alters the morphology of eutectic silicon phase from faceted to more or less spheroidal. However, in some places spheroidization of silicon is incomplete and large faceted silicon phase is left behind. Such particles are fractured during sliding wear and gave rise to sharp edged faceted wear particle in the debris. A typical scanning electron micrograph (Fig.5.47.e shows the fractured silicon particle obtained from heat treated LM13-3% graphite particle composite.

The particle size distribution of sharp edged faceted silicon particles is shown in Fig.5.48. It can be seen from the histogram that fragmented silicon particles lie in the size range of 40-90 μm . Near about 30% of the particles lie in the size range of 40-60 μm and 40% in the size range of 60-70 μm . remaining 30% of particle lie in the size range of 70-90 μm . The mean particle size (\bar{x}) and the corresponding standard mean deviation (σ) are calculated and shown in Table V.16. The average particle size is $66 \pm 12.2\mu\text{m}$.

(iv) Machining chips: The fourth type debris is similar in appearance to machining chips. Such type of debris particles, however, are found occasionally during sliding wear. A typical machining chip collected from the die cast LM13 alloy, is shown in Fig.5.49. Machining chips are characteristically smooth on one surface and serrated marks on the other surface can clearly be seen in Fig.5.49.

5.5.4 X-Ray Diffraction Studies of Wear Debris

Debris particles are analysed with the help of a X-ray diffractometer using Cu-K α radiation in order to identify the phases present. X-ray diffractograms from debris particles in die cast LM30 alloy, LM30-graphite composite in heat treated condition and die cast LM6-graphite composite are shown in Figs. 5.50.a,b and c respectively. The X-ray diffraction results show the presence of aluminium and silicon only. Tables V.17 and V.18 show the diffraction angle (2θ), interplanar spacing (d) and relative intensities along with the standard interplanar spacing obtained from JCPDS files.

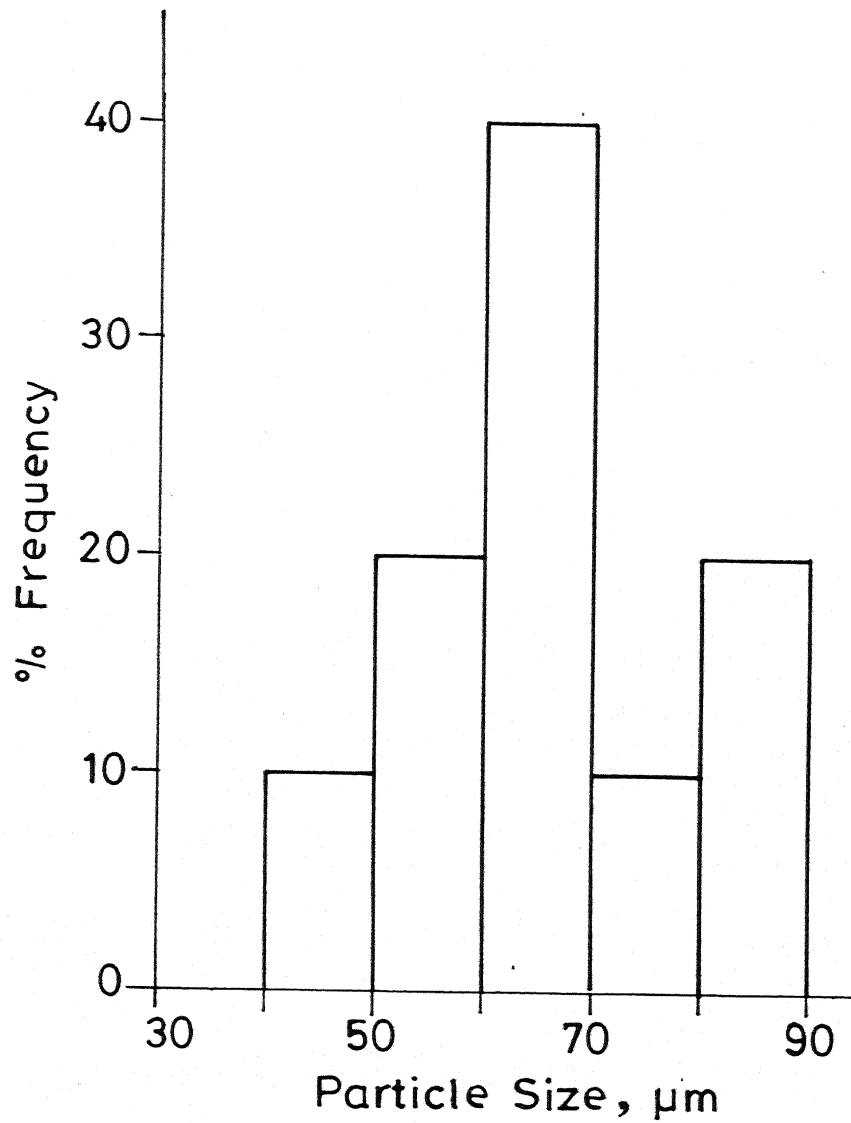


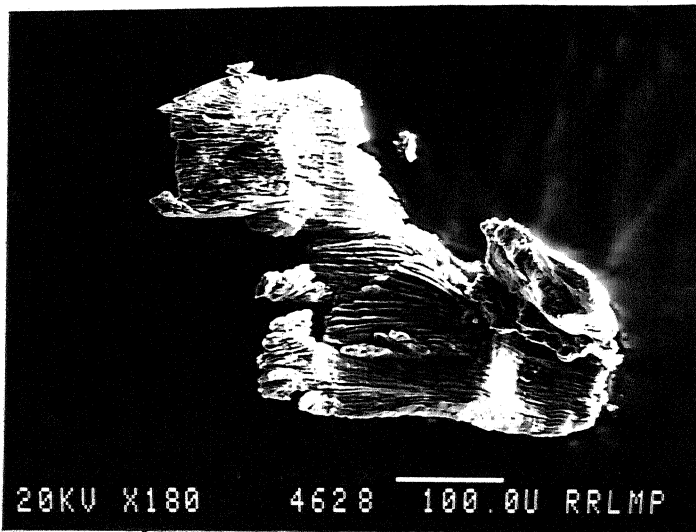
Fig.5.48 Particle Size Distribution of Sharp Edged Faceted Wear Debris Collected from Die Cast LM30 Alloy (Pressure : 3 MPa).

Table V.15 : Particle size distribution of Flaky Wear Debris of Die Cast LM30 Alloy

Size range (μm)	% of the total no.of particles	Mean particle size (μm)	Standard Mean deviation (μm)
40-60	10	97.25	27.54
60-80	20		
80-100	20		
100-120	30		
120-140	15		
140-170	5		

Table V.16 : Particle size distribution of Sharp-Edged Silicon Wear Debris obtained from Die Cast LM30 Alloy

Size range (μm)	% of the total no.of particles	Mean particle size (μm)	Standard Mean deviation (μm)
40-50	10	66.0	12.2
50-60	20		
60-70	40		
70-80	10		
80-90	20		



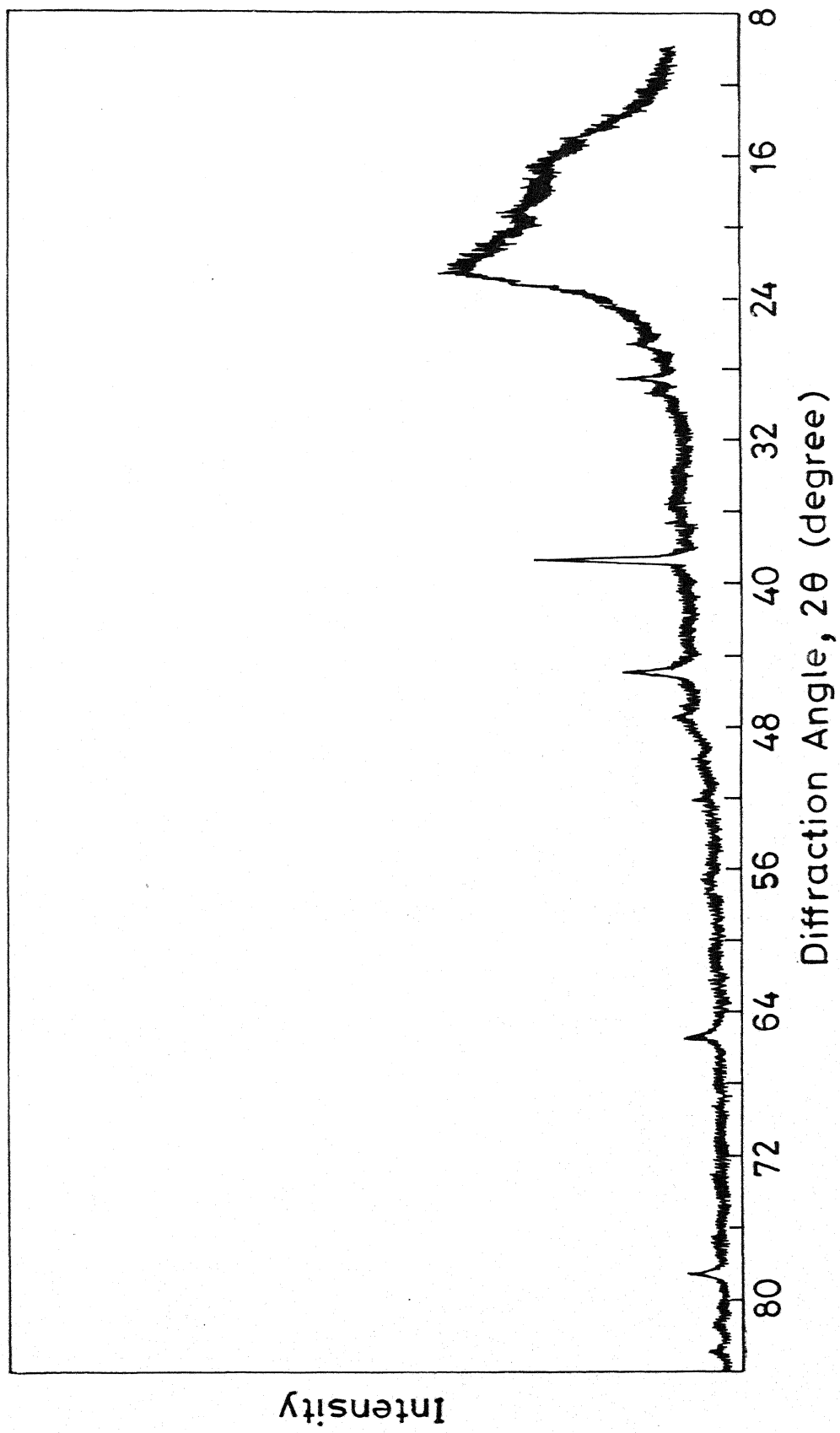


Fig. 5.50 (a) X-Ray Diffraction Trace of Wear Debris of Die Cast LM30 Alloy (Pressure: 4.5 MPa).

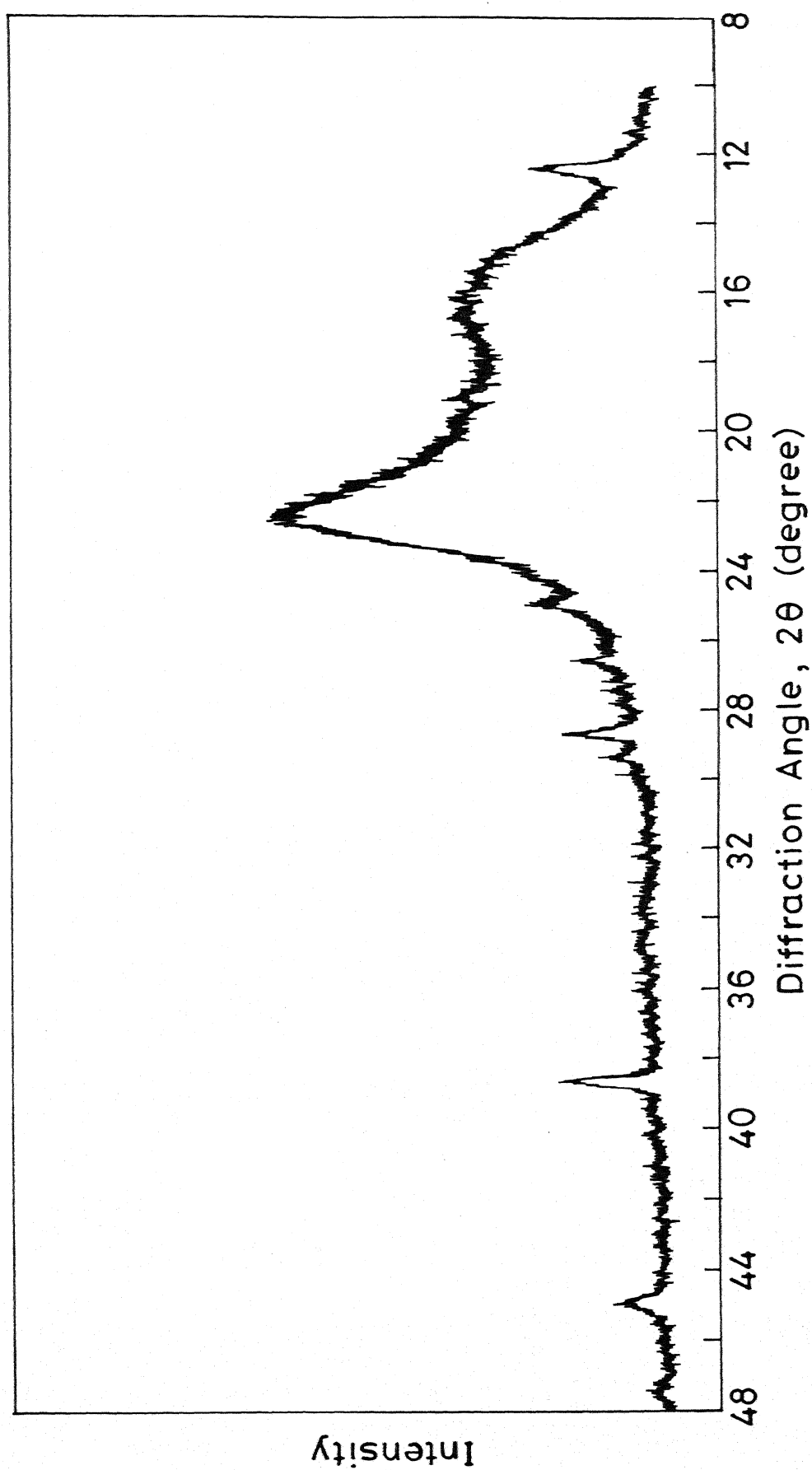


Fig. 5.50(b) X-Ray Diffraction Trace of Wear Debris of Heat Treated LM30-3 wt. % Graphite Composite (Pressure : 4 MPa)

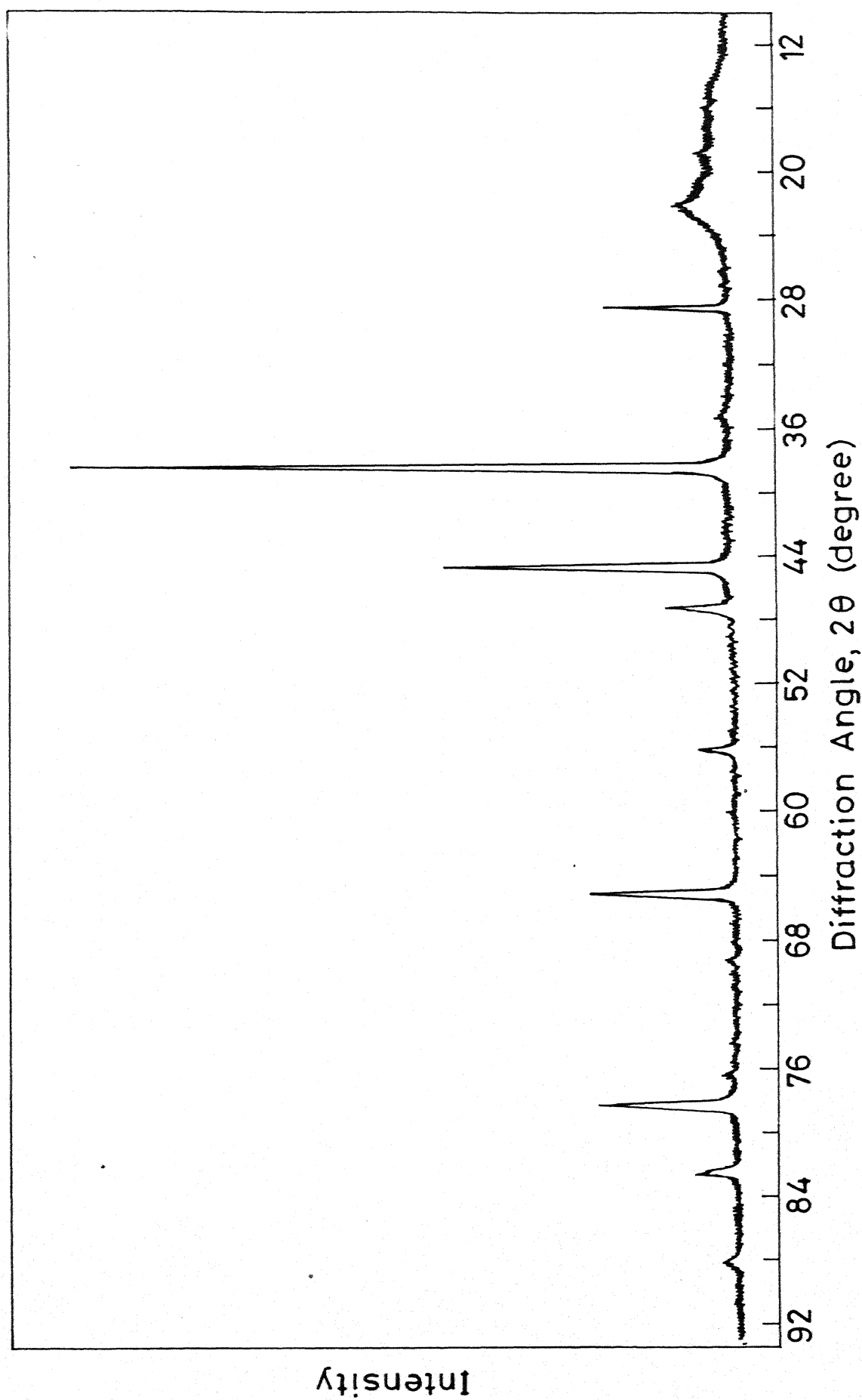


Fig. 5.50(c) X-Ray Diffraction Trace of Wear Debris of Die Cast LM6-3 wt.% Graphite Composite (Pressure : 2MPa)

Table V.17 : X-Ray Diffraction Results of Wear Debris (Die cast LM30 Alloy)

PARAMETERS					
Voltage Current Scanning speed Target Material Wavelength of X-radiation (Cu-K α) Recorder Full Scale Recorder speed			40 KV 20 mA 0.02 °2 θ /Sec Copper 1.5418 (Å) 2000 2 cm/°2 θ		
Diffraction angle 2 θ (degree)	Interplanar spacing d (Å)	Intensity	From Standard data card (JCPDS file)		
			Interplanar spacing d (Å)	Planes (hkl)	Phases
28.67	3.113	Strong	3.135	(111)	Silicon
38.71	2.326	Very Strong	2.338	(111)	Aluminium
44.95	2.016	Strong	2.024	(200)	Aluminium
47.52	1.913	Weak	1.920	(220)	Silicon
65.28	1.429	Weak	1.432	(220)	Aluminium
78.43	1.219	Very Weak	1.221	(311)	Aluminium

Table V.18 : X-Ray Diffraction Results of Wear Debris (Heat Treated LM30-Graphite and LM6-Graphite)

LM30-Graphite (Heat Treated)		LM6-Graphite		From Standard data card(JCPDS Files)	
PARAMETERS					
Voltage	40 KV				
Current	20 mA				
Scanning speed	0.02 °2θ/Sec				
Target Material	Copper				
Wavelength of x-radiation (Cu-Kα)	1.5418 (Å)				
Recorder Full Scale	2000				
Recorder speed	1 cm/°2θ				
Diffraction Angle, 2θ (degree)	Interplanar Spacing, d (Å)	Diffraction angle, 2θ (degree)	Interplanar spacing, d (Å)	Planes (hkl)	Phases
28.63	3.117	28.52	3.129	(111)	Silicon
38.62	2.330	38.60	2.332	(111)	Aluminium
44.84	2.021	44.84	2.021	(200)	Aluminium
		47.42	1.916	(220)	Silicon
		56.23	1.635	(311)	Silicon
65.24	1.430	65.22	1.430	(220)	Aluminium
78.48	1.218	78.33	1.220	(311)	Aluminium
		82.48	1.169	(222)	Aluminium

The diffuse peak seen in the initial range of the diffraction angle of the diffractograms is due to the adhesive tape on which the wear particles are mounted. A typical diffractogram of adhesive tape is shown in Fig.5.50.d. The detection of iron on the debris surfaces is difficult from the observation of angular positions of diffraction peaks, since all the low index peaks of iron overlap with the peaks from aluminium. No evidence for the presence of intermetallic phases in the debris particles is seen by X-ray diffraction. It has not been possible to establish the presence of intermetallic phases in the debris particles from X-ray diffraction studies.

5.5.5 Scanning Electron Microscopic Examination of Subsurface

The subsurface region of a dry sliding wear surface is studied with increasing interest because the surface wear is influenced by subsurface deformation to a great extent as proposed by Suh and coworkers (169) in delamination theory of wear. With a view to investigate the subsurface structure, the wear pin is sectioned perpendicular to the worn surface. The sectioned surface is cold mounted and mechanically polished using standard metallographic procedure and observed in scanning electron microscope. The detailed description of the experimental procedure is described in chapter 4 and the results are shown below.

A typical scanning electron micrograph Fig.5.51.a shows subsurface structure of die cast LM30 alloy. The sample is run at a sliding speed of 2.68 m/s at a pressure of 3 MPa. It can be clearly seen from Fig.5.51.a that the plate-shaped eutectic silicon is fragmented into fine equiaxed particles of average size below 5 μm . The heavily deformed layer is extended upto a distance of 60 μm below the sliding surface. It is also to be noticed that the microstructure in the subsurface region changes gradually from the heavily deformed one immediately below the sliding surfaces to the one corresponding to the bulk structure. In some instances, the large primary silicon is also seen to be fragmented under the influence of normal and tangential stresses introduced during sliding. Fig.5.51.c. shows a typical scanning electron micrograph of the subsurface region of LM13-3% graphite particle composite. The wear test in this case is carried out at an applied pressure of 2.0 MPa.

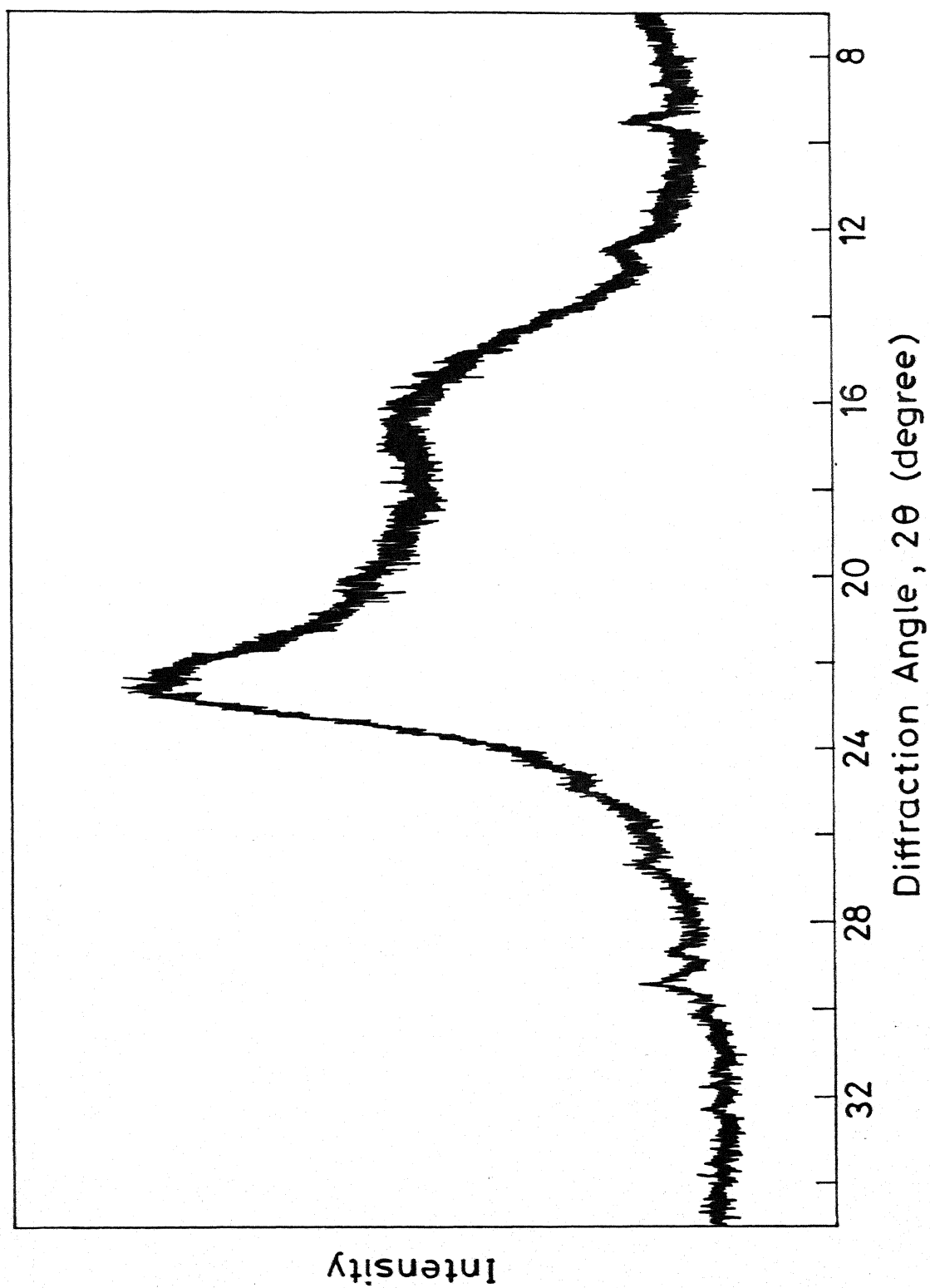
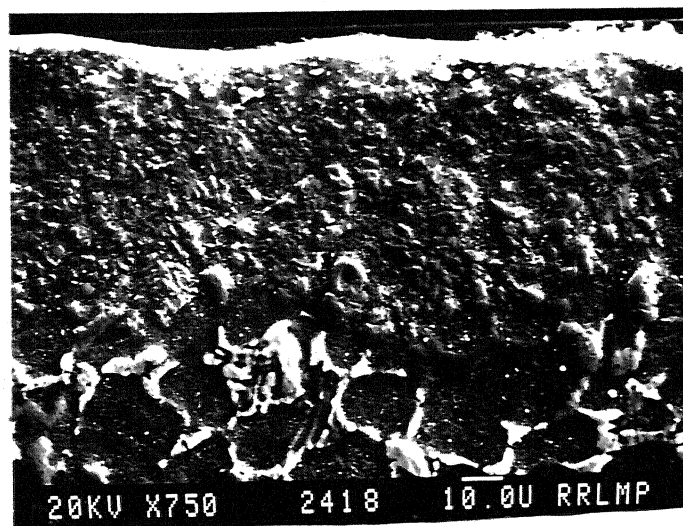
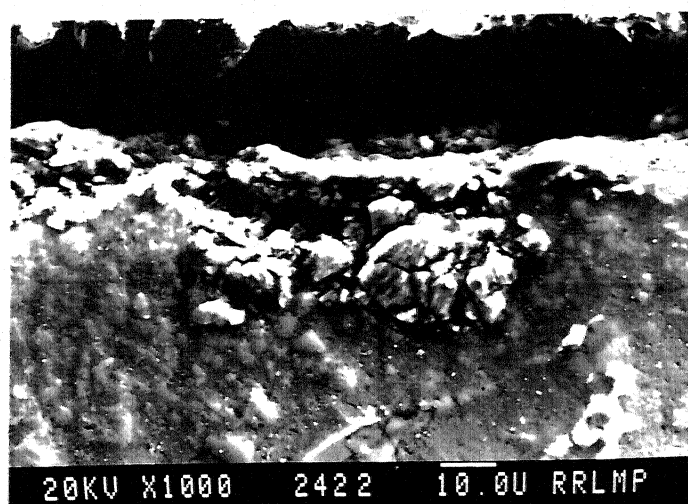


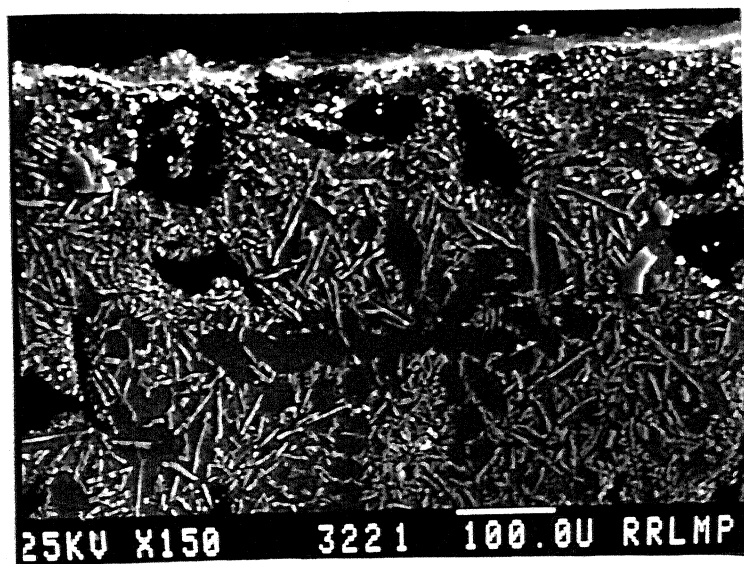
Fig. 5.50 (d) X-Ray Diffraction Trace of Adhesive Tape.



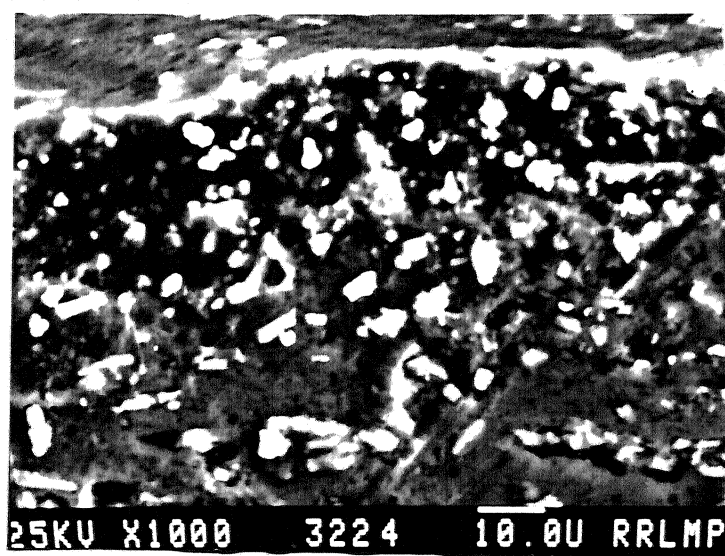
(a)



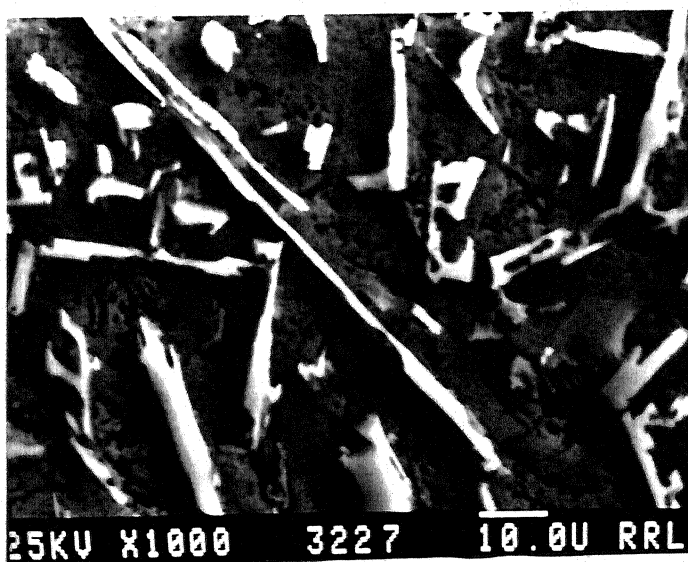
(b)



(c)



(d)



(e)

It clearly shows fractured eutectic silicon, dispersion of graphite particles and matrix microstructure. The fragmentation of plate-shaped eutectic silicon into fine equiaxed particles is clearly seen in a magnified picture (Fig.5.51.d). The deformed layer is extended upto a distance of 60 μm from the sliding surface. The unaffected eutectic silicon is also seen in Fig.5.51.e. Rohatgi and Pai (45) have reported that in aluminium-graphite system, the extensive deformation at the surface results in deformation and fragmentation of the surface and subsurface graphite particles. However, the present results have not shown any such fragmentation of graphite particles (Fig.5.51.c).

5.5.6 Partially Lubricated Sliding Wear

The conventional way of rating the performance of a material for bearing application is in terms of its P-V limits i.e., the maximum allowable bearing pressure (P) at a particular speed (V). P-V limits of a particular bearing alloy are determined by excessive wear caused either due to heavy loads approaching the elastic limit or due to thermal softening. The P-V limits of Al-Si alloys and composites are evaluated in partially lubricated condition using a Cameron-Plint pin-on-disc wear test machine.

All lubricated wear tests are carried out at sliding distances upto 2500 m. Disc rotation is first fixed at 330 RPM (corresponding sliding velocity: 1.38 m/s). A pressure of 1.0 MPa is applied to the specimen and the test is run for 2500 m. If the sample did not seize at this pressure the disc is removed, cleaned, reimmersed in SAE 30 oil, excess oil removed and the applied pressure is increased in steps of 0.5 MPa. By this means a critical applied pressure is determined where seizure occurred within a sliding distance of 2500 m. Complete details of the experimental procedure are given in the previous chapter and the results are given in the following sections.

5.5.6.1 P-V Limits of Die cast LM6, LM13 and LM30 Alloys

The P-V limits for die cast LM6, LM13 and LM30 alloys sliding against steel disc are shown in Fig.5.5 2. Each point in the Fig.5.52 represents the seizure load (bearing pressure) at a particular velocity i.e., the limiting values

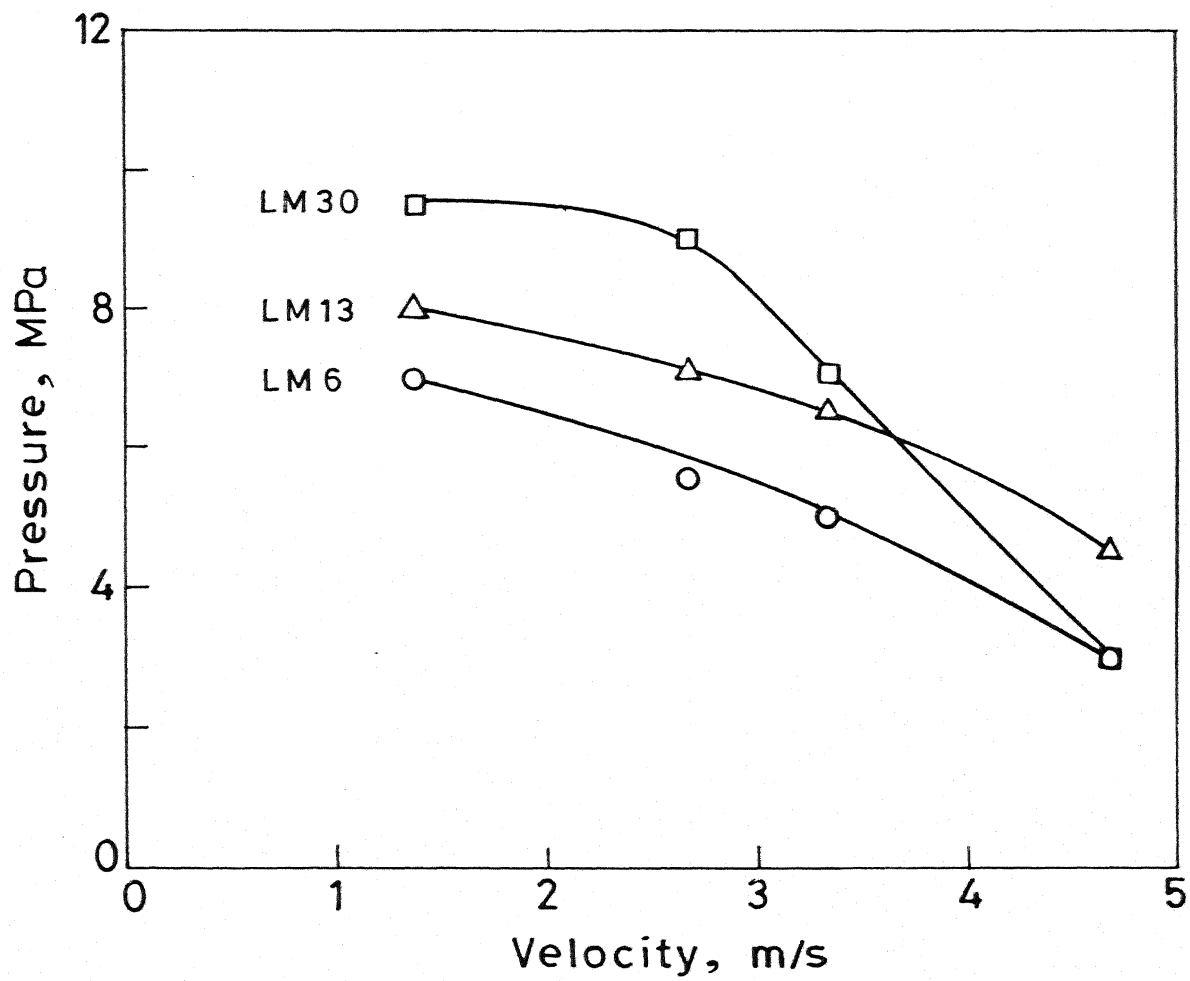


Fig. 5.52 Pressure Velocity Limits of Die Cast LM6, LM13 and LM30 Alloys.

of P-V at which the specimen begins to seize. The load bearing capacity (LBC) of a material would be less than that shown in Fig.5.52. It can be seen from Fig.5.52 that die cast LM30 alloy seized at a sliding speed of 1.38 m/s when the bearing pressure is increased to 9.5 MPa. This indicates that the LBC of die cast LM30 alloy is less than 9.5 MPa at a sliding speed of 1.38 m/s. Similarly, the LBC for LM13 and LM6 alloys at a sliding speed of 1.38 m/s, are less than 8 and 7 MPa respectively. It can also be noted that the LBC of any particular alloy is decreased as the sliding speed is increased. For example, the LBC of die cast LM30 alloy is decreased from 9.5 to 7 MPa as the sliding speed is increased from 1.38 to 3.35 m/s. Additionally, there is a steep decrease in LBC of die cast LM30 alloy above a sliding speed of 2.6 m/s whereas, the decrease in the cases of LM13 and LM6 alloys are progressive in nature. It is interesting to note that the LBC of die cast LM30 alloy is inferior to that of LM13 alloy above a sliding speed of 3.6 m/s. For instance, at a sliding speed of 4.0 m/s, the LBC of LM30 alloy is 5.1 MPa, whereas, for LM13 alloy, it is 5.7 MPa. These data might be useful for the selection of bearing materials to be used in high speed applications. Die cast LM6 alloy is found to be inferior to that of LM13 alloy as far as their LBC is concerned over the entire range of speeds used in the present investigation.

5.5.6.2 LM6 Alloy and LM6-Graphite Particle Composites

The P-V limits of LM6 alloy and composites in partially lubricated condition are shown in Fig.5.53. It can be seen that die cast LM6 alloy seized at a pressure of 7.0 MPa at a sliding speed of 1.38 m/s. By dispersing 3% graphite particles in die cast LM6 alloy, the limiting bearing pressure is increased by 21%. Furthermore, the limiting bearing pressure of heat treated LM6-3% graphite particle composites is found to be 36% higher than that of the die cast LM6 alloy. It can be noted from Fig.5.53 that the limiting bearing pressure of LM6 alloy and composites is decreased as the sliding speed is increased. For instance, at a sliding speed of 3.35 m/s, the die cast LM6 alloy seized at a pressure of 5.0 MPa whereas, at 1.38 m/s the limiting bearing pressure is 28% higher. It is also interesting to note that the performance of LM6-3% graphite particle composites in die cast, sodium modified and heat

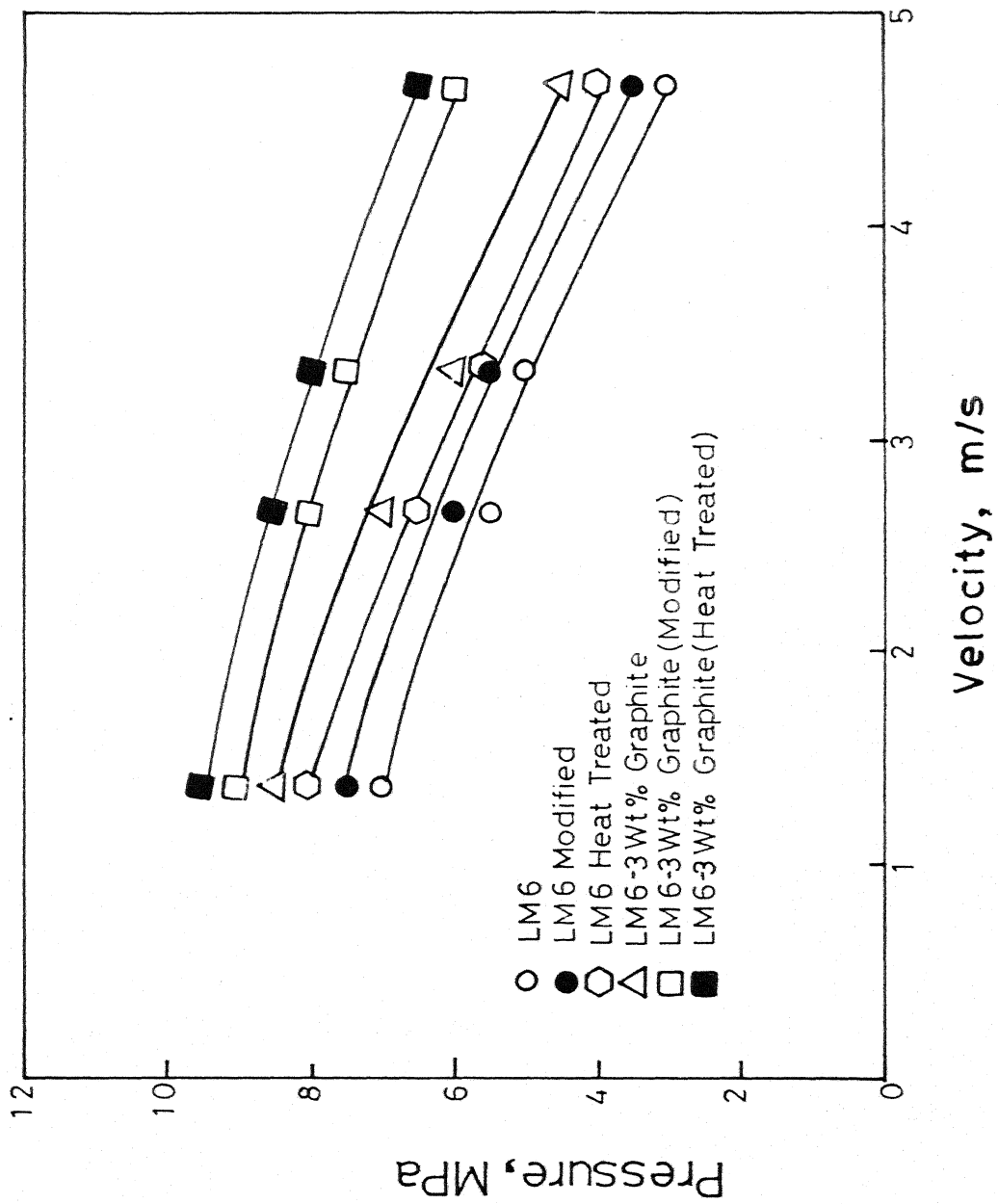


Fig. 5.53 Pressure-Velocity Limits for LM6 Alloy and Composites

treated conditions is found to be superior to those of base alloys in all the above conditions. Amongst all combinations heat treated LM6-3% graphite composites is found to be superior to the rest as far as their bearing performance is concerned.

The maximum temperature attained during sliding wear at a particular applied pressure and disc speed of LM6 alloy and composites is shown in Table V.19. The results indicate that the temperature of the pin increases with applied pressure and a sudden increase in sample temperature is observed when the sample tends to seize. For example, at an applied pressure of 4.0 MPa, the temperature of heat treated LM6 alloy pin rose to 79°C whereas, at 5 MPa pressure, the temperature rose to 99°C at a disc speed of 800 RPM. At the same speed, and with an applied pressure of 5.5 MPa, the temperature of heat treated LM6 alloy pin rose to 135°C well before the specified sliding distance.

The tangential force of LM6 alloy and composites is measured during sliding wear test and coefficient of friction is evaluated. Normal and tangential force and coefficient of friction are shown in Table V.20. The results show that the coefficient of friction is independent of normal force and disc speed. The main function of the lubricant is to reduce metallic contacts between the sliding surfaces by interposing a lubricant film. During sliding action, the metal to metal contact occurs in the regions where the pressure is highest. A local breakdown of the oil film results in metallic adhesion. Further, if the speed of sliding is appreciable, high local temperatures are developed and the samples tend to seize. In this situation the coefficient of friction is increased. For example, at a disc speed of 800 RPM, the coefficient of friction is found to be about 0.05 at an applied pressure of 4 MPa and at 5 MPa pressure when the sample tends to seize the coefficient of friction is increased to 0.15.

5.5.6.3 LM13 Alloy and LM13-Graphite Particle Composites

The P-V limits of LM13 alloy and composites are shown in Fig.5.54. It can be clearly seen that the load bearing capacity (LBC) of composites is more than the matrix alloy at all sliding speeds. At a sliding speed of 1.38 m/s,

Table V.19 : Maximum Temperature Attained during partially Lubricated Sliding Wear of LM6 Alloy and Composites

LM6 (Die cast)				LM6 (Modified)				LM6 (Heat Treated)			
Disc speed (RPM)	Applied pressure (MPa)	Temperature (°C)	Disc speed (RPM)	Applied Pressure (MPa)	Temperature (°C)	Disc speed (RPM)	Applied pressure (MPa)	Temperature (°C)	Disc speed (RPM)	Applied pressure (MPa)	Temperature (°C)
330	6.0	109	330	7.0	102	330	6.0	86	330	6.0	86
	7.0 *	159		7.5*	192		7.0	112		7.0	112
							8.0*	192		8.0*	192
640	5.0	85	640	5.0	95	640	5.0	90	640	5.0	90
	5.5*	138		5.5	108		6.0	98		6.0	98
				6.0*	152		6.5*	192		6.5*	192
800	4.0	82	800	5.0	95	800	4.0	79	800	4.0	79
	5.0*	122		5.5*	129		5.0	99		5.0	99
							5.5*	135		5.5*	135
1100	2.0	102	1100	3.0	102	1100	3.0	95	1100	3.0	95
	3.0*	134		3.5*	156		4.0*	192		4.0*	192

*:Seizure

LM6-Graphite (Die cast)			LM6-Graphite (Modified)			LM6-Graphite (Heat Treated)		
330	8.0	125	330	8.0	82	330	8.0	79
	8.0*	185		9.0*	165		9.0	105
							9.5*	145
640	5.0	76	640	5.0	94	640	6.0	86
	6.0	93		7.0	115		7.0	89
	7.0*	126		8.0*	115		8.0	102
							8.5*	195
800	5.0	95	800	5.0	97	800	6.0	98
	6.0*	129		7.0	105		7.0	111
				7.5*	150		8.0*	185
1100	4.0	104	1100	5.0	116	1100	5.0	105
	4.5*	135		5.5	119		6.0	115
				6.0*	145		6.5*	205

* : Seizure

Table V.20 : Coefficient of Friction of LM6 Alloy and Composites
(during Partially Lubricated Sliding Wear)

LM6 (Die cast)							LM6 (Modified)		
Disc speed (RPM)	Normal force (N)	Friction force (N)	Coefficient of friction	Average coefficient of friction	Disc speed (RPM)	Normal force (N)	Friction force (N)	Coefficient of friction	Average coefficient of friction
330	301.44	15.0	0.049	0.049	330	351.68	16.0	0.045	0.045
	351.68*	35.0	0.099			376.80*	20.0	0.053	
640	175.84	14.0	0.079		640	251.20	7.0	0.027	0.026
	251.20	16.0	0.063	0.071		276.32	7.0	0.025	
	301.44*	26.0	0.086			301.44	38.0	0.126	
800	200.96	11.0	0.054	0.054	800	251.20	16.0	0.063	0.063
	251.20*	38.0	0.151			276.32	32.0	0.115	
1100	100.48	12.0	0.119	0.119	1100	150.72	16.0	0.106	0.106
	150.72*	30.0	0.199			175.84*	25.0	0.142	

* : Seizure

LM6 (Heat Treated)				LM6-Graphite			
330	301.44	10.0	0.033	330	401.92	16.0	0.039
	351.68	15.0	0.042		427.04*	25.0	0.058
	401.92*	32.0	0.079				0.039
640	251.2	9.0	0.035	640	251.2	11.0	0.043
	301.44	10.0	0.033		301.44	14.0	0.046
	326.56*	28.0	0.085		351.68*	35.0	0.099
800	200.96	12.0	0.059	800	251.2	12.0	0.047
	251.2	15.0	0.059		301.44*	40.0	0.132
	276.32*	30.0	0.108				
1100	150.72	14.0	0.092	1100	200.96	16.0	0.079
	200.96*	35.0	0.174		226.08*	40.0	0.176

* : Seizure

LM6-Graphite (Modified)				LM6-Graphite (Heat Treated)				
330	401.92	14.0	0.034	0.034	330	401.92	9.0	0.022
	452.16*	40.0	0.088			452.16	9.0	0.0199
						477.28*	10.0	0.020
640	251.2	15.0	0.059		640	301.44	10.0	0.033
	351.68	12.0	0.034	0.046	640	351.68	12.0	0.034
	401.92*	28.0	0.069			401.92	15.0	0.037
						427.04*	26.0	0.060
800	251.2	13.0	0.051		800	301.44	12.0	0.039
	351.68	19.0	0.054	0.052		351.68	15.0	0.042
	376.80*	25.0	0.066			401.92	29.0	0.072
1100	251.2	7.0	0.027		1100	251.2	15.0	0.059
	276.32	11.0	0.039	0.033		301.44	18.0	0.059
	301.44*	35.0	0.116			326.56*	45.0	0.137

* : Seizure

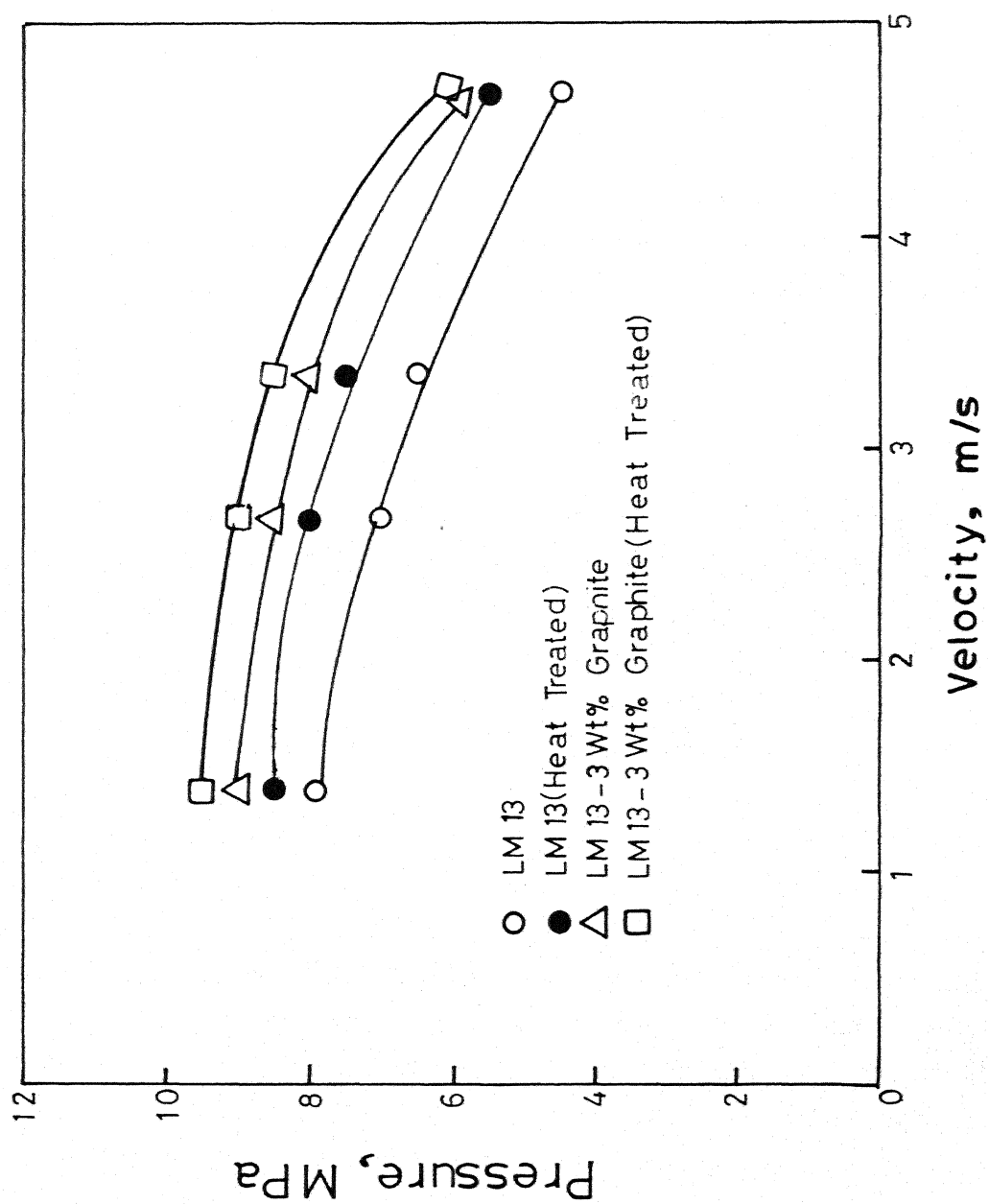


Fig.5.54 Pressure -Velocity Limits for LM13 Alloy and Composites.

die cast LM13 alloy seized at a pressure of 8.0 MPa whereas, LM13-3% graphite particle composite seized at a pressure of 9.0 MPa. This indicates that by dispersing graphite particles in die cast LM13 alloy the limiting bearing pressure can be increased by a magnitude of 12%. After heat treatment the limiting bearing pressure of the composite is further increased by 19%. It is also to be noted that limiting bearing pressure of LM13 alloy and composites is decreased with increase in sliding speed as in the case of LM6 alloy and composites. It is also to be noted that there is a marked improvement in wear resistance of heat treated LM13 alloy as compared to die cast LM13 alloy, for example, at a sliding speed of 3.35 m/s, the limiting bearing pressure of heat treated LM13 alloy is improved by 15% as compared to die cast LM13 alloy. At a higher sliding speed (4.61 m/s), the limiting bearing pressure of heat treated LM13 alloy is increased by 22% as compared to the die cast LM13 alloy. This clearly indicates that the percentage increase in the bearing pressure of heat treated LM13 alloy is more at higher sliding speeds. Similar trend is observed for ^{the} composite also.

The bearing performance of heat treated LM13-3% graphite particle composite is found to be superior to ~~that~~ of die cast LM13, heat treated LM13 alloy and die cast composites. The maximum temperature attained during the sliding wear test of LM13 alloy and composites is shown in Table V.21. The results are found to be similar to those of LM6 alloy and composites; i.e., temperature of the sample increases with applied pressure and a sudden increase in the sample temperature is found when the sample tends to seize.

The coefficient of frictions of LM13 alloy and composites are shown in Table V.22. The results show that the coefficient of friction of die cast LM13 alloy, at a disc speed of 330 RPM, is found 0.033 at a normal pressure of 301.44 N; and it increased to 0.053 when the normal force is increased to 376.8 N. Similar trends are followed for the sliding speeds of 640 and 800 RPM, i.e., coefficient of friction is increased with applied pressure. However, the above statement is not found ^{to be} true at a disc speed of 1100 RPM. For instance, at a normal force of 125.6 N, coefficient of friction is found 0.087 and it decreased to 0.053 at a normal force of 150.72 N; again the coefficient of friction increased to 0.073 at a normal force of 175.84 N and

Table V.21 : Maximum temperature attained during partially Lubricated Sliding Wear of LM13 Alloy and Composites

LM13 (Die Cast)				LM13(Heat Treated)				LM13-Graphite (Die cast)				LM13-Graphite (Heat Treated)			
Disc speed (RPM)	Applied pressure (MPa)	Temperature (°C)	Disc speed (RPM)	Applied pressure (MPa)	Temperature (°C)	Disc speed (RPM)	Applied pressure (MPa)	Disc speed (RPM)	Applied pressure (MPa)	Temperature (°C)	Disc speed (RPM)	Applied pressure (MPa)	Disc speed (RPM)	Applied pressure (MPa)	Temperature (°C)
330	6.0	78	330	7.0	113	330	7.0	330	7.0	115	330	9.0	330	9.0	111
	7.0	84		8.0	121		8.0		8.0	116		9.5*		9.5*	152
	8.0*	143		8.5*	175		9.0*		9.0*	154					
640	5.0	86	640	5.0	101	640	8.0	640	8.0	110	640	8.0	640	8.0	110
	6.0	93		6.0	111		8.5		8.5	121		8.5		8.5	110
	7.0*	140		7.0	120		9.0*		9.0*	155		9.0*		9.0*	169
				8.0*	149										
800	5.0	63	800	6.0	112	800	7.0	800	7.0	115	800	8.0	800	8.0	99
	6.0	70		7.0	120		8.0*		8.0*	162		8.5*		8.5*	159
	6.5*	147		7.5*	148										
1100	2.5	70	1100	5.0	93	1100	5.0	1100	5.0	111	1100	5.5	1100	5.5	102
	3.0	80		5.5*	167		6.0*		6.0*	162		6.0*		6.0*	192
	4.0	84													
	4.5*	142													

* : Seizure

Table V.22 : Coefficient of Friction of LM13 Alloy and Composites
(during Partially Lubricated Sliding Wear)

Disc speed (RPM)	LM13 (Die cast)			Average coefficient of friction
	Normal force (N)	Friction force (N)	Coefficient of friction	
330	301.44	10.0	0.033	0.04
	351.68	13.0	0.036	
	376.80	20.0	0.053	
	401.92*	34.0	0.084	
640	251.20	9.0	0.035	0.035
	301.44	11.0	0.036	
	351.68*	35.0	0.099	
	251.20	14.0	0.055	
800	301.44	18.0	0.059	0.057
	326.56*	35.0	0.107	
	125.6	11.0	0.087	
	151.72	8.0	0.53	
1100	175.84	13.0	0.073	0.069
	200.96	13.0	0.064	
	226.08*	35.0	0.154	

* : Seizure

LM13 (Heat Treated)

Disc speed (RPM)	Normal force (N)	Friction force (N)	Coefficient of friction	Average coefficient of friction
330	351.68	9.0	0.025	
	401.92	15.0	0.037	0.031
	427.04*	35.0	0.081	
	251.20	19.0	0.075	
640	301.44	22.0	0.072	
	326.56	25.0	0.076	0.068
	351.68	19.0	0.054	
	376.80	25.0	0.066	
800	401.92*	37.0	0.092	
	301.44	19.0	0.063	
	351.68	22.0	0.062	0.062
	376.80*	35.0	0.092	
1100	251.2	18.0	0.071	0.071
	276.32*	34.0	0.123	

* : Seizure

LM13-Graphite

Disc speed (RPM)	Normal force (N)	Friction force (N)	Coefficient of friction	Average coefficient of friction
330	351.68	10.0	0.028	0.028
	401.92	12.0	0.029	
	452.16*	39.0	0.086	
640	351.68	11.0	0.031	0.032
	401.92	14.0	0.034	
	427.04*	38.0	0.088	
800	351.68	20.0	0.056	0.056
	401.92*	39.0	0.097	
1100	251.20	22.0	0.087	0.087
	301.44*	34.0	0.112	

* : Seizure

LM13-Graphite (Heat Treated)

Disc speed (RPM)	Normal force (N)	Friction force (N)	Coefficient of friction	Average coefficient of friction
330	452.16	15.0	0.033	0.033
	477.28*	38.0	0.079	
640	401.92	22.0	0.054	0.057
	427.04	26.0	0.060	
	452.16*	40.0	0.088	
800	401.92	20.0	0.049	0.049
	427.04*	41.0	0.096	
1100	276.32	20.0	0.072	0.072
	301.44*	40.0	0.132	

* : Seizure

decreased to 0.064 at a normal force of 200.96 N. This suggests that coefficient of friction is independent of normal force. It is also to be noted that the coefficient of friction is independent of disc speed too. For instance, at a disc speed of 330 RPM, and normal force of 351.68 N, the coefficient of friction of heat treated LM13 alloy is 0.025 and at the same normal force, the coefficient of friction at 800 RPM is 0.062. On the other hand at a disc speed of 640 RPM the coefficient of friction of heat treated LM13 alloy is 0.072 and at 800 RPM, it is 0.063 both at a normal force of 6.0 N.

5.5.6.4 LM30 Alloy and LM30-Graphite Particle Composites

The P-V limits of LM30 alloy and composites are shown in Fig.5.55. It shows similar trend between pressure and velocity as is observed for LM6 and LM13 alloys. The bearing pressure of LM30 alloy and composites is decreased with increase in sliding speed. However, there is a steep decrease in bearing pressure above a sliding speed of 2.68 m/s unlike LM6 and LM13 alloys, where a progressive decrease is observed. It can be noted that refinement and modification of primary and eutectic silicon respectively of die cast LM30 alloy did not improve the limiting bearing pressure at any sliding speed used in the present studies. However, the modification of eutectic silicon in LM6 alloy improved the load bearing pressure.

Dispersing graphite particles in die cast LM30 and refined and modified LM30 alloy lead to significant improvements in the bearing performance. For instance, at a sliding speed of 1.38 m/s, the bearing pressure of die cast LM30 alloy is increased by 16% due to 3% graphite particle dispersion. The limiting bearing pressure of refined and modified composites is increased by 26% as compared to that of die cast LM30 alloy at a speed of 1.38 m/s. A marked improvement in limiting bearing pressure is found in heat treated composites. For example, at a sliding speed of 4.61 m/s the wear resistance of heat-treated LM30-3% graphite composite is increased by 83% as compared to that of die cast LM30 alloy. At low speeds i.e., 1.38, 2.68 and 3.35 m/s, the increase in wear resistance is 26, 22 and 36% respectively. It is also interesting to note that percentage increase of limiting bearing pressure is

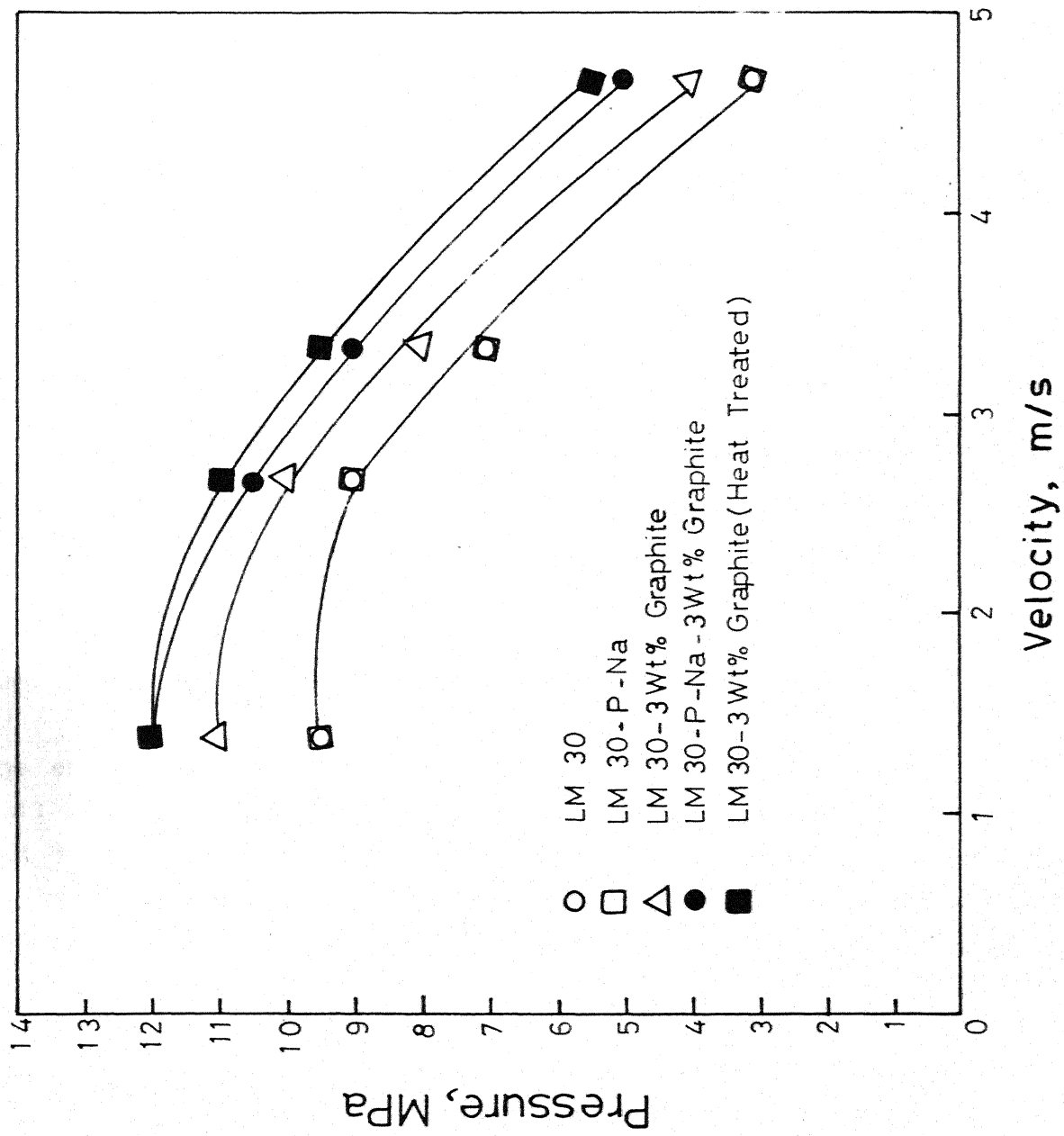


Fig.5.55 Pressure - Velocity Limits for LM30 Alloy and Composites.

more at higher sliding speed compared to that at low speeds. Similar trend is observed for LM6 and LM13 alloys also. The maximum sample temperature attained during sliding wear test of LM30 alloy and composites is shown in Table V.23. The results are similar to those for LM6 and LM13 alloys. The frictional force and coefficient of friction of LM30 alloy and composites are shown in Table V.24. The results show a similar trend as those for LM6 and LM13 alloys and composites.

It is not appropriate to make a direct comparison of coefficient of friction values of Al-Si alloy (LM6, LM13, LM30) in different condition and composites, because of the fact that the each value for coefficient of friction corresponding to the pressure applied on the sample, which is different in different alloys depending upon the load bearing capacity.

5.5.7 Abrasive Wear of Rapidly Solidified LM13 Alloy

The thin ribbons of LM13 alloy produced by rapid solidification processing are subjected to abrasive wear (against SiC emery papers) using Suga abrasion tester. No other type of wear study could be performed on rapidly solidified ribbons due to limitations on the sample dimension. It should be noted that in the present investigation no attempt is made to consolidate the ribbon into larger samples. For comparison purposes die cast Al-Si alloy is subjected to abrasive wear under identical conditions. Complete description of the experimental procedure is given in chapter 4.

The effect of distance on the wear loss of die cast and rapidly solidified LM13 alloy at an applied load of 0.8 N is shown in Fig.5.56. It can be seen that the wear volume is found to be a linear function of distance for both the rapidly solidified and die cast alloy. The effect of load on the wear rate is shown in Fig.5.57.a. The wear rate-load curve shows a pronounced discontinuity at loads exceeding 2.0 N, for the rapidly solidified alloy. At lower loads the rapidly solidified alloy is found to wear less than the die cast alloy, whereas, at loads in excess of 2.0 N, the reverse behaviour is observed. In order to get an idea of the abrasive wear rate of rapidly solidified alloy relative to that of die cast alloy, a parameter R_a (relative abrasive

Table V.23 : Maximum Temperature Attained during partially Lubricated Sliding Wear of LM30 Alloy and Composites

LM30 (Die cast)			LM30-P-Na			LM30-Graphite		
Disc speed (RPM)	Applied Pressure (MPa)	Temperature (°C)	Disc speed (RPM)	Applied pressure (MPa)	Temperature (°C)	Disc speed (RPM)	Applied pressure (MPa)	Temperature (°C)
330	9.0	129	330	8.0	130	330	9.0	136
	9.5*	152		9.0	132		10.0	142
				9.5*	164		11.0*	182
640			640			640		
	5.0	89		8.5	120		9.5	118
	6.0	98		9.0*	185		10.0*	181
	7.0	99						
	8.0	104						
800	9.0	114	800			800		
	9.5*	147						
1100			1100			1100		
	6.0	198		5.0	119		7.0	139
	7.0*	248		6.0	121		8.0*	142
				7.0*	201			
1100	2.0	60	1100	2.0	74	1100	3.0	118
	2.5	70		3.0*	150		4.0*	175
	3.0*	121						

* : Seizure

LM30-P-Na-Graphite				LM30-Graphite (Heat Treated)			
Disc speed (RPM)	Applied pressure (MPa)	Temperature (°C)	Disc speed (RPM)	Applied pressure (MPa)	Temperature (°C)	Disc speed (RPM)	Applied pressure (MPa)
330	11.5	131	330	10.0	88		
	12.*	152		11.0	92		
				12.0*	162		
640	7.0	110	640	9.0	84		
	8.0	132		10.0	89		
	9.0	139		11.0*	162		
	10.0	145					
	10.5*	171					
800	6.0	90	800	7.0	92		
	7.0	121		8.0	102		
	8.0	132		9.0	111		
	9.0*	232		9.5*	192		
1100	2.0	61	1100	4.0	98		
	3.0	64		5.0	108		
	4.0	83		5.5*	198		
	5.0*	194					

* : Seizure

Table V.24 : Coefficient of Friction of LM30 Alloy and Composites
(during Partially Lubricated Sliding Wear)

Disc speed (RPM)	LM30 (Die cast)			Average coefficient of friction
	Normal force (N)	Friction force (N)	Coefficient of friction	
330	452.16	7.0	0.015	0.015
	477.28*	38.0	0.079	
640	251.20	4.0	0.015	0.024
	301.44	6.0	0.019	
	376.80	11.0	0.029	
	452.16	15.0	0.033	
800	477.28*	39.0	0.081	0.033
	301.44	10.0	0.033	
	351.68*	27.0	0.076	
1100	100.48	8.0	0.079	0.087
	125.60	12.0	0.095	
	150.72*	22.0	0.145	

* : Seizure

LM30-P-Na

Disc speed (RPM)	Normal force (N)	Friction force (N)	Coefficient of friction	Average coefficient of friction
330	401.92	7.0	0.017	0.017
	477.28*	26.0	0.054	
640	427.04	12.0	0.028	0.028
	452.16*	28.0	0.061	
800	251.20	7.0	0.027	
	301.44	9.0	0.029	0.028
	351.68*	12.0	0.034	
1100	100.48	5.0	0.049	0.049
	150.72*	15.0	0.097	

LM30-Graphite

330	452.16	8.0	0.017	0.018
	502.40	10.0	0.019	
640	552.64*	28.0	0.050	0.014
	477.28	7.0	0.014	
	502.40*	22.0	0.043	0.028
800	351.68	10.0	0.028	
	401.92*	19.0	0.047	0.059
1100	151.72	9.0	0.059	
	200.96*	30.0	0.149	

* : Seizure

LM30-P-Na-Graphite

Disc speed (RPM)	Normal force (N)	Friction force (N)	Coefficient of friction	Average coefficient of friction
330	552.64	8.0	0.014	0.014
	602.88*	45.0	0.074	
640	351.68	7.0	0.019	0.019
	401.92	7.0	0.017	
	452.16	8.0	0.017	
	502.40	12.0	0.023	
800	527.52*	28.0	0.053	0.022
	301.44	5.0	0.016	
	351.68	8.0	0.022	
	401.92	12.0	0.029	
1100	452.16*	15.0	0.033	0.049
	100.48	7.0	0.069	
	150.72	7.0	0.046	
	200.96	7.0	0.034	
	251.20*	7.0	0.151	

* : Seizure

LM30-Graphite (Heat Treated)

Disc speed (RPM)	Normal force (N)	Friction force (N)	Coefficient of friction	Average coefficient of friction
330	351.68	17.0	0.048	0.043
	452.16	18.0	0.039	
	502.40*	39.0	0.077	
640	452.16	17.0	0.037	0.036
	502.40	18.0	0.035	
	552.64*	42.0	0.075	
800	351.68	16.0	0.045	0.043
	401.92	17.0	0.042	
	452.16	20.0	0.044	
1100	477.28*	28.0	0.058	0.077
	200.96	17.0	0.084	
	251.20	18.0	0.071	
	276.32*	35.0	0.126	

* : Seizure

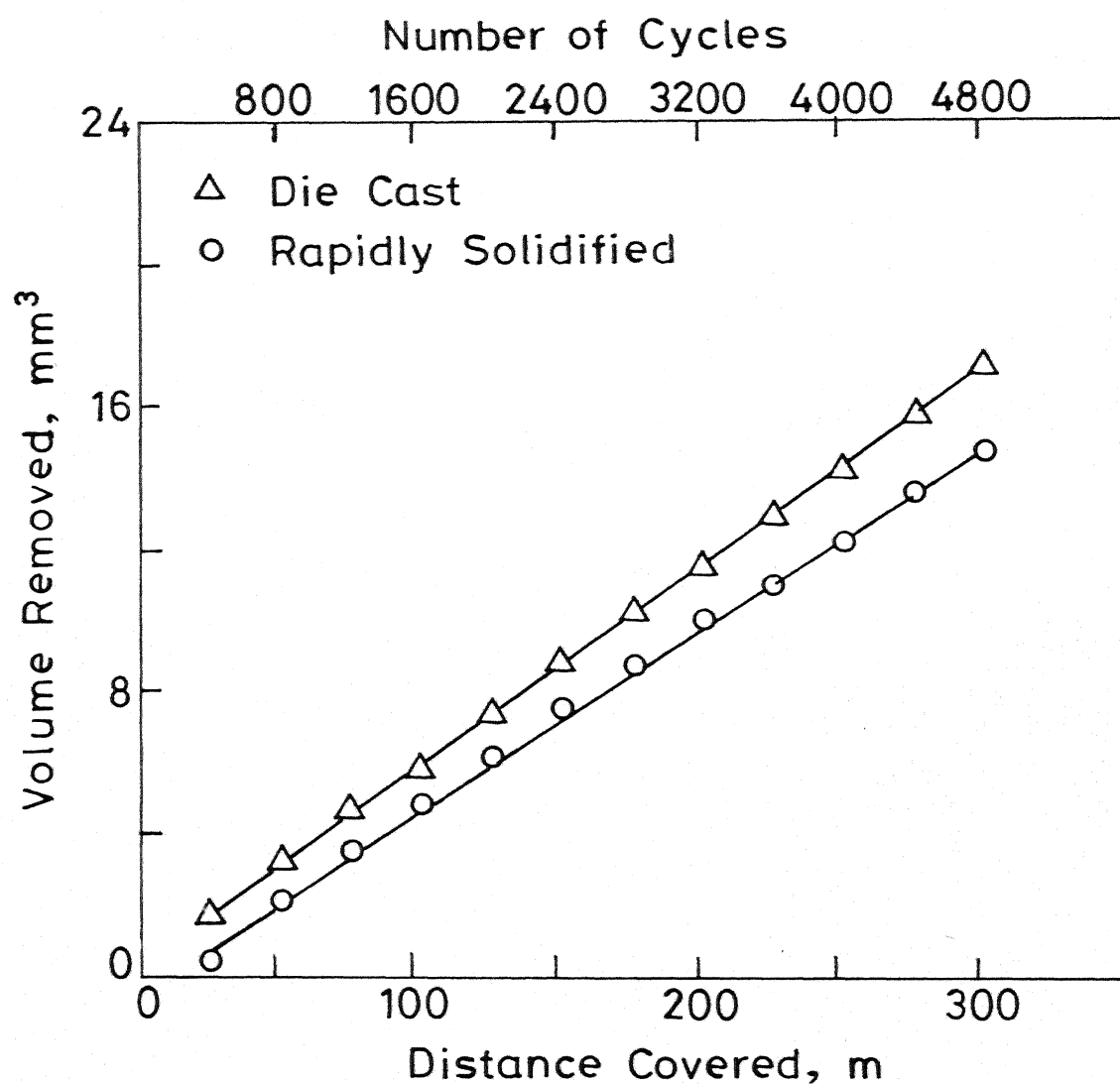


Fig.5.56 Effect of Sliding Distance on the Abrasive Wear of Die Cast and Rapidly Solidified LM13 Alloy (Load: 0.8N)

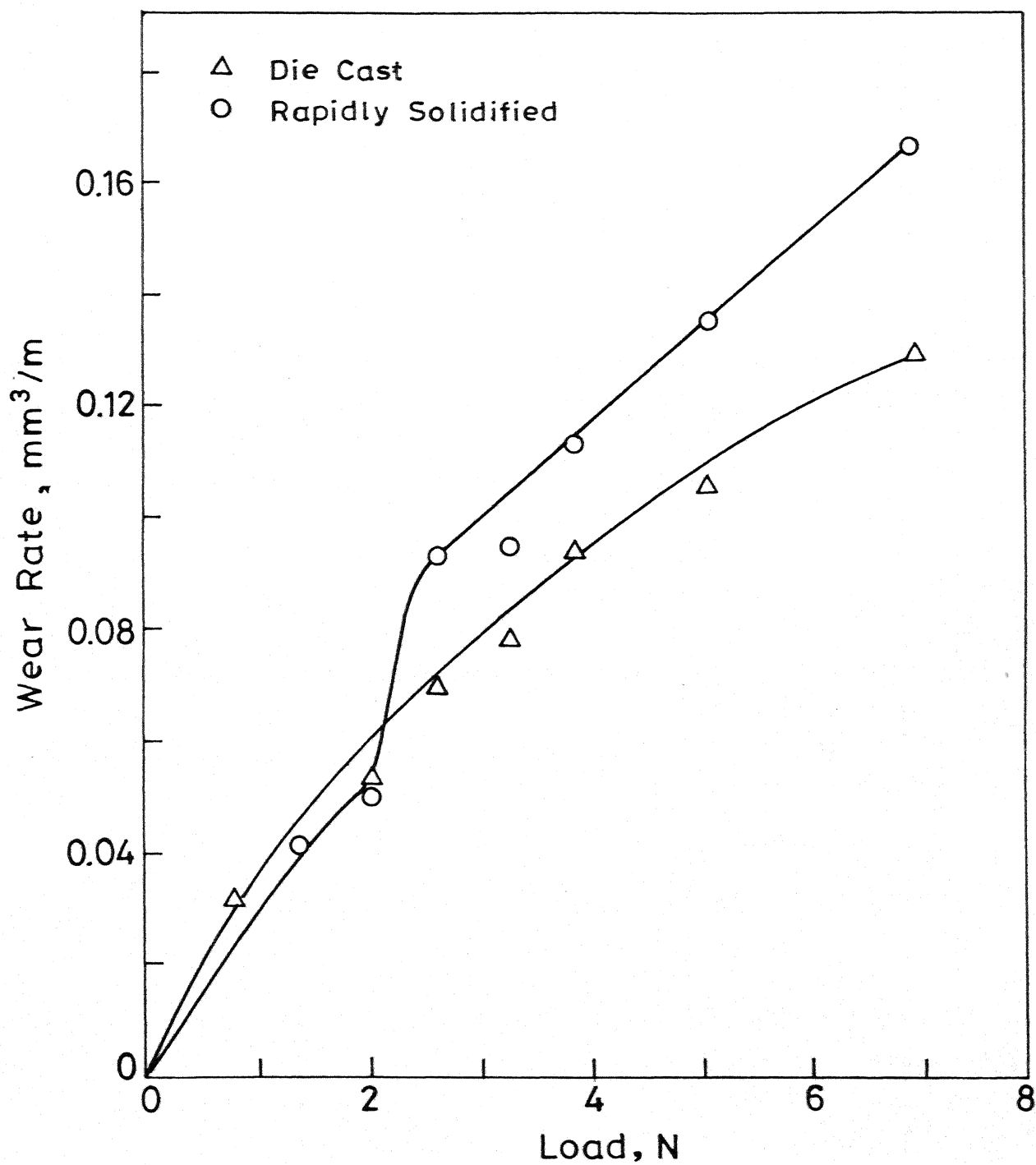


Fig.5.57 (a) Effect of Applied Load on the Abrasive Wear of Die Cast and Rapidly Solidified LM13 Alloy.

wear rate) defined as the ratio between the wear rate of rapidly solidified alloy and the die cast alloy, has been used. Fig.5.57.b. shows the value of R_a as a function of applied load. At loads below 2.0 N, the value of R_a is found to be less than unity, indicating that the abrasion resistance of rapidly solidified alloy is superior to that of die cast alloy. The value of R_a increases with load upto about 4.0 N and thereafter it is stabilised at around 1.20. This indicates that at higher loads (exceeding 4.0 N) the wear rate of the rapidly solidified alloy is 20% higher than that of the die cast alloy.

In order to understand the mechanism of material removal, abraded surfaces are examined in scanning electron microscope. The abraded surfaces of die cast and rapidly solidified alloys, abraded at lower loads (1.4 N) are shown in Figs.5.58.a,b and c,d respectively. In both cases, the abraded surfaces show long and continuous grooves. Abraded surfaces of die cast alloys showed a number of pits. A higher magnification micrograph, Fig.5.58.b, clearly shows these pits. On the contrary, rapidly solidified alloy did not show any significant amount of pitting, Fig.5.58.c. There is not much difference between the surfaces of die cast alloy abraded at lower load 1.4 N, (Figs. 5.58.a,b) and higher load, 7.0 N, (Figs.5.59.a,b). Abraded surfaces at higher loads are also characterised by long and continuous grooves and some amount of pitting. Surfaces of rapidly solidified alloy abraded at higher loads, show considerably more number of parallel lips (Figs.5.59.c,d), as compared to die cast alloy, Figs.5.59.a,b. These lips appeared on the abraded surfaces due to tearing action. At higher load the depth of cracking is comparable to the thickness of the sample and caused severe wear. To confirm the above proposition, the opposite side of an abraded sample of rapidly solidified LM13 alloy (applied load: 7.0 N) is examined in scanning electron microscope. The microstructural observation delineates cracks on the opposite side of the abraded surface (Fig.5.60).

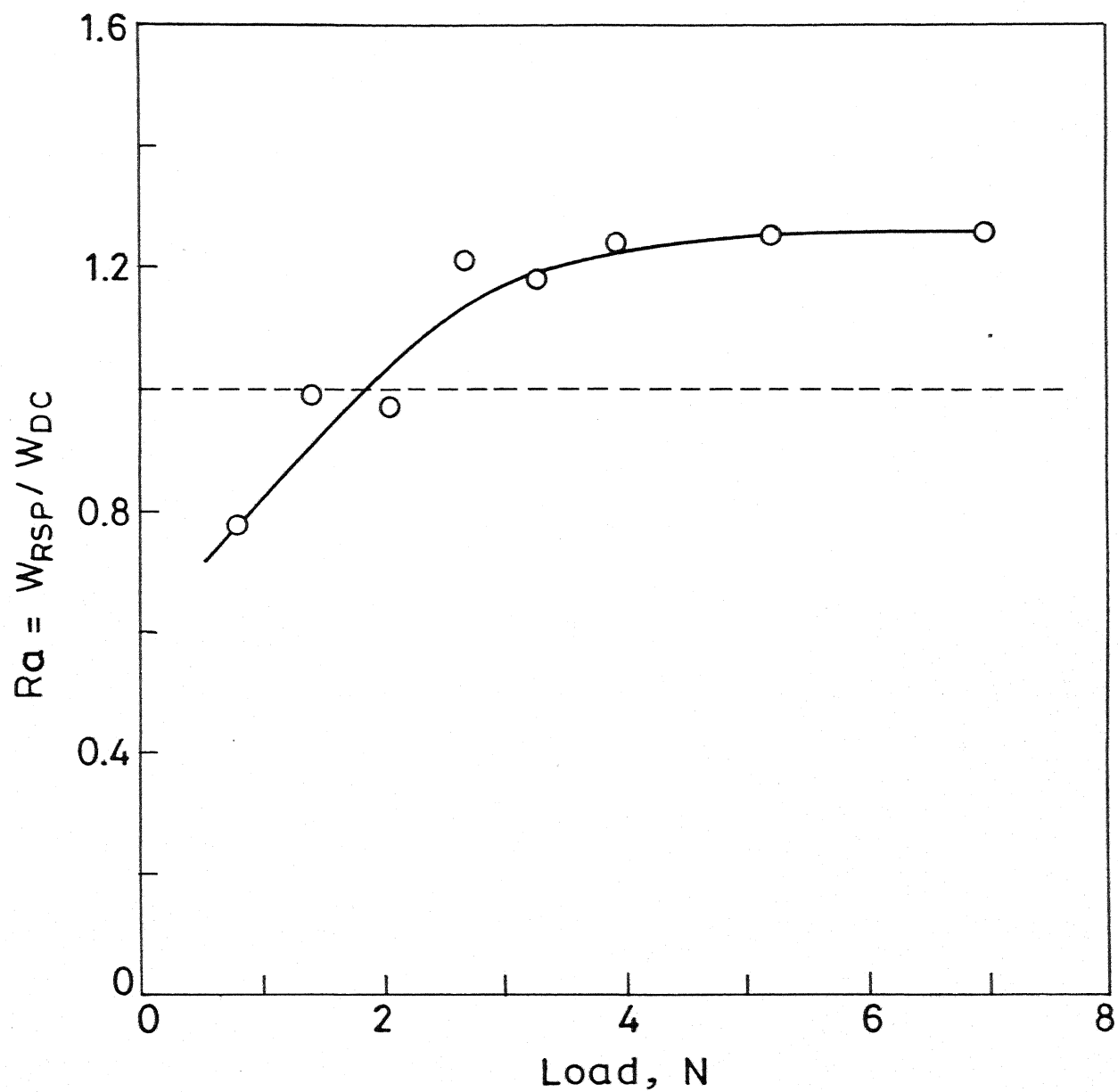
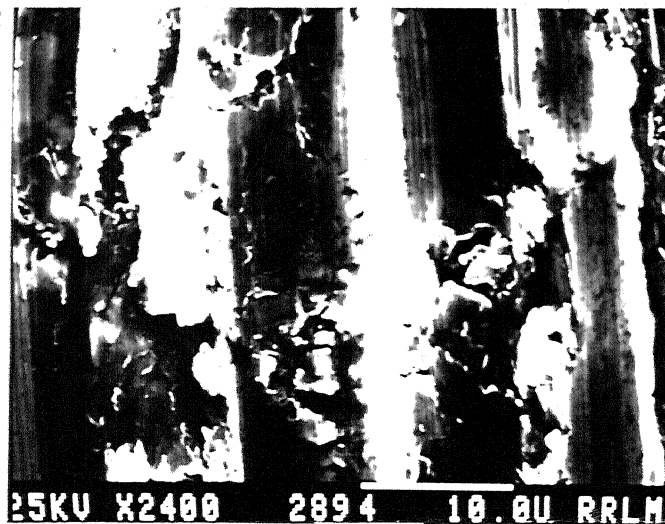


Fig.5.57 (b) Effect of Applied Load on the Relative Abrasion (Ra) of Die Cast and Rapidly Solidified LM 13 Alloy.

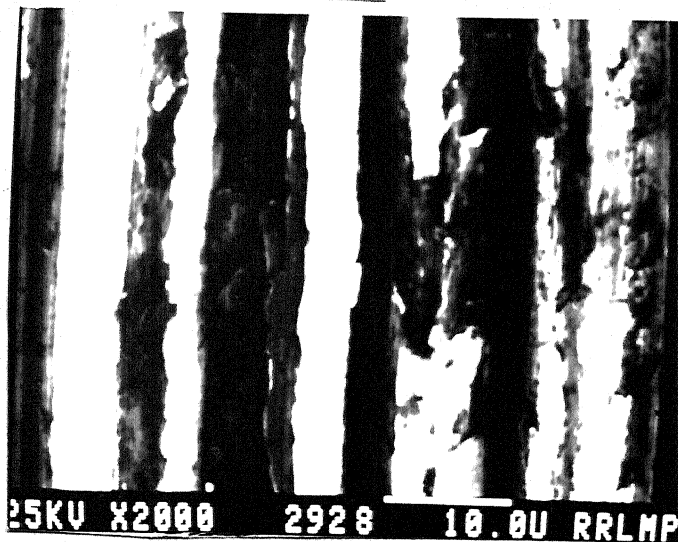
Fig.5.58 Scanning electron micrographs of abraded samples of LM13 alloy: (a) and (b) die cast alloy; (c) and (d) rapidly solidified alloy (Load 1.4 N)



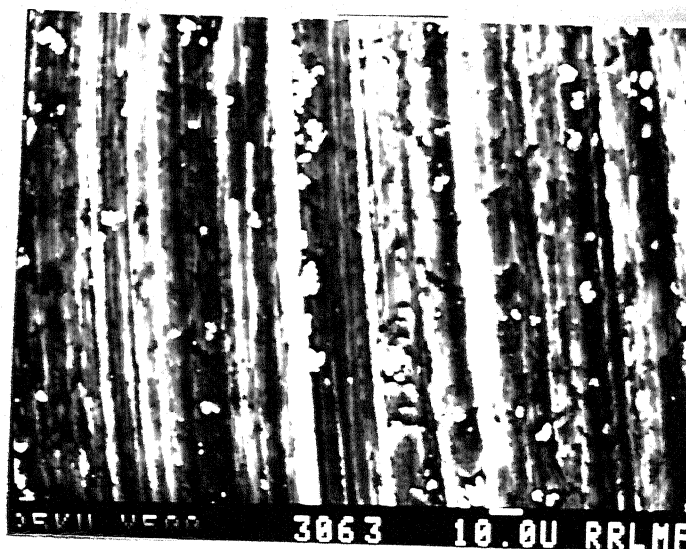
(a)



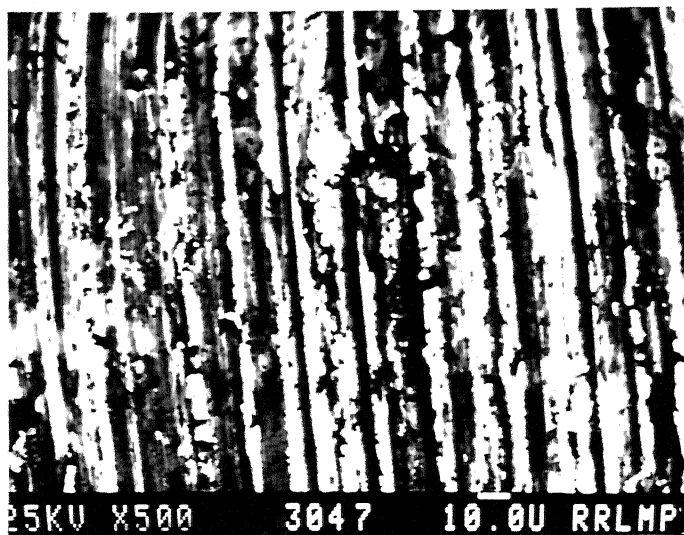
(b)



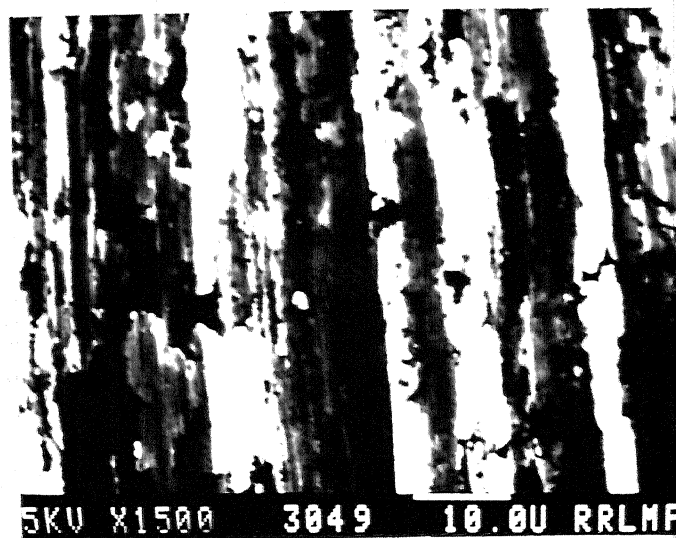
(c)



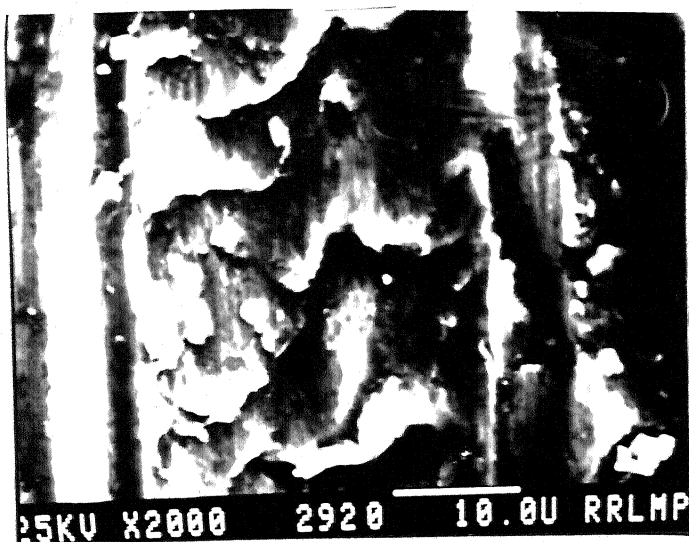
(d)



(a)



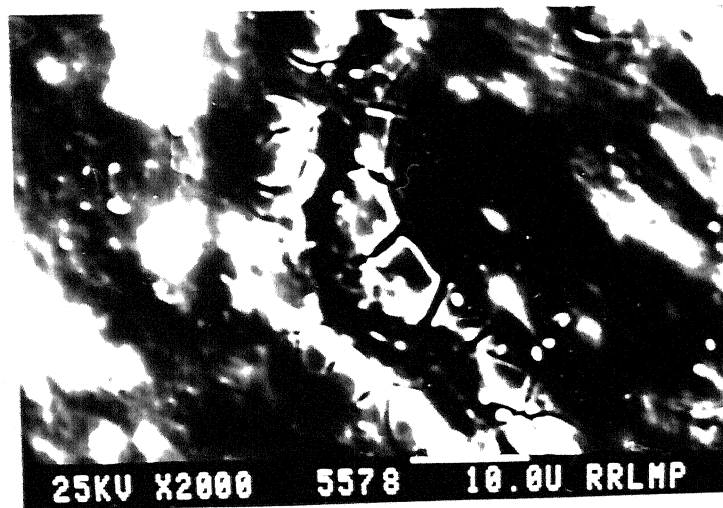
(b)



(c)



(d)



CHAPTER 6

GENERAL DISCUSSION

6.1 Introduction

The aim of this chapter is to discuss the observation of various microstructures in Al-Si alloys with special reference to the morphology of silicon. As pointed out earlier, silicon is a faceted phase and grows anisotropically by twin plane reentrant edge mechanism. The growth of such a faceted phase is sensitive to solidification conditions and the presence of alloying elements. The effect of silicon morphology in Al-Si alloys on the wear behaviour is also discussed. Further, the effect of dispersed graphite particles on the microstructure of Al-Si alloys and wear behaviour is also discussed in greater detail. The conditions for graphite film formation on the tribo-surfaces during sliding wear are identified. The initial part of this chapter deals with the microstructural aspect of Al-Si alloys and Al-Si-graphite composites; this will be followed by wear behaviour and finally an attempt is made to correlate the microstructure and wear behaviour of Al-Si alloys and composites.

6.2 Microstructure of Al-Si Alloys

The microstructure of Al-Si alloys depends essentially on the concentration of silicon. As stated earlier, in hypoeutectic Al-Si alloys such as LM6 and LM13 ($\text{Si} < 12.6 \text{ wt.}\%$) the first phase to solidify is primary aluminium with dendritic morphology. The local cooling rate can be determined from the secondary dendrite arm spacing according to the following equation (194):

$$\log \left(\frac{dT}{dt} \right) = - \left[\frac{\log (\text{DAS}) - 1.66}{0.40} \right] \quad \text{..... 6.1}$$

where, $\left(\frac{dT}{dt} \right)$ ($^{\circ}\text{C}/\text{Sec}$) is the local cooling rate and DAS is the secondary dendrite arm spacing (μm). The local cooling rate in the present case (i.e., for a DAS of $20 \mu\text{m}$) works out to be $8^{\circ}\text{C}/\text{Sec}$.

The presence of the hard silicon phase (Hardness: 1450 HV) ⁱⁿ the aluminium matrix enhances the tensile strength as well as hardness of the alloy (Table:

V.8). In general, binary Al-Si alloy is not heat treatable but addition of alloying elements such as Mg, Cu, Ni makes the alloy amenable to heat treatment and improves elevated temperature properties (195). The improvement of tensile strength and hardness of LM6, LM13 and LM30 alloys after heat treatment is shown in Table V.8.

In hypereutectic Al-Si alloy, the presence of primary aluminium halos surrounding the primary silicon was observed (Fig.5.12.c). The formation of halos in hypereutectic Al-Si (LM30) alloy and other alloy system such as Pb_2Bi-Bi , $Sn-Bi$, $Al-CuAl_2$ has also been reported by many investigators (196-199) and mechanisms for halo formation have also been proposed (196, 199). As stated earlier, the first phase to solidify in hypereutectic Al-Si alloy, is primary silicon. After the nucleation of primary silicon, the liquid composition around the primary phase will be enriched with aluminium following the liquidus line. Since primary silicon is a poor nucleant for α -aluminium, the liquid composition follows the metastable extension (Fig.2.7) till primary aluminium is nucleated due to higher growth rates. After the nucleation of primary aluminium, the composition of ^{the} alloy melt shifts back to eutectic composition and the latent heat released by aluminium raises the eutectic temperature and coupled eutectic growth begins at which both primary aluminium and primary silicon phases have the same growth rates.

6.3 Microstructure of Al-Si alloys in the presence of Dispersed Graphite Particles

In hypoeutectic Al-Si alloy-graphite particle composites, the suspended particles are pushed by the initial crystallising primary aluminium dendrites into the last freezing eutectic liquid during solidification (Fig.5.19.a). Since the size of major fraction of graphite particles (about 60% of the particles are found to lie in the size range of 37.5 to 120 μm , Fig.5.2) is more than the average secondary dendrite arm spacing (20 μm) of primary aluminium, the entrapment of graphite particles in the interdendritic region is ruled out. Moreover, no such evidence of entrapment of even smaller graphite particles of 20 μm or less in size, is found in the interdendritic region (Fig.5.7). A variety of microstructures is observed around the dispersed

graphite particles and the most common one is Al-Si eutectic phase, in which plate-shaped eutectic silicon is randomly oriented in aluminium matrix (Fig.5.19.b). The microinhomogeneity in particle distribution in the cast structure is ~~largely dependent~~ upon the alloy composition. Large amount of eutectic phase (Al-Si) is desirable as the primary phase (aluminium) tends to push the dispersed particles into the last freezing eutectic liquid. This above fact is very important while selecting the matrix alloy.

Another important microstructural observation of Al-Si-graphite system is the modification of eutectic silicon. The modification of eutectic silicon is observed when solidification takes place in the narrow intergraphite particle channels, Fig.5.23.b, or in the corridors between graphite particles and primary aluminium dendrites. The mechanism of modification appears to be due to physical constraints to the anisotropic growth of silicon. The dispersed graphite particles serve as physical barriers to the various transport processes controlling the evolution of solidification microstructures. Given the obstruction to heat and mass transfer as a result of thermal or diffusion field impingement on the physical barrier, inhibition of the anisotropic growth of silicon crystals would be expected. This will be assisted by the progressive decrease in the undercooling at the growth interface as the latter advances in the low undercooling regions in the vicinity of thermally insulating particles. Krishnan and Rohatgi (41) have also shown that in centrifugal castings of Al-Si-graphite particle composites, extensive shape modification of silicon was observed in the regions having highest graphite concentrations; the degree of modification decreased progressively with graphite content across the radial section of the casting.

In hypereutectic Al-Si-graphite particle composites, the primary silicon crystals showed a tendency to preferentially nucleate on the surfaces of dispersed particles (Fig.5.15.b). While the exact nucleation mechanism and crystallographic features for selective affinities between the primary silicon and dispersed graphite particles are not clear at present, possible occurrence of heterogeneous nucleation events which promote preferential nucleation of primary silicon on the particle surface can not be ruled out. It has been reported that the dispersed particles like alumina, illite clay

shell char(55,145,30) in hypereutectic Al-Si alloys, offer sites for heterogeneous nucleation of primary silicon. Humerik and Kingery (200) have shown that silicon wets partially most of the refractories like Al_2O_3 , ZrO_2 , MgO , BeO etc., however, complete wettability i.e., contact angle $(\theta)=0$ occurred only on graphite and beryllium carbide at 1450°C in both hydrogen and helium atmosphere. Although there is no direct relationship between the results of Humerik and Kingery (200) and those of the present investigation of primary silicon nucleation on graphite particle, as far as the experimental conditions are concerned, it, however, provides some evidence of heterogeneous nucleation of silicon on graphite surfaces. In the present investigation, because of the paucity of quantitative information on the exact crystallographic features such as lattice registry and nucleation mechanism, the discussion here is confined solely to the microstructural aspects of nucleation and growth of phases.

Another interesting feature which is generally observed around the primary silicon phase, is the halo formation. It is observed in the present investigation that the dispersed graphite particles in LM30 alloy suppressed the halo formation around the primary silicon crystals (Fig.5.15.a). In the presence of graphite, halo formation is suppressed presumably because the low undercooling of local liquid in the vicinity of thermally insulating graphite particle does not depress the melt temperature to a level necessary for formation of aluminium.

6.4 Modification of Eutectic Silicon

It can be recalled from the previous discussion that the mechanical properties of aluminium-silicon alloy castings depend on the morphology of the eutectic silicon. The sharp-edged faceted silicon causes premature crack initiation and fracture in tension. With a view to restrict the unfavourable growth of eutectic silicon, several attempts are made to modify the eutectic silicon in Al-Si alloys. This inturn improves the mechanical properties and alters the fracture behaviour of these alloys (15,47). Of the various modification techniques proposed (13), the most commercially adopted technique involves the addition of minute quantities of alloying elements such

as Na or Sr. It is proposed that the modifier atoms get selectively absorbed at the reentrant twin grooves and reduce the rate of atomic attachment to the silicon growth tips. Sodium is likely to affect the growth morphology of the eutectic silicon thus increasing the twin density (17). There are some reports indicating that sodium acts as nucleation site for silicon crystals (13). A recent investigation on the sodium modified silicon morphology (51) indicates that the silicon is heavily twinned; although the size of the eutectic silicon is scaled down considerably, the growth morphology is found to be microfaceted. In the present investigation, modified eutectic silicon is found to be microfaceted (5.4.d) as discussed above.

6.5 Refinement of Primary Silicon

During solidification of hypereutectic Al-Si alloys, the coarse silicon crystal tends to segregate making the alloy brittle and difficult to machine. To minimise these problems, it is necessary to refine the primary silicon. The refinement of primary silicon is carried out by the addition of phosphorus. Phosphorus reacts with aluminium to form small insoluble particles of aluminium phosphide (AlP), which serve as potential sites for heterogeneous nucleation on which primary silicon is formed. The crystal structure of AlP is the same as that of silicon i.e., diamond cubic.

In hypereutectic Al-Si (LM30) alloy, the coarse primary silicon crystallises first and then primary aluminium is nucleated around the primary silicon and remaining liquid will solidify as Al-Si eutectic. The coarse primary silicon and plate-shaped eutectic silicon can be refined and modified by adding minute quantities of phosphorus and sodium (Na) respectively in LM30 alloy melt. It is also reported (55) that phosphorus is ineffective in modifying the eutectic silicon. This suggests need to add both phosphorus and sodium in hypereutectic Al-Si alloy to achieve the combined effect of refinement of primary silicon as well as modification of eutectic silicon.

There have been several reports describing the use of phosphorus and sodium to refine and modify the primary and eutectic silicon respectively. Mascré (57) has reported that sodium tends to drop the effectiveness of phosphorus when both were added to the melt at the same time. It is also reported

that phosphorus and sodium react together to form Na_3P which leads to a limited refinement and modification of silicon phase. Moreover, since sodium is added to the melt above the liquidus temperature, there is a tendency for increased sodium losses and thereby reducing the modification effect. In contrast, the work of Sugiyama et al. (58) have indicated that simultaneous introduction of phosphorus and sodium promotes refinement and modification of primary and eutectic silicon respectively. Clegg and Das (56) have also assessed the refinement and modification effects in hypereutectic Al-Si, LM30, alloy. Their data indicated that sulphur is a superior refining agent for the primary silicon rich polyhedra. Refinement and modification of primary and eutectic silicon respectively are achieved by sequential addition of sulphur followed by sodium in gravity die cast LM30 alloy.

In the present investigation a series of experiments were conducted to achieve optimum effect of refinement and modification of silicon in Al-Si-graphite composites. In order to avoid fuming of elemental sodium during the preparation of composites due to mechanical stirring of the melt, sodium was originally added to the melt after dispersing graphite particles and prior to casting the composite melt. But the microstructural investigation confirmed that the eutectic silicon remained unmodified (Fig.5.14). It appears from the above fact that sodium might have ^{been} absorbed by the dispersed graphite particles and thereby unable to act effectively. However, there was no direct evidence of it and the discussion solely confined on the nucleation and growth of the phases. Results of our studies confirmed that sodium must be added prior to the dispersion of graphite particles, if it has to work effectively to modify the shape of the eutectic silicon. In hypereutectic Al-Si LM30 alloy, phosphorus was added first and then after 2 minutes sodium was added followed by graphite particle dispersion to achieve both refinement and modification reactions effectively. Generally, 0.01-0.05 wt.% Na is sufficient to provide substantial eutectic modification, however, in order to compensate the sodium fuming, the quantity of sodium addition was increased to 0.288 wt.%.

6.6 Heat Treatment

In general, binary Al-Si alloy is not heat treatable but addition of alloying elements (i.e., Cu, Mg, Ni) makes this alloy heat treatable. Nickel, in particular, improves elevated temperature properties by forming stable intermetallic compounds that cause dispersion hardening. Mg. and Cu enhance the mechanical strength by improving solid solution strengthening and precipitation. Heat treatment (annealing) of Al-Si alloy can also alter the shape and size of eutectic silicon to a large extent. The present investigation shows that the plate-shaped eutectic silicon is fragmented into near spherical (average size: 5 μm) due to heat treatment. A mechanism for spheroidization of plate-lets and rods during annealing treatment was proposed by Zhu and Liu (201). During annealing treatment the faceted eutectic silicon first fragmented and then spheroidized.

6.7 Shape and Morphology of Silicon in Al-Si Eutectic

The l/d ratios (length to width) of eutectic silicon in Al-Si (LM6, LM13) alloys and composites were computed using two dimensional metallography. A minimum of hundred measurements were made on each sample. The l/d ratios of eutectic silicon in LM6 alloy in die cast, modified, heat treated and LM6-graphite in heat treated conditions are shown in Fig.6.1a as % frequency histograms. The l/d ratio of faceted eutectic silicon in die cast LM6 alloy is found to be in the range from 5 to 13; the maximum % frequency is found around 33% at a l/d ratio of 7-9. It is noted that modification of LM6 alloy, reduced considerably the l/d ratio of eutectic silicon. For instance, the l/d ratio of modified eutectic silicon is found from 1 to 6 and the maximum % frequency is found around 44% at a l/d ratio of 2 to 3. 20% of the eutectic silicon is found to have l/d ratios in the range of 1 to 2. Further decrease in l/d ratio is observed in heat treated LM6 alloy. For instance 33% of eutectic silicon spheroidized (i.e., $l/d \approx 1$) and 30% with l/d ratio less than 1.5. It can also be noted that dispersion of graphite particle in LM6 alloy in heat treated condition did not have any significant effect on the spheroidization of eutectic silicon. Similar observations have been made for LM13 alloy and the histogram are shown in Fig.6.1.b.

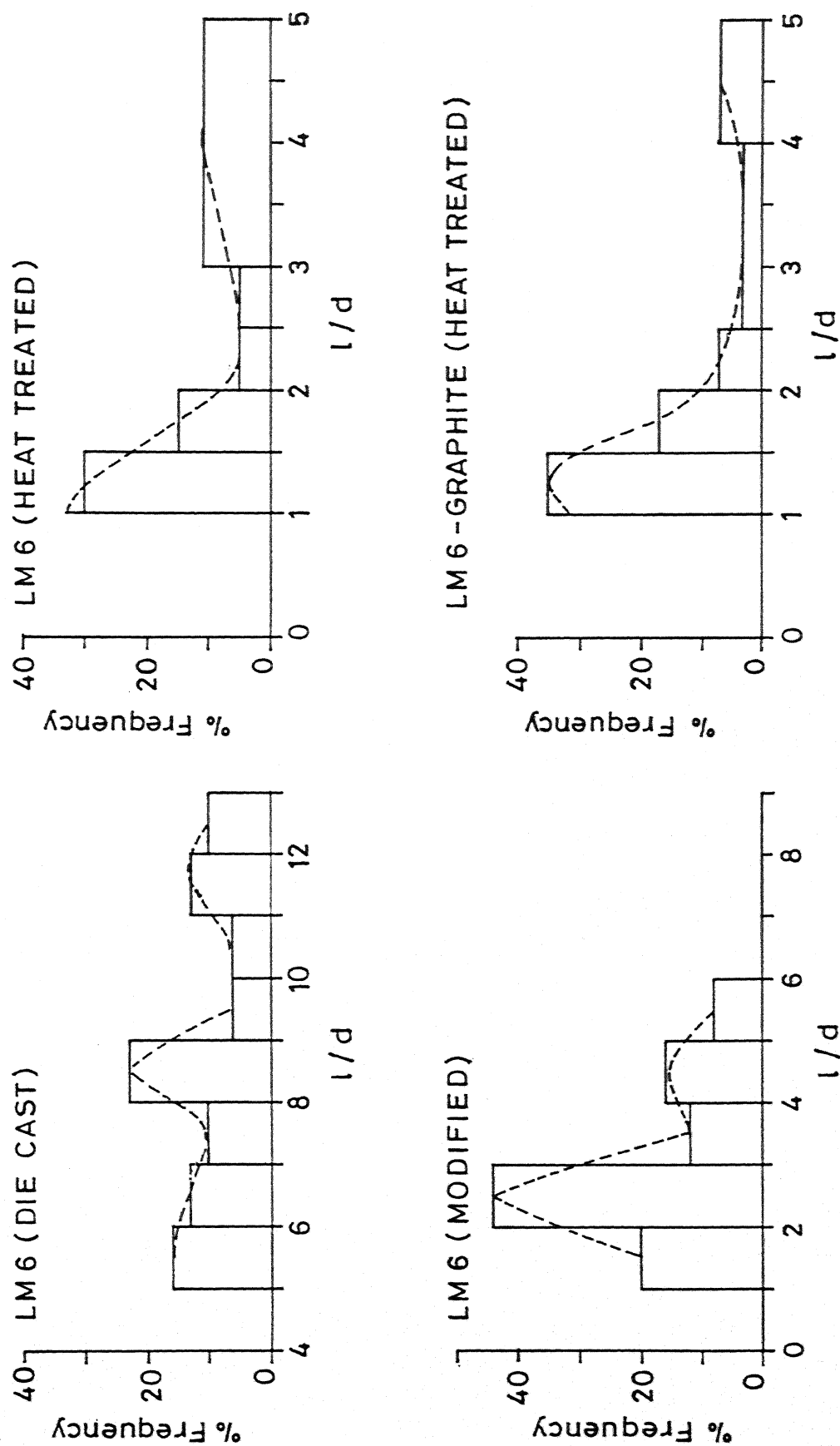


Fig. 6.1(a) l/d Ratio of LM6 Alloy and Composites.

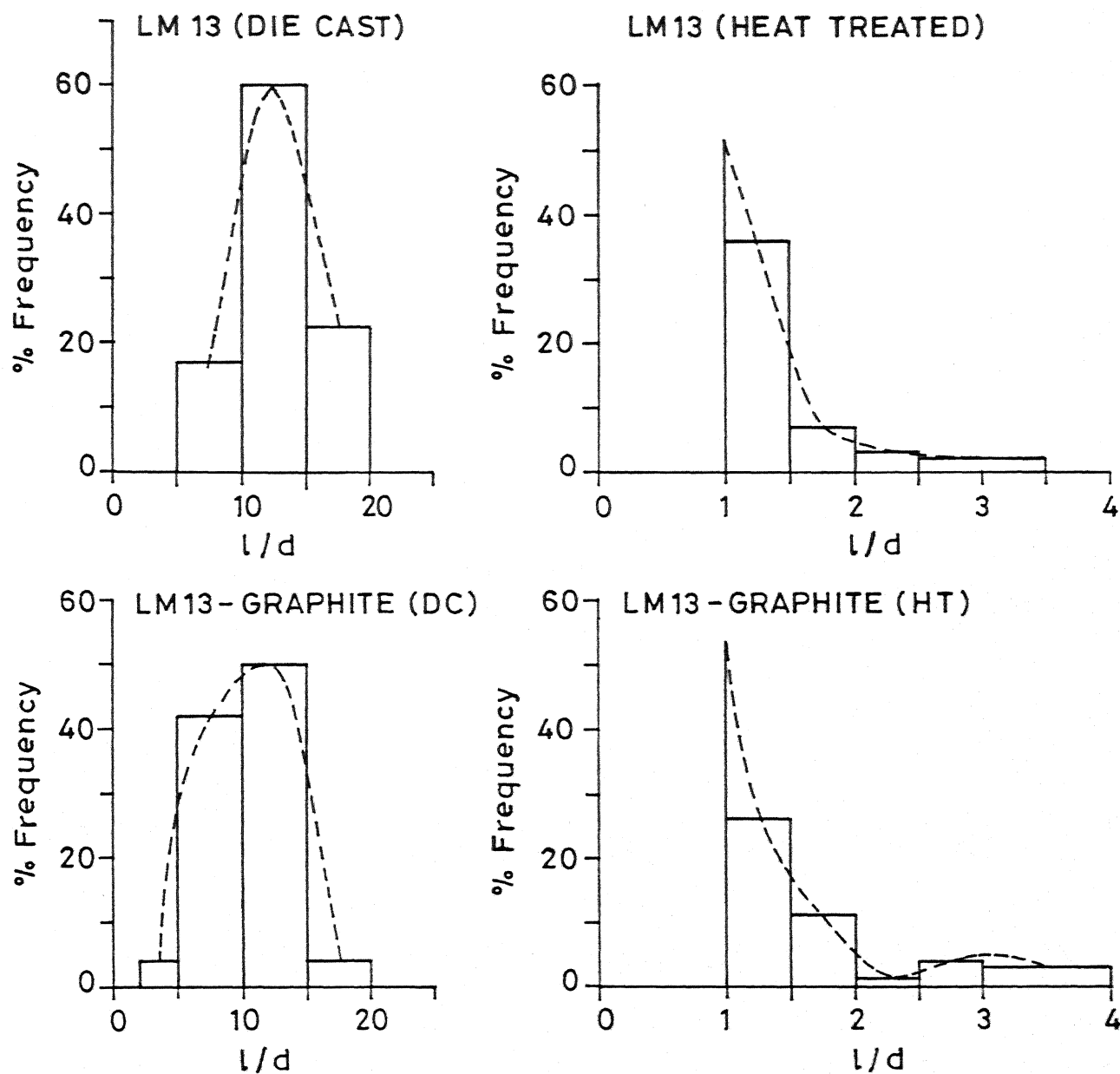


Fig. 6.1(b) l/d Ratio of LM 13 Alloy and Composites.

So far, the discussion was confined to the microstructures of Al-Si alloys with special reference to various silicon morphologies in the presence of dispersed graphite particles. The role of matrix microstructure and dispersed graphite particles on the sliding wear behaviour of Al-Si alloys will now be established. First, we shall briefly discuss the structure and lubricating properties of graphite which was used as a dispersoid in the present investigation.

6.8 Tribology of Graphite

The lubricity property of graphite arises mainly due to weak interlamellar bonding between the basal planes. The presence of water vapour and crystal defects such as dislocations are also found to be necessary for interlamellar shear (202). The interlamellar shearing of graphite layers also depends upon the surrounding atmosphere. It has been reported (202) that graphite ceases to be a solid lubricant in vacuum. In the present investigation graphite is dispersed in Al-Si alloy matrices in order to reduce the metal to metal contact during sliding wear. Results of the present investigation have demonstrated that the structure of the Al-Si alloy matrix also plays an equally important role in governing the wear of the composites.

6.9 Role of Interfaces

Additionally, particle-matrix interface plays a critical role in governing not only the mechanical properties but also tribological properties of composites. With the help of schematic illustrations, Prasad and Rohatgi (190) have demonstrated the role of particle-matrix interface on the dry sliding wear behaviour of metal-graphite particle composites. The two cases shown in Fig.6.2 are extreme examples of the variations in particle-matrix interfaces. In case A (Fig.6.2) the graphite particle and the matrix are separated by interfacial porosity whereas in case B graphite particle is tightly held by the matrix. In case A there is every possibility that the graphite particle will be pulled out during sliding wear, leaving behind a void. On the other hand, if the interfacial bonding is greater than the lateral force, graphite will not be pulled out from the matrix and the possibility

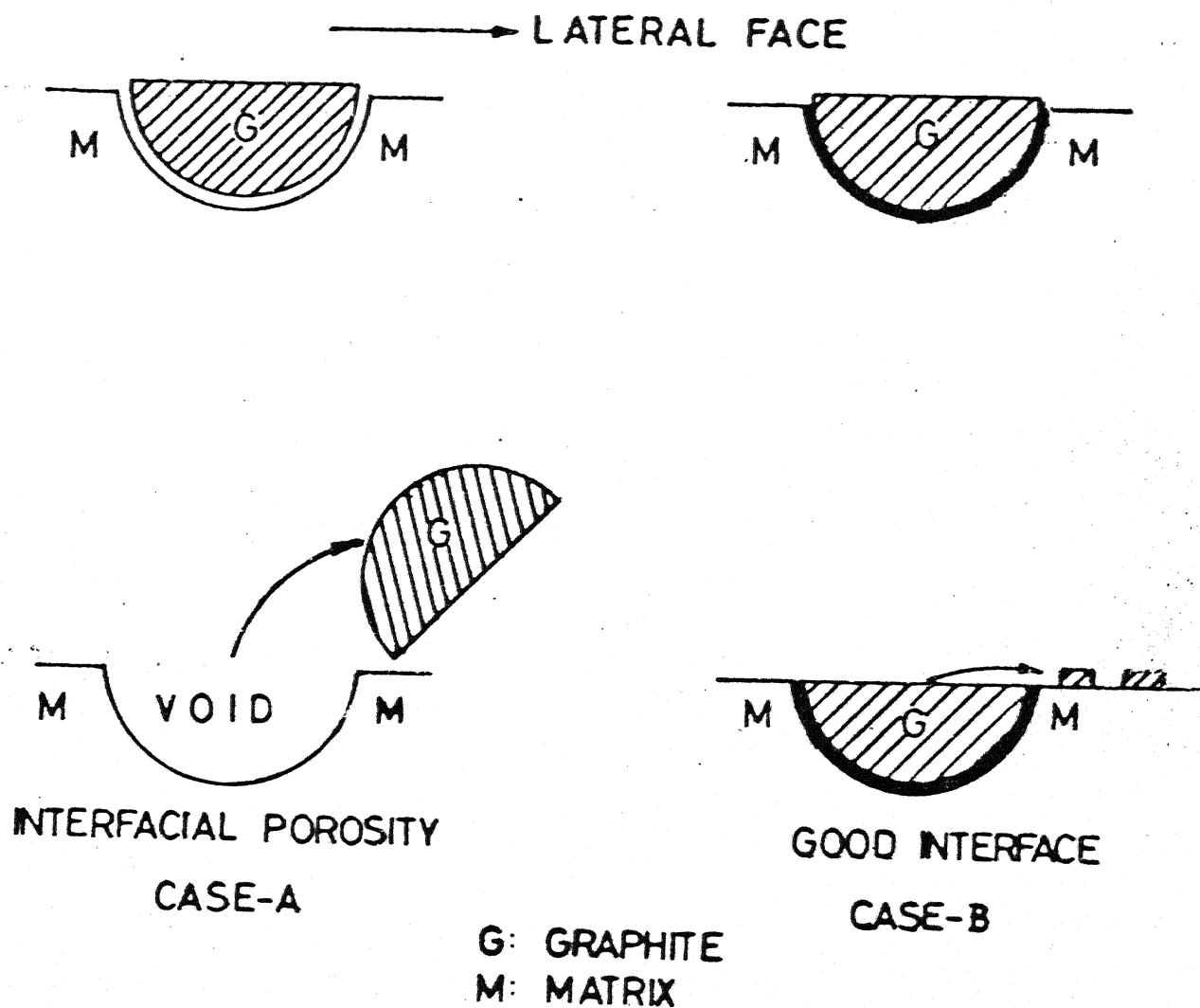


Fig6-2 Schematic Drawing Illustrating the Importance of Particle-Matrix Interfacial Bond During Sliding Wear. G = Graphite, M = Matrix. (190)

of shearing of graphite particle along the basal plane will be enhanced (case B). In the present investigation metallographic examination of composites (See Fig.5.19.b) revealed the absence of interfacial porosity. Therefore, the probability of the dispersed graphite particle to be pulled out from the matrix during the course of sliding wear (as described in case A, Fig. 6.2) is extremely remote in the present case.

6.10 Role of the matrix

In addition to the above two factors (namely presence of dispersed graphite and its interface with the matrix) the present study has revealed that the microstructure of the matrix also plays a significant role in governing the wear of Al-Si alloys and composites. Before we analyse the role of matrix microstructure on the wear of composites, we shall examine first the possible wear mechanisms in Al-Si alloys and composites.

As mentioned in the earlier chapter, Al-Si alloys exhibit two distinct wear regimes: one is the mild wear regime, generally, encountered in the low applied pressure regime and the second is the severe wear regime associated at higher applied pressures (Fig.5.25). The transition from mild to severe wear will depend on : (i) type of the matrix alloy (ii) its microstructure and (iii) graphite particle dispersion. It may be recalled that the morphology of wear debris in these two regimes also differs significantly from each other. For instance, in the mild wear regime wear debris is in the form of fine equiaxed particles (average size: $3.0 \pm 1.7 \mu\text{m}$) whereas, in severe wear regime flake-shaped debris particles are observed. The average size of the flakes (measured in two dimensional metallography) for die cast LM13 alloy is around $290 \mu\text{m}$ (see Table V.11). The fine equiaxed wear debris is likely to be the result of the removal of the oxide layer on the aluminium alloy surface during the early stages of wear. Because of the small quantities of equiaxed wear debris, their identification by X-ray diffraction could not be carried out. However, wave-length dispersive X-ray spectroscopy analysis confirmed that these fine debris contain aluminium. This wear regime is some times referred to as oxidative wear (174).

After the removal of oxide layer and at higher applied pressures there will be severe metal to metal contact and the operating mechanism could be adhesion and/or delamination. The mechanism of adhesive wear is already described in Chapter 2. The softer metal (aluminium alloy pin) has a tendency to adhere to the hard counterface (steel disc) during sliding action. This leads to the formation of junctions which are later ruptured due to external forces (tangential force). This process of adherence and successive rupture is termed as stick-slip mechanism of wear (203). The appearance of parallel lips on the worn surface (Fig.5.36.d) is an indication, of the occurrence of stick-slip process. At higher applied pressures the smaller asperities can grow in size by plastic deformation. The formation of wear debris is favoured when the deformed asperities exceeds a critical size (204). Adhesive wear can produce both fine as well as big wear debris depending upon the magnitude of load.

6.11 Delamination

Delamination is another wear mechanism proposed by Suh and coworkers (169) to explain the flake-shaped wear debris commonly found in wear studies. This model is based on the concept that the accumulation of plastic deformation causes crack nucleation in the subsurface region of the wear surface. Schematic representation of the various stages involved in the formation of wear sheet is shown in Fig.6.3. Scanning electron microscopic studies of wear surfaces indicated evidence of stick-slip movement (Fig. 5.35.d) and cracked portion suggesting that both adhesion and delamination are the operating mechanisms. However, the evidence of large number of flake-shaped debris suggest that delamination may be the rate controlling mechanism. If this is so then crack nucleation (if there are no preexisting cracks) and crack propagation determine the wear behaviour of Al-Si alloys.

6.12 Sources of crack Nucleation and Effect of Silicon Morphology

Aluminium-silicon-graphite is a three component system and the interfaces between aluminium and silicon phases and between them and graphite can act as preferential sites for crack nucleation during sliding wear. As

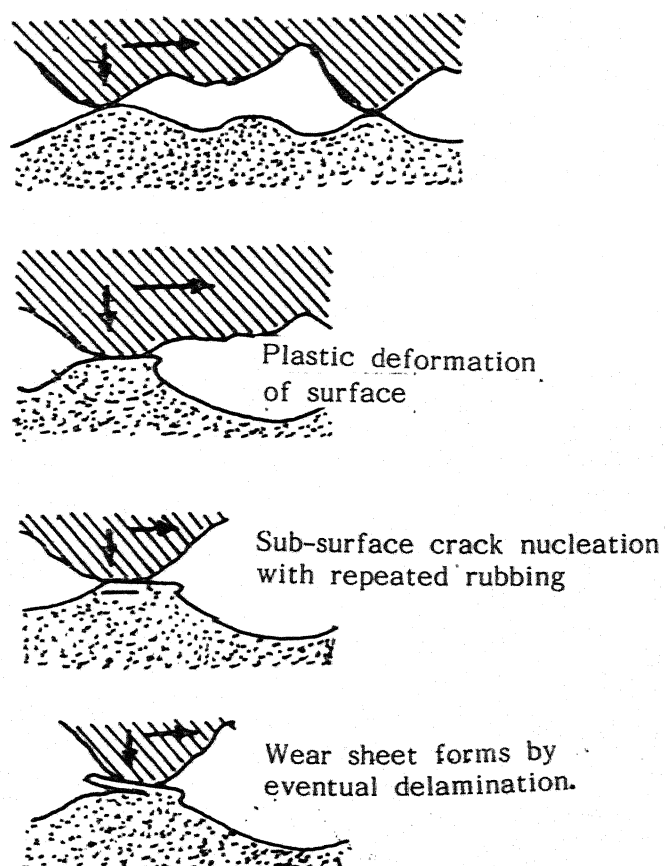
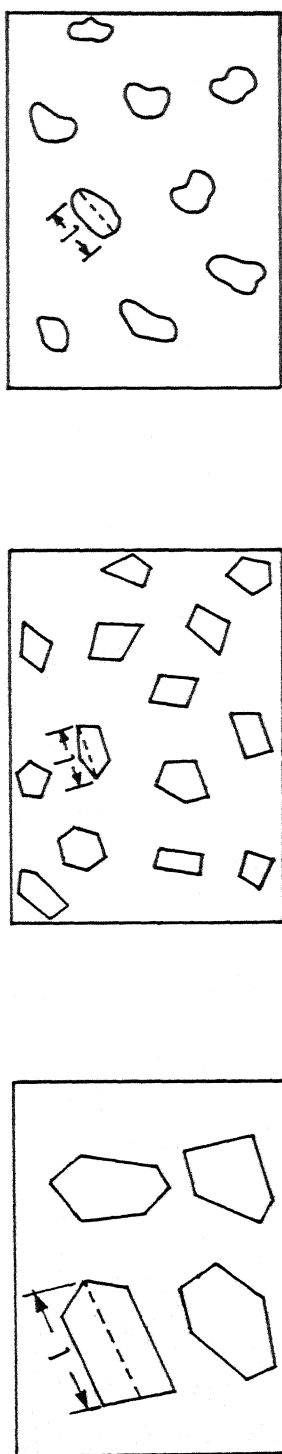


Fig.6.3 Schematic Representation of the Various Stages Involved in the Formation of Delamination Wear Sheets.(200)

mentioned in the earlier section, Al-Si alloy system is an abnormal eutectic, in which one phase (Al) is nonfaceted and other one (Si) is faceted with sharp edges. These sharp edges of silicon can act stress riser in aluminium matrix and offer preferential sites for easy crack nucleation.

The effect of silicon morphology on the fracture behaviour of Al-Si alloy is shown with the help of schematic illustration in Fig.6.4. Case I in Fig. 6.4 shows plate-shaped eutectic silicon in aluminium matrix usually discernible in conventional die cast alloy (Figs.5.4 a & b). Fracture of such coarse plate-shaped silicon can result in big cracks of length (l) in the matrix (Fig.6.4, case I). Case II, (Fig.6.4) represents schematically the microstructure of sodium modified Al-Si alloy. Although the anisotropic growth of silicon is restricted in this case, its faceted nature still remains. In this situation the crack length (l) is smaller than that in the die cast condition but the propensity for crack nucleation due to sharp edges is almost retained. Case III shows a schematic illustration of heat treated Al-Si alloy microstructure. It depicts fine near spherical eutectic silicon distributed in aluminium matrix (Fig.5.8.d). The near spherical shape of silicon particles considerably reduces the stress concentration effect. In the present investigation, l/d ratio measurements as shown in Fig.6.1, indicate that the average value varied from 9.0 in die cast alloy to 2.0 in sodium modified alloy and further reduced to 1.6 in the case of heat treated alloy.

The above reasoning implies that the propensity of crack nucleation will be minimized in the case of heat treated Al-Si alloys, where the morphology of eutectic silicon is near spherical and the size of the silicon is the smallest. This suggests that the size of the flake type debris in the case of heat treated alloy and composites should be considerably less than those of die cast alloy and composites. If the size of the flaky debris is large (as in the case of die cast composites; Table V.11) there is every likelihood that dispersed graphite particles are engulfed in the debris without actually participating in the wear process as shown schematically in Fig.6.5. On the other hand if the size of the debris is finer (as in the case of heat treated composites; Table V.12) graphite can stand exposed at the mating



(i) Die Cast Al-Si Alloy

(ii) Na-Modified Al-Si Alloy

(iii) Heat Treated Al-Si Alloy

Fig. 6.4 Schematic Representation of Silicon Morphologies in Al-Si Alloys.

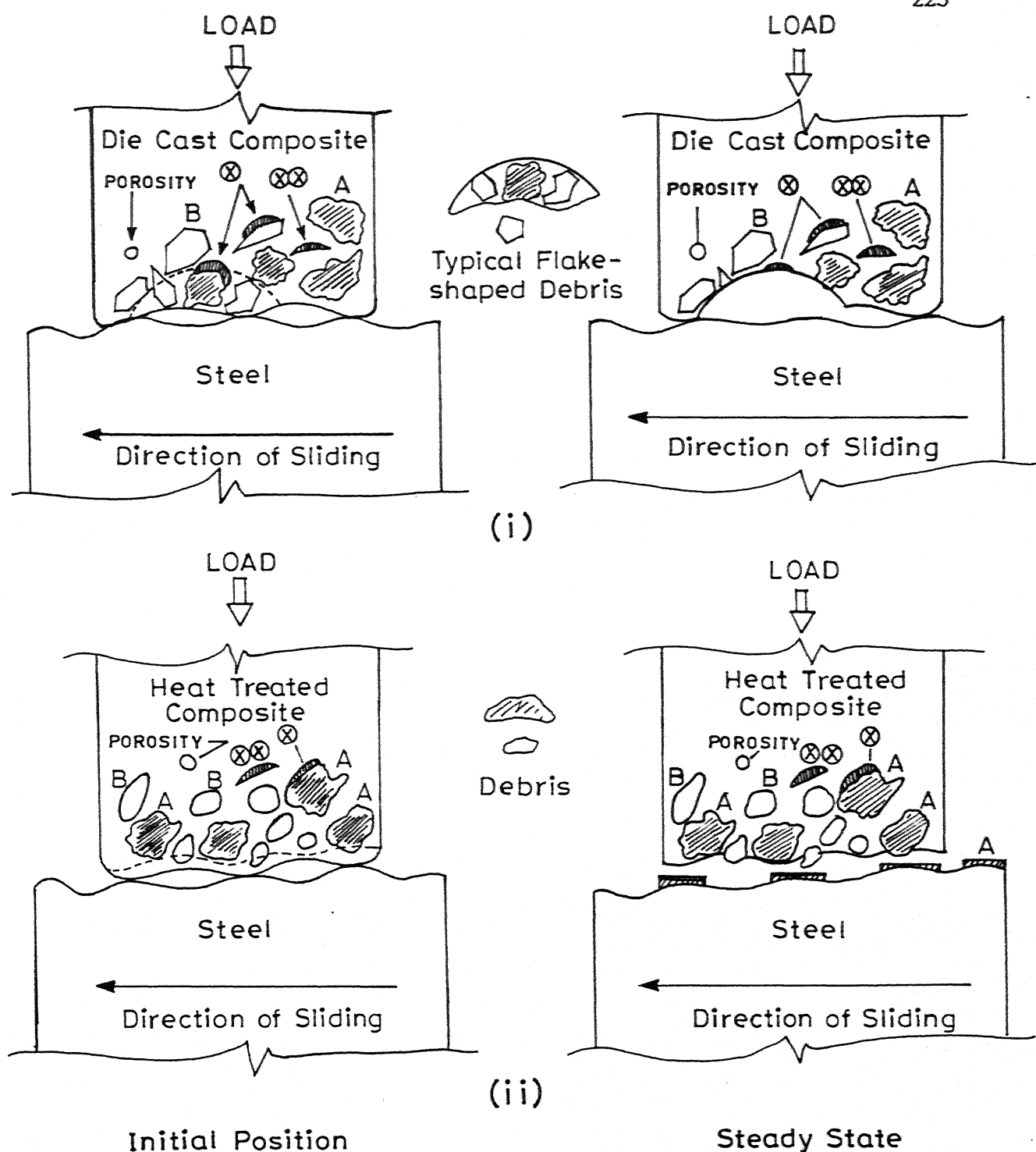


Fig. 6.5 Schematic Illustration of the Conditions :
 (i) Graphite not Offering Lubrication and
 (ii) Graphite Offering Lubrication

surfaces and form a triboinduced film resulting in lesser metal to metal contact and coefficient of friction.

6.13 Graphite Film Formation and Wear of Composites

The lubricating properties of aluminium alloy-graphite composites during dry sliding wear would depend on the efficiency of graphite film formation on wear surfaces.

According to the analysis described above, it is unlikely for the formation of such graphite film on die cast composite surfaces since the probability of graphite particle engulfing in debris is high. The absence of graphite films on the worn surfaces of all die cast composites as evidenced by scanning electron microscopic examination (Fig.5.36) confirms this point. Secondly there is no significant decrease in coefficient of friction in LM6, LM13 and LM30 alloys in the die cast condition due to graphite particle dispersion (Fig.6.6). On the contrary, worn surfaces of composites clearly showed the presence of graphite films on them (Fig.5.42). This could be due to following two reasons: (i) increase in toughness of the matrix alloy due to the change in silicon morphology resulting in finer wear debris (Fig. 5.46.a) and exposing graphite particles to the steel surface. It is also interesting to note that an occasional machining chip type debris observed in heat treated composites (Fig.5.49) confirming the increase in ductility due to heat treatment, (ii) secondly, the efficiency of graphite film formation may be dependent on type of adhesion between matrix alloy and sheared graphite layers. In the case of heat treated composites the area fraction of silicon in wear surfaces is significantly higher in view of the finer size of the silicon; this may be responsible for better adhesion.

It is interesting to note that the graphite film formation on wear surfaces of heat treated composites resulted in significant improvement of friction and wear behaviour of composite materials.

The situation in partially lubricated case, may be less stringent than the dry sliding wear. In this case, lubricating oil is present in the beginning

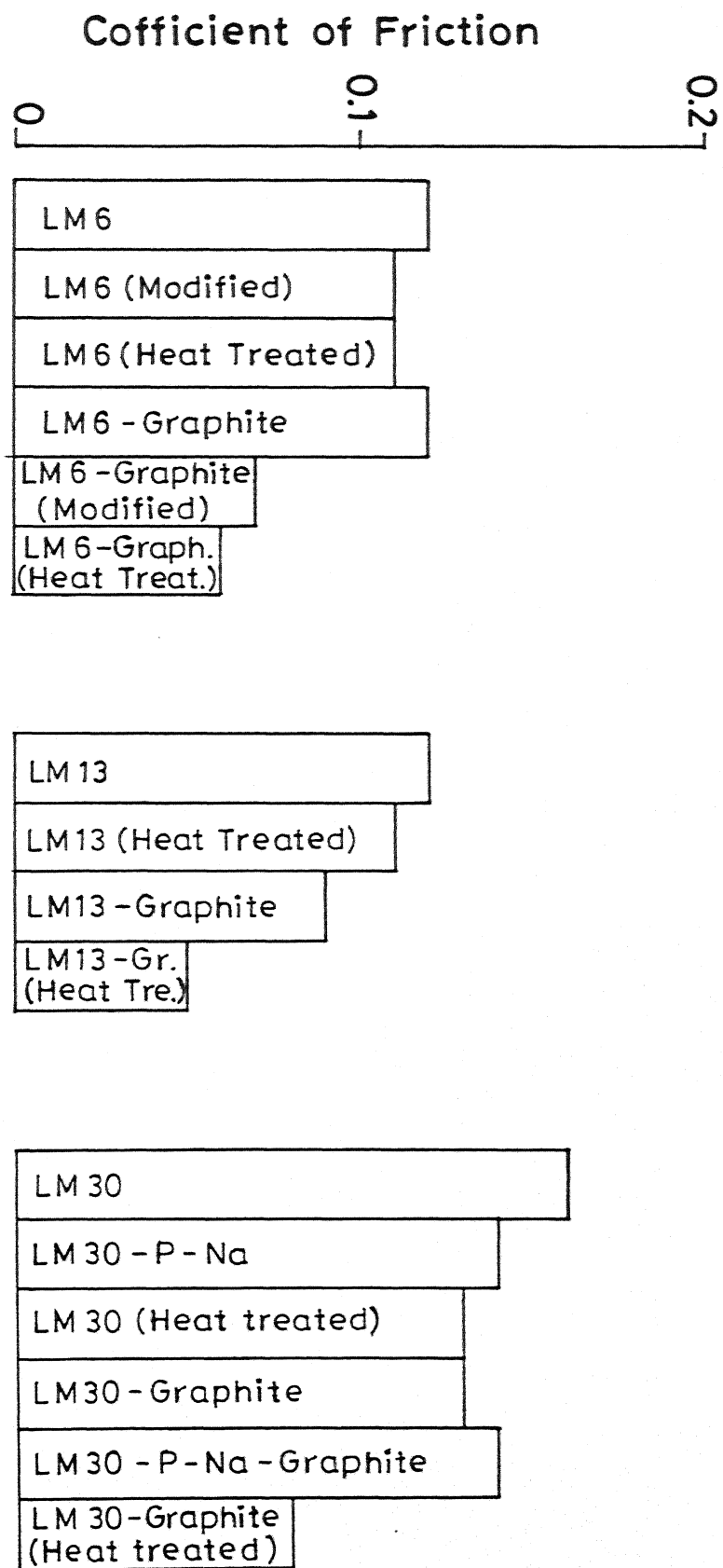


Fig. 6.6 Coefficient of Friction of Al-Si Alloys and Composites During Dry Sliding Wear.

of the experiment to prevent the metal to metal contact and coefficient of friction values are found to be more or less the same in all the samples. However, in this case also, the performance of heat treated composites was superior to those of the rest as their P-V limits are highest.

It can be concluded from the present investigation that the efficiency of solid lubrication by graphite in aluminium alloy-graphite composites depends on the microstructure of the matrix. With rapid solidification processing the size of the eutectic silicon could be further reduced to less than 1.0 μm with near spherical morphology. Rapidly solidified alloys also offer excellent strength as well as ductility. However, their shapes at present, are restricted to thin ribbons, powders and platelets but the recent advancements in processing technologies have enabled the consolidation of these powders into useful shapes. Using rapid solidification techniques, it may even be possible to fabricate potentially important tribo-components.

CHAPTER 7

CONCLUSIONS

1. Graphite particle dispersed Al-Si alloys have been produced by casting route. Both hypoeutectic alloys (B.S.:LM6 and LM13) and hypereutectic (B.S.:LM30) alloy are used as matrix materials. The alloys and composites containing 3 wt.% graphite particles were subjected to heat treatment. In the case of hypereutectic alloy and its based composites, minute quantities of phosphorus and sodium were added in a variety of sequences to achieve modification of eutectic silicon and refinement of primary silicon. Microstructural analysis was carried out on samples cast in 18 mm diameter cast iron moulds.
2. Distribution of graphite particle size and interparticle spacing across three different sections along the ingot height-top, middle and bottom has been evaluated using optical microscopy. Results indicated the absence of particle clustering.
3. Microstructure of hypoeutectic alloy consisted of primary aluminium and eutectic phases; while those of hypereutectic alloy contained primary silicon in addition to Al-Si eutectic. Additionally, halo of primary aluminium was observed around the primary silicon.
4. The microstructures of hypoeutectic Al-Si alloy solidified in the presence of graphite particles showed that primary aluminium did not nucleate on the surface of graphite particle. Instead α -aluminium was found to nucleate in the centre of intergraphite channels avoiding the graphite particles.
5. In the case of hypereutectic alloy composites, primary silicon was found to nucleate preferentially on graphite particle. Halo formation was found to ^{be} suppressed when solidification took place in presence of dispersed graphite particles.

6. In hypoeutectic Al-Si (LM6) alloy composites, the anisotropic growth of eutectic silicon was suppressed by the addition of modifiers (e.g., sodium in elemental form) before dispersion of graphite particles. Modification of eutectic silicon resulted in scaled down the size of eutectic silicon but its morphology remained microfaceted.

Sequential addition of phosphorus and sodium to the hypereutectic Al-Si (LM30) alloy melt was found to refine and modify the primary and eutectic silicon respectively. In LM30-graphite particle composites, sodium must be added prior to dispersing graphite particles to achieve effective modification.

7. Heat treatment of Al-Si alloys, altered the silicon morphology from faceted to nearly spherical.

8. The l/d ratios of silicon in Al-Si eutectic alloy were measured using two dimensional metallography. The average l/d ratio varied from 9.0 in die cast alloy to 2.0 in sodium modified alloy. It was further reduced to 1.6 in the case of heat treated alloy.

9. Single roll melt spinning technique was employed to produce rapidly solidified LM6 alloy and LM6-10 wt.% graphite particle composites. Microstructural observation revealed that the plate-shaped silicon in conventional die cast alloy could be altered to nearly spherical in rapidly quenched alloys. For instance, the plate-shaped eutectic silicon in die cast alloy was in the size range of 5-12 μm long and 1-2 μm wide whereas, the average size of near spherical silicon in the case of rapidly solidified alloy was around 1 μm . A marked difference in the growth morphology of eutectic silicon near and away from the dispersed graphite particles was observed. Near the graphite particles eutectic silicon was plate-shaped whereas away from the graphite particles it was found to grow as near-spherical. This alteration of growth morphology of eutectic silicon (which could be a major limitation of producing rapidly solidified composites) was attributed to the thermal barrier offered by the suspended graphite particles during solidification.

10. Tensile strength of Al-Si (LM6,LM13,LM30) alloys was decreased by approximately 30% due to the dispersion of 3 wt.% graphite particles. Considerable increase in tensile strength was achieved due to heat treatment. Percentage elongation is restricted to 1.0% in all the samples except in the case of heat treated LM6 alloy, where the % elongation was around 4.0%.

11. The sliding wear rates (against rotating EN25 steel disc) of all the three Al-Si alloys were found to increase with applied pressure. In die cast condition, LM30 alloy was found to be superior to LM6 and LM13 alloys as far as the wear and seizure resistances were concerned. Depending upon the magnitude of applied pressure two distinct wear regimes were observed; one is mild wear and the other one is severe wear. In mild wear regime, fine equiaxed debris particles were generated whereas in severe wear coarse flaky-debris were observed.

12. The worn surfaces of die cast Al-Si alloys showed continuous grooves, damaged regions and the presence of surface cracks. Worn surfaces of die cast composites showed identical features. The tendency to fracture was reduced in the case of heat treated alloys.

13. Heat treated composites (LM6,LM13 and LM30 based) showed least wear and maximum resistance to seizure. In contrast, worn surfaces of heat treated composites showed the presence of graphite film on them.

14. The coefficient of friction for hypereutectic (LM30) alloy (0.172) was found to be higher than LM13 alloy (0.125). There was slight reduction in the coefficient of friction due to graphite particle dispersion. For example, the coefficient of friction of LM13 alloy was reduced to 0.103 while that of LM30 alloy to 0.140 due to graphite particle dispersion. In contrast, the coefficients of friction of heat treated composites in both cases were reduced by more than 50%. The temperature rises in the case of heat treated composites were also found to be minimum.

15. The debris at higher applied pressures was found to be large and flake-shaped. In the case of die cast LM13 alloy mean debris size was found

to be 289 μm . The size of the debris is significantly reduced to 76 μm in the case of heat treated LM13 alloy composites. Wear debris in the case of LM30 alloy consisted of flakes (Mean particle size: 97 μm) and sharp edged fragmented silicon particles (mean particle size: 66 μm).

16. The P-V limits i.e., the maximum allowable bearing pressure (P) at a particular speed (V) of Al-Si (LM6, LM13 and LM30) alloys and composites were evaluated in partially lubricated condition. P-V limits of the heat treated composites under partially lubricated conditions were found to be higher than those of the other materials.

17. The essence of this thesis is that the solid lubricating property of graphite in aluminium-graphite composites could be exploited if the micro-structure of the matrix alloy is optimized.

REFERENCES

1. Aluminium: Properties and Physical Metallurgy, John E. Hatch, Ed. American Society for Metals, Metals Park, Ohio, p.2,1984.
2. Light Alloys: Metallurgy of the Light Metals, I.J. Polmear, Edward Arnold (Publishers) Ltd., London, p.76,1981.
3. Reference No.1 p.341.
4. Reference No.2 p.121
5. Reference No.1,pp.347; Reference No.2, p.121.
6. J.L. Jorstad Trans. Met.Soc.AIME, 242 (1968) 1217.
7. Reference No.1, p.30
8. A.P. Bates and D.S. Calvert, The British Foundryman,(March,1966)119.
9. P.H. Shingu and Jin-Ichi Takamura, Met.Trans.,1 (August,1970)2339.
10. A. Pacz, U.S. Patent No.1,387,900, (1921).
11. R.C. Plumb and J.E. Lewis, J.Inst. Metals, 86 (1957-58) 393.
12. C.B. Kim and R.W. Heine, J.Inst. Metals,92 (1963-64) 367.
13. N. Kanani and G.R. Abbaschian, Aluminium, 60 (1984) E 505.
14. D.C. Jenkinson and L.M. Hogan, J.Cryst. Growth,28 (1975) 171.
15. M.D. Hanna, Shu-Zu-Lu and A. Hellawell, Met.Tran., 15A, (March 1984) 459.

16. B.M. Thall and B. Chalmers, J. Inst. Metals, 77 (1950) 79.
17. Shu-Zu-Lu and A. Hellawell, Aluminium Alloys-Physical and Mechanical Properties, (Conf. Proc.) Vol.1, Charlottesville, Virginia, USA, 15-20 June, p.81, 1986.
18. R. Elliott, Mater.Sci.Engg., 65 (1984) 85.
19. S. Das, A.H. Yegneswaran and P.K. Rohatgi, J.Mater. Sci.,22 (1987) 3173.
20. Clifford F. Lewis, Materials Engg., (May 1986) 33.
21. A.A. Das and S. Chatterjee, The Metallurgist and Materials Technologist, (March 1981) 137.
22. B.F. Quigley, G.J. Abbaschian, R. Wunderlin and R. Mehrabian, Met. Trans., 13A, (1982) 93.
23. F.A. Badia and P.K. Rohatgi, SAE Trans.,78 (1969) 1200.
24. A.M. Patton, J. Inst. Met., C 100 (1972) 197.
25. P.R. Gibson, A.J. Clegg and A.A. Das, Foundry Trade J., 25 (1982) 253-256, 262-263.
26. L. Bruni and P. Iguera, Automotive Engineer, 3(1) (1978) 29.
27. M. Suwa, K. Komaro and K. Sueno, Jpn. Soc. Lubr. Engg., 40 (1976) 1074.
28. Deonath and P.K. Rohatgi, J. Mater. Sci., 16 (1981) 1599.
29. Akira Sato and Robert Mehrabian, Met. Trans., 7B (Sept. 1976) 443.

30. T.P. Murali, M.K. Surappa and P.K. Rohatgi, Met. Tran., 13B (1982) 485.
31. A.K. Jha, T.K. Dan, S.V. Prasad and P.K. Rohatgi, J. Mater.Sci., 21 (1986) 3681.
32. A. Banerjee, M.S. Thesis, University of Kerala, India (1982).
33. R. Mehrabian, R.G. Riek and M.C. Flemings, Met. Trans. 5 (August 1974) 1899.
34. M.K. Surappa and P.K. Rohatgi, J. Mater. Sci. 16(4) (1981) 983.
35. P.K. Rohatgi, B.C. Pai and S.C. Panda, J. Mater.Sci., 14 (1979) 227.
36. K.J. Bhansali and R. Mehrabian, J. Met., 34(9) (1982) 30.
37. A. Sato and R. Mehrabian, Met. Tran., 7B (1976) 443.
38. P.K. Rohatgi, R. Asthana and S. Das, Int. Met. Rev., 31(3) (1986) 115.
39. A. Mortensen, M.N. Gungor, J.A. Cornie and M.C. Flemings, J.Met., (March 1986) 30.
40. M.C. Flemings, A. Mortensen and J.A. Cornie, Metallurgical Science and Tech., 5(1) (1987) 3.
41. B.P. Krishnan and P.K. Rohatgi, Metal Tech., 11 (1984) 41.
42. P.R. Gibson, A.J. Clegg and A.A. Das, Wear 95 (1984) 193.
43. S.K. Biswas and B.N. Pramila Bai, Wear 68 (1981) 347.
44. C. Subramanian and Kishore, J. Reinforced Plastics and Composites 3 (Oct. 1984) 278.

45. P.K. Rohatgi and B.C. Pai, Tran. ASME, 101 (july 1979) 376.
46. B.C. Pai, P.K. Rohatgi and S. Venkatesh, Wear 30 (1974) 117.
47. K.F. Kobayashi and L.M. Hogan, J. Mater. Sci., 20 (1985) 1961.
48. 'Eutectic Alloy Solidification', by G.A. Chadwick in Progress in Materials Science, B. Chalmers, ed., Vol.12, Pergamon Press, Oxford, England, p.160 (1963).
49. A. Hellawell, Prog. Materials Science, 15 (1970) 1.
50. G.K. Sigworth, Trans. A.F.S. 91 (1983) 7.
51. Shu-Zu-Lu and A. Hellawell, Met., Trans., 18A (1987) 1721.
52. M.G. Dey and A. Hellawell, J. Inst. Metals, 95 (1967) 377.
53. S. Chatterjee and A.A. Das, Brit. Foundryman 66 (1973) 118.
54. W.F. Shaw and T. Watmough, Foundry 97 (1969) 166.
55. J. Cisse, G.F. Bolling and H.W. Kerr, Met. Trans., 6B (March 1975) 195.
56. A.J. Clegg and A.A. Das, Brit. Foundryman 70 (1977) 56.
57. C. Mascré, Foundry Trade J. 25 (1953) 725.
58. M. Sugiyama, J. Sata, J. Jpn. Foundrymen's Soc. 37 (1965) 209.
59. G.F. Bolling, J. Cisse and G.S. Cole, US Patent No.3,607,241 (1971).
60. H. Fredriksson, M. Hillert and N. Lange, J. Inst. Metals, 101 (1973) 285.

61. M. Itagaki, B.C. Giessen and N.J. Grant, Trans. ASM, 61 (1968) 330.
62. S.K. Bose and R. Kumar, J. Mater. Sci., 8 (1973) 1795.
63. R.H. Shingu, K. Kabayashi, K. Shimomura and R. Ozaki, Trans. Jpn. Inst. Met., 37(4) (1973) 433.
64. J. Axon and W. Hume-Rothery, Proc. Roy. Soc. (London), A 193, (1948) 1.
65. S.C. Agarwal, M.J. Koczak and H. Herman, Scrp. Met. 7 (1973) 365.
66. P. Van-Mourik, E.J. Mittemeijer and Th.H.De Keijser, J. Mater.Sci., 18 (1983) 2706.
67. A. Bendijk, R. Delhez, L. Katgerman, Th.H.De Keijser, E.J. Mittemeijer and N.M. Van Der Pers, J. Mater. Sci., 15 (1980) 2803.
68. K.N. Ishihara and P.H. Shingu, J. Mater.Sci., Lett., 3 (1984) 1015.
69. J.C. Baker and J.W. Cahn, 'Sodification', American Society for Metals, Metals Park, Ohio, (1971) 23.
70. C.G. Levi and R. Mehrabian, 'Rapid Solidification Technology-Source book', compiled by R.L. Ashbrook, ASM, (1983) 403.
71. B.A. Mueller, J.J. Richmond and J.H. Perepezko, Rapidly Quenched Metals, Vol.I, (Conf. Proc.) S. Steeb and H. Warlimont, Eds., Wurzburg, Germany, September 3-7, (1984) p. 47.
72. J.A. Van Der Hoeven, P. Van Mourik and E.J. Mittemeijer, J. Mater. Sci., Lett.,2 (1983) 158.
73. R. Delhez, Th. H.De Keijser, E.J. Mittemeijer, P. Van. Mourik, N.M.Van Der Pers, L. Katgerman and W.E. Zalm, J. Mater. Sci., 17 (1982) 2887.

74. S. Paidassi and J. Chevrier, Rapidly Quenched Metals (Conf. Proc.) Vol.1, S. Steeb and H. Warlimont, Eds., Wurzburg, Germany, Sept., 3-7, (1984) p. 957.
75. Anne-Marie Papon and Serge Paidassi, 'Rapidly solidified Materials', (Conf.Proc.), P.W. Lee and R.S. Carbonara Eds., San Diego, California, USA, February 3-5 (1985), published by American Society for Metals, p. 317.
76. K. Marsdem, J. Metals, 37(6), (1985) 59.
77. J.A. Dicarlo, J. Metals. 37(6), (1985) 44.
78. Technology forecast '86, Nonferrous Metals, H.E. Chandler and A.L. Hitchcox, Metal progress 129(1) (1986) 76.
79. W. Harrigan, J. Metals, 37(6) (1985) 58.
80. M.K. Surappa and P.K. Rohatgi, Met. Technol., 5 (1982) 1209.
81. B.P. Krishnan and P.K. Rohatgi, J. Mater. Sci., 16 (1982) 1209.
82. T.P. Murali, M.S. Thesis, Univ. of Kerala, India, 1982.
83. Deonath, Ph.D. Thesis, IISc., Bangalore, India (1977).
84. B.S. Majumdar, A.H. Yegneswaran and P.K. Rohatgi, Mater. Sci., and Engg., 68 (1984) 85.
85. T.W. Chou, A. Kelly and A. Okura, Composites, 16(3) (1985) 187.
86. Hand Book of Composites, George Lubin, Ed., published by Van Nostrand Reinhold Company Inc., New York, USA (1982) 479.
87. F.A. Badia and P.K. Rohatgi, Trans. AFS., 77 (1969) 402.

88. M.K. Surappa and P.K. Rohatgi, Met. Technol., 7 (1980) 378.
89. R.J. Omalley, C.E. Dremann and D. Apelian, J. Metals, 31 (1979) 14.
90. B.P. Krishnan, M.K. Surappa and P.K. Rohatgi, J. Mater. Sci., 16 (1981) 1209.
91. A. Banerjee, M.K. Suprappa and P.K. Rohatgi, Met. Trans. 14B (1983) 273.
92. B.C. Pai, S. Ray, K.V. Prabhakar and P.K. Rohatgi, Mater. Sci. Engg., 24 (1976) 31.
93. S. Biswas, V. Srinivasa, S. Seshan and P.K. Rohatgi, Trans. AFS, 88 (1980) 159.
94. J. Sugishita, S. Fujiyoshi and T. Imura Wear 81 (1982) 209.
95. D.M. Karpinos, P.M. Askarov and O.V. Abramov, Sov. Powd. Metall. Met. Ceram., 21 (1982) 213.
96. L.E. Kindliman and G.S. Ansell, Met. Trans., 1 (1970) 507.
97. G.J. London, Document R 59, SD, 407 General Electric Tech., Inf. Service (1959).
98. T. Tawarda, S. Okaniwa and K. Nagahashi, US Patent No.3,877,844 (Aug. 15, 1975).
99. T. Young, Trans. Roy. Soc., 95 (1805) 65.
100. B.C. Pai and P.K. Rohatgi, Mater. Sci. Engg., 21 (1975) 161.
101. H. Tokisue and G.J. Abbaschian, Mater. Sci. Engg., 34 (1978) 75.
102. K. Gopakumar, T.P. Murali and P.K. Rohatgi, J. Mater.Sci., 17 (1982) 1041.

103. A.C.D. Chakladar and K.R. Linger, Composites (Oct. 1976) 239.
104. T. Erturk, V. Gupta, A.S. Argon and J.A. Cornie, Sixth Int. Conf. on Composite Materials, ICCM and ECCM held on 20-24 July 1987 at Imperial college of Science and Technology, London, (Conf. Proc.) Vol.2, F.L. Mathews, N.C.R. Buskell, J.M. Hodgkinson and J.Morton, Eds.
105. A.K. Dhingra, Phil. Trans. Royl. Soc., A294 (1980) 151.
106. Mitsubishi Industries, Japanese Patent No.5834148 (1983).
107. F. Delannay, L. Foryen A. Deruyttere, J. Mat. Sci., 22 (1987) 1.
108. M. Suwa and K. Komuro, U.S. Patent No.4,207,096, (1980).
109. P.K. Rohatgi, B.C. Pai and S.C. Panda, J. Mater. Sci., 15 (1980) 1241.
110. Deonath, R.T. Bhat and P.K. Rohatgi, J. Mater. Sci., 16 (1981) 1209.
111. B.N. Keshavram, A. Banerjee, M.K. Surappa and P.K. Rohatgi, J. Mater. Sci. Lett., 1 (1982) 29.
112. S. Das, T.K. Dan, S.V. Prasad and P.K. Rohatgi, J. Mater. Sci. Lett., 5 (1986). 562.
113. A. Banerjee, P.K. Rohatgi and W. Reif, Metall. 38 (1984) 656.
114. A. Banerjee and P.K. Rohatgi, J. Mater. Sci., 17 (1982) 335.
115. Takao Choh, Roland Kammel and Takeo Oki, Z. Metallkde., 78 (1987) 286.
116. S.Y. Oh, J.A. Cornie and K.C. Russell, Ceramic Engineering and Science Proceedings of the 11th Annual Conf. on composites and advanced ceramic materials, January 18-23, 1987.

117. C.G. Levi, G.J. Abbaschian and R. Mehrabian, Met. Trans., 9A (1978) 697.
118. R.G. Riewald, W.H. Krueger and A.K. Dhingra, US patent No.4,012,204, March 15 (1977).
119. S.K. Rhee, J. of the American Ceramic Society, 55(6) (1972) 300.
120. N. Eustathopoulos, J.C. Joud, P. Desre and J.M. Hicter, J. Mater. Sci., 9 (1974) 1233.
121. J.A. Champion, B.J. Keene and J.M. Silwood, J. Mater. Sci., 14 (1969) 39. .
122. V. Agarwal and D. Dixit, Trans. Japan Inst. Met., 22 (1981) 521.
123. P.R. Gibson, A.J. Clegg and A.A. Das, Mater. Sci. Tech., 1 (1985) 559.
124. P.K. Ghosh, S. Ray and P.K. Rohatgi, Tran. Jpn. Inst. Met., 25 (1984) 57.
125. D.R. Uhlman, B. Chalmers and K.A. Jackson, J. Appl. Phys., 35(10) (Oct. 1964) 2986.
126. J. Cisse and G.F. Bolling, J. Cryst. Growth, 10 (1971) 67.
127. A.A. Chernov and A.M. Melnikova, Sov. Phys. crystt., 10 (1966) 66.
128. S.N. Omenyi and A.W. Neumann, J. Appl. phy., 47 (1976) 3956.
129. M.K. Surappa, M.Sc. Thesis, Indian Institute of Science, Bangalore, India (1975).
130. M.K. Surappa and P.K. Rohatgi, J. Mater. Sci. Lett., 16 (1981) 562.

131. A.M. Zubko, V.G. Lobanov and U.V. Nikonova, *Sov. Phys. Cryst.* 18(2) (1973) 239.
132. R. Asthana, S. Das, T.K. Dan and P.K. Rohatgi, *J. Mater. Sci. Lett.*, 5 (1986) 1083.
133. E.G. Kendall, *Composite Materials, Vol.4 Metallic Matrix Composites*, K.G. Krieder Eds., Acad. Press (1974).
134. E. Nakata, Y. Kayawa and H. Terao, Report of the castings Research Laboratory, Waseda University, Japan, No.34, (1983) p.27.
135. T.W. Clyna, M.G. Bader, G.R. Capplemann and P.A. Hubert, *J. Mater. Sci.*, 20 (1985) 85.
136. S. Towata and S. Yamada, *J. Jpn. Inst. of Metals*, 48(12) (1984) 1282.
137. Y. Sawada and M.G. Bader, *Proc. Fifth Int. Conf. on Composite Materials ICCM V*, San Diego (Aug. 1985) p.785.
138. A.R. Champion, W.H. Krueger, H.S. Hartmann and A.K. Dhingra, *Proc. of the Int. Conf. on Composite Mater. AIME, ICCM 2*, (1978) p.883.
139. W.C. Harrigan and D.M. Goddard, *Proc. of the Int. Conf. on Composite Materials, ICCM I*, Scala et al., Eds., TMS of AIME, (1975) p.849.
140. H. Fukunaga and K. Goda, *Bull. of the Jap. Soc. of Mech. Engg.*, 28(235) (Jan. 1985) 1.
141. S. Towata, S. Yamada and T. Ohwari, *Trans. of the Japan Inst. of Metals*, 26(8) (1985) 563.
142. J.A. Cornie, A. Mortensen, M.N. Gungor and M.C. Flemings, *Proc. of the Fifth Int. Conf. on Composite Materials, ICCM V*, San Diego, Harrigan et al., Eds., (1985) p.807.

143. M.N. Gungor, J.A. Cornie and M.C. Flemings Proc. of the Sym. of Interfaces in Metal-Matrix composites, TMS-AIME Annual Meeting, New Orleans, Louisiana, USA, March 2-6 (1986).
144. B. Chalmers, 'Principles of Solidification', (Robert E Krieger Publ. Co. Huntingdon, New York p.229).
145. M.K. Surappa, Ph.D. Thesis, Indian Institute of Science, Bangalore, India (1979).
146. B.P. Krishnan, Ph.D. Thesis, Indian Institute of Science, Bangalore, India (1980).
147. P.K. Rohatgi, N. Murali, H.R. Shetty and R. Chandrasekhar, Mater. Sci. Engg. 26 (1976) 115.
148. Deonath, R. Narayan and P.K. Rohatgi, J. Mater. Sci., 16 (1981) 3025.
149. P.K. Ghosh, P.R. Prasad and S. Ray, Z. Metallu, 75 (1984) 934.
150. M. Hasegawa and N. Taueshita, Metal. Tran. 9B (1978) 383.
151. P.K. Rohatgi and M.K. Surappa, Mater. Sci. Engg. 62 (1984) 159.
152. A.P. Divecha, S.G. Fishman and S.P. Karmarkar, J. Metals., 33 (1981) 12.
153. H.W. Bergman, Z. Metalln 70 (1979) 82.
154. E. Yuasa and T. Moroona, J. Jpn. Soc. Techn. Plast. 22 (1981) 482.
155. E. Yuasa and T. Moroona, In Proc. 25th Jpn. Congress on Mater. Res. Non metallic materials, (March 1982) Soc. Mater. Sci. Japan p.307.

156. U.T.S. Pillai, R.K. Pandey and U.D.P. Nigam Vth Int. Conf. on Composite Materials, ICCM V, (Conf. proc.) San Diego, California, USA (July 1985).
157. S. Ray, Bull. Mater. Sci., India 6 (1984) 799.
158. S.D. Tsai, D. Mahulinar, H.L. Marcus, T.C. Noyan and J.B. Cohen, Mater. Sci. Engg. 47 (1981) 145.
159. C.A. Brown and M.K. Surappa, Mater. Sci. Engg. 102 (1988) 31.
160. A.R.E. Singer, Int. J. Powder Metall. 21(3) (1985) 219.
161. A.R.E. Singer, Ann. CIRP, 32(1) (1983) 145.
162. J.D. Ayers, R.J. Schaefer and W.P. Robey, J. Metals (Aug. 1981) 19.
163. J.D. Ayers, Wear 97 (1984) 249.
164. J.D. Ayers and R.N. Bolster, Wear 93 (1984) 193.
165. P.G. Zielinski and D.G. Ast. J. Mater. Sci. Lett. 2 (1983) 495.
166. H. Kimura, T. Masumota and M. Hasegawa, J. Mater Sci. Lett., 3 (1984) 1003.
167. J.T. Burwell, Wear 1 (1958) 119.
168. E. Rabinowicz, 'Friction and Wear of Materials', John Wiley and Sons Inc. (1965) p.114.
169. Nam P. Suh and Coworkers 'The delamination theory of Wear', Elsevier Sequoia S.A. Lausanne, (1977).
170. E. Rabinowicz, L.A. Dunn and P.G. Russell Lub. Engg. 17 (1961a) 587.

171. E. Rabinowicz, L.A. Dunn and P.G. Russell, *Wear*, 4 (1961b) 345.
172. P.K. Rohatgi and B.C. Pai, *Wear* 28 (1974) 353.
173. A.D. Sarkar, *Wear* 31 (1975) 331.
174. R. Shivanath, P.K. Sengupta and T.S. Eyre, *Br. Found.* 70 (1977) 349.
175. J. Clarke and A.D. Sarkar, *Wear* 54 (1979) 7.
176. A.D. Sarkar and J. Clarke, *Wear*, 61 (1980) 157.
177. J. Clarke and A.D. Sarkar, *Wear* 69 (1981) 1.
178. J. Clarke and A.D. Sarkar, *Wear* 82 (1982) 179.
179. M.J. Kadhim, E.S. Dwarakadasa, *J. Mater. Sci. Lett.* 1 (1982) 503.
180. A.D. Sarkar and J. Clarke, *Wear* 75 (1982) 71.
181. B.N. Pramila Bai, S.K. Biswas and N.N. Kumtekar, *Wear* 87 (1983) 237.
182. Ross Antoniou and Douglas W. Borland, *Mater. Sci. Engg.* 93 (1987) 57.
183. K. Okabayshi and M. Kawamoto, *Bull. Univ. Osaka, Prefecture A*, 17 (1968) 199.
184. G. Vandelli, *Aluminio*, 37 (1968) 121.
185. K. Okabayashi, Y. Nakatani, H. Notani and M. Iawamoto, *Keikinzoku*, 14 (1964) 57.
186. G.A. Colligon, *Trans. Am. Foundrymen's Soc.* 81 (1973) 359.

187. E.E. Stonebrook, Mod. Cast., 38 (1960) 111.
188. Mohammed Jasim & E.S. Dwarakadasa, Trans. IIM 37 (5) (1984) 581.
189. B.P. Krishnan, N. Raman, K. Narayanaswamy and P.K. Rohatgi, Tribology Int. 16(5) (oct. 1983) 239.
190. S.V. Prasad and P.K. Rohatgi, J. Metals (Nov. 1987) 22.
191. B.P. Krishnan, N. Raman, K. Narayanaswamy and P.K. Rohatgi, Tribology Int. 14(5) (1981) 301.
192. B.P. Krishnan, N. Raman, K. Narayanaswamy and P.K. Rohatgi, Wear 60 (1980) 205.
193. V.G. Gorbunov, V.D. Parshin and V.V. Panin, Liteinoe Proizod 8 (1974) 20.
194. G. Gustafsson, T. Thorvaldsson and G.L. Dunlop, Met. Trans., 17A (1986) 45.
195. Metallurgy for Engineers, E.C. Rollason, ELBC and Edwar Arnold (Publishers) Ltd. (1973) p. 340.
196. M.F.X. Gigliotti, Jr., G.A. Colligan and G.L.F. Powell, Met. Trans., 1 (1970) 891.
197. B.E. Sundquist, R. Bruscatto and L.F. Mondolfo, J. Inst. Metals, 91 (1962-63) 204.
198. A. Kofler, J. Astral. Inst. Metals, 10 (1965) 132.
199. F. Yilmaz and R. Elliott, Met. Sci., 18 (1984) 362.
200. M. Humenik Jr. and W.D. Kingery, J. Am.Ceram. Soc. 37(1) (1954) 18.

201. P.Y. Zhu and Q.Y. Liu, Mater. Sci. Tech., 2(5) (1986) 500.
202. E.R. Braithwaite and G.W. Rowe, Scientific Lubrication (March 1963) 92.
203. Wear of Metals by A.D. Sarkar, International Series on Materials Science and Technology Vol.18, Pergamon Press, (1976) p. 36.
204. Reference No.203 p. 75.

2.3 Wear

Wear is defined as the damage to a solid surface, generally involving a progressive loss of material, due to relative motion between that surface and a contacting substance or substances (166a).

Wear of a material is controlled by the material characteristics as well as test parameters such as applied pressure, sliding speed, environment and the type of sliding interaction. Burwell (167) classified wear into the following major groups: adhesive, abrasive, corrosive, surface fatigue and erosive.

(i) Adhesive or sliding wear: Adhesive or sliding wear occurs as a result of relative sliding between two surfaces under the influence of an applied load (168). In general, on a microscopic level, the machined surface of a material is not exactly flat but consists of sharp asperities. When two solid surfaces are brought in close proximity, the surface would be touching only at a few points, and they adhere strongly to each other and form asperity junctions. As the contact area is very small, the pressure exerted on each asperity is extremely high. This results in elastic and plastic deformation of the softer of the two materials in contact until the areas of the contact junctions are large enough to support the load. If the strength of the junction is more than the shear strength of the softer material then during sliding action the tangential force will shear the softer junctions and leave clean surface at the softer asperity (168a, 168b). The consequences of the above process result in the transfer of softer material to the harder counterface (168c, 168d). There is every possibility that the transferred material may remain adhered to the harder surface or in subsequent sliding may get knocked down resulting in loose wear debris. The possibility of the softer material either adhering or getting knocked off from the harder surface has been explained with the help of an energy model as shown by Davies (168e). The energy model states that the adhered material will get detached from the harder surface only when the residual energy of the transferred material is more than the adhesion energy. The residual energy is accumulated by the way of repetitive collisions. The morphology of these transferred materials has been studied by Chen and Rigney (168f). Their results indicate that initial transfer events form discrete fragments and on prolonged sliding give rise to layer or patches, mainly consisting of finely mixed material on the surface.

Formation of oxide films on the tribo-surfaces during sliding wear has been the subject of many investigators (168, 168g, 168h). Such oxide films retard further material loss and alter the friction and wear behaviour of sliding materials.

Blau (168i) has discussed various processes that may cause transition in the friction and wear behaviour. Some of these processes are: (i) metal transfer, (ii) film formation, (iii) debris generation and (iv) cyclic surface deterioration.

In addition to the above, the temperature and the nature of the sliding surfaces profoundly affect the quantity of transferred material. It has been pointed out that the high temperature of the sliding assembly increases and accelerates adhesive wear (168). The temperature of the sliding assembly may also be enhanced by way of frictional heating. It has been reported (168) that during adhesive transfer, a material produces a spot on the surfaces, which effectively increases the friction and then rate of heating. This consequently raises the temperature and leads to heavy damage to the sliding materials. Sata (168j) has made attempts to study the dependence of wear rate on temperature of the sliding surfaces. The microstructure of the material at or below the wear surface (i.e. in the subsurface regions) is reported to change due to sliding wear (168k) and the extent of this change in microstructure depends upon the sliding conditions and properties of the sliding materials.

A critical evaluation of the assumptions of the adhesion theory of wear leads to the following points (169):

- a) The adhesion theory of wear assumes that the material removal due to shearing of junctions is only possible when the strength of the junction is more than the shear strength of the softer material. This proposition is questionable because the interface cannot be stronger than the contacting materials as it is likely to contain vacancies, impurities or oxides. Therefore, complete adhesion and material removal may not be possible.
- b) Adhesion theory does not make any concrete predictions on how the fracture occurs in one of the surfaces.
- c) The theory also ignores the controlling effect of friction force on the wear rate.
- d) Adhesion theory does not consider the structure and the mechanical properties of the materials.

Suh et.al. (169) have proposed the delamination theory in order to explain the sliding wear of material and the generation of flake-type wear debris. This theory describes the following sequential events which lead to loose wear particles: during sliding wear, the normal and tangential loads are transmitted through the contact points by adhesive and plowing action. The asperities of the softer material may either be deformed or fractured. This makes the surface of the soft

material smooth and the contact is not just an asperity to asperity, but rather asperity to plane. The surface fraction exerted by the hard asperities on the softer surface induces plastic deformation. The continuous deformation results in void formation below the sliding surfaces. Void nucleation on the surface is ruled out as the compressive state of stress is maximum at the surface. Once, the cracks are nucleated further loading and deformation cause cracks to propagate. When these subsurface cracks reach a critical length they become unstable and shear to the surface at some weak positions. This mechanism of wear has become the subject of much discussion and certain aspects of the crack nucleation and propagation remain unclear.

ii) Abrasive wear: Abrasive wear is accomplished by plowing or cutting action of hard particles on a relatively softer surface of the material. The hard particles may be either loosely held between two sliding surfaces as in three body abrasive wear or part of the second surface as in two body abrasive wear using abrasive papers. A semi-quantitative expression to predict abrasive wear was derived by Rabinowicz and coworkers (170,171) assuming that the asperities on the hard surface are conical in nature. Misra and Finnie (171a, 171b) have recently reviewed the abrasive wear of metals. Kosel and Fiore (171c) have also reviewed the abrasive wear mechanism in dual phase alloys.

iii) Corrosive wear: Corrosive wear occurs whenever sliding takes place in corrosive environments. Corrosion products are formed and their removal from the surface is accomplished by sliding action thereby allowing corrosive attack to continue (171d, 171e). Air, at room temperature, containing humidity is the most commonly occurring corrosive medium. It reacts with sliding surfaces and forms oxides and hydroxides. These compounds are loosely adherent to the metal surface and get peeled off during sliding action. In addition, chlorides and oxychlorides are commonly formed in industrial environments near the coastal regions. It has been reported (167) that most of the passenger car engine's piston rings and cylinders can be deteriorated by corrosive wear.

iv) Surface Fatigue Wear: Surface fatigue wear is caused by the removal of particles from the surface due to cyclic loading. This is generally associated with the surfaces in rolling contact, where the friction coefficient is negligible (171f). Wear due to fatigue can also occur during sliding operation by way of cyclic crack growth (171f,171g). The wear mechanism is mainly governed by the formation of surface or subsurface cracks and fatigue crack propagation. The crack nucleation process in rolling contact fatigue is similar to the fatigue wear due to sliding action. The main difference is that in sliding wear the plastic zone

- 166a. ASTM standard G-40
- 168a. J.F. Archard, J. Appl. Phys., 24 (1953) 981.
- 168b. F.P. Bowden and D.Tabor, 'The Friction and Lubrication of Solids', Clarendon Press, Oxford (1954).
- 168c. I.M. Feng. J. Appl. Phys. 23 (9) (1952) 1011.
- 168d. J.T. Burwell and C.D. Stany, J. Appl. Phys. 23(1) (1952) 18.
- 168e. R. Davies, 'Friction and Wear,' Elsevier, Amsterdam (1953).
- 168f. L.H. Chen and D.A. Rigney, Wear, 105 (1985) 47.
- 168g. I.V.Kragelskii, 'Friction and Wear', Butterworth, London, 1965.
- 168h. T.F. Quinn, J.L. Sullivan and D.M. Rowson, Proc. Int. conf. on Wear of Materials, Dearborn, MI, 1979, ASME, New York, (1979) pp.1-11.
- 168i. Peter J. Blau, Wear, 72 (1981) 55.
- 168j. T. Sata, Proc. 3rd Japan Natl. Cong. Appl. Mechanics, (1953) 153.
- 168k. Peter J. Balu, Solid contact and lubrication, AMD-vol.39 H.S. Cheng and LM Keer, Eds., published by ASME, pp 185-191.
- 171a. A. Misra and I. Finnie, J. Eng. Mater. Technol. (Trans ASME) 104 (1982) 94.
- 171b. A. Misra and I. Finnie, Wear 65 (1981) 359.
- 171c. T.H. Kosel and N.F. Fiore J. Mater. Energy system, 3 (1981)7.
- 171d. T.J.F. Quinn, ASLE Trans, 10 (1967)158.
- 171e. R.M. Bentley and D.J. Duguet, ASM Materials Science Seminar, Pennsylvania, 1980.
- 171f. S. Jahanmir, 'Fundamentals of Tribology,' N.P. Suh and N. Saka, Eds., Proc. Int. conf. on the Fundamentals of Tribology, held at MIT, Massachusetts (June 1978) 461.
- 171g. Y. Kimura, 'Fundamentals of Friction and Wear of Materials, ASM Materials Science Seminar, Pennsylvania, D.A. Rigney, Ed., ASM, Ohio (1981) p.187.
- 171h. C.S. Yust, Int. Met. Revs., 30 (3) (1985) 141.
- 171i. Horst Czichos, 'Tribology,' Elsevier Scientific publishing company (1986) p.105.
- 171j. D.A. Rigney and W.A. Glaeser, Wear, 46, (1978) 241.
- 171k. Ref. No. 1711, p. 459.
- 193a. Ref. No. 171g, pp. 235-289.